



HAL
open science

High-speed confined granular flows down smooth inclines

Yajuan Zhu

► **To cite this version:**

Yajuan Zhu. High-speed confined granular flows down smooth inclines. Structural mechanics [physics.class-ph]. Université Rennes 1, 2021. English. NNT : 2021REN1S058 . tel-03522753

HAL Id: tel-03522753

<https://theses.hal.science/tel-03522753>

Submitted on 12 Jan 2022

HAL is a multi-disciplinary open access archive for the deposit and dissemination of scientific research documents, whether they are published or not. The documents may come from teaching and research institutions in France or abroad, or from public or private research centers.

L'archive ouverte pluridisciplinaire **HAL**, est destinée au dépôt et à la diffusion de documents scientifiques de niveau recherche, publiés ou non, émanant des établissements d'enseignement et de recherche français ou étrangers, des laboratoires publics ou privés.

THESE DE DOCTORAT DE

L'UNIVERSITE DE RENNES 1

ECOLE DOCTORALE N° 596

Matière, Molécules, Matériaux

Spécialité : *Physique*

Par

Yajuan ZHU

Ecoulements Granulaires Confinés Sur Forte Pente

Thèse présentée et soutenue à Rennes, le 8 Octobre 2021

Unité de recherche : Institut de Physique de Rennes – UMR 6251

Rapporteurs avant soutenance :

Thierry FAUG Chargé de Recherche, INRAE, Université Grenoble Alpes
Nicolas TABERLET Maître de Conférences, Laboratoire de Physique, Ecole Normale Supérieure de Lyon

Composition du Jury :

Président : Patrick RICHARD Directeur de recherche, IFSTTAR, Université Nantes Angers Le Mans

Examineur : Lydie STARON Chargée de recherche, CNRS, Institut d'Alembert, Sorbonne Université

Co-encadrants de thèse :

Alexandre VALANCE Directeur de recherche, CNRS, IPR, Université de Rennes 1

Directeurs de thèse :

Renaud DELANNAY Professeur, IPR, Université de Rennes 1

Remerciements

Je tiens à exprimer, dans un premier temps, mes plus vifs remerciements à Renaud DELANNAY et Alexandre VALANCE qui ont encadré ma thèse. Je les remercie pour m'avoir accompagné tout au long de cette thèse. Particulièrement pour ces deux dernières années, pendant la durée de Covid, je les remercie pour leur patience, leur confiance et leur aide.

J'adresse également mes remerciements à Patrick RICHARD, Lydie STARON, Thierry FAUG et Nicolas TABERLET, qui m'ont fait l'honneur d'être membres de mon jury de thèse.

Je remercie Bénédicte FAURE et Éric COLLET pour leur aide pendant la confinement et aussi le directeur du laboratoire Jean-Christophe SANGLEBŒUF. Et aussi Valérie FERRI et Amandine POIRIER tout au long de cette thèse.

Je remercie les membres des collectifs au sein desquels j'ai pu grandir intellectuellement. Je pense aux membres du laboratoire IPR, surtout aux membres du département Milieux Divisés. Avec une attention particulière pour Jean-Luc en face de moi dans mon bureau, mon compagnon de route au quotidien : il m'a beaucoup aidé pendant la thèse ; pareillement à Nolwenn, Jean-Baptiste, Philippe, Édouard, Luc, Sean et bien entendu le responsable de notre équipe Hervé à qui je dis un grand merci.

Enfin, je souhaite témoigner une infinie reconnaissance aux membres de ma famille qui m'ont voué un soutien affectif et effectif inconditionnel, notamment à mes parents, qui ont supporté ces années d'indisponibilité, à mon frère Yashuai, et ma sœur Yaqiu, qui m'ont apporté un soutien indéfectible, ainsi qu'à mes amis toujours présents quand j'étais dans le besoin.

Résumé étendu en français

Ce travail de thèse porte sur les écoulements granulaires sur un fond plan incliné et lisse, confinés entre deux parois également lisses. Ces écoulements ont été simulés numériquement en utilisant la méthode des éléments discrets. Dans cette étude, nous avons considéré une très large gamme d'angles d'inclinaison et de débits, et différentes largeurs du canal, en se focalisant sur les régimes stationnaires. Nous avons également fait varier les paramètres mécaniques des grains et des parois, notamment le coefficient de restitution grain/grain et les coefficients de frottement grain/grain et grain/parois.

Ce manuscrit se divise en 6 chapitres. Le premier chapitre est un état de l'art portant sur les écoulements granulaires sur plan incliné. Dans le deuxième chapitre, nous étudions numériquement l'écoulement de particules sphériques de diamètre D dans un canal de largeur $W = 68D$, en faisant varier l'angle d'inclinaison θ et le nombre de particules impliquées dans l'écoulement. Au chapitre 3, nous étudions l'influence de la largeur du canal sur les caractéristiques de l'écoulement. Le chapitre 4 porte sur le rôle du coefficient de restitution grain/grain. Le chapitre 5 s'intéresse à l'effet d'autres paramètres mécaniques : coefficients de frottement grain/paroi et grain/grain. Le chapitre 6 expose la conclusion et les perspectives.

Le premier chapitre présente l'état de l'art sur les écoulements sur plan incliné. Lorsque l'angle d'inclinaison est faible, des écoulements stationnaires établis, unidirectionnels et denses, sont observés. Avec l'augmentation de l'angle d'inclinaison (typiquement au-dessus de 20 degrés), on observe une déstabilisation des écoulements denses avec l'apparition de rouleaux et une augmentation de la longueur d'établissement, si bien que les écoulements observés expérimentalement à ces angles-là sont généralement accélérés. Lorsque les écoulements sont confinés entre deux parois, on obtient des régimes stationnaires et établis sur une plus large gamme d'angles d'inclinaison. On observe le même type de transition régime dense/régime à rouleaux mais en restant dans un régime stationnaire. Des simulations numériques récentes [Brodu et al. \(2015\)](#) montrent l'existence de nouveaux régimes à très forts angles (au-delà de 30 degrés). Un régime particulièrement intéressant est le régime dit "supporté" qui présente un noyau dense entouré d'une couche "gazeuse" très diluée. Ce nouveau régime s'avère être un excellent candidat pour expliquer les écoulements naturels à longue portée.

Dans le deuxième chapitre, nous étudions numériquement les écoulements stationnaires obtenus dans une configuration confinée où l'écartement entre les parois est $W = 68d$. Ce travail constitue un approfondissement des résultats obtenus par Nicolas Brodu [Brodu et al. \(2015\)](#). Nous décrivons les différents régimes stationnaires obtenus en fonction de l'angle θ et de la masse par unité de surface mesurée en terme de hauteur H et nous définissons des critères quantitatifs pour caractériser les transitions observées. L'organisation du chapitre est la suivante. Nous présentons en préambule la méthode des éléments discrets utilisée pour les simulations et la géométrie de l'écoulement. Le reste constitue un article publié dans la revue "Granular Matter". Nous fournissons dans celui-ci une étude détaillée des différents régimes stationnaires d'écoulement, à savoir les écoulements denses unidirectionnels, les régimes à rouleaux, les régimes supportés symétriques et asymétriques. Nous décrivons les transitions entre ces régimes en suivant les variations de certaines grandeurs physiques clés, telles que la vorticit , la fraction volumique maximale et l'asym trie du pro-

fil instantané de fraction volumique transversale intégré en profondeur.

Nous montrons ensuite que la vitesse moyenne de ces écoulements est essentiellement contrôlée par la vitesse de glissement, de sorte que les deux vitesses sont fortement corrélées. Ainsi la connaissance et la caractérisation de la vitesse de glissement sont d'une grande importance. Nous montrons en particulier que la vitesse de glissement en régime stationnaire dépend principalement de l'angle d'inclinaison et dépend peu de la hauteur H de grains dans l'écoulement.

Nous étudions enfin comment le frottement effectif en parois et au fond varie avec l'angle et la masse de l'écoulement. Nous trouvons de façon remarquable que le frottement est une fonction monotone croissante qui dépend uniquement d'un nombre sans dimension, le nombre de Froude, construit à partir de la vitesse de glissement et de la pression mesurées en parois ou au fond. Nous montrons que cette loi de frottement, appelée par la suite $\mu(Fr)$, est valable à une échelle locale et globale et que celle-ci s'applique non seulement aux écoulements stationnaires, mais aussi aux écoulements instationnaires.

Dans le chapitre 3, nous étudions l'influence de la largeur du canal sur les caractéristiques d'écoulement. Les résultats sont présentés sous la forme d'un article qui sera soumis prochainement. Dans le chapitre précédent, nous avons mis en évidence l'existence d'une loi universelle pour le frottement basal et latéral et nous avons montré que ce dernier peut être décrit comme une fonction unique du nombre de Froude. Ce résultat a été établi pour une largeur de canal fixe $W = 68D$. Il est donc naturel de se demander si la loi de frottement vaut également pour d'autres largeurs de canal. Pour répondre à cette question, nous avons réalisés des simulations pour les largeurs suivantes: $W = 20D, 40D, 60D, 75D$ et $140D$.

On montre que l'effet principal d'une variation de la largeur du canal est de modifier les seuils d'apparition des différents régimes stationnaires. À mesure que la largeur du canal diminue, les transitions se produisent à des angles de plus en plus élevées. Cela conduit à la disparition de certains régimes d'écoulement dans des configurations très confinées. À titre d'exemple, le régime "supporté" disparaît pour une largeur de canal inférieure ou égale $W = 20D$. En revanche, il semble subsister, au moins en régime instationnaire, jusqu'à des largeurs arbitrairement grandes. En d'autres termes, les parois latérales ne sont probablement pas la cause de l'existence du régime d'écoulement "supporté", mais peuvent être la cause de sa disparition.

Par ailleurs, nous montrons que la vitesse moyenne stationnaire V_L des écoulements supportés obéit à des lois d'échelles très simples avec H et W :

$$V_L - V_L^c \propto W^{0.7} H^{0.3} (\sin \theta - \sin \theta_c) , \quad (1)$$

où θ_c l'angle critique au-dessus duquel les états supportés apparaissent et V_L^c est leur vitesse critique. On trouve que θ_c diminue avec W ($\theta_c \approx 26.5^\circ$ pour $W = 40D$ et $\theta_c \approx 23.5^\circ$ pour $W = 140D$) alors que la vitesse critique est indépendante de W . Nous confirmons que les vitesses de glissement V_g restent très corrélées à la vitesse moyenne de l'écoulement. Celles-ci dépendent de la même façon de W mais sont indépendantes de H :

$$V_g - V_g^c \propto W^{0.7} (\sin \theta - \sin \theta_c) . \quad (2)$$

Un des résultats majeurs de ce chapitre concerne les lois sur le frottement et la fraction volumique en parois et au fond (i.e., $\mu(Fr)$ et $\phi(Fr)$). Nous montrons que ces lois restent valables et sont inchangées quand on modifie la largeur du canal ce qui tend à montrer l'universalité de celles-ci. Ces lois fournissent ainsi une description complète des conditions

aux limites aux parois et au fond. Nous proposons une expression approchée de ces lois à partir de fonctions exponentielles:

$$\mu = \mu_2 + (\mu_1 - \mu_2) \exp\left(-\frac{Fr}{Fr_{\mu_0}}\right) \quad (3)$$

$$\phi = \phi_2 + (\phi_1 - \phi_2) \exp\left(-\frac{Fr}{Fr_{\phi_0}}\right) \quad (4)$$

où $Fr = V / \sqrt{P/\rho}$ est le nombre de Froude construit sur la vitesse de glissement V et la pression P en parois. Les coefficients $\mu_1, \mu_2, Fr_{\mu_0}, \phi_1, \phi_2$ et Fr_{ϕ_0} sont des paramètres indépendants de la largeur du chenal mais ils peuvent être sensibles aux paramètres mécaniques des grains et des parois comme nous le verrons dans le chapitre suivant.

Nous avons regardé quelles étaient les propriétés de l'écoulement qui peuvent être décrites par la théorie cinétique des gaz granulaires. Nous montrons que les pressions et les contraintes cisailantes au niveau des parois et du fond sont relativement bien décrites par les prédictions de la théorie cinétique tant que l'écoulement n'est pas trop dense. Nous avons aussi fait quelques tests préliminaires pour savoir si la rhéologie $\mu(I)$ est pertinente pour décrire la rhéologie de nos écoulements. Les écoulements denses et les régimes à rouleaux semblent pouvoir être décrits correctement par cette rhéologie.

Une autre loi importante a été mise en évidence. Elle concerne la hauteur de frottement Z qui caractérise la hauteur sur laquelle le frottement latéral contribue de manière significative. Cette hauteur est bien sûr inférieure à la hauteur totale de l'écoulement h . Nous trouvons que le rapport (Z/H) ne dépend que de la fraction volumique moyenne de l'écoulement $\bar{\phi}$ et qu'il est une fonction monotone décroissante. Cette loi combinée avec les versions globales des lois $\mu(Fr)$ et $\phi(Fr)$ fournit les informations nécessaires pour résoudre les équations régissant la dynamique du système.

Le chapitre 4 étudie l'effet de la variation du coefficient de restitution e sur les propriétés des écoulements. Le coefficient e caractérise l'élasticité de la collision entre les grains. Un coefficient égal à 1 correspond à une collision parfaitement élastique alors qu'une valeur inférieure à 1 indique une collision inélastique. Plus e est petit, plus la dissipation est importante. Les résultats de nos simulations indiquent que le coefficient de restitution e joue un rôle majeur notamment sur les propriétés cinématiques de l'écoulement. La vitesse moyenne stationnaire de l'écoulement augmente lorsque e diminue. Cet effet contre-intuitif s'explique par le fait que l'écoulement se contracte lorsque la dissipation augmente. De ce fait, l'écoulement présente une hauteur plus faible et a ainsi une surface de frottement réduite lui permettant d'augmenter sa vitesse. On montre également qu'un abaissement du coefficient de restitution favorise l'apparition des régimes supportés. Ainsi, il est possible d'obtenir des écoulements supportés à $W = 20D$ si on utilise un coefficient de restitution abaissé. De nouvelles figures d'écoulement apparaissent aussi quand on baisse e , avec des structures secondaires dont la direction d'enroulement est très sensible aux variations de e . Ainsi un abaissement de e peut conduire à un changement du sens de rotation des rouleaux.

Nous nous sommes également intéressés à l'effet de e sur les lois $\mu(Fr)$ et $\phi(Fr)$ établies dans les chapitres précédents. Nous montrons que ces lois sont robustes: elles sont invariantes dans leur forme mais peuvent changer de manière quantitative. Une variation de e n'affecte que marginalement la loi $\mu(Fr)$ alors qu'elle a un effet quantitatif majeur sur la loi $\phi(Fr)$. Nous montrons également que la loi sur la hauteur de frottement reste inchangée dans sa forme et ses valeurs. Elle semble avoir un caractère universel (i.e., indépendante des paramètres mécaniques), ce qui sera confirmé dans le chapitre suivant.

Dans le chapitre 5, nous abordons l'effet de la variation des autres paramètres mécaniques sur les propriétés de l'écoulement. On étudie en particulier le rôle des coefficients de frottement grain/grain (μ_{gg}) et grain-paroi (μ_{gw}). L'étude est réalisée pour $W = 40D$. Nous analysons d'abord comment ces paramètres mécaniques modifient la vitesse moyenne stationnaire de l'écoulement. Nous avons trouvé des effets contrastés. Comme e , μ_{gw} a une influence monotone sur la vitesse moyenne. Une augmentation de μ_{gw} entraîne une diminution de cette vitesse. Ce n'est pas le cas pour μ_{gg} . Nous avons en effet une évolution qui dépend de l'angle d'inclinaison. En dessous d'un certain angle, la vitesse de l'écoulement diminue quand μ_{gg} augmente, tandis qu'au-dessus l'évolution inverse est observée. Cette inclinaison critique dépend de μ_{gw} . Les raisons de ce changement d'évolution restent pour l'instant inexplicables. Les variations de la vitesse moyenne sont liées principalement à des changements de la vitesse de glissement. Ces résultats peuvent donc avoir une certaine utilité pour guider les recherches pratiques et déterminer les conditions optimales pour minimiser la dissipation lors du transport de matériaux granulaires.

Nous étudions ensuite comment les lois de frottement et de fraction volumique aux parois et au fond sont affectées par une modification des coefficients de frottement microscopiques μ_{gw} et μ_{gg} . Nous confirmons la robustesse de ces lois vis à vis des variations des coefficients de frottement microscopiques. Les valeurs des paramètres de ces lois changent mais celles-ci gardent la même forme.

Enfin, la loi qui décrit l'évolution de Z/H en fonction de $\bar{\phi}$ reste inchangée quand on fait varier les paramètres μ_{gg} et μ_{gw} . Cette loi s'avère non seulement indépendante de la largeur de l'écoulement W mais aussi des paramètres mécaniques. Cela suggère fortement que cette loi doit résulter d'une équation de conservation que nous n'avons pas encore identifiée.

En conclusion, nous avons réalisé des simulations numériques d'écoulements granulaires, confinés entre parois lisses, en faisant varier de manière systématique l'angle d'inclinaison du canal et la hauteur (masse par unité de surface) H de l'écoulement pour des largeurs de canaux allant de $W = 20D$ à $W = 140D$. Nous avons également fait varier les paramètres mécaniques du système, dont le coefficient de restitution normal entre grains, le coefficient de frottement grain/grain et le coefficient de frottement grain-paroi. Nous avons montré que la vitesse moyenne stationnaire de ces écoulements est essentiellement contrôlée par la vitesse de glissement, de sorte que les deux vitesses sont fortement corrélées. Ainsi comprendre comment la vitesse de glissement évolue avec H , θ et W est une question cruciale. Nous avons donc étudié en détail les caractéristiques de ces écoulements et mis en évidence que le frottement et la fraction volumique aux parois et au fond peuvent s'exprimer comme des fonctions simples du nombre de Froude pariétal construit à partir de la vitesse de glissement et la pression. Ces lois sont robustes aux modifications des propriétés mécaniques des particules et des parois. Seuls les paramètres de ces lois sont affectés par ces changements. Les relations entre les paramètres de ces lois et les paramètres mécaniques du système sont, pour certaines d'entre elles, complexes et encore difficiles à interpréter.

Nous avons identifié quelques pistes importantes pour de futures recherches. Une extension de notre travail au cas des écoulements instationnaires de même qu'une confirmation expérimentale des résultats numériques sont des perspectives intéressantes. Ces deux questions sont en fait étroitement liées. Les écoulements rapides stationnaires sont difficiles à réaliser dans des expériences réelles parce qu'ils nécessitent une très grande longueur de chute. Par conséquent, les écoulements rapides expérimentaux sont souvent observés dans des états non matures (accélérés). Ainsi, si nous avons une compréhension claire des écoulements instationnaires, cela pourrait grandement aider à l'analyse et à l'interprétation

des écoulements expérimentaux rapides.

Aussi, la description rhéologique de ces écoulements rapides reste une question ouverte. Nous ne l'avons que timidement abordé dans ce travail de thèse. Enfin, les travaux expérimentaux sur les écoulements rapides se heurtent à la difficulté d'accéder à la structure interne de l'écoulement et de mesurer les forces mises en jeu. L'effort devrait se porter sur le développement de nouvelles techniques expérimentales pour sonder l'intérieur de l'écoulement et quantifier les forces de frottement aux parois et au fond.

Contents

1	State of the art	1
1	Introduction	1
2	Unconfined flows	3
2.1	Conditions for SFD flows	4
2.2	SFD flows	5
2.2.1	Dense flows	5
2.2.2	Rolls	10
2.3	Unsteady flows	11
3	Confined flows	11
3.1	Conditions for SFD flows	11
3.2	SFD flows	12
3.2.1	Dense flows	12
3.2.2	Roll regime	14
3.2.3	Supported flow regime	14
3.2.4	Effective friction coefficient at boundaries	16
3.2.5	Scaling law	17
3.2.6	SSH and others flows	18
3.3	Unsteady flows	20
4	Questions	20
5	Research aims and approaches	21
6	Outline of dissertation	21
2	Scaling and wall friction laws for channel width $W = 68D$	23
1	Introduction	23
2	Modeling	23
3	Scaling and wall friction laws for $W = 68D$ (copy published article)	26
4	Conclusion and perspectives	39
3	Effect of channel width on confined granular flows	41
1	Introduction	41
2	Article: Discrete simulations of confined high-speed granular flows: Influence of the channel width	41
2.1	Introduction	41
2.2	DEM	42
2.3	Transient	43
2.4	Phase diagram	45
2.5	Flow features for $W = 40D$	47
2.5.1	Mean flow velocity	47

2.5.2	Packing fraction, velocity and temperature profiles	48
2.5.3	Velocity and temperature at the bottom and side walls	50
2.5.4	Characterization of the flow regime transition	53
2.5.5	Effective friction and packing fraction at the boundaries	57
2.5.6	Effective frictional flow height Z	60
2.6	Role of the channel width W	61
2.6.1	On the critical inclination for the appearance of the supported flows	61
2.6.2	On the velocity scaling	63
2.6.3	On the friction and packing fraction law at the walls	63
2.6.4	On the effective frictional flow height Z	64
2.7	Kinetic theory for granular gas and $\mu(I)$ rheology	65
2.8	Phenomenological model for predicting the slip velocities at the boundaries	68
2.9	Conclusion	69
3	Perspectives	69
4	The effect of normal restitution coefficient e on confined granular flows	71
1	Introduction	71
2	Dissipation in rapid gravitational granular flows (copy of a published article)	72
3	The effect of normal restitution coefficient e on confined granular flows	77
3.1	Introduction	77
3.2	Characterization of the flows at $H = 5D$	77
3.2.1	Phase diagram in space $e - \theta$	77
3.2.2	Cross-section of the flows	79
3.2.3	Variation of effective flow height	81
3.3	Mean velocity scaling law	81
3.3.1	Effect of restitution coefficient on mean flow velocity at $H = 5D$	81
3.3.2	Cross-sections of the flow at $H = 12D$	82
3.3.3	Mean velocity scaling law	84
3.4	Boundary friction and packing fraction laws	85
3.4.1	Effective coefficient of friction	85
3.4.2	Mean packing fraction	85
3.5	Effective frictional flow height Z	86
4	Conclusion and perspectives	87
5	The effect of mechanical parameters e, μ_{gw}, μ_{gg} on granular flows	89
1	Introduction	89
2	Phase diagram in the parameter space $e - \theta, \mu_{gw} - \theta, \mu_{gg} - \theta$	89
2.1	Parameter space $e - \theta$	89
2.2	Parameter space $\mu_{gw} - \theta$	91
2.3	Parameter space $\mu_{gg} - \theta$	91
3	Kinematic and structural properties of the flow	94
3.1	Mean flow velocity vs mechanical parameters	94
3.2	Packing fraction, velocity and temperature profiles vs e	95
3.3	Packing fraction, velocity and temperature profiles vs μ_{gw}	98
3.4	Packing fraction, velocity and temperature profiles vs μ_{gg}	100
3.5	Cross-influence of the mechanical parameters	104

4	Friction and packing fraction laws	104
4.1	Local effective friction law	105
4.2	Global effective friction law	106
4.3	Packing fraction law	108
4.4	Effective frictional flow height Z	110
5	Conclusion	111
6	Conclusion and perspectives	113
1	Conclusion	113
2	Perspectives	114

Chapter 1

State of the art

1 Introduction

A granular material can be defined as any material composed of many individual solid particles, irrespective of the particle size. In this thesis, we will only study dry granular flows, with grain size ($D > 100\mu\text{m}$), in this case, we do not have to take into account electrostatic interactions, capillary or van der Waals forces etc. . Even with this restriction, the behavior of assemblies of grains can be very complex. As we know, granular flows are found in many industrial processes, especially in the mining, food-processing and building industries like transportation, powdering, mixing, storage etc. (Ramaioli, 2008; Smith and T., 2015; Torres-Serra et al., 2017). They are also important in nature, mountain slopes, avalanches and volcanic edifices (Drake, 1990; Calder et al., 2002; GDR MiDi, 2004; Delannay et al., 2017), and even in the area of space exploration (Treiman and Louge, 2004). In fact, the second most common substance manipulated by humans is granular material (Duran, 1997), the importance of granular materials should not be underestimated.



Figure 1.1: An example of granular flow in nature. Pictured: Earthquake-triggered landslide in Las Colinas, Santa Tecla (El Salvador, 13 January 2001).

The understanding and modeling of granular flows is still an active field of research; there is no unified theory describing the diversity of the behaviors observed in granular flows. They often exhibit flow regimes where "solid", motionless, phases coexist with "liquid" ones (dense flows) and "gaseous" ones (dilute flows) (Taberlet et al., 2003; Richard et al., 2008; Forterre and Pouliquen, 2008). The complexity of the granular flows mainly arises from the nature of the interactions between grains: according to the relative contribu-

tion of brief, collisional contacts dominant in the dilute parts compared to enduring contacts associated with friction, dominant in the dense parts, the macroscopic behavior of the flows changes drastically in space and time (Treiman and Louge, 2004).

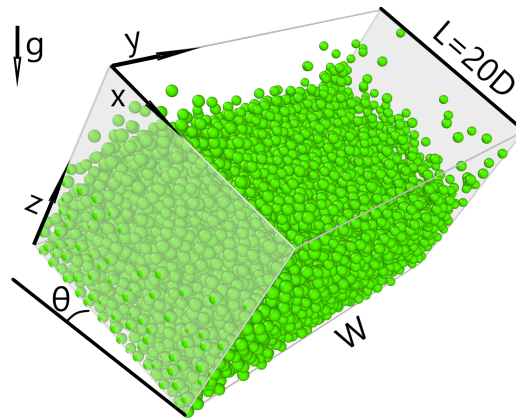


Figure 1.2: Scheme of the simulated system. The channel is inclined with an angle θ with respect to the horizontal. Cartesian coordinate system with unit vectors x along the flow, y perpendicular to side-walls, and z normal to bottom.

Gravity driven dry Granular flows down an inclined plane are important for a large number of problems. For example, rock avalanches are composed of individual particles flowing down an inclined plane. Therefore they are important in natural as well as in industrial processes (grain and mineral transport). So it is of great significance to understand these flows and develop predictive models. For studying granular flows, two different methods are mainly used: experiment and numerical simulations using discrete elements (DEM).

This thesis focus on flows down an inclined plane chute. According to the lateral boundary conditions, granular flows are usually divided into unconfined flows and confined flows. The numerical simulations generally have periodic boundary conditions in the flow direction: x (see figure 1.2). In the width direction (y) they may also have periodic condition, in this case they produce "unconfined flows" without lateral boundaries. On the contrary, there are side walls perpendicular to y -axis in the case of "confined flows". Experimental set-ups for granular flows always have side walls. If the grains are not injected along the whole width, they begin by spreading out until they flow between levees or occupy the entire width, the flow is then confined between the side walls. It is an important question to know what is the effect of these side-walls on the flow. When the walls are very far apart from each other, it is tempting to presume that their effect on the flow is negligible, so that the flow could be considered as unconfined and compared to unconfined numerically simulated flows. We lack here a precise definition to distinguish when the influence of the side-walls on granular flows can be ignored. This is one of the reasons to study confined granular flows.

Starting from initial position and velocity, which are chosen according to some rule in the numerical simulations, and given by the way of injection in the experiments, the grains begin to move. The position and velocity of the grains will thus evolve with time, giving birth to a flow. The properties of this flow consequently change, for example, its mean velocity increases. After some time, and thus some travelled distance, the properties of the flow eventually become invariant in time and space, in the direction of the flow. The transient is thus followed by a stationary fully and developed flow (SFD). In fact, the SFD flow is a limit which is never exactly achieved. Although the amount of change in velocity, for example, is getting smaller and smaller, the velocity is always changing. Therefore, it is

difficult to distinguish between accelerating flows with small acceleration and SFD flows. We lack a precise definition to determine when we can ignore the change and study it as SFD flows.

In the following chapters we will give some of the results described in the literature, concerning first the unconfined flows, and then confined flows, in each case we will point out in which conditions appear the SFD flows, their different flow regimes and their properties. We will also describe what is known about transients.

2 Unconfined flows

Many chute flow experiments and numerical simulations have been carried out and different configurations have been investigated, changing the bumpiness of the bed, using different kinds of materials etc. The typical experimental set-up of unconfined flows down an inclined plane is shown in Fig.1.3. It consists of an inclined plane at an angle θ from horizontal.

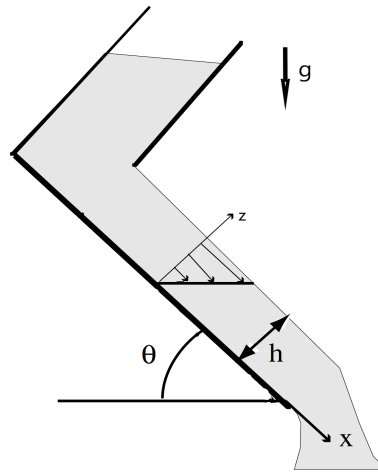


Figure 1.3: Typical experimental configuration of unconfined flows on inclined plane extracted from article [GDR MiDi \(2004\)](#).

If we increase the inclination angle θ above a critical angle θ_{start} , an initially static bed of thickness h will start to flow. Conversely, if we decrease the inclination, an initially flowing grain layer of thickness h will stop when the inclination decreases below θ_{stop} . These two critical angles, θ_{start} and θ_{stop} , depend on h . Correspondingly, for a given inclination angle θ , there exists a critical thickness h_{stop} where the flow stops. [Pouliquen \(1999\)](#) studied the change of the critical thickness h_{stop} with the inclination angles θ , using a 2m long and 70cm wide plane (data used in this section are summarised in in Table (1.1)). Those critical numbers divide the phase diagram (h, θ) in two regions (see Fig.1.4): no flow for $h < h_{stop}$; for $h > h_{stop}$ the particles flow. The curves h_{stop} exhibit the same shape for all the materials (see Fig.1.4 (b)) and can be fitted by:

$$h_{stop}(\theta) = LD \frac{\mu_2 - \tan \theta}{\tan \theta - \mu_1} \quad (1.1)$$

where D is the particle diameter, L is a characteristic dimensionless thickness, $\mu_1 = \tan \theta_1$, $\mu_2 = \tan \theta_2$; θ_1 corresponds to the angle where h_{stop} diverges, θ_2 to the angle where h_{stop} vanishes. The fit parameters depend on both the bulk material and roughness conditions

of the base (see Fig.1.4(a,b)). [Weinhart et al. \(2012\)](#) showed that for a nearly smooth base, steady flows initiate and reside at or very tightly around one small inclination for all heights. This conclusion is in agreement with the angle found in the experimental research of [Goujon et al. \(2003\)](#). This shows that h_{stop} does not exist for a smooth base. In their experiments [Louge and Keast \(2001\)](#) find a relatively large angle range for which SFD flows occur. This is an indication of confinement effects. From this point of view, the experiments of [Louge and Keast \(2001\)](#) are confined flow experiments.

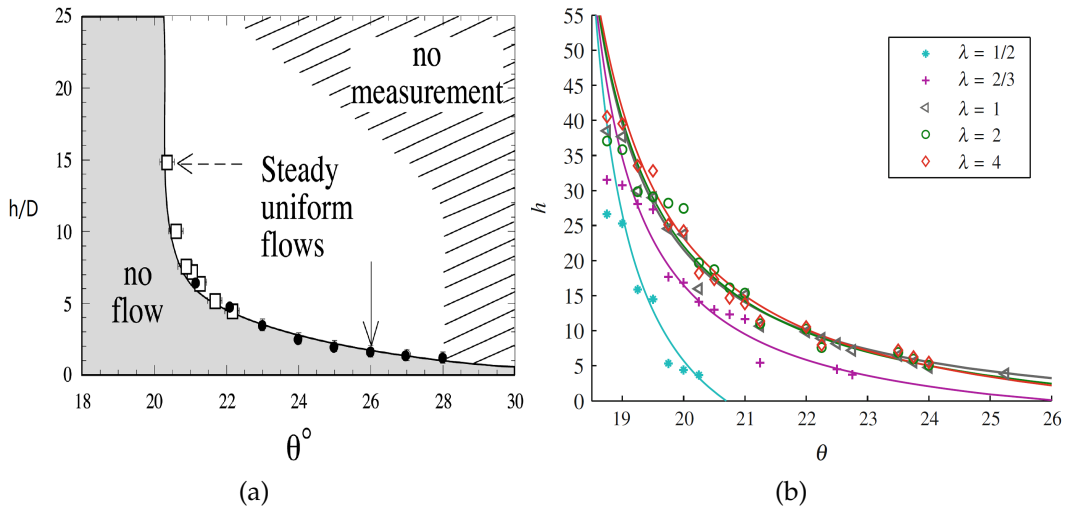


Figure 1.4: (a) Phase diagram in space $(h/D, \theta^\circ)$ extracted from [Pouliquen \(1999\)](#). (b), dimensionless h as a function of θ for different basal roughness λ . λ is the size ratio of the flowing particles and those fixed at the base. When λ becomes small, the demarcation line tends to become vertical at $\theta = 12.5^\circ$ (not shown). Extracted from [Weinhart et al. \(2012\)](#).

2.1 Conditions for SFD flows

As already mentioned, when the inclined plane is smooth ([Augenstein and Hogg, 1978](#); [Goujon et al., 2003](#); [Weinhart et al., 2012](#); [Artoni et al., 2012](#); [Kumaran and Bharathraj, 2013](#); [Zhang et al., 2019](#)), SFD flows only exist in a very narrow range of inclination angles. Below these angles the material stops, and above these angles the granular flow seems to continuously accelerate along the inclined plane (or during the whole running time in numerical simulations). On a bumpy bed, for moderate inclinations, the flow becomes SFD after a short time (or distance). But, at large inclinations, the flows continuously accelerate along the slope length L of the plane in experiments and during the whole running time in numerical simulations ([Silbert et al., 2002](#); [Forterre and Pouliquen, 2001](#); [Börzsönyi et al., 2009](#)). For example, [Forterre and Pouliquen \(2001\)](#) have observed continuously accelerating flows for an inclination larger than $\theta = 38^\circ$ and h larger than $20D$ (hatched zone in figure 1.5). In these flows, the granular material flowing out from the reservoir accelerates along the whole slope while the thickness of the granular layer decreases. As we will discuss later in this chapter, these flows exhibit longitudinal rolls. Using numerical method (DEM), [Börzsönyi et al. \(2009\)](#) have also found this instability over a range of parameter values: slope angle 34° – 39° , restitution 0.80–0.95 and width greater than $50D$.

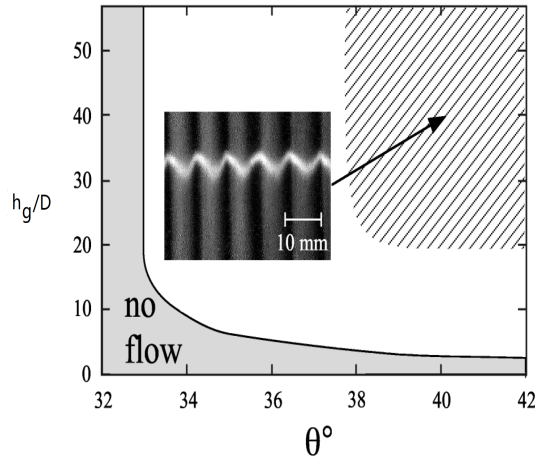


Figure 1.5: Phase diagram in space $(h_g/D, \theta^\circ)$ the roll instability is observed in the hatched zone. The picture is a close-up of the free surface in the saturated regime ($\theta = 41^\circ$ and $h_g = 13\text{mm}$). extracted from article [Forterre and Pouliquen \(2001\)](#).

2.2 SFD flows

There is some experimental research on a flat base ([Augenstein and Hogg, 1978](#); [Goujon et al., 2003](#)), but SFD flows on a smooth base have been mainly studied with numerical methods ([Weinhart et al., 2012](#); [Artoni et al., 2012](#); [Kumaran and Bharathraj, 2013](#); [Zhang et al., 2019](#)). A much larger corpus of studies exists on dense granular flows down rough base. The steady fully developed flows have been discussed, in both experiments ([Pouliquen, 1999](#); [GDR MiDi, 2004](#); [Forterre and Pouliquen, 2008](#); [Börzsönyi et al., 2009](#); [Kumaran and Bharathraj, 2013](#)) and numerical simulations ([Silbert et al., 2001](#); [GDR MiDi, 2004](#); [Börzsönyi et al., 2009](#)).

Since it is difficult to reach a steady state, there is not much research on smooth base. So in the following parts, we will start with the rough base and then compare it, when possible, with smooth base.

2.2.1 Dense flows

Velocity scaling law: In the SFD flow regimes, with rough base, [Pouliquen \(1999\)](#) observed that the Froude number built with the mean velocity varies linearly with $\frac{h}{h_{stop}}$:

$$Fr = \frac{\langle V \rangle}{\sqrt{gh}} = \beta \frac{h}{h_{stop}(\theta)} \quad (1.2)$$

Where β is a number independent of the inclination, the bead size, and the roughness of the base.

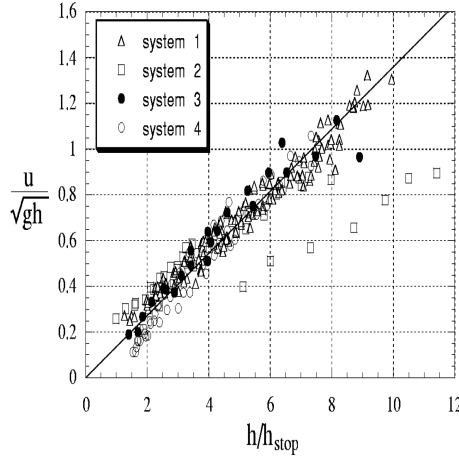


Figure 1.6: Froude number as a function of h/h_{stop} extracted from article [Pouliquen \(1999\)](#).

Velocity profiles [Silbert et al. \(2001\)](#) simulated gravity-driven 3D granular flow on a bumpy base using DEM (with friction coefficient $\mu = 0.5$ and restitution coefficient $e = 0.88$). The bottom of figure 1.7 (a,b) shows that the velocity reaches its maximum at the free-surface of granular flows, and that increasing θ and h increases velocity. The sliding velocity is very small compared to the average speed and can be ignored. The velocity roughly obeys a Bagnold-like profile where $V_x(z) \propto h^\alpha$, with $\alpha \approx 1.5$ ([Bagnold, 1954](#)) :

$$\frac{V_x(z)}{\sqrt{gd}} = A(\theta) \frac{h^{3/2} - (h-z)^{3/2}}{D^{3/2}} \quad (1.3)$$

Where A is a dimensionless coefficient containing the inclination θ dependency. From equation (1.3), it is possible to express the mean flow velocity $\langle V \rangle$ as:

$$\langle V \rangle = \frac{1}{h} \int_0^h V_x(z) dz = \frac{3}{5} \sqrt{gh} \frac{h}{D} A(\theta) \quad (1.4)$$

By identification to the empirical scaling law (equation (1.2)), we get an expression of $A(\theta)$:

$$A(\theta) = \frac{5}{3} \beta \frac{D}{h_{stop}(\theta)} \quad (1.5)$$

For a smooth base, the form of the velocity profile is similar, but the sliding velocity is much greater ([Delannay et al., 2007](#); [Weinhart et al., 2012](#); [Artoni et al., 2012](#); [Kumaran and Bharathraj, 2013](#); [Zhang et al., 2019](#)). The Bagnold velocity profile is a robust feature of dense SFD flows on incline plane and has been checked numerically and experimentally ([Pouliquen, 1999](#); [Silbert et al., 2001](#); [GDR MiDi, 2004](#); [Baran et al., 2006](#); [Börzsönyi et al., 2009](#); [Weinhart et al., 2012](#); [Kumaran and Bharathraj, 2013](#)).

Packing fraction profile For rough bottom, dense SFD flows exhibit a nearly constant packing fraction through the depth. This is nicely shown in the DEM simulations of [Silbert et al. \(2001\)](#) (see Fig.1.7). Packing fraction decreases with increasing inclination but it is rather independent of the thickness of the flows.

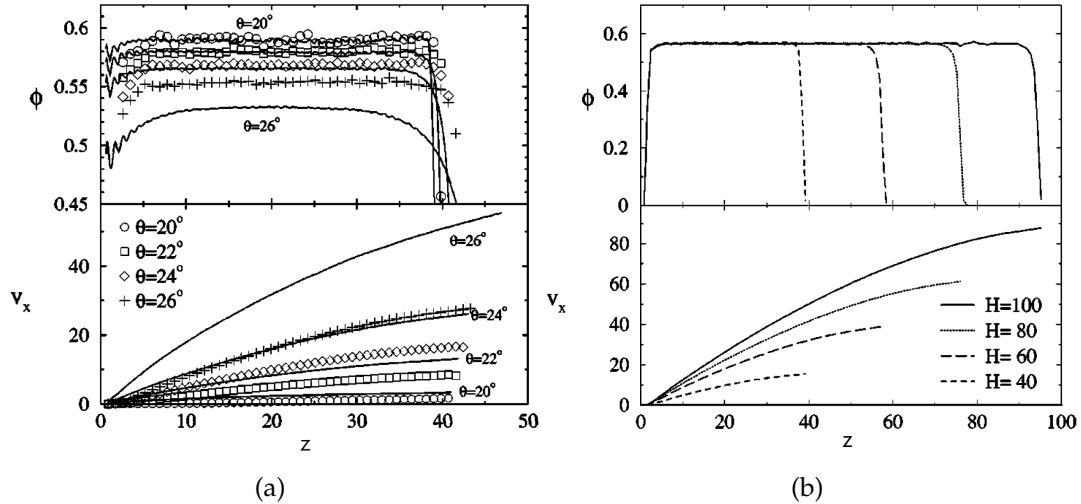


Figure 1.7: Velocity V_x and packing fraction ϕ profiles for thin flows from 3D simulations for (a) various angles $\theta = [20^\circ, 26^\circ]$ at height $H = 40$ and (b) for heights $H = [40, 100]$ at an inclination angle $\theta = 24^\circ$. Extracted from [Silbert et al. \(2001\)](#).

The height H is calculated by the formula: $H = ND^2/A$ (or ND/L in two dimensions), where N is the number of grains, D is the grain diameter and A is the basal area (L is the length in two dimensions). The packing fraction profile for smooth base are similar ([Artoni et al., 2012](#); [Kumaran and Bharathraj, 2013](#)).

Role of particle interaction parameters There is no experience studying the influence of the particle interaction parameters because it is difficult. For bumpy base, [Silbert et al. \(2001\)](#) have studied, by numerical simulations, the sensitivity of the results to variations of the coefficient of restitution e and of the Coulomb friction coefficient μ . Figure 1.8 (a) presents the effect of a variation of the restitution coefficient e on velocity profiles for $\theta = 22^\circ$, $H = 40$ and for $e = 0.58, 0.78, 0.88, 0.98$. The results show that the variation of e has little effect on the flow behavior over this range of e . Nonetheless, we can see that the speed slightly increases as the restitution coefficient e decreases. Similarly, figure 1.8 (b) presents the velocity and volume fraction profiles for the same system as the one described in Figure 1.8 (a), but with a fixed $e = 0.88$ for various friction coefficients $\mu = [0.15, 0.25, 0.5, 1]$. The data shows that the velocity increases with decreasing μ . The packing fraction is weakly dependent of the restitution and friction coefficients, but the packing fraction when $\mu = 0.15$ is slightly smaller.

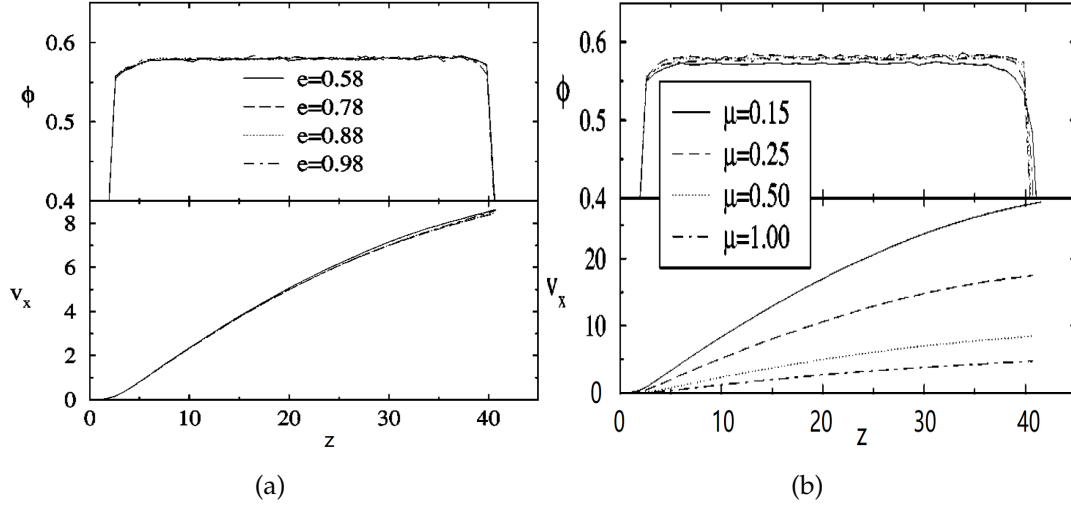


Figure 1.8: Velocity and packing fraction profiles for (a) various restitution coefficients $e = [0.58, 0.98]$ ($\theta = 22^\circ$, $H = 40$) and (b) various friction coefficients $\mu = [0.15, 1]$ ($\theta = 22^\circ$, $H = 40$). Figure extracted from [Silbert et al. \(2001\)](#).

For smooth flat frictional base the velocity profiles exhibit a large sliding velocity at the base, but are always of the Bagnold form. The average velocity decreases as the friction coefficient increases ([Artoni et al., 2012](#)). But if the sliding velocity is subtracted, then unlike for the bumpy base (see Fig.1.8(b)), the averaged velocity does not change when the friction coefficient varies. For smooth base, there is a lack of research on the role of the coefficient of restitution.

Basal friction law for rough bottom From the scaling properties, one can extract some information about the friction forces that arise between the flowing layer and the base. In a SFD regime, a simple depth-averaged force balance on an elementary slice of material yields the following relation:

$$\tau_b = \rho g h \sin \theta$$

where ρ is the density of the granular medium and τ_b is the shear stress at the base. When divided by the normal stress - the pressure, assumed to be hydrostatic: $P_b = \rho g h \cos \theta$ - on the base, the force balance can be written in terms of an effective friction coefficient μ_b defined as the ratio of the shear to the normal stress:

$$\mu_b = \frac{\tau_b}{P_b} = \tan \theta$$

Using the results of [Pouliquen \(1999\)](#), it can be expressed as a simple function of $h_{stop}(\theta)$ by inverting equation (1.1):

$$\mu_b = \frac{\mu_1 \frac{h_{stop}}{LD} + \mu_2}{1 + \frac{h_{stop}}{LD}} = \mu_1 + \frac{\mu_2 - \mu_1}{1 + \frac{h_{stop}}{LD}}$$

Additionally, we have seen that the Froude number associated to the mean flow velocity $Fr = \langle V \rangle / \sqrt{gh}$ is proportional to h/h_{stop} such that μ_b can be written as an explicit function of $\langle V \rangle$ and h :

$$\mu_b = \mu_1 + \frac{\mu_2 - \mu_1}{1 + \beta \frac{h\sqrt{gh}}{LD\langle V \rangle}} \quad (1.6)$$

This empirical relation raises several issues. The first one concerns the high velocity regime. Equation (1.6) indicates that the effective friction tends to a limit equal to $\mu_2 = \tan \theta_2$ when the mean velocity tends to infinity. The existence of an upper limit implies that SFD flows cannot be obtained for inclination greater than θ_2 . The second issue concerns the low velocity regime which is not well described by equation (1.6). The latter indicates that SFD flows can be achieved for arbitrary small thickness h as soon as the inclination is greater than $\theta_1 = \arctan(\mu_1)$. However, one should keep in mind that equation (1.6) was derived using the equation (1.2) which is only valid for $h > h_{stop}$ and thus for $Fr > \beta$. Consequently, equation (1.6) is also only valid for $Fr > \beta$.

In summary the effective friction μ_B can be written as:

$$\mu_b = \mu_1 + \frac{\mu_2 - \mu_1}{1 + \frac{h}{LD} \frac{Fr_0}{Fr}} \quad (1.7)$$

where $Fr_0 = \beta$, with the requirement $Fr > Fr_0$.

Rheology $\mu(I)$ The $\mu(I)$ rheology (da Cruz et al., 2005) (in two dimensions 2D) stipulates that in a 2D uni-directional dense granular flow (homogeneous simple shear flow), the local effective friction μ_{eff} - defined on surfaces parallel to the base as the ratio of the local shear stress to the normal stress - is a unique function of the local inertial number. The dimensionless inertial number I is the square root of the previously defined Savage number (Savage and Hutter, 1989) or Coulomb number (Ancy et al., 1999). It can also be expressed as the ratio of two time scales: $I = \frac{T_p}{T_\gamma}$. T_p is the confinement time scale: $T_p = D \sqrt{\frac{\rho}{P}}$, where P is the normal stress (pressure) and ρ the density. T_γ , is the typical time scale of deformation: $T_\gamma = \frac{1}{\dot{\gamma}}$, with shear rate $\dot{\gamma} = \frac{dv}{dz}$ (see Fig. (1.9)).

$$\mu_{eff} = \frac{\tau}{P} = \mu_{eff}(I) \quad (1.8)$$

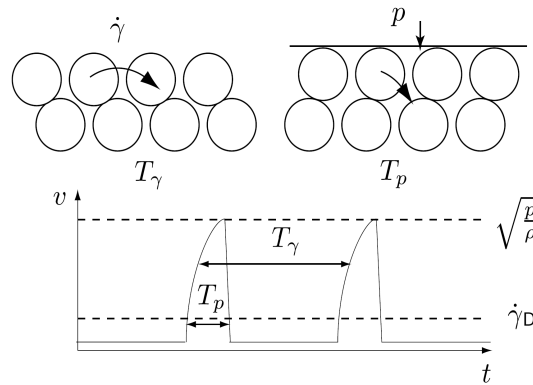


Figure 1.9: Schema presenting the physical meaning of the typical time of deformation and of the confinement time scale. Figure extracted from GDR MiDi (2004).

Based on experiments, several function forms have been proposed for $\mu_{eff}(I)$. The most widely used has the following form (see Fig.1.10):

$$\mu(I) = \mu_1 + \frac{\mu_2 - \mu_1}{I_0/I + 1} \quad (1.9)$$

where I_0, μ_1, μ_2 are parameters which are obtained empirically. The parameters μ_1, μ_2 have the same meaning that those introduced for the basal friction law (equation (1.6)). Indeed, if we calculate the value I_b of the number I at the base of the flow for a Bagnold profile, and we replace its expression in equation (1.9), we recover an equation of the same form as the basal friction law, we can interpret it as $\mu(I_b) = \mu_b$.

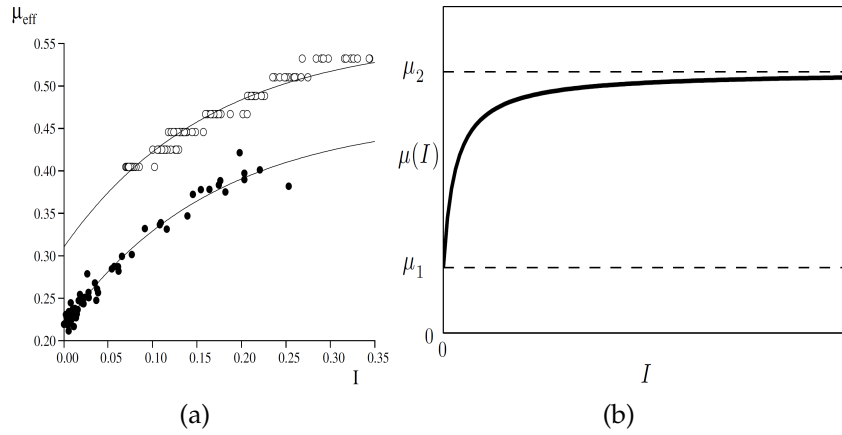


Figure 1.10: The form of $\mu(I)$. Figure extracted from [GDR MiDi \(2004\)](#).

The research in this area is mainly focused on the rough base, and there is a lack of research on the smooth base. The rheology $\mu(I)$ has been tested ([GDR MiDi, 2004](#); [da Cruz et al., 2005](#); [Baran et al., 2006](#); [Forterre and Pouliquen, 2008](#); [Börzsönyi et al., 2009](#)) for small I : $I < 0.5$. If we have a large I or a very small I , the rheology $\mu(I)$ has been shown to be ill-posed at least for incompressible flows ([Barker et al., 2015](#)).

2.2.2 Rolls

For inclination $\theta = 37^\circ$, [Börzsönyi et al. \(2009\)](#) have found that longitudinal rolls exist in numerical simulations of SFD flows on a bumpy base (data used in this section are summarised in Table (1.1)). This convection is similar to the *Rayleigh – Bénard* regime ([Eshuis et al., 2010](#)). In bumpy base system, the bumpiness of the base leads generally to a higher granular temperature at the base. The granular bed is then heated from below and cooled from above. [Börzsönyi et al. \(2009\)](#) showed that as H increases, there is a transition from a dilute regime to a dense regime. Meanwhile, both regimes exhibit rolls. In the diluted regime, there are longitudinal rolls leading to a downward motion in the denser part of the flow, where the height is lower (see figure 1.11). In the dense regime, there are longitudinal rolls leading to a downward motion where the height is higher, in the dense part of the top flow. With the emergence of dense rolls, [Börzsönyi et al. \(2009\)](#) have observed that the flow height is large and the density is inverted i.e. the density decreases with z at the bottom (the same situation appeared in [Forterre and Pouliquen \(2002\)](#) for rolls in accelerated flows). Also [Börzsönyi et al. \(2009\)](#) observed a strong correlation between the packing fraction and the inertial number I for both dense and diluted roll regimes.

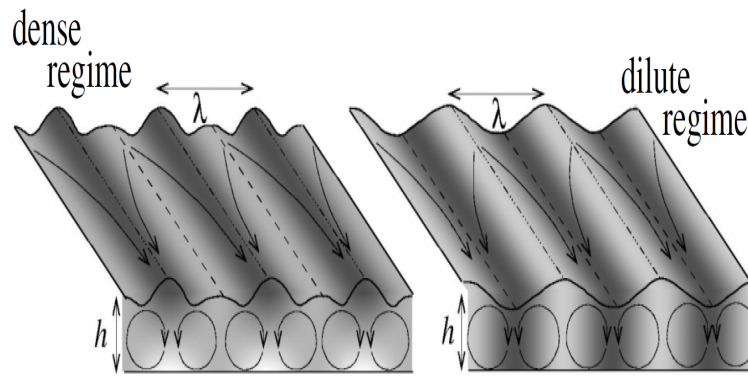


Figure 1.11: The dense regime (left) and dilute regime (right) flow structures. The gray levels indicate the local density.

However, for this inclination where longitudinal rolls exist, it takes a long running time (a few months) to reach the steady state, so correspondingly, if experimental methods were adopted, a very long plane would probably be needed to reach the stable state. So there are currently no experiments to prove the existence of rolls for unconfined SFD flows. For smooth base, there is a complete lack of research on rolls regime for unconfined flows.

2.3 Unsteady flows

Before reaching a SFD flow regime, the particles which compose the flow have to accelerate (or decelerate). This acceleration generally decreases with time, the velocity eventually becomes constant to enter the SFD regime. In experiments, the length of the accelerating phase changes with the inclination. In numerical simulations, this length corresponds to a running time which also varies with inclination. So if the length or duration of the accelerating phase is too long, we don't observe any SFD flow. The acceleration phase is possibly divided in two parts: a monotonically increasing or decreasing acceleration part (which may occupy the whole acceleration phase), and a constant acceleration part (where the constant is zero if a SFD regime is effectively reached). In their experiments or numerical simulations performed at large inclination angle (see Table (1.1)), [Augenstein and Hogg \(1978\)](#); [Forterre and Pouliquen \(2001\)](#); [Börzsönyi et al. \(2009\)](#) didn't reach SFD regime for both rough and smooth bottom. For rough base, longitudinal rolls exist in both experimental and numerical methods for accelerating flows ([Forterre and Pouliquen, 2001, 2002](#); [Börzsönyi et al., 2009](#)).

3 Confined flows

We report here gravitational granular flows which are confined between two parallel side-walls (see Fig.1.12). In the following, unless otherwise mentioned, x is the flow direction, y the transverse direction perpendicular to the side-walls and z is the direction normal to the base.

3.1 Conditions for SFD flows

Because of the role of lateral walls, a steady state can possibly be obtained, even for very high inclination angles. [Brodu et al. \(2015\)](#) run simulations with $W = 68D$, for a large interval of inclination angles and mass hold-up, up to $t = 1200\sqrt{D/g}$ time units. All the flows he

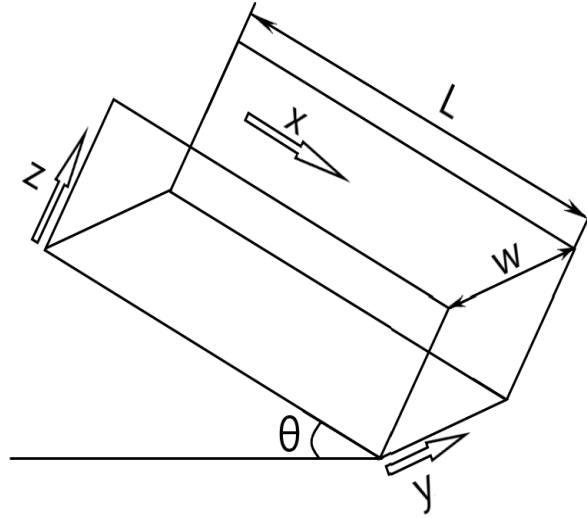


Figure 1.12: Inclined plane configuration with two parallel rigid walls separated by a gap W .

studied become SFD via an exponential saturation with time. Furthermore, flows definitely stop below $\theta \approx 14^\circ$. The transient regime toward a stationary regime can be described by:

$$V(t) = V_L - (V_L - V_0) \exp(-t/\tau) \quad (1.10)$$

Here $V(t)$ is the average flow velocity at time t , V_0 is the initial flow velocity and V_L is the stationary limit of the mean velocity. τ is the characteristic time which depends on the mass hold-up H and on the inclination angle θ .

But experimentally with a slope of limited length, [JOP et al. \(2005\)](#); [Holyoake and McElwaine \(2012\)](#); [Faug et al. \(2015\)](#) showed that confined granular flows accelerate along the whole chute when its inclination is larger than a critical value that depends of the channel length and width, of the mass flow rate etc.. For the accelerating flows, they didn't indicate whether the acceleration decreases or remains constant.

3.2 SFD flows

3.2.1 Dense flows

As shown experimentally ([Louge and Keast, 2001](#); [JOP et al., 2005](#); [Holyoake and McElwaine, 2012](#); [Faug et al., 2015](#); [Heyman et al., 2017](#)) and numerically ([Brodu et al., 2013, 2015](#); [Ralaiarisoa et al., 2017](#); [Zhang et al., 2019](#)) the granular flows bounded by smooth walls and base exhibit considerable slip velocity at the boundaries. The velocity profiles of dense flows, in the sheared portion of the flow above the basal slip, were well reproduced by a Bagnold profile (Eq.1.11), they also exhibit a packing fraction nearly constant through the depth ([Brodu et al., 2013](#); [Faug et al., 2015](#); [Zhang et al., 2019](#)), like unconfined granular flows. The velocity may thus be written under the form:

$$V(z, y) = V_b + A(\theta, y) \sqrt{gD} \left[\left(\frac{h_s}{D} \right)^{\frac{3}{2}} - \left(\frac{z - z_0}{D} \right)^{\frac{3}{2}} \right] \quad (1.11)$$

where $z_0 = 1.5D$ is the thickness of the sliding boundary layer. The sliding velocity V_b is thus defined at $z_0 = 1.5D$: $V_b = V(z_0, y)$ and $h_s = h - z_0$ is the effective thickness of the sheared flow.

Channel flows down flat frictional surfaces, in a dense regime, are adapted to the $\mu(I)$ rheology theory. JOP et al. (2005); Faug et al. (2015), using experimental methods, and Brodu et al. (2013) using numerical simulations, showed that $\mu(I)$ roughly holds.

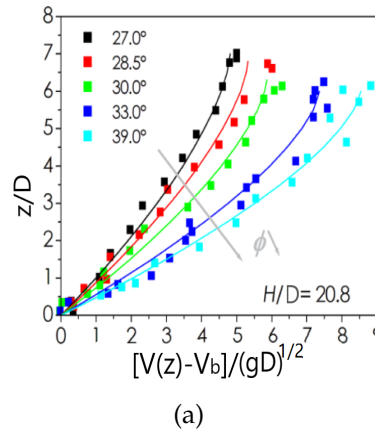


Figure 1.13: Velocity-profiles at the sidewall after subtraction of the basal sliding velocity. The solid lines show the Bagnold fits given by Eq.1.11. Figure extracted from Faug et al. (2015).

Zhang et al. (2019) also show that the walls play an important role, they look at what happens when the coefficient of friction between the grains and the lateral walls is decreased. Figure 1.14 shows that the velocity increases with decreasing friction coefficient at side walls (noted here μ_{ps}), and reaches a maximum when $\mu_{ps} = 0.0$. When $\mu_{ps} = 0.0$, the velocity is the same as for unconfined flows. The velocity profile shows that the velocity is nearly constant (plug flow), except for a thin layer near the bottom that is extremely sheared (boundary layer).

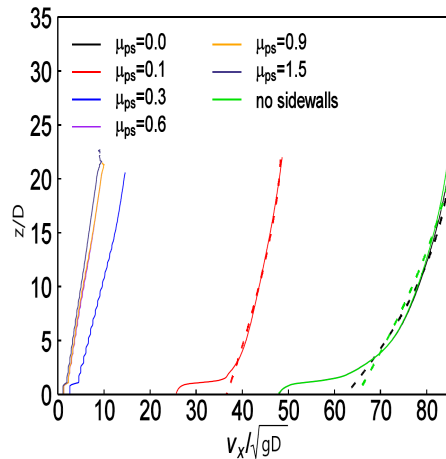


Figure 1.14: Vertical profiles with fixed $\theta = 26^\circ$ and $H = 21D$, for various friction coefficients between particles and side walls μ_{ps} . Figure extracted from Zhang et al. (2019).

So, for dense flows, if we compare the properties of unconfined flows on bumpy bottom with those of confined flows with smooth boundaries, we see that they are qualitatively similar. The main difference is the non-negligible sliding velocity at the boundaries for smooth boundaries, and the possibility of varying the velocity gradient by changing the friction coefficient between the walls and the particles. This shows that $A(\theta, y)$ in equation 1.11 varies with μ_{ps} and probably with the width W of the channel.

3.2.2 Roll regime

As in unconfined flows, roll regimes also exist in confined flows in both experiments and simulations (Brodu et al., 2013, 2015; Heyman et al., 2017; Ralaiarisoa et al., 2017; Zhang et al., 2019). Because of the lateral walls, the rolls can be observed for small inclinations like $\theta = 23^\circ$ (Brodu et al., 2013). Figure 1.15 shows the temperature and transverse velocity map in the cross-section yz plane in SFD flow obtained at $\theta = 23^\circ$. There is a pair of rolls in the traverse plane. The grains move towards the bottom in the center of channel (the denser part of the flow), and with a reverse movement along side walls (lower density zone). This type of rolls is similar to the dense rolls which have been previously observed for unconfined flows on a bumpy base (Börzsönyi et al., 2009).

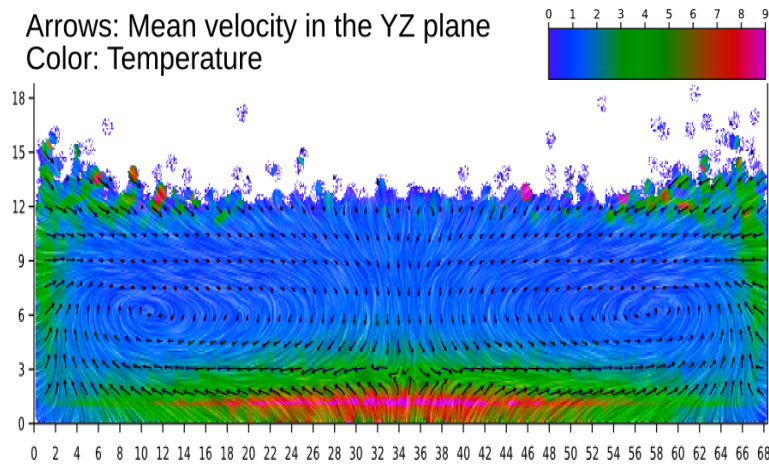


Figure 1.15: Temperature map with velocity in the transverse plane. Figure extracted from Brodu et al. (2013).

3.2.3 Supported flow regime

When the inclination angle increases, a new interesting flow pattern can appear. It has been named "supported" flow regime (Brodu et al., 2015; Ralaiarisoa et al., 2017; Zhang et al., 2019). This regime was also discovered experimentally by Heyman et al. (2017). For this regime the distribution of packing fraction is strongly modified. The packing fraction profile becomes inverted i.e. the maximum of density is in the middle of flow, where a dense core is floating over a diluted layer of grains (figure 1.16). The temperature is higher at the bottom and the dense core is very cool. Therefore, these "supported" flows have been observed when the temperature gradient between the base and the dense core was strong enough to overcome the gravity (Liedenfrost effect).

Rapid granular flows in inclined channels with smooth boundaries have been studied experimentally (Holyoake and McElwaine (2012); Heyman et al. (2017)) and by numerical simulations (Brodu et al. (2015); Ralaiarisoa et al. (2017); Zhang et al. (2019)). Brodu et al. (2015) showed the vertical profile of the volume fraction and of the velocity for SFD supported regimes (figure 1.17). The granular material in the dense core moves with a greater velocity. As the mass hold-up H increases, the dense core rises and becomes denser. The packing fraction reaches a value $\phi = 0.6$. Meanwhile the difference in packing fraction between bottom and the dense core increases. The dense core slowly becomes less dense as the inclination angle increases. However the position of the maximum of packing fraction is independent of the inclination angle θ , even if the thickness of the dense core decreases. The

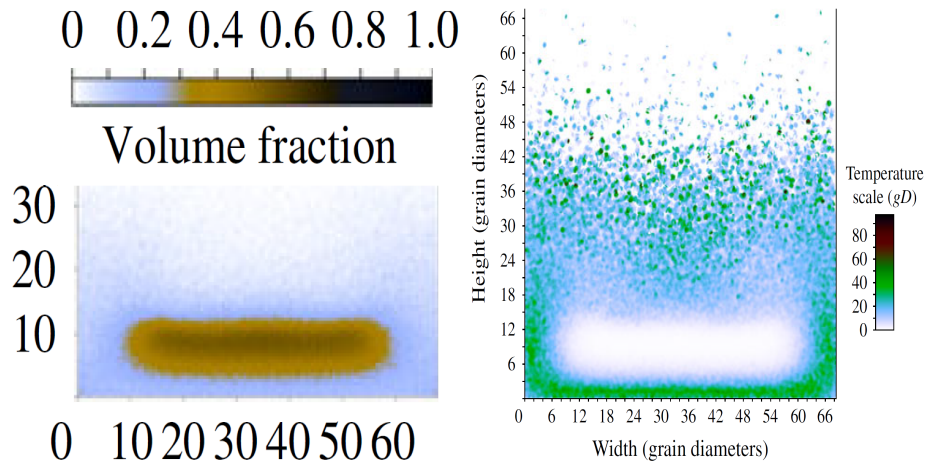


Figure 1.16: Supported flow regime. Temperature and packing fraction maps. Figure extracted from [Brodu et al. \(2015\)](#).

velocity at the base (sliding velocity) plays a dominant role. It increases with mass hold-up and then remains constant, it always increases with inclination angle θ .

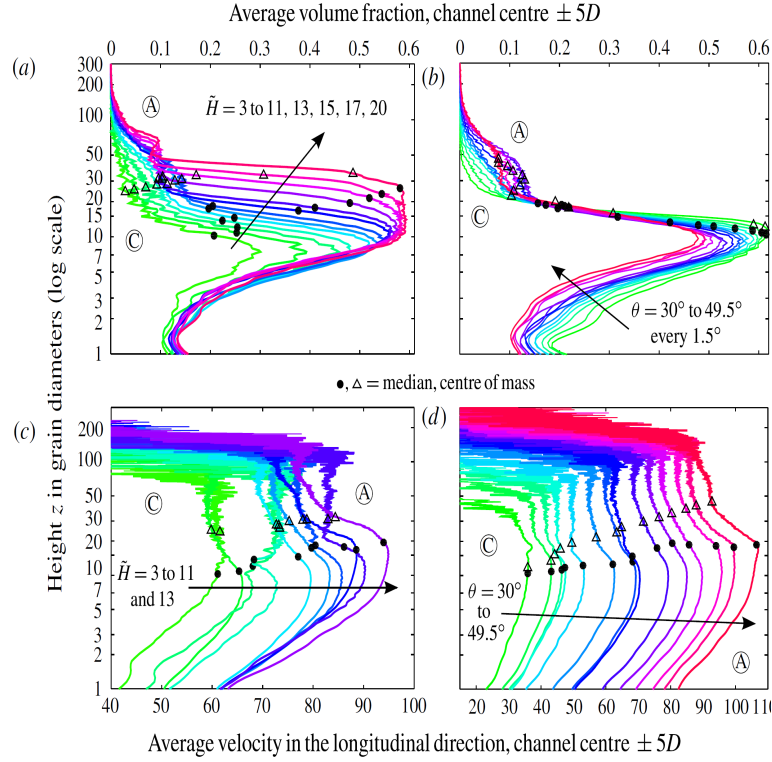


Figure 1.17: (Top (a,b)): vertical profiles of the packing fraction and (base (c,d)) of the stream-wise velocity, for (left (a,c)) $\theta = 42^\circ$ and various values of the mass hold up H and (right (b,d)) $H = 8D$ and various values of the inclination angle. Figure extracted from Brodu et al. (2015).

3.2.4 Effective friction coefficient at boundaries

As we know, the boundary conditions are important for the confined flows. So Brodu et al. (2015) measured the effective mean friction coefficient at the base μ_b and at the walls μ_w as a function of θ (see Fig.1.18). Here the effective coefficients μ_b and μ_w are defined as the ratio of tangential to normal stresses:

$$\mu_w = \frac{\overline{S_w}}{\overline{N_w}}, \mu_b = \frac{\overline{S_b}}{\overline{N_b}} \quad (1.12)$$

here $\overline{S_w}$ and $\overline{S_b}$ correspond respectively to the norm of wall-averaged and bottom-averaged tangential stresses, $\overline{N_w}$ and $\overline{N_b}$ correspond to the wall-averaged and bottom-averaged normal stresses. The effective friction coefficients μ_w and μ_b increase with angle θ , and decrease with increasing mass hold up.

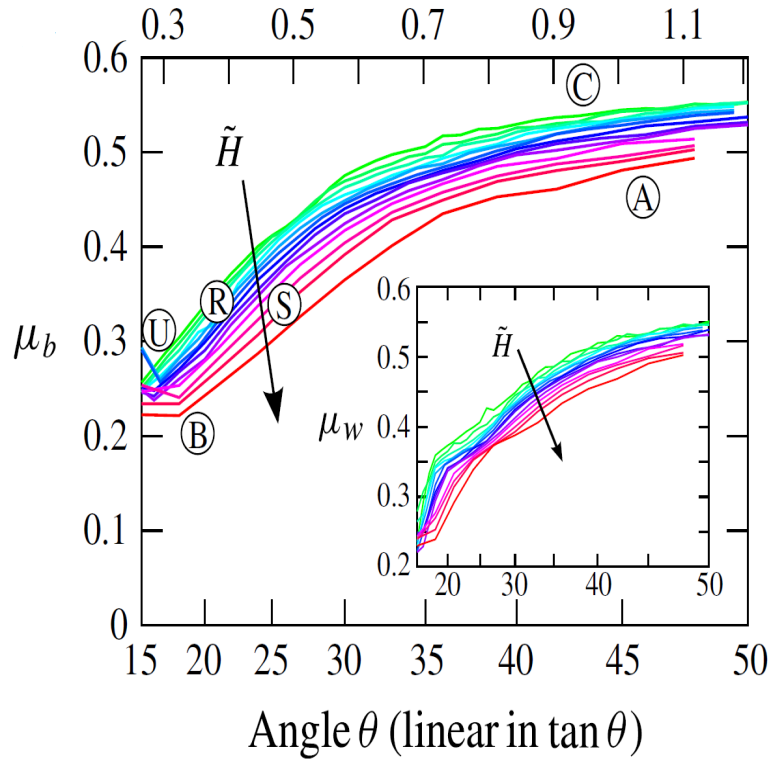


Figure 1.18: Effective friction coefficients at the walls and at the base as functions of the inclination angle, for different values of the mass hold up. Figure extracted from Brodu et al. (2015).

3.2.5 Scaling law

Brodu et al. (2015) found a scaling law for the mean velocity of steady and fully developed flows (see Fig.1.19). It can be described as:

$$V_L \propto H^{\alpha_L} \quad (1.13)$$

with $\alpha_L \approx 1/4$.

The mass flow rate is $Q = V_L H$, giving $Q \propto H^{5/4}$. So it corresponds approximately to the experimental result of Louge and Keast (2001): $Q \propto H^{3/2}$ for the uni-directional regime and to the numerical simulation result: $Q \propto H^{3/2}$ of Zhang et al. (2019). In any case the exponent of the scaling is always much smaller than for the Bagnold scaling (exponent 3/2 for the velocity). As we have seen on figure 1.17, the sliding velocity doesn't vary when H is great enough, and the variation of the average velocity - which is dominated by contribution of the sliding velocity - with H becomes thus very small.

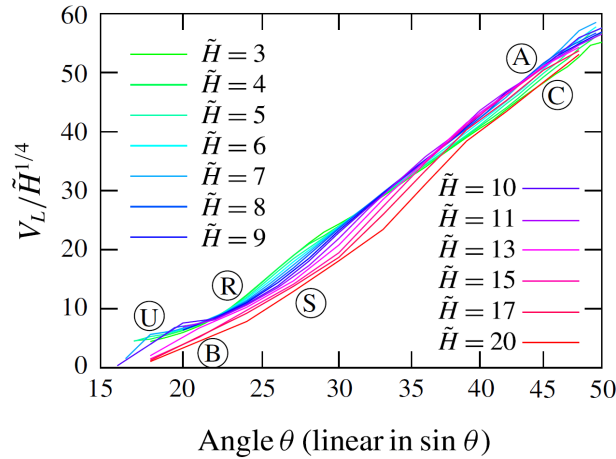


Figure 1.19: Rescaled SFD mean velocity $V_L/H^{1/4}$ as a function of $\sin\theta$ for various mass holdups. Figure extracted from Brodu et al. (2015).

3.2.6 SSH and others flows

Previous experimental work on granular flows down inclines can be classified in two categories: height-controlled flows (Pouliquen (1999)) and flow-rate controlled flows (Drake (1990, 1991); Ancy (2001)).

Using a flow-rate-controlled set-up, Komatsu et al. (2001); Taberlet et al. (2003); JOP et al. (2005) experimentally observed super-stable heaps (SSH) for granular flows in an inclined thin channel with flat frictional walls. Later, through numerical simulations using periodic boundary conditions in the direction of the flow, with high mass hold-up H , Bi et al. (2005); Richard et al. (2008); Zhang et al. (2019) also obtained this flow pattern. As illustrated in Fig.1.20 this regime consists apparently in two streaming modes: moving grains in a top layer at the free-surface and, quasi-static grains in a bottom layer. The figure 1.20 also shows that the velocity doesn't change completely abruptly. The velocity profile reveals an exponential variation of this velocity near the transition between the two modes. We have to change a little our conventions for this SSH section. Following the configuration shown in the figure 1.20, the flow direction is always x , y is the transverse direction (in the vertical plane, but oriented downward) and z is the horizontal direction perpendicular to the side walls.

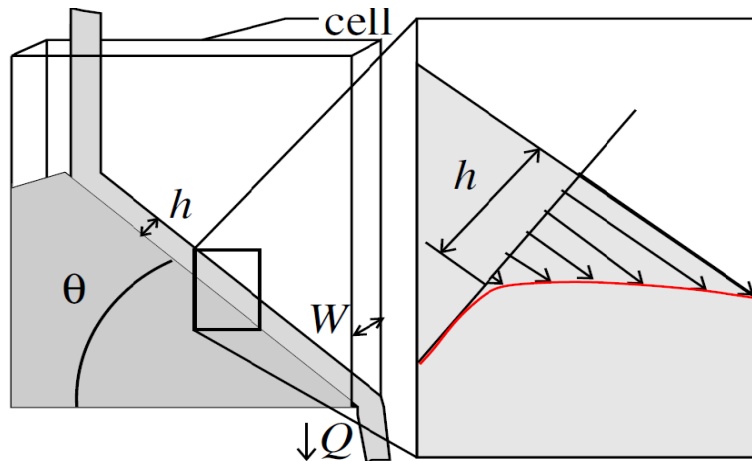


Figure 1.20: SSH flow regime. Figure extracted from Richard et al. (2008).

Figure 1.21 shows the packing fraction and the stream-wise velocity profiles for various inclination angles $\theta = [35^\circ, 40^\circ, 45^\circ, 50^\circ, 55^\circ]$. The quasi-immobile pile corresponds to a packing fraction $\nu_0 \approx 0.6$. In the flowing part, the stream-wise velocity V_x / \sqrt{gD} is approximately linear in y/D and the packing fraction ν increases with depth y/D . The latter can be approximated by:

$$\nu(y) = \frac{\nu_0}{2}(1 + \tanh(y/l_v)) \quad (1.14)$$

with a characteristic length l_v varying linearly with W and θ :

$$l_v/W = \eta(\tan \theta - \tan \theta_0) \quad (1.15)$$

If we plot ν/ν_0 as a function of y/l_v , all the curves corresponding to different inclination angles and gap widths W collapse (inset of Fig.1.21 (a)). Meanwhile, l_v is also a characteristic length for the velocity V_x as shown in inset of Fig.1.21 (b) which presents $V_x/2l_v$ as a function y/l_v . For the part where ν is significantly greater than zero and $\theta > 35^\circ$, the rescaled velocity is independent of the angle θ and of W .

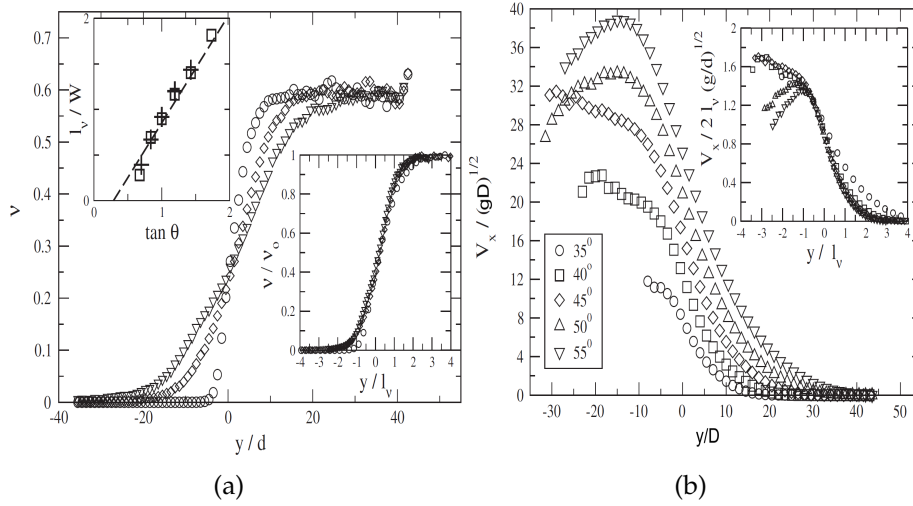


Figure 1.21: (a) Packing fraction and (b) velocity profiles for various angles $\theta = [35^\circ, 55^\circ]$. Inset of (a): linear variation of the rescaled characteristic length l_v/W as a function of $\tan(\theta)$ for $W/D = 5$: symbol (\square) and $W/D = 10$: symbol (+), inset of (b): $V_x/2l_v$ as a function y/l_v for various angles .Figure extracted from Richard et al. (2008).

Richard et al. (2008) related the depth of flowing part h to the characteristic length l_v : $h = 2l_v$. If we write $\mu_w = 1/(2\eta)$ then the equation ((1.15)) is consistent with the SSH equation of Taberlet et al. (2003), deduced from the force balance equation applied on a flowing slab:

$$\tan \theta = \tan \theta_0 + \mu_w h / W \quad (1.16)$$

where, μ_w is the effective side wall friction coefficient and θ_0 is the internal friction angle of the granular material.

The local side wall coefficient of friction is defined as $\mu_\tau \equiv \|\vec{\tau}_w\| / |\sigma_{zz}^w|$ where the $\vec{\tau}_w \equiv \sigma_{zx}^w \vec{x} + \sigma_{zy}^w \vec{y}$ is the tangential stress and σ_{zz}^w is the normal stress. Figure 1.22 shows that μ_τ is not constant, and decreases with depth. The inset of figure 1.22, shows that the value of μ_τ remains constant - equal to the microscopic friction coefficient μ - in the flowing part, and μ/μ_τ collapses on a single linear line for $\theta > 35^\circ$, in the quasi-static part .

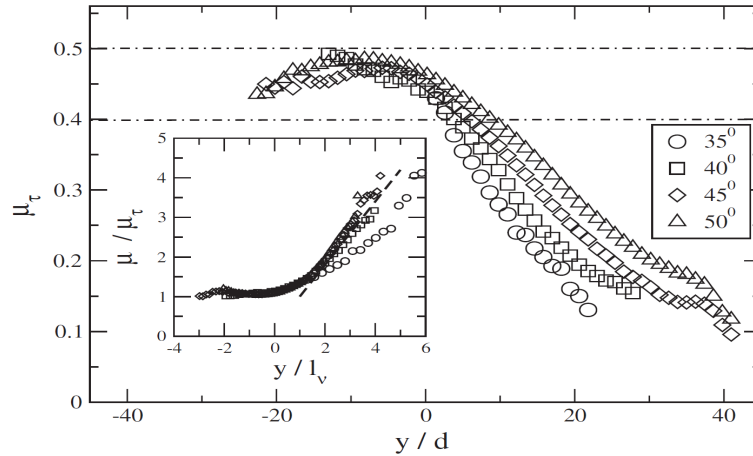


Figure 1.22: Friction coefficient profiles for various angles $\theta = [35^\circ, 55^\circ]$. Inset: variation of μ/μ_τ - where $\mu = 0.5$ is the microscopic coefficient of friction - with y/l_v , showing that l_v is also a characteristic length for μ . Figure extracted from [Richard et al. \(2008\)](#).

3.3 Unsteady flows

Experimentally, with a limited channel length, [JOP et al. \(2005\)](#); [Holyoake and McElwaine \(2012\)](#); [Faug et al. \(2015\)](#) obtained confined granular flows accelerating along the whole chute at large inclination. If this acceleration decreases along the chute, we can assume that for an increased channel length, the flow may turn into SFD flow. Even in accelerated flows, there are still rolls and "supported" states. For high speed granular flows, the rheology $\mu(I)$ is probably not valid ([Holyoake and McElwaine \(2012\)](#)).

4 Questions

For confined flows:

i) [Brodu et al. \(2015\)](#) provide, for $W = 68D$, a complete phase diagram, but quantitative methods to distinguish the different flow regimes are missing, can we give them?

ii) For confined flows, the boundaries conditions are very important, and for SSH regime [Richard et al. \(2008\)](#) showed that the local friction coefficient at side walls μ_τ varies with depth. Can we obtain a local friction describing the variation of μ_τ , how could it be expressed?

iii) The flow regimes observed for unsteady flows also exist in SFD flows ([Holyoake and McElwaine \(2012\)](#)), is there a certain connection between steady flows and unsteady flows?

iv) [Ralaiarisoa et al. \(2017\)](#); [Brodu et al. \(2015\)](#) studied the effect of the variations of mass hold-up and inclination angle for different channel widths: $W = 34D$ for [Ralaiarisoa et al. \(2017\)](#) and $W = 68D$ for [Brodu et al. \(2015\)](#). They give the same mean steady state velocity scaling law, so, is it independent of the channel width? More generally, what is the effect of the channel width on the flow?

v) [Zhang et al. \(2019\)](#) showed that some interaction parameters, like the restitution coefficient between particles, may have an influence on the flow, on the appearances of the flow regimes for example. Can we give some insight on the effect of the restitution coefficients between particles and between particles and walls, of the coefficients of friction between particles and between particles and walls?

With these questions, I will present my work.

5 Research aims and approaches

This thesis work focuses on granular flows in flat frictional inclined channels.

This work aims to characterize thoroughly the various regimes observed in fast granular confined flows with smooth boundaries (e.g., longitudinal rolls, supported flows with dense core, oscillatory instabilities) and determine the phase diagram in the control parameter space (including the inclination angle θ , the mass hold-up H , the channel width W , the restitution coefficient between grains e^{gg} and between grains and walls e^{gw} , the friction coefficient between grains μ_{gg} , and between grains and wall μ_{gw}). Beyond this systematic approach, we look for any kind of law which could give us information concerning the boundary conditions. The most evident of these laws would be a friction law involving the sliding velocity, this is thus in this direction that we shall go first. Numerical simulations are necessary because there is a dearth of experimental techniques that would allow complete observations of the interior of the granular flows. Consequently, computer simulations are necessary to elucidate the behavior of all types of granular flow. For these studies, we will employ numerical simulations based on a discrete element method (DEM) code implemented by Brodu et al. (2013).

6 Outline of dissertation

In chapter 2, we further analysed the results obtained in (Brodu et al., 2015) for a channel width $W = 68D$. We uncover that the effective friction μ at the basal and side walls can be described as a unique function of a dimensionless boundary Froude number Fr . This Froude number is called boundary as it is calculated with the sliding velocity and the pressure at the boundary.

In chapter 3, we study the role of channel width W on granular flows. By changing the width of the channel, we discover new flow regimes and extend the mean stationary velocity scaling law obtained by (Brodu et al., 2015) at $W = 68D$. We verify the universality of the friction law $\mu(Fr)$ and we propose a packing fraction law $\bar{\phi}^*(Fr)$ and a rescaled effective frictional flow height law $Z/H(\bar{\phi}^*)$ - the length Z is a friction length defined by using the balance equation (1.16) - valid for different channel widths W , mass hold-ups H and inclinations θ .

In chapter 4, we study the effect of the normal restitution coefficient between grains $e = e_n^{gg}$. Interestingly, the mean velocity decreases as e increases. We show that for "supported" flow regimes, the mean steady velocity follows a power law H^α where the exponent α decreases linearly when e decreases.

In chapter 5, we focus on the effect of the mechanical parameters: the friction coefficient between grain and wall (μ_{gw}), the friction coefficient between particles (μ_{gg}), on our granular flows. We observe new flow regimes for small μ_{gg} where the dense core falls down on the base. And we find that for θ larger than a critical value θ_c the velocity interestingly increases with increasing μ_{gg} . We verify the robustness of form of the friction law, of the packing fraction law and of the rescale effective frictional flow height law when varying e , μ_{gg} and μ_{gw} and the effect of these variations on the parameters appearing in the laws.

In chapter 6, we discuss our conclusions and perspectives.

22 State of the art

Exp/Num	Material	Wall	mass holdup (H) mass flow (Q) flows height (h)	θ	refs
Exp	glass beads $D = 0.5 - 1.3mm$	Rough $\frac{L}{m} = 1.23 - 2.9$ $W = 70cm$	$h/D = 4 - 25$	$20^\circ - 28^\circ$	Pouliquen 1999
Num	$e = 0.58 - 0.98$ $\mu = 0.15 - 1$	Rough $L = 20D$ $W = 10D$	$H/D = 2 - 200$	$18^\circ - 26^\circ$	Silbert et al. 2001
Exp	sand & glass beads $D = 0.25 \pm 0.03mm$	Rough $L = 1.3m$ $W = 0.3m$	$h/D = 0 - 55$	$32^\circ - 42^\circ$	Forterre and Pouliquen 2001
Num	$\mu = 0.6$	Rough $L = 20D$ $W = 10D$	$H/D = 40 - 100$	$18^\circ - 26^\circ$	Silbert et al. 2002
Exp	glass beads $D(\text{glued}) = 225\mu m - 2mm$ $D = 150\mu m - 2mm$	Rough $L = 2m$ $W = 60cm$	$h/mm = 0 - 5$	$18^\circ - 30^\circ$	Goujon et al. 2003
Exp/Num	Exp: sand & glass beads $D = 0.17 - 0.45mm$ Num: $\mu = 0.5$ $e = 0.8 - 0.95$	Rough Exp: $L = 2.27m$ $W = 0.4m.$ Num: $L = 24.3/D$ $W = 120.15$	$h/D = 20 - 120$	Exp: $20.9^\circ - 33.8^\circ$ Num: $34^\circ - 39^\circ$	Börzsönyi et al. 2009
Num	Fixed beads: D_1 Free beads: D_2 $m = 1$ $g = 1$ $e = 0.88$ $\mu = 0.5$	$\lambda = \frac{D_1}{D_2}: 0 - 4$ $L = 10 - 40D$ $W = 5 - 20D$	$H/D = 10 - 400$	$20^\circ - 60^\circ$	Weinhart et al. 2012
Exp	$D = 2.968 \pm 0.02mm$ $e = 0.972$ $\mu = 0.593$	Rough $W = 203mm$ Smooth $L = 3.6m$ $W = 152mm$	$H/D = 0.95 - 6.56$	$15^\circ - 21^\circ$	Louge and Keast 2001
Num	$D = 2.968 \pm 0.02mm$ $e = 0.972$ $\mu_{gw} = 0.596$	Smooth $L = 20D$ $W = 68D$	$H/D = 4$	$15^\circ - 23^\circ$	Brodu et al. 2013
Exp	glass beads $D = 1.2mm$	Smooth $L = 1m$ $W = 100mm$	$H/D = [0, 25]$	$25^\circ - 40^\circ$	Faug et al. 2015
Exp	$D = 0.53 \pm 0.05mm$	Rough $L = 1.5m$ $W = [1, 30]cm$	$Q/(D\sqrt{gD}) = [0, 50]$	$25^\circ - 40^\circ$	JOP et al. 2005
Exp	sand $D = 0.5 - 2.5mm$	Smooth & Rough $L = 3m$ $W = 0.25m$	$h/D = 4 - 130$	$30^\circ - 55^\circ$	Holyoake and McElwaine 2012
Exp	sand & glass beads $D = 0.1 - 0.9mm$	Rough $L = 50cm$ $W = [5, 20]mm$	$Q/(g/mms) = 0 - 25$	$30^\circ - 60^\circ$	Taberlet et al. 2003
Exp/Num	Exp: glass beads $D = 0.5 \pm 0.1mm$ Num: $\mu = 0.5$ $e = 0.88$	Rough & Smooth $W = 225mm$ $L = 3m$	$h/D = 4 - 130$	$35^\circ - 55^\circ$	Richard et al. 2008
Num	$D = 2.968 \pm 0.02mm$ $e = 0.972$ $\mu = 0.593$	Smooth $L = 20D$ $W = 68D$	$H/D = 1 - 20$	$15^\circ - 50^\circ$	Brodu et al. 2015
Exp	glass beads $D = 1mm$	Smooth $L = 1.5m$ $W = 44mm$	$H/D = 3 - 12$	30°	Heyman et al. 2017
Num	$D = 1mm$ $e = 0.8$ $\mu_{gg} = 0.3$ $\mu_{gb} = 0.6$ $\mu_{gw} = 0.1 - 1.5$	Rough $L = 40D$ $W = 20D$	$H/D = 1 - 35$	$15^\circ - 50^\circ$	Zhang et al. 2019

Table 1.1: Data sources for inclined-plane flow. For the numerical simulations, in flow direction take the periodic boundary condition. Above the red line is the unconfined granular flows. For numerical simulations, the unconfined granular flow in transverse direction y also take the periodic boundary condition.

Chapter 2

Scaling and wall friction laws for channel width $W = 68D$

1 Introduction

In this chapter, we further analysed the results obtained by [Brodu et al. \(2015\)](#) on high-speed confined granular flows for channel width $W = 68D$.

In chapter 1, we discussed the rich flow regimes obtained for confined granular flows with $W = 68D$ and the lack of precise description of the transitions between these flow regimes. We also reported that the effective boundary friction coefficient increases with the inclination and decreases with the mass hold-up. In this chapter we will study in more detail the transition between the flow regimes, including unidirectional, rolls and supported flow regimes. We will further study the relationship between the effective boundary friction coefficient, the mass hold-up - defined as the depth-integrated particle packing fraction - and the inclination.

The outline of the chapter is the following. In Sect. 2 we present the flow geometry and the discrete element method used for the simulations throughout this thesis work.

Section 3 is a published article, in this article, we provide a detailed study of our granular flow simulations for various flow regimes. We describe the transitions between these regimes by following the variations of some key physical quantities: vorticity; maximum packing fraction and asymmetry of the instantaneous depth-integrated transverse packing fraction profile $\phi(y)$ through its skewness. Then we propose a boundary friction law where the effective boundary friction coefficient $\mu_{b,w}$ can be simply described as a function of a dimensionless boundary Froude number $Fr_{b,w}$. We prove that this friction law is also valid at a local level and that this local law applies not only to SFD flows, but also to unsteady flows.

Finally, we conclude in Sect. 4.

2 Modeling

This thesis work uses the computational code implemented by Nicolas Brodu ([Brodu et al. \(2013\)](#)). This code adopts the molecular dynamics method to study granular flows. The discrete element method is a classical numerical simulation method that we will now quickly recall.

In the soft-sphere molecular dynamics simulations, each grain is a non-deformable sphere

with diameter D and density ρ . The walls are treated like spheres of infinite mass and radius. The grains in contact can overlap. The contact forces between two particles have both a normal and a tangential component (figure 2.1). The normal force $F_n^{i \rightarrow j}$ is modelled by a spring and a dash-pot: $F_n = (k_n \delta + \gamma_n v_n) \mathbf{n}^{i \rightarrow j}$ with δ the overlap, $\mathbf{n}^{i \rightarrow j}$ the contact normal (unit vector directed from the center of grain i to grain j), $v_n = (\mathbf{v}_i - \mathbf{v}_j) \cdot \mathbf{n}^{i \rightarrow j}$ the relative translational grain velocity, k_n and γ_n the spring stiffness and viscous damping coefficients.

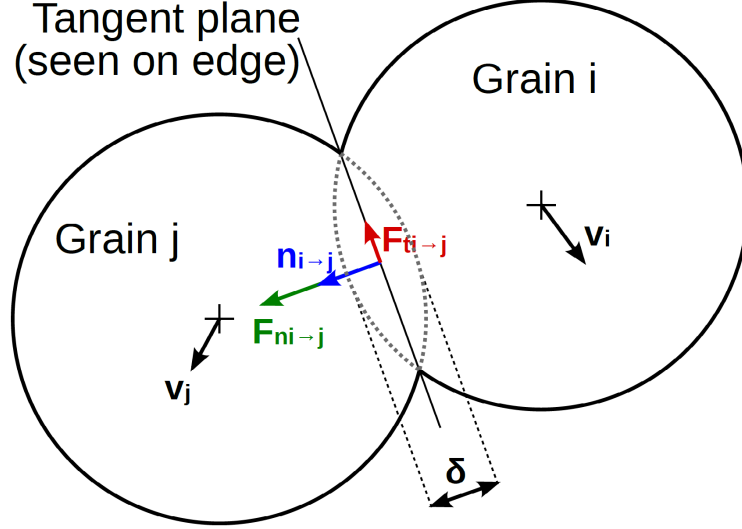


Figure 2.1: The overlapping spheres contact model. Grain i moves with a translation velocity \mathbf{v}_i , and similarly for j . The force exerted by grain i on grain j during contact (characterized by the normal vector $\mathbf{n}^{i \rightarrow j}$) is divided into a tangential component $F_t^{i \rightarrow j}$ and a normal component $F_n^{i \rightarrow j}$. They depend on the overlap δ according to a contact model detailed in the main text. Figure extracted from Brodu et al. (2013).

A similar model is used for the tangential component $F_t = (k_t s + \gamma_t v_t) \mathbf{t}^{i \rightarrow j}$ with $v_t \mathbf{t}^{i \rightarrow j} = (\mathbf{v}_i - \mathbf{v}_j) - v_n \mathbf{n}^{i \rightarrow j}$ the tangential impact velocity. The coefficients k_t and γ_t are the spring stiffness and the viscous damping, and $|s| \leq |F_t|/k_t$. It is a bounded version of the sliding displacement $\int_{\tau_0}^{\tau} v_t d\tau$ in tangential plane, since contact time τ_0 . On the tangential component, the Coulomb friction is enforced, that is $|F_t| \leq \mu |F_n|$ where μ is the friction coefficient. For boundaries, the same method is used but with different parameters: $k_n^{gw}, k_t^{gw}, \gamma_n^{gw}, \gamma_t^{gw}, \mu^{gw}$.

The torque acting on a grain is $\mathbf{q} = -r(\mathbf{F}_t \times \mathbf{n})$ where $r = D/2$ is the radius of a grain. Both force and torque are applied in integrating the motion equation $\Sigma \mathbf{F} = m\mathbf{a}$ and $\Sigma \mathbf{q} = I\dot{\boldsymbol{\omega}}$ where m is the mass of a grain, \mathbf{a} is the grain acceleration, I is the grain moment of inertia, and $\boldsymbol{\omega}$ is the grain angular velocity vector. Numerical integration use the Verlet method.

For a normal collision between two particles the damped harmonic oscillator defined by the above interaction model leads to a contact duration τ_c during which $\delta > 0$. The normal relative velocities before and after contact are related by a constant normal restitution coefficient e_n that sets γ_n . Similarly, for tangential model, the same duration time leads to a relation $7k_t(\pi^2 + (\ln e_n)^2) = 2k_n(\pi^2 + (\ln e_t)^2)$, which corrects the $7k_t = 2k_n$ relation from (Silbert et al., 2001) when $e_n \neq e_t$.

Throughout the thesis work, the numerical system is a channel with flat bottom and side walls. The later are separated by a gap width W whose value can be fixed (control parameter). Periodic boundary conditions are applied in the x direction. the length of the periodic cell is $L = 20D$ (it doesn't change). The y direction is perpendicular to the side walls (and to the direction x), the direction z is perpendicular to the bottom (see figure 2.2).

An external gravity field g is applied, with an inclination angle θ between the directions of g and z .

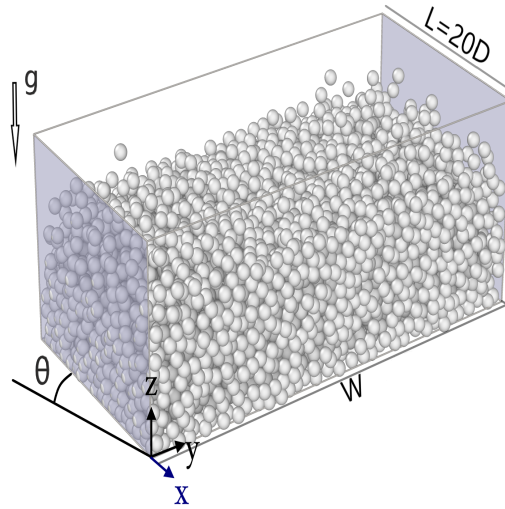


Figure 2.2: Figure for numerical simulation system (periodic cell). The flow is driven by gravity g , periodic conditions are applied in direction x . The flow direction corresponds thus to x , y is the horizontal transverse direction perpendicular to the side walls and z is perpendicular to the base. The angle θ between z and g is the inclination angle.

At time $t = 0$, N particles are randomly distributed in the cell and have a small initial velocity $V_0(x, y, z)$ (and no rotation). This initial velocity include a fixed, deterministic part of module $5/\sqrt{gD}$ in the direction x , and a random one whose components along x , y and z are uniformly distributed between $-2.5/\sqrt{gD}$ and $2.5/\sqrt{gD}$. After letting the program run during a time t , we obtain the position and velocity of the particles at time t , as well as the forces acting at contacts. To calculate the packing fraction field $\phi(y, z, t)$ and velocity field $V_{x,y,z}(y, z, t)$ we have to divide the space into small volumes $dydzdx = 0.1D \times 0.1D \times L$ and add (or average) the contributions of the grains which are in those small volumes. The temperature and angular velocity fields are obtained in a similar manner.

We use those data to analyse the granular flows, they are independent of the variable x as the flow is supposed to be fully developed in virtue of the periodical character of the simulation cell. Some of the quantities of interest like the mean value of the velocity of the grains at time t : $V(t)$, can be obtained by direct calculation of the average of the velocities of the grains as well as by integration of $V_x(y, z, t) \times \phi(y, z, t)$.

We calculate two types of data, instantaneous data and time averaged data, according to the time average used during the process. So called instantaneous data is the data per time unit $\delta t = 3\sqrt{D/g}$, the time averaged data at time t is the average value within 20 time units before t .

To calculate the boundary force fields, we divide the base in small surfaces of area $dydx = 0.1D \times L$ and the side walls in surfaces of area $dzdx = 0.1D \times 20D$. By adding the contributions of the contacts at these portions of surface during a given interval of time, we obtain the normal force field $f_n(y, t)$ (resp. $f_n(z, t)$) and the tangential force field $f_t(y, t)$ (resp. $f_t(z, t)$) exerted on the base (resp. on the side-walls) during this interval of time. The effective friction coefficient μ_b and μ_w are the ratio of the tangential force to the the normal force norms, on the bottom and on the side walls, respectively. They can be calculated globally, on the whole surface, or locally, on small surfaces.

To generate a simulation we have to choose the values of the mechanical parameters e_n^{gg} , e_n^{gw} , e_t^{gg} , e_t^{gw} , μ_{gw} and μ_{gg} , the inclination angle θ , the gap width W , the number of grains N , and the running time t . The number of grains is encoded in the form of the mass hold up $H = \sum_i (m_i / A) / (\rho D)$, $A = L \times W$ is the basal area of the cell, m_i , is the mass of the grain i . The grains have not exactly the same mass, as we have to vary their diameter to try to avoid ordering and crystallization. The diameter of the grains is uniformly distributed around D : $D \pm 0.1D\%$.

We take as standard values of the normal restitution coefficient between grains $e_n^{gg} = 0.972$, and between grains and walls $e_n^{gw} = 0.8$, and for the tangential ones $e_t^{gg} = 0.25$, $e_t^{gw} = 0.35$. The standard value of the coefficient of friction between grains is $\mu_{gg} = 0.33$ and between grains and walls $\mu_{gw} = 0.593$. The spring stiffness between grains and between grains and walls is $k_n^{gg} = k_n^{gw} = 210^5 mg / D$. The integration time step is $dt = 10^{-4} \sqrt{D/g}$.

In the thesis we study the effect of changing H and θ , but also W , e_n^{gg} , μ_{gw} and μ_{gg} , as summarized in the tables

channel width W/D	mass holdup H/D	inclination angle $\theta(^{\circ})$
20	4 – 22	17 – 65
40	4 – 22	15 – 85
60	4 – 14, 18	20 – 50
68	4 – 14	20 – 85
75	4 – 14	20 – 50
140	4 – 6	20 – 40

Table 2.1: The role of channel width W (chapter 3).

e_n^{gg}	mass holdup H/D	inclination angle $\theta(^{\circ})$
0.49 – 1, $\delta e \approx 0.03$	4, 5, 7, 12, 13, 15	17 – 65

Table 2.2: The role of normal restitution coefficient between particles e , for channel width $W = 20, 40D$ (chapter 4,5).

μ_{gg}	μ_{gw}	mass holdup H/D	inclination angle $\theta(^{\circ})$
0.1 – 1, $\delta \mu_{gg} \approx 0.1$	0.1 – 1.5, $\delta \mu_{gw} \approx 0.1$	5	11 – 65

Table 2.3: The role of normal friction coefficient between particle and wall μ_{gw} and between particles μ_{gg} for channel width $W = 40D$ (chapter 5)

During a run we can study non steady flows as the mean velocity varies with t . We consider that the SFD regime is achieved when the mean velocity appears to be converging to within 1% ($(dV / < V >) < 1\%$).

3 Scaling and wall friction laws for $W = 68D$ (copy published article)



High-speed confined granular flows down smooth inclines: scaling and wall friction laws

Yajuan Zhu¹ · Renaud Delannay¹ · Alexandre Valance¹Received: 15 April 2020
© Springer-Verlag GmbH Germany, part of Springer Nature 2020

Abstract

Recent numerical work has shown that high-speed confined granular flows down smooth inclines exhibit a rich variety of flow patterns, including dense unidirectional flows, flows with longitudinal vortices and supported flows characterized by a dense core surrounded by a dilute hot granular gas [1]. Here, we further analyzed the results obtained in [1]. More precisely, we characterize carefully the transition between the different flow regimes, including unidirectional, roll and supported flow regimes and propose for each transition an appropriate order parameter. Importantly, we also uncover that the effective friction at the basal and side walls can be described as a unique function of a dimensionless number which is the analog of a Froude number: $Fr = V/\sqrt{gH \cos \theta}$ where V is the particle velocity at the walls, θ is the inclination angle and H the particle holdup (defined as the depth-integrated particle volume fraction). This universal function provides a boundary condition for granular flows running on smooth boundaries. Additionally, we show that there exists a similar universal law relating the local friction to a local Froude number $Fr^{loc} = V^{loc}/\sqrt{P^{loc}/\rho}$ (where V^{loc} and P^{loc} are the local velocity and pressure at the boundary, respectively, and ρ the particle density) and that the latter holds for unsteady flows.

Keywords High-speed granular flows · Longitudinal vortices · Supported flows · Effective friction

1 Introduction

The scientific community has paid particular attention to gravitational granular flows over the past 20 years. These flows are ubiquitous in natural and industrial processes [2, 3]. However, their modeling and understanding still leave us with open issues. The complexity arises from grain-grain interactions, and also from grain-boundary interactions which may induce correlations over distances much greater than a grain diameter.

The inclined plane geometry was the most employed configuration to study gravity-driven granular flows [4, 5]. It is simple and relevant for many practical situations, but it can be also seen as a rheological test with constant friction.

To date, experiments [4] and simulations [6] have focused mainly on mildly sloping and bumpy planes, leading to slow and dense flows which are now fairly well understood [2, 7]. More complex flows, including span-wise vortices [8–10], were obtained at slightly higher angles suggesting that upon further steepening, granular flows may reveal original features.

Obtaining steady and fully developed (SFD) flows at steep angles is both an experimental and numerical challenge. Indeed, for unconfined flows, there is in general a limit angle above which flows keep accelerating. This limit angle may depend on many parameters such as the mechanical properties of the grain and the nature of the base (flat or bumpy). A simple way to obtain SFD flows at high angles is to introduce frictional side walls. Indeed, if the grain–wall friction coefficient is high enough, one may expect that the base friction supplemented by the sidewall friction will be able to balance the driving component of the weight. This is what has been done recently by Brodu et al. [1] by means of discrete element method simulations. These simulations showed that SFD flows can be produced at high angles and revealed the existence of new flow regimes characterized by complex internal structures with heterogeneous particle

This article is part of the Topical Collection: Flow regimes and phase transitions in granular matter: multiscale modeling from micromechanics to continuum.

✉ Alexandre Valance
Alexandre.Valance@univ-rennes1.fr

¹ Institut de Physique de Rennes, CNRS UMR 6251, Univ Rennes, 35042 Rennes CEDEX, France

volume fraction and secondary flows [1, 11, 12]. One of these regimes, referred to as “supported flow”, is particularly interesting since it displays uncommonly high bulk velocity, the granular flow being “supported” on a dilute granular gaseous layer of highly agitated grains. Similarly to an air-cushion suspension, this layer reduces the effective wall friction and increases significantly the bulk velocity. These “supported” flows are particularly interesting with respect to geophysical issues. The reduction in the effective friction due to the gaseous granular layer could indeed explain unexpected long run-out distances of large granular avalanches.

In this paper, we further analyzed the results obtained by Brodu et al [1] on high-speed confined granular flows. We describe in details the transition between the different flow regimes, including unidirectional, roll and supported flow regimes and provide a unified picture to describe the variation of the effective friction at the boundaries, in terms of a Froude number defined as $Fr = V/\sqrt{gH \cos \theta}$ where V is the particle velocity at the walls, θ is the inclination angle and H the particle holdup (defined as the depth-integrated particle volume fraction). This universal function can be seen as a boundary condition for granular flows running on smooth boundaries. In addition, we find that a similar universal law relating the local friction to a local Froude number $Fr^{loc} = V^{loc}/\sqrt{P^{loc}/\rho}$ (where V^{loc} and P^{loc} are the local velocity and pressure at the boundary, respectively, and ρ the particle density) can be established and that the latter holds for unsteady flows.

The outline of the paper is the following. In Sect. 2 we briefly present the flow geometry and the discrete element method used for the simulations. Then, in Sect. 3 we recall the different steady and fully developed flow regimes and their main properties. Section 4 is devoted to the detailed analysis of the transition between the different flow regimes. In Sect. 5, we focus on the basal and sidewall frictions and discuss their relationship with velocities at the boundary. Finally, we conclude in Sect. 6.

2 Flow geometry

We consider gravity-driven chute flows with flat frictional bottom and side walls, as shown in Fig. 1. The chute is inclined with an angle θ with respect to the horizontal. $(0x)$ is the main direction flow, $(0y)$ the cross-wise direction and $(0z)$ is the direction perpendicular to the flow base. This geometry is similar to that used in [1, 11, 13, 14]. Here, the simulation cell has similar dimensions as those employed by Brodu and co-workers [1, 11]. In particular, the longitudinal length L and the gap W between the side-walls are set to $L = 20D$ and $W = 68D$, respectively (where D is the particle diameter). The channel is not bounded in

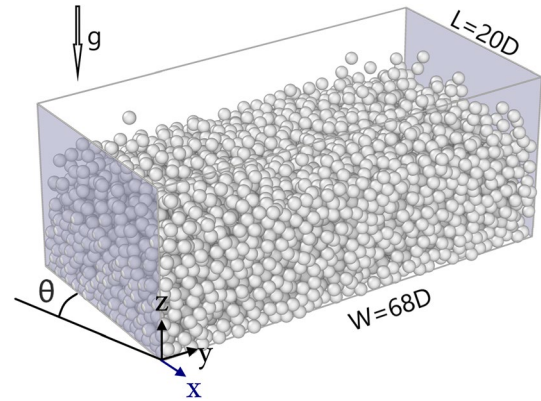


Fig. 1 Scheme of the simulated system. The channel consists of frictional and flat bottom and sides and is inclined with an angle θ with respect to the horizontal. The longitudinal length L and width W of the channel are set to $20D$ and to $68D$, respectively. The channel is not bounded in the $(0z)$ direction and we use periodic boundary conditions in the stream-wise direction

the $(0z)$ direction and periodic boundary conditions are employed in the stream-wise direction $(0x)$.

We use soft-sphere molecular dynamics simulations where particles in contact can overlap [1, 11]. The contact forces between two particles have both a normal and a tangential component. The normal force, F_n , is modeled by a spring and a dashpot: $F_n = k_n \delta + \gamma_n \dot{\delta}$, where δ is the overlap and $\dot{\delta}$ its derivation with respect to time, respectively, and, k_n and γ_n are the spring stiffness and the viscous damping coefficient, respectively. A similar model is used for the tangential component enforced by the Coulomb friction $|F_t| \leq \mu |F_n|$ where μ is the friction coefficient.

We employ the same mechanical parameters as those in the experiments by Louge et al. [15] and in the numerical simulations of Brodu and co-workers [1, 11]. We choose values for k_n and γ_n (resp. k_t and γ_t) such that the normal restitution coefficient e_g^n (resp. the tangential one e_g^t) is equal to $e_g^n = 0.972$ (resp. $e_g^t = 0.25$). The particle-particle friction coefficient is set to $\mu_g = 0.33$.

The walls (i.e., the bottom and the side-walls) are treated like spheres of infinite mass and radius. The normal restitution coefficient e_w^n and the friction coefficient μ_w for the grain-wall interaction are set to $e_w^n = 0.8$ and $\mu_w = 0.593$, respectively. These values are also taken from Louge’s experiments [15].

The control parameters of the simulation are the mass holdup H and the inclination angle θ , while the the channel width W is kept fixed (i.e., $W = 68D$). The particle hold-up H , defined as the depth-integrated particle volume fraction (i.e., $H = \int_0^\infty \phi(z) dz$, where ϕ is the particle volume fraction at height z averaged over the width and length of the cell) is varied from $4D$ to $12D$, and the inclination from 15° to 50° .

In the following, unless otherwise specified, particle volume fraction, velocity and velocity fluctuations are averaged spatially in the stream-wise direction and over time during 30 time units (i.e., $\sqrt{D/g}$). We mainly focus on steady and fully developed (SFD) flow regimes, that are flows with an averaged velocity that is time-independent.

3 Steady and fully developed flow regimes

3.1 General description of the flow regimes

In [1], 5 different steady and fully developed flow regimes were identified: (i) A unidirectional, dense and layered flow; (ii) a dense and layered flow regime with two longitudinal vortices located at the side wall and close to the free surface; (iii) a roll regime which exhibits a pair of counter-rotative longitudinal vortices that spans the entire width of the cell; (iv) and (v) two types of unusual flows characterized by a dense core floating over a dilute basal layer (referred here after to as supported regimes). Four of these regimes are illustrated in Fig. 2 for $H = 6D$ where the two-dimensional particle volume fraction map in the cross-section of the flow are presented together with the streamlines.

Additional features are worth mentioning. While the unidirectional flow presents a layered structure (see "Appendix" for further details) with a high particle volume fraction (i.e., the depth-averaged volume fraction is close to 0.6), the roll regime exhibits a slight density inversion, that is a lower particle volume fraction close to the bottom and a higher volume fraction in the bulk flow (see Fig. 2e). The appearance of the longitudinal rolls can be explained as the result of a "Rayleigh-Bénard"-like instability [9]. This roll regime has been observed in discrete numerical simulations for the first time for unconfined geometries [10] (i.e., with absence of lateral walls). Our simulations indicate that the lateral confinement does not prevent from the emergence of the roll regime. Interestingly, with the gap width used here (i.e., $W = 68D$), we always get a single pair of rolls. We could however conjecture that flow configurations with a much larger gap width should give rise to the formation of several pairs of rolls. In our configuration, the pair of rolls always exhibits the same direction of rotation, leading to a downward motion of the particles in the center of the cell and an upward motion at the lateral walls.

Supported flows exhibit striking feature with a dense core floating on a dilute basal layer. This regime has been first uncovered by Brodu et al. [1]. In comparison with the roll regime, the density inversion of the volume fraction profile is much more marked (see Fig. 2e) and the core get denser with increasing angle as detailed in the next section. As argued in [1], the appearance of a dense core is possibly linked to the clustering instability observed in the cooling

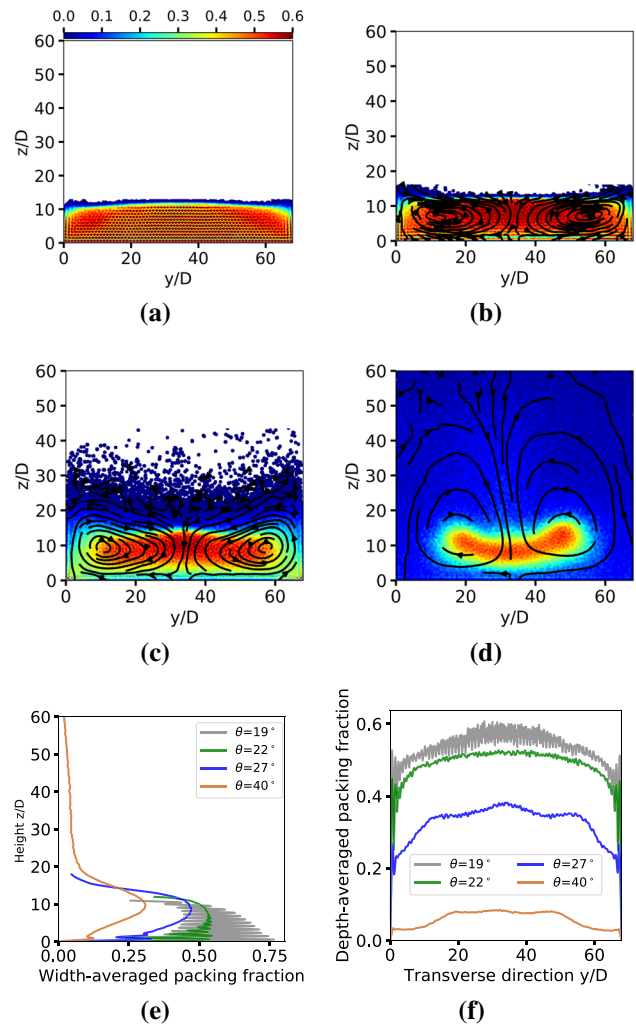


Fig. 2 Volume fraction map in the cross-section of the flow for different flow regimes with a fixed particle hold-up ($H = 6D$). The color codes the volume particle fraction (blue indicates dilute regions while red dense ones) and the solid lines stands for the streamlines. **a** Unidirectional, dense and layered flow ($\theta = 19^\circ$); **b** Roll regime ($\theta = 22^\circ$); **c** and **d** supported flow regimes with a symmetric core ($\theta = 27^\circ$) and an asymmetric core ($\theta = 40^\circ$), respectively. **e** and **f** Correspond vertical and transverse profiles of the packing fraction (color figure online)

process of granular gas [16, 17] and in vibrated granular systems [18, 19]. Gravity-driven flows are of course somewhat different from vibro-fluidized granular systems but share some similarities. The former can be seen as the result of two effects: a shearing, induced by gravity and collisions with the boundaries, which act as an energy source. Thus, the motion along the flow, mainly driven by gravity, could be considered as independent from the motion in the transverse direction, which, according to this hypothesis, would be mainly driven by the interactions of the grains with the boundaries.

Additionally, it is important to note that the longitudinal rolls are still present in the supported flow regime and

are not suppressed by the presence of the dense core. They give rise to particle exchange between the dense core and the dilute surrounding region. At the onset of the supported regime (i.e., $\theta = 25^\circ$ for $H = 6D$), the core possesses two planes of symmetry, a vertical and an horizontal one. However, for larger inclination angles (i.e., $\theta > 30^\circ$), the horizontal symmetry is broken and the core get bended. As a result, the core starts to rock back and forth. This transition will be discussed in further detail in the next section.

The above flow regimes are all steady and fully developed: they have an averaged velocity V_L which is time-independent. Each of them has a limited domain of existence in the parameter space (H, θ) as illustrated in Fig. 3. Several remarks follow. First, at low angles (i.e., $\theta \leq 17^\circ$), the flow is not steady: the mean flow velocity does not reach a steady value but fluctuates a lot. These flows are close to the jamming transition and have been named as intermittent flows. Brodu et al. [1] indicated that flows definitively stop below $\theta_{min} \approx 14^\circ$. Second, we can note that the inclination angle is the main parameter which drives the transition of the different flow regimes. As the inclination angle is increased, several transitions occurs successively: at roughly 20° unidirectional flows give rise to roll regime which itself leads to supported flow above 25° . The critical angles characterizing these transitions increases slightly with increasing particle hold-up. We will describe carefully these transitions in Sect. 4.

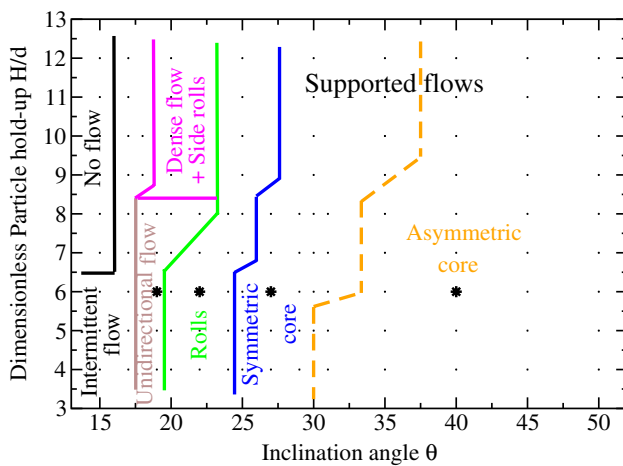


Fig. 3 Phase diagram in the parameter space (H, θ) for $W = 68D$. Unidirectional and dense flows with layering observed close to the base; Dense flow regime with longitudinal vortices located at the flow surface and close to the side walls; Flows with a pair of longitudinal rolls that spans over the entire cell width; Supported flows with a symmetric dense core; Supported flows with an asymmetric dense core. The black asterisk correspond to the flow regimes illustrated in Fig. 2 (color figure online)

3.2 Velocity and granular temperature

Vertical and transverse profiles of the stream-wise particle velocity for different flow regimes are displayed in Fig. 4. As expected, the flow velocity increases with increasing angle. We can note however that the increase is not only due to an increase of the shear rate but also to a large augmentation of the velocity at the boundaries. It is important to realize that the velocity is discontinuous in the two first layers close to the walls (in particular for moderate inclination angles), indicating that the latter play a peculiar role. This discontinuity may pause a problem to define the relevant slip velocity. However, the velocity difference between the first and second layer remains small and never exceeds a few \sqrt{gD} . In the vertical direction, the flow is sheared over the whole flow depth at low inclination angles (i.e., 19° and 20°), while the shear zone is essentially localized in the dilute layer close to the bottom at higher angles (i.e., for supported flows). In the transverse direction, similar features are observed. At low inclination angles, the flow is sheared almost uniformly over the whole width. In contrast, at larger angles, the shear rate is more pronounced in the dilute layer close to the vertical walls than within the dense core. At $\theta = 40^\circ$, the dense core flows as a plug and does not exhibit any shear within it.

Importantly, we confirm the scaling law proposed by Brodu et al. [1] concerning the mean flow velocity V_L :

$$\frac{V_L}{\sqrt{gD}} \approx A(H/D)^\alpha (\sin \theta - \sin \theta_c) \tag{1}$$

with $\alpha \approx 0.25$, $A \approx 122$ and $\theta_c \approx 17.5^\circ$. One can note that the value of the critical angle θ_c is very close to the lower boundary for SFD flows (see Fig. 3). The values of the fitting parameters A and θ_c are expected to be dependent both of the channel width W and the microscopic friction coefficients μ_g and μ_w . This scaling indicates that the mean velocity increases both with the inclination angle and the

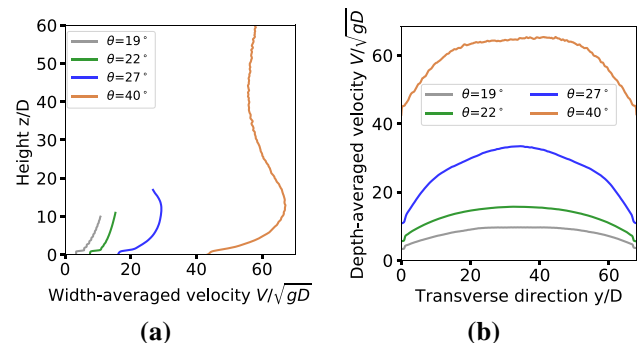


Fig. 4 **a** Vertical and **b** transverse profiles of the stream-wise particle velocity for $\theta = 19, 20, 27$ and 40° and a fixed particle hold-up $H = 6D$

particle hold-up. However, it is important to note that the increase of the mean flow velocity with the particle hold-up is rather mild and drastically differs from the Bagnold scaling law (i.e., $V_L \propto H^{3/2}$) which is relevant for slow and dense granular flows on bumpy bottoms. For the latter, the particle velocity almost vanishes at the bumpy bottom while our flows that run over a smooth base have a finite and large velocity at the base. We believe that the difference in the scaling law results essentially from the different nature of the basal boundary condition.

In addition to the mean flow velocity, the velocities at the boundaries are also interesting and relevant quantities. The basal and side-wall slip velocities are calculated at $z = 0.5D$ and at $y = 0.5D$, respectively, that is within the first wall particle layer. Note that this choice differs from that made in [11], where the basal slip velocity was evaluated in the second particle layer at $z = 1.5D$. Although velocities are discontinuous in the two first layers, their difference remains small and both definitions of the slip velocity leads to similar results. The velocities at the bottom and at the side walls are found to be almost independent of the particle hold-up within the range investigated so far (i.e., $4 \leq H/D \leq 12$) and increase with increasing inclination angle (see Fig. 5). Interestingly, they are quantitatively similar and are linearly correlated with the rescaled flow velocity $V_L/(H/D)^{0.25}$:

$$V_b \approx V_w \approx V_L/(H/D)^{0.25} \approx A(\sin \theta - \sin \theta_c) \sqrt{gD}. \quad (2)$$

This invariance with the particle hold-up is quite surprising but it is in line with the fact that the mean velocity V_L moderately increases with H . It is important to note that this invariance is well verified for supported flows but does not hold for flows with small inclination angles (i.e., $\theta < 25^\circ$), including both unidirectional and dense flows and the roll

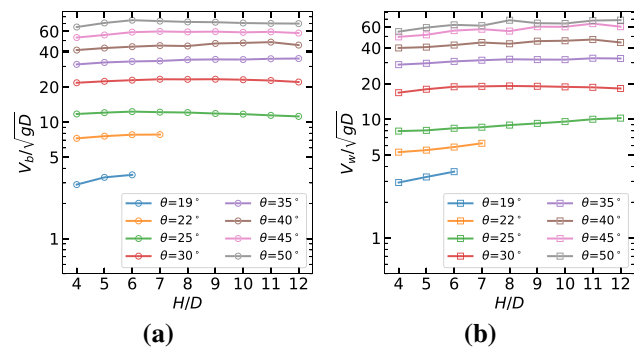


Fig. 5 a Particle velocity V_b and V_w , respectively at the base and at the side-walls, as function of the particle hold-up H for increasing inclination. Both velocities are almost invariant with the particle hold-up H , except for small inclination angles where a slight increase is observed. In contrast, they increases significantly with increasing inclination angle

regime. For the latter, we observe a clear increase of V_b and V_w for increasing particle hold-up.

Granular temperature is a measure of the particle velocity fluctuations. It is an important parameter in various theories aiming to capture granular flow behaviors. It is defined as $T = (T_{xx} + T_{yy} + T_{zz})/3$ where $T_{ij} = \langle u_i u_j \rangle - \langle u_i \rangle \langle u_j \rangle$, u_i is the i component of the instantaneous particle velocity and $\langle . \rangle$ stands for time averaging and spatial averaging in the stream-wise direction. We provide in Fig. 6 temperature map within the cross-section of the flow as well as vertical and transverse profiles of the temperature for various flow regimes. We observe contrasting features for slow and large angles, respectively. For unidirectional flows, the temperature is

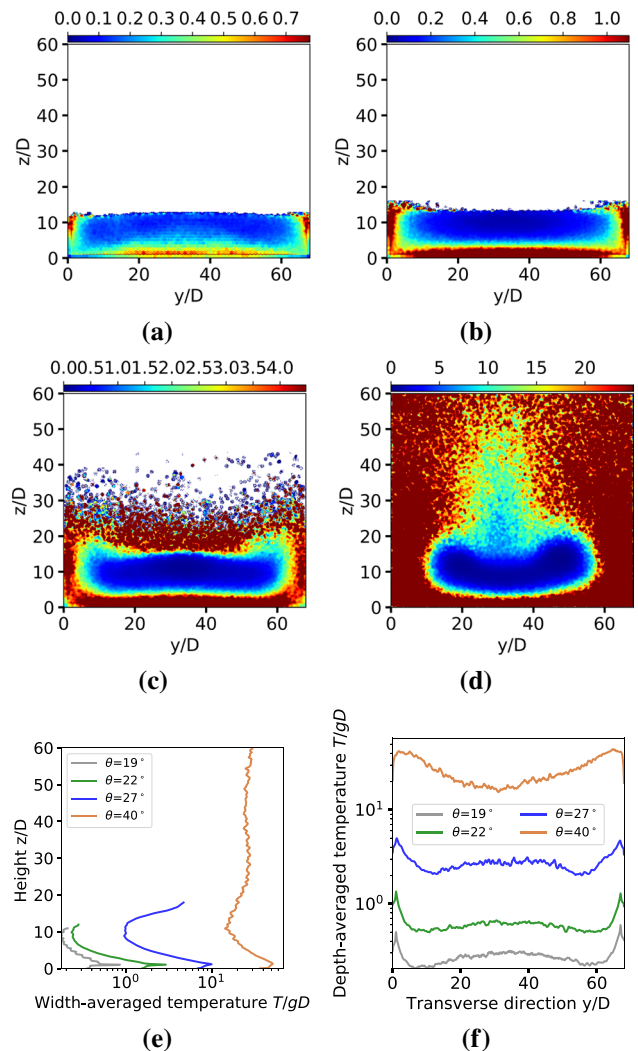


Fig. 6 Temperature map for different flow regimes. $H = 6D$ and $W = 68D$. a Unidirectional dense regime; ($\theta = 19^\circ$); b Roll regime ($\theta = 22^\circ$); c and d supported flows: symmetric core ($\theta = 27^\circ$) and asymmetric core ($\theta = 40^\circ$); e Corresponding vertical and f transverse profiles of the granular temperature

relatively homogeneous with a temperature at the bottom slightly greater than within the bulk flow (see Fig. 6a). In the roll regime, the temperature is still very homogeneous within the bulk flow but there is a larger contrast of temperature between the bottom temperature and the bulk one. For large angles (i.e., for supported flows), the temperature map exhibits contrasting features. The supported dense core is very cold and surrounded by a dilute hot gas. This flow regime thus displays strong heterogeneities of temperature which is strongly correlated to particle volume fraction.

Lastly, it should be noted that the granular temperature profile exhibits discontinuities close to the boundaries, similarly as the velocity profile: the first wall layer is generally much colder than the second layer, emphasizing that the two first wall layers play an important role.

4 Flow regime transition

In this section, we describe the transition between the different flow regimes. For that purpose, we investigate the variation of several key parameters that highlight the flow regime transition.

4.1 Vorticity

We first consider the transition from the unidirectional flow regime towards the roll regime. The vorticity is the natural quantity for characterizing the presence of longitudinal vortices. It is defined as $\Omega = \nabla \times \mathbf{v}$.

In Fig. 7, we present the vorticity map for different flow regimes. For unidirectional flows, (e.g., $H = 6D$ and $\theta = 19^\circ$), the vorticity is close to zero (i.e., less than $2.10^{-2} \sqrt{g/D}$). Upon increasing inclination angle (i.e., for $\theta = 22^\circ$), roll regime develops with a visible pair of counter-rotative longitudinal vortices (see Fig. 7b). Upon further increase of the inclination angle (i.e., for $\theta = 27^\circ$ and 40°), the flow exhibits similar vorticity pattern but with increasing values of the vorticity. The behavior is illustrated in Fig. 8 that displays the maximum value of the vorticity within the vortex as a function of the inclination angle for various particle hold-up. This plot confirms that for dense unidirectional flows ($\theta < 20^\circ$) the maximum vorticity is extremely small and start to increase at the onset of the roll regime. Besides, one can note that the vorticity increases with the inclination angle at a greater rate when one enters the supported regime (i.e., for $\theta \approx 25^\circ$) and tends to saturate at large angles corresponding to the asymmetric core regime (i.e., $\theta > 30^\circ$).

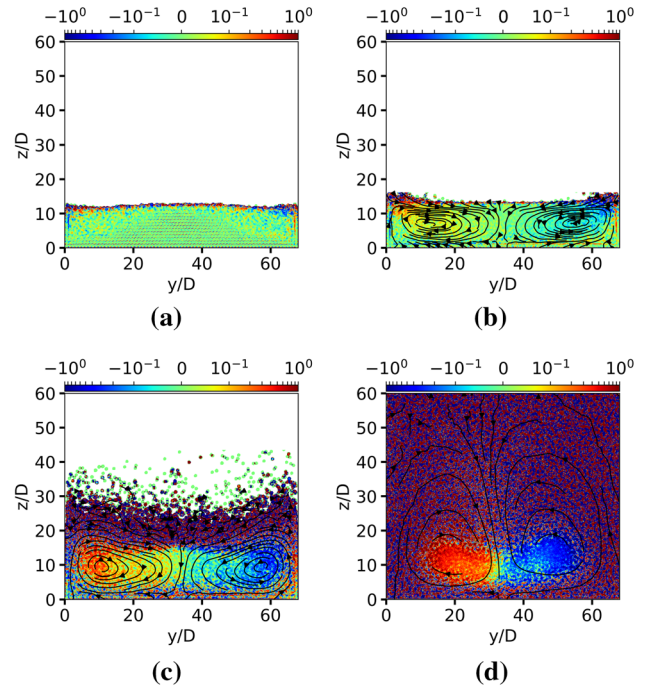


Fig. 7 Vorticity map for different flow regimes. $H = 6D$ and $W = 68D$. Solid lines represents the streamline in the flow cross-section. **a** Unidirectional dense regime; ($\theta = 19^\circ$); **b** Roll regime ($\theta = 22^\circ$); **c** and **d** supported flows: symmetric core ($\theta = 27^\circ$) and asymmetric core ($\theta = 40^\circ$)

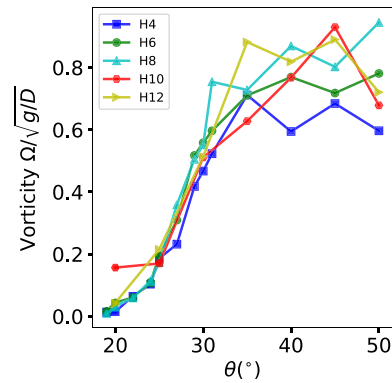


Fig. 8 Vorticity versus inclination angle for various particle hold-up. The value of the vorticity stands for the maximum value of the vorticity within the rolls (see Fig. 7)

As a summary, we confirmed that the vorticity is the appropriate parameter to delineate the transition from the dense flow regime towards the roll regime.

4.2 Maximum packing fraction

We then focus on the transition from the roll regime towards the supported regime. As the supported regime is

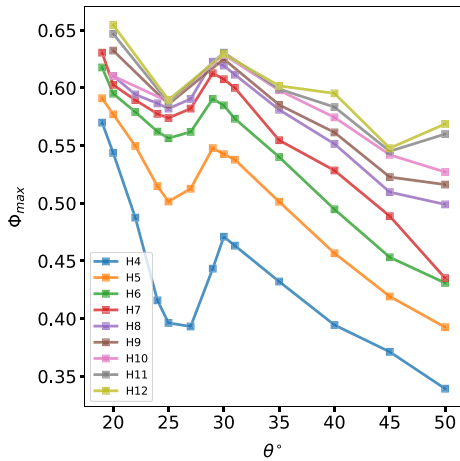


Fig. 9 Maximum packing fraction ϕ_{max} as a function the inclination angle for various particle hold-up

accompanied with the formation of a dense core, it is then natural to investigate how the volume fraction evolves with increasing inclination angle.

In Fig. 9, we present the maximum value of the volume fraction ϕ_{max} in the cross-section of the flow as a function of the inclination angle. For a given particle hold-up, this value first decreases with increasing angle, as naturally expected. However, we observe a critical angle around 25° at which the decrease is stopped and the packing fraction reaches a local minimum. Above this critical angle, the maximum packing fraction increases with increasing angle and eventually reaches a peak value at $\theta \approx 30^\circ$ before decreasing again. The appearance of the local minimum coincides with the emergence of the supported flow regime with a dense core floating on a gaseous layer. As previously discussed, the increase of the packing fraction can be seen as the signature of the clustering instability in granular gas [16].

Importantly, the local maximum of the packing fraction is reached just before the transition towards the asymmetric core regime. After the local maximum, the packing fraction starts a new decrease with increasing angle. This decrease is concomitant with a shrinkage of the latter: particles from the core evaporate and enter the surrounding gaseous region.

Upon increasing the particle hold-up, the same trend is observed for the maximum packing fraction. The packing fractions at the local minima and maxima both increase with increasing particle hold-up but the difference between the maximum and minimum packing fraction tends to decrease. This behavior of the packing fraction is reminiscent of the liquid-gas first-order transition of a molecular gas. There is indeed a striking resemblance with the isothermal curves of a simple gas in the pressure-volume diagram.

As a conclusion, the evolution of the maximum packing fraction ϕ_{max} as a function of the inclination provides a clear

indicator of the transition between the roll regime and the supported flows. The minimum of the curve $\phi_{max}(\theta)$ delineates the onset of the supported flow regimes.

4.3 Skewness

The last transition concerns the supported regime with a asymmetric core. We attempted to characterize the asymmetry of the dense core by investigating the asymmetry of the instantaneous depth-integrated transverse packing fraction profiles $\phi(y)$ through the skewness parameter S defined as

$$S = \frac{\int_0^W dy \phi(y) (y - \mu)^3 / \left(\int_0^W dy \phi(y) \right)}{\left[\int_0^W dy \phi(y) (y - \mu)^2 / \left(\int_0^W dy \phi(y) \right) \right]^{3/2}} \quad (3)$$

with $\mu = \int_0^W dy \phi(y) y / \int_0^W dy \phi(y)$.

We present in Fig. 10a the skewness as a function of time. The skewness S is small at low and moderate inclination angles (e.g., $\theta = 19, 22$ and 27°) but becomes significant at larger inclination angle (e.g., $\theta \geq 40^\circ$) and oscillates between positive and negative values with a well defined periodicity which is directly related to the rocking motion of the dense core. The variation of the amplitude of the skewness as a function of the inclination is shown in Fig. 10b for various particle hold-up H . The amplitude is negligible (i.e., smaller than 0.005) for low inclinations and starts to increase progressively at the onset of the appearance of the supported regime (i.e., for $\theta > 25^\circ$). This means that the asymmetry of the flow develops as soon as the supported regime emerges. However, the amplitude of the asymmetry reaches a significant value for larger inclination angles. For definiteness, we have set the onset of the transition when the amplitude of the asymmetry goes beyond the critical value $\sigma_c = 0.01$. With this criterion, we find that the asymmetric transition slightly increases with increasing particle hold-up: it occurs

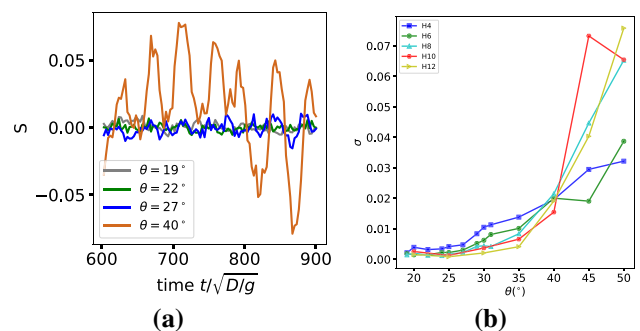


Fig. 10 a Evolution of the skewness S of the depth-integrated transverse packing fraction profile $\phi(y)$ as function of time for inclination angles $\theta = 19, 22, 27$ and 40° and a fixed particle hold-up $H = 6D$. b Standard deviation of the skewness S as a function of the inclination angle for various particle hold-up

at $\theta \approx 30^\circ, 35^\circ$ and 37° for $H = 4D, 8D$ and $12D$, respectively. This parameter thus allows to delineate a transition between supported regimes with a symmetric and asymmetric core, respectively.

5 Sidewall and basal friction

In these types of confined flows, boundaries play an important role. It is thus instructive to investigate in particular how the effective sidewall and bottom friction, defined as the ratio of tangential to normal stresses, evolve according to the flow regimes reported below. Brodu and co-workers [1] showed the sidewall and bottom friction both increase with increasing inclination angle but surprisingly decrease with increasing particle hold-up. Here, we are going further by investigating how these trends could be cast into simple laws.

We first investigate the averaged effective friction at the basal and lateral walls computed from the ratio of the wall-averaged tangential stress to the wall-averaged normal stress. Second, we analyze the basal and lateral friction at the local scale.

5.1 Averaged friction law

The salient outcome of our data analysis is that the variation of both the averaged basal and sidewall friction can be simply described through a unique dimensionless number, analog to a Froude number, $Fr = V_{boundary} / \sqrt{gH \cos \theta}$, where H is the particle hold-up, θ the angle of inclination and $V_{boundary}$ the velocity at the considered boundary (i.e., either V_b or V_w). Indeed, if we plot the effective basal friction and sidewall friction as a function of the Froude number Fr for all the SFD flow regimes investigated so far (i.e., within the parameter range: $4 \leq H/D \leq 12$ and $15^\circ \leq \theta \leq 50^\circ$), we get a nice collapse of all the data onto a unique curve (see Fig. 11).

The $\mu(Fr)$ curve increases monotonically with the Froude number and seems to saturate at large Froude number to an asymptotic value. Interestingly, the $\mu(Fr)$ curve shares strong resemblance with the $\mu(I)$ rheological curve for dense granular flows over bumpy bottoms and can be well approximated by a similar functional form:

$$\mu(Fr) = \mu_1 + \frac{\mu_2 - \mu_1}{1 + Fr_0/Fr}, \tag{4}$$

where μ_1, μ_2 and Fr_0 are fitting parameters. The best fit to the data provides $\mu_1 \approx 0.24, \mu_2 \approx 0.63$ and $Fr_0 \approx 8$. Formally, the parameters μ_1 and μ_2 correspond to the value of the wall friction for vanishing and large Froude number, respectively. For the basal friction law, $\theta_1 = \arctan(\mu_1) \approx 13.5^\circ$ has the same physical meaning as the corresponding parameter in the $\mu(I)$ rheology and stands for the minimum inclination

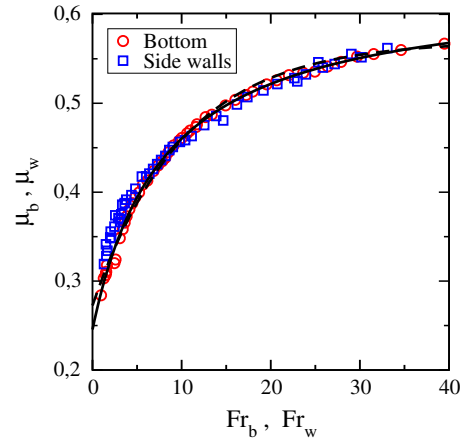


Fig. 11 Effective basal friction μ_b (circle symbols) and sidewall friction μ_w (square symbols) as a function of the Froude number $Fr_b = V_b / \sqrt{gH \cos \theta}$ and $Fr_w = V_w / \sqrt{gH \cos \theta}$, respectively, for all the SFD flow regimes investigated so far (i.e., within the parameter range: $4 \leq H/D \leq 12$ and $15^\circ \leq \theta \leq 50^\circ$). All the data collapse on a unique master curve (solid line) which is obtained by a fit using Eq. 4. An exponential fit (dash line) of the form $\mu(Fr) = \mu_2 + (\mu_1 - \mu_2) \exp(-Fr/Fr_0)$ with $\mu_1 \approx 0.27, \mu_2 = 0.57$ and $Fr_0 \approx 10.1$ works well too

angle at which a flow is sustainable. This value is smaller but reasonably close to the critical inclination angle inclination below which the flow stops: $\theta_{min} \approx 14^\circ$ [11]. Similarly, $\theta_2 = \arctan(\mu_2)$ can be interpreted as the maximum inclination angle at which steady flows can be achieved in absence of side-wall friction. Physically, this value is bounded by the microscopic friction angle between the particles and the wall (i.e., $\theta_w = \arctan(\mu_w) = 30.7^\circ$). The best fit gives $\theta_2 \approx 32.2^\circ$ which is greater than the theoretical upper bound θ_w . This means that the functional form we employ, although it provides a good approximation in the range of studied Froude number, is probably not fully relevant. A functional form based on the exponential law,

$$\mu(Fr) = \mu_2 + (\mu_1 - \mu_2) \exp(-Fr/Fr_0), \tag{5}$$

seems to provide a better alternative. This functional form is similar to the original friction law proposed by Pouliquen for flows over bumpy bases in [4]. However, it differs in a subtle aspect. The original Pouliquen's friction law phrased as a function of the Froude number would be written as $\mu = \mu_1 + (\mu_2 - \mu_1) \exp(-Fr_0/Fr)$. This form has the same asymptotic values for vanishing and large Froude number (μ_1 and μ_2 , respectively) but has a different slope at zero Froude number: the slope is zero whereas with the form given by Eq. 5 the slope is finite. A detailed analysis at vanishing Froude number would be required to determine which is the better form. With the functional form given by Eq. 5, the best fit gives $\mu_1 \approx 0.27, \mu_2 = 0.57$ and $Fr_0 \approx 10.1$. This fit

provides a value of μ_2 which is satisfactorily smaller than the upper bound $\mu_w = 0.593$.

Several additional comments follow. (i) It is important to note that the $\mu_b(Fr_b)$ law (resp. $\mu_w(Fr_w)$) should be considered as a boundary condition which relates the effective friction at smooth boundaries to the flow velocity at the boundaries (through the Froude number Fr_b or Fr_w). Consequently, they do not have the same status as the frictional $\mu(I)$ rheology which relates the internal effective friction (between adjacent granular layers parallel to the base) to the local internal shear rate through the inertial number I .

(ii) The Froude numbers Fr_b and Fr_w are defined from the flow velocity evaluated at the boundary (i.e., V_b or V_w) because we are interested in what occurs at the boundaries. Our definition of the Froude number thus differs from the one used in related works [4, 20, 21] and which is based on the mean flow or free surface velocity. If we use the latter definition for the Froude number, we also obtain a good collapse but with a slightly larger scattering. This result is not surprising since we have seen that the mean flow velocity is of the same order of magnitude as the velocities at the boundaries (see Eq. 2). In contrast, dense and slow flows over a bumpy bottom have a vanishing basal velocity (i.e., no-slip condition) and thus the latter does not scale with the mean flow velocity.

(iii) It is worthwhile to highlight the similarities and differences between the $\mu_b(Fr_b)$ law and the $\mu(I)$ rheological law obtained for dense flows over a bumpy bottom. As already mentioned, the latter describes the internal effective friction as a function of the local inertial number I or equivalently to the local shear rate. By continuity of the stresses, one can deduce a relationship between the friction and the inertial number at the base, respectively μ_b and I_b . The $\mu(I)$ rheology thus provides a relationship between the basal friction and I_b while the $\mu_b(Fr_b)$ law relates the basal friction to the flow velocity at the base through the Froude number Fr_b . The question that arises is how the basal inertial number I_b is related to the Froude number Fr_b . For dense flows over bumpy bottom, the basal velocity is generally assumed to vanish such that the Froude number Fr_b is reduced to zero. This contrasts with flows on smooth inclines, where the flow velocity V_b at the base is finite and closely related to the mean flow velocity V_L ($V_b \propto V_L/H^{1/4}$). The relation between Fr_b and I_b in the context of granular flows on smooth inclines is not known in general, except for unidirectional and dense flows. In the latter regime, the bulk flow can be still reasonably well described by the $\mu(I)$ rheology as shown in [11] (this is not the case for the other flow regimes), while the basal friction was shown to obey the $\mu_b(Fr_b)$ law. The continuity of the friction at the bottom provides us with the following relation $\mu(I_b) = \mu_b(Fr_b)$, which thus relates I_b and Fr_b .

(iv) The $\mu(Fr)$ friction law provides a simple explanation for the decrease of the bottom and wall friction with increasing particle hold-up. Indeed, recalling that the velocities at the boundaries are almost invariant with the particle hold-up (see Eq. 2), the Froude number decreases with increasing particle hold-up at a fixed inclination angle. This results in a decrease of the basal friction since $\mu(Fr)$ is an increasing function of the Froude number.

(v) Equation 4 or Eq. 5 together with Eq. 2 and the definition of the Froude number provides us with an explicit expression of the basal and sidewall friction as a function of the inclination angle and particle hold-up.

(vi) In kinetic theories for granular flows, the effective friction at bumpy wall is often expressed as a function of the dimensionless quantity V/\sqrt{T} [22]. In the case of flat frictional wall [22], the relevant quantity is g/\sqrt{T} where $g = ||\mathbf{V} - (D/2)\omega \times \mathbf{n}||$ is the contact slip velocity at the wall (\mathbf{n} is the unit vector normal to the wall and ω is the mean angular velocity). It is thus instructive to check whether the friction at the basal and side walls can be also described in terms of the ratio g/\sqrt{T} . We present in Fig. 12 the effective bottom friction as a function of the dimensionless quantity $g_b/\sqrt{T_b}$ calculated at the base. We find a nice collapse of the data on a single curve which is very similar to the $\mu(Fr)$ curve. We can note however a deviation of the monotonic behavior at low value of the friction (i.e., at small inclination angles corresponding to dense flows). It thus turns out that the Froude number and the dimensionless contact slip velocity g/\sqrt{T} play a similar role and are closely related. We find indeed the following correlation:

$$Fr_b \approx 9.95 \left(\frac{g_b}{\sqrt{T_b}} - 1.86 \right). \tag{6}$$

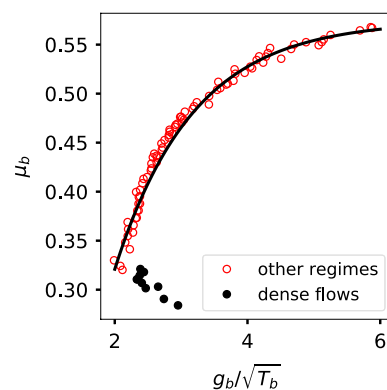


Fig. 12 Bottom friction μ_b as a function of the dimensionless contact slip velocity $g_b/\sqrt{T_b}$. The solid line represent the best exponential fit of the form: $\mu_b = \mu_2 + (\mu_1 - \mu_2) \exp[-0.85(g_b/\sqrt{T_b} - 1.86)]$ with $\mu_1 \approx 0.32$ and $\mu_2 = 0.575$. The data corresponding to unidirectional dense flows do not fall on the master curve represented by the solid line

The above correlation works well for large Froude number but fails for small Froude number below 2, corresponding to dense flows.

(vii) Interestingly, we noted that if we use a definition of the Froude number based on the contact slip velocity g_b (resp. g_w) instead of the translational velocity V_b (resp. V_w), we also obtain a nice collapse of the data on a unique master curve. This confirms that there is a close relationship between the contact slip velocity and translational velocity at the boundaries (see Fig. 13).

(vii) Finally, the exact form of the $\mu(Fr)$ curve is expected to be dependent of the material properties of the grains and the walls and in particular of the microscopic friction coefficients μ_w (resp. μ_g) between the particles and the walls (resp. between the particles). Preliminary numerical investigations indicate that the scaling with the Froude number is however preserved when changing the material properties of the grains and the walls. In other words, only the fitting parameters μ_1 , μ_2 and Fr_0 are sensitive to a change of the micro-mechanical parameters.

5.2 Local friction law

In the previous subsection, we analyzed the effective friction at the base and at the side-walls at a global scale. It can be interesting to check whether the friction law established previously also holds at a local scale. The effective friction at the base and at the side-walls are not uniform along the cross-wise direction (y) and the depth (z), respectively, as illustrated in Fig. 14. The basal wall friction is smaller close to the side-walls than in the center of the channel. The influence of the sidewall extends over $10D-20D$. Similarly, side-wall friction exhibits a strong gradient according to the depth: it decreases with increasing depth and reaches its minimum value at the base.

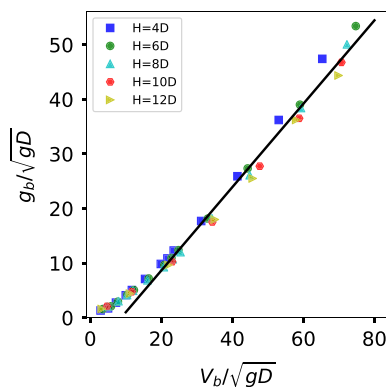


Fig. 13 Relationship between the contact slip velocity g_b and the translational velocity V_b at the base for increasing particle hold-up from $H = 4D$ to $H = 12D$. The solid line is an affine fit to the data

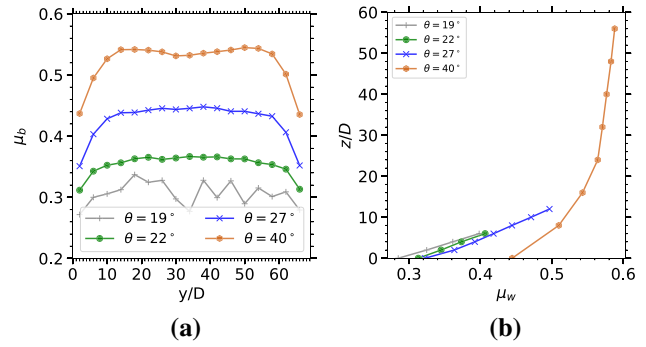


Fig. 14 **a** Cross-wise profiles of the effective basal friction $\mu_b(y)$ for $H = 6D$ and various inclination angles. **b** Vertical profiles of the effective sidewall friction $\mu_w(z)$ for $H = 6D$ and various inclination angles

Defining a local Froude number (i.e., $Fr^{loc} = V^{loc} / \sqrt{P^{loc} / \rho}$, where V^{loc} and P^{loc} are the local particle velocity and pressure, respectively, at a given location at the basal or side wall, and ρ is the particle density), we can display how the local friction varies as a function of the local Froude number. Similarly, as for the global friction, we obtain for both the local basal and side-wall friction a nice collapse on a unique master curve $\mu^{loc}(Fr^{loc})$ (see Fig. 15a). This curve differs slightly from the global law $\mu(Fr)$ essentially at large Froude number. Using an exponential fit (cf Eq. 5), we obtained slightly different values for the fitting parameters: $\mu_1^{loc} \approx 0.25$, $\mu_2^{loc} \approx 0.59$ and $Fr_0^{loc} \approx 9.6$. The most significant difference concerns the value of μ_2 (0.59 against 0.57) which is closer to the upper bound $\mu_w = 0.593$.

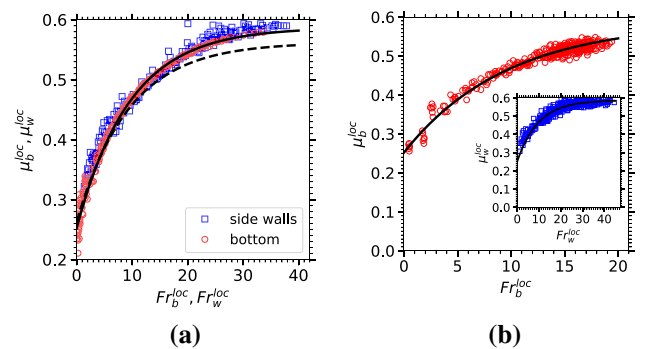


Fig. 15 **a** Local basal friction μ_b^{loc} and sidewall friction μ_w^{loc} as a function the local Froude number $Fr_b^{loc} = V_b^{loc} / \sqrt{P_b^{loc} / \rho}$ and $Fr_w^{loc} = V_w^{loc} / \sqrt{P_w^{loc} / \rho}$, respectively. The solid line stands for the best exponential fit while the dash line represents the exponential fit for the global friction $\mu(Fr)$. **b** Evolution of the local basal friction in the transient regime for $H = 10D$ and $\theta = 40^\circ$ as a function of the local Froude number $Fr_b^{loc} = V_b^{loc} / \sqrt{P_b^{loc} / \rho}$. The solid line stands for the master local friction curve established in (a). Inset: Evolution of the local side-wall friction in the transient regime for $H = 10D$ and $\theta = 40^\circ$ as a function the local Froude number $Fr_w^{loc} = V_w^{loc} / \sqrt{P_w^{loc} / \rho}$

Interestingly, the local friction law seems to hold also for unsteady flows. As detailed in [1], the flow exhibits a transient before reaching a steady state: the mean velocity increases monotonically in course of time and eventually saturates to a steady value. Figure 15b shows that even during the transient regime, the local friction both at the base and at the side-walls evolves along the master local friction curve $\mu^{loc}(Fr^{loc})$. This result thus indicates that the local friction laws are robust features for both steady and unsteady flows.

6 Conclusion

We have studied high-speed confined granular flows down smooth inclines and describe in detail the different SFD flow regimes, including unidirectional dense flows, roll regime and supported flows. We have identified key parameters that allows to delineate precisely the domain of existence of the different flow regimes in the parameter space (H, θ) . Importantly, we have highlighted that the friction at the basal and side walls can be described by a unique curve that depends solely of the Froude number defined as $V/\sqrt{gH \cos \theta}$, where V is the particle velocity at the walls. We showed additionally that the friction at the local scale also obeys a unique law as a function of the local Froude number defined as $Fr^{loc} = V^{loc}/\sqrt{P^{loc}/\rho}$. This local friction law is shown to be very robust since it holds both for steady and unsteady flows. We thus strongly believe that the local friction law may be used successfully as a reliable boundary condition for flows running on smooth walls.

A crucial question is the extent to which the SFD flow regimes and their features are specific to the material parameters and the confined geometry that we have considered. Further extensive simulations where the material parameters (friction and restitution coefficient) and channel width W are varied would be required to check the generality of our outcomes. This is a work planned for the near future. Preliminary results show that the SFD flows identified in this paper are very robust to parameter change but their onset of appearance may be significantly affected. For example, increasing the dissipation in the grain-grain collision favors and reinforces the development of supported flows.

Finally, these results provide a unique set of very complex granular flow regimes for testing theoretical and rheological models.

Acknowledgements We acknowledge the support of the French Research National Agency through the project ANR-16-CE01-0005.

Compliance with ethical standards

Conflict of interest The authors declare that they have no conflict of interest.

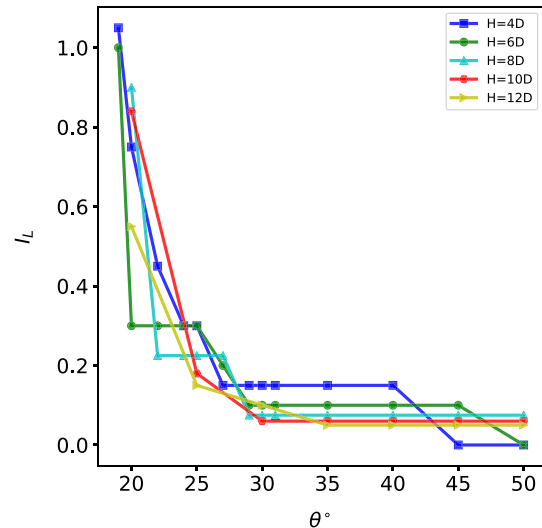


Fig. 16 Layering index I_L as a function of the inclination angles for various particle hold-up: $I_L = (1/N_{max}) \sum_i Y(\phi_i^{max} - \phi_i^{min} - 0.1)$ where Y is the Heaviside function

A Layering index

In the unidirectional and dense flow regime, the particle volume fraction exhibits strong oscillations. It could be interesting to introduce a layering index I_L to quantify the number of oscillation cycles. It is defined as follows. As the wavelength of the oscillation is of the order of one grain diameter, we look at within each layer of one diameter thickness and parallel to the bottom whether the volume fraction oscillates.

In each layer i , we thus calculate the maximum and the minimum of the volume fraction, ϕ_i^{min} and ϕ_i^{max} , respectively. If the amplitude of the oscillation (i.e., $\phi_i^{max} - \phi_i^{min}$) in a given layer is greater than a critical value $\Delta\phi$, the layer is associated to an ordered layer of particles and the layering index is incremented by one unit. The layer index I_L is defined as $I_L = (1/N_{max}) \sum_i Y(\phi_i^{max} - \phi_i^{min} - \Delta\phi)$ where Y is the Heaviside function and $N_{max} = H/0.6$ is the highest possible number of ordered layers within a uniform and dense flow with a mean volume fraction of 0.6 and particle hold-up H . The renormalization of I_L by N_{max} provides an index which is bounded by 1. The critical value $\Delta\phi$ used to quantify the layering is taken to be 0.1. This choice is somewhat arbitrary but it is good comprise to capture the oscillation of the packing fraction and eliminate random fluctuations of the packing fraction profile.

The variation of the layering index with the inclination angle is shown in Fig. 16. SFD unidirectional and dense flows exhibit a strong layering with a layering index close to 1, indicating that the whole depth of the flow dense

flows) is layered. Upon increasing the inclination angle (from 20° to 25°), the layering index decreases progressively towards zero. Above 25° (i.e., in the supported flow regime), the layering index has fallen to a small but finite residual value (below 0.2). This means that even in the supported regime, there remains one ordered layer which is located at the bottom. This residual dense ordered layer disappears at very large inclination angle. The layering index can thus not be employed to delineate the transition towards the supported flow regime.

References

1. Brodu, N., Delannay, R., Valance, A., Richard, P.: New patterns in high-speed granular flows. *J. Fluid Mech.* **769**, 218–228 (2015)
2. GDR MiDi: On dense granular flows. *Eur. Phys. J. E* **14**(4), 341 (2004)
3. Delannay, R., Valance, A., Mangeney, A., Roche, O., Richard, P.: Granular and particle-laden flows: from laboratory experiments to field observations. *J. Phys. D Appl. Phys.* **50**(5), 053001 (2017)
4. Pouliquen, O.: Scaling laws in granular flows down rough inclined planes. *Phys. Fluids* **11**(3), 542 (1999)
5. Forterre, Y., Pouliquen, O.: Flows of dense granular media. *Ann. Rev. Fluid Mech.* **40**(1), 1 (2008)
6. Silbert, L.E., Ertas, D., Grest, G.S., Halsey, T.C., Levine, D., Plimpton, S.J.: Granular flow down an inclined plane: bagnold scaling and rheology. *Phys. Rev. E* **64**, 051302 (2001)
7. Delannay, R., Louge, M., Richard, P., Taberlet, N., Valance, A.: Towards a theoretical picture of dense granular flows down inclines. *Nat. Mater.* **6**, 99 (2007)
8. Forterre, Y., Pouliquen, O.: Longitudinal vortices in granular flows. *Phys. Rev. Lett.* **86**, 5886 (2001)
9. Forterre, Y., Pouliquen, O.: Stability analysis of rapid granular chute flows: formation of longitudinal vortices. *J. Fluid Mech.* **467**, 361–387 (2002)
10. Börzsönyi, T., Ecke, R.E., McElwaine, J.N.: Patterns in flowing sand: understanding the physics of granular flow. *Phys. Rev. Lett.* **103**, 178302 (2009)
11. Brodu, N., Richard, P., Delannay, R.: Shallow granular flows down flat frictional channels: steady flows and longitudinal vortices. *Phys. Rev. E* **87**, 022202 (2013)
12. Ralairisoa, J.L., Valance, A., Brodu, N., Delannay, R.: High speed confined granular flows down inclined: numerical simulations. *EPJ Web Conf.* **140**, 03081 (2017)
13. Taberlet, N., Richard, P., Valance, A., Losert, W., Pasini, J.M., Jenkins, J.T., Delannay, R.: Superstable granular heap in a thin channel. *Phys. Rev. Lett.* **91**, 264301 (2003)
14. Richard, P., Valance, A., Métayer, J.F., Sanchez, P., Crassous, J., Louge, M., Delannay, R.: Rheology of confined granular flows: scale invariance, glass transition, and friction weakening. *Phys. Rev. Lett.* **101**(24), 248002 (2008)
15. Louge, M.Y., Keast, S.C.: On dense granular flows down flat frictional inclines. *Phys. Fluids* **13**(5), 1213 (2001)
16. Goldhirsch, I., Zanetti, G.: Clustering instability in dissipative gases. *Phys. Rev. Lett.* **70**, 1619 (1993)
17. McNamara, S., Young, W.R.: Inelastic collapse in two dimensions. *Phys. Rev. E* **50**, R28 (1994)
18. Opsomer, E., Ludewig, F., Vandewalle, N.: Dynamical clustering in driven granular gas. *EPL* **99**(4), 40001 (2012)
19. Eshuis, P., van der Weel, K., Alam, M., van der Hoef, M., Kuipers, H., Luding, S., van der Meer, D., Lhose, D.: Buoyancy driven convection in vertically shaken granular matter: experiment, numerics, and theory. *Granul. Matter* **15**, 893 (2013)
20. Holyoake, A.J., McElwaine, J.N.: High-speed granular chute flows. *J. Fluid Mech.* **710**, 35–71 (2012)
21. Gray, J.M.N.T., Edwards, A.N.: A depth-averaged $\mu(I)$ -rheology for shallow granular free-surface flows. *J. Fluid Mech.* **755**, 503–534 (2014)
22. Jenkins, J.T.: Boundary conditions for rapid granular flow: flat, frictional walls. *J. Appl. Mech.* **59**(1), 120 (1992)

Publisher's Note Springer Nature remains neutral with regard to jurisdictional claims in published maps and institutional affiliations.

4 Conclusion and perspectives

In this chapter, we revisited the results of [Brodu et al. \(2015\)](#). we gave some precisions on granular flows in an inclined smooth channel with a gap width $W = 68D$, we describe in details, the transitions between the different flow regimes, including unidirectional, roll and supported ones. We highlight that the variation of the effective boundary friction as a function of the mass hold up H and the inclination angle θ can be expressed as a boundary friction law: $\mu(Fr)$. It can be interpreted as a boundary condition since the Froude number Fr is obtained from the sliding velocity and the normal stress at the boundary. This local friction law holds for all the flows: steady as unsteady.

From a theoretical point of view, this boundary condition is an important information which could be used in complement of an internal rheology - like the $\mu(I)$ rheology, or the kinetic theory - to determine the flow, but it will not be enough to allow a full resolution. We can see it in the article above (section 3): even at a global scale, it is necessary to use the mean velocity scaling law if we want resolve the problem of finding the SFD velocity for a given set of parameters (θ, H) . An important question is thus to see if one can find complementary laws. Another question is the universality of the friction law: how does it change, if we change the channel width, the coefficient of restitution, the coefficients of friction?

Chapter 3

Effect of channel width on confined granular flows

1 Introduction

In this chapter, we study the influence of the channel width on the flow features. The outcomes have been presented in an article which is under preparation for a forthcoming submission. We briefly here introduce the content of the article which is reproduced in Sect 2.

In the previous chapter, we have highlighted the existence of a universal law for the basal and side-wall friction and have shown that the latter can be described as a unique function of a dimensionless Froude number. This outcome was established for a fixed channel width set to $W = 68D$. It is thus natural to wonder whether the friction law $\mu(Fr)$ holds for other channel widths W . Also, we would like to know whether the different flow regimes identified for $W = 68D$ persist for smaller and wider channel widths. In this article, we present first a rather exhaustive and detailed picture on the flow regimes obtained for a gap width $W = 40D$. We then make an analysis of the role of W by comparing outcomes obtained for various gap widths $W = 20, 40, 60, 68, 75$ and $140D$.

2 Article: Discrete simulations of confined high-speed granular flows: Influence of the channel width

2.1 Introduction

Recently, several works have been devoted to the effect of lateral confinement on the properties of granular flows [Brodu et al. \(2013, 2015\)](#). Both experimental and numerical studies have pointed out that frictional lateral walls induce new flow properties. For example, steady and fully developed (SFD) flows have been observed up to large angles of inclination whereas accelerated ones are usually expected ([Brodu et al., 2015](#)). These SFD regime exhibit a rich variety of flow patterns, depending on inclination angle θ and mass holdup H (defined as the depth-integrated particle volume fraction). [Brodu et al. \(2015\)](#) found in particular a new SFD regime, called "supported flow" and characterized by a dense core moving at a rapid and uniform speed and surrounded by a very dilute and agitated granular gas. The mean velocity V_L of the supported flows obeys a simple scaling law with the mass hold-up H : $V_L \propto H^{1/4}$ for a given inclination angle and a fixed gap width $W = 68D$ (where D is the particle diameter). This scaling law differs drastically from the Bagnold law or the one

derived from the $\mu(I)$ rheology for dense granular flows (i.e., $V_L \propto H^{3/2}$). The origin of this new scaling has not yet been identified and requires definitively further studies.

Additionally, the simulations of Brodu et al. (2013, 2015); Zhu et al. (2020) was conducted with a fixed gap width $W = 68D$. An subsequent issue is to determine where the supported flow regime is robust and can emerge in flow configurations with smaller gap widths. In this paper, we study the effect of channel width on the flow regimes and analyse the key influence of the bottom and side-wall friction. We provide a complete phase diagram for reduced gap width $W = 40D$ and describe the new flow regimes we uncovered. Interestingly, we extend the validity of the scaling law by Brodu et al. (2015) for different gap width and establish that for supported flows $V_L \propto H^\alpha W_L^\beta$ with $\alpha = 0.3 \pm 0.05$ and $\beta = 0.7 \pm 0.05$. Importantly, we show that the effective friction at the base and at the side walls obey a universal behavior which can be captured by a unique dimensionless number, the Froude number defined as $Fr = V_s / \sqrt{gH \cos \theta}$ where V_s is the slip velocity at the boundary.

2.2 DEM

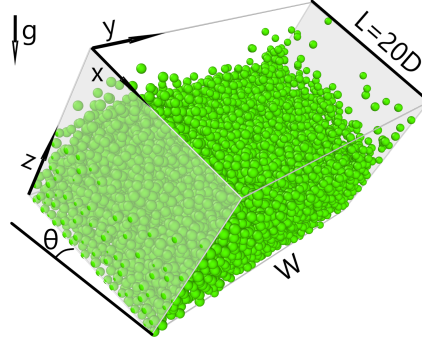


Figure 3.1: Figure for numerical simulation system on $W = 40D$. The system is driven by gravity \mathbf{g} with periodic condition ($L = 20D$) along the flow direction \mathbf{x} , \mathbf{y} is the transverse direction normal to the flat side-walls (width of the cell: W) and \mathbf{z} is normal to the flat base. The angle θ between \mathbf{g} and \mathbf{z} is the inclination angle.

The discrete element method (DEM) is a classical numerical simulation method for studying granular flows. The principle of DEM simulations is to treat each grain as a sphere (of diameter D) subject to gravity and contact forces with both the other grains and the boundaries. Particle-particle interaction is modelled by using linear visco-elastic approach. Two grains i and j interact when they overlap. The overlapping distance between i and j is defined as $\delta_{ij} = (D_i + D_j)/2 - r_{ij}$ where r_{ij} is the center-to-center grain separation. The force applied by the grain i on grain j is decomposed into normal and tangential components (respectively F_n and F_t). The normal contact force is given by: $F_n = (k_n \delta_{ij} + \gamma_n v_n)$ where k_n is a spring constant, γ_n a damping coefficient set by the normal coefficient of restitution e_n , and v_n the normal component of the relative translational grain velocity. A similar model is used for the tangential component enforced by the Coulomb friction $|F_t| \leq \mu |F_n|$ where μ is the model friction coefficient. The torque acting on a grain is given by: $q = -(D/2)(F_t \times n)$ where n is the normal unit vector. We use the same microscopic mechanical parameters as in Louge and Keast (2001); Brodu et al. (2013, 2015) with $e_n^{ss} = 0.972$ and $\mu_{gg} = 0.33$ for the particle-particle interactions and $e_n^{sw} = 0.8$ and $\mu_{gw} = 0.593$ for the particle-wall interactions.

We adopt this method to study gravity-driven chute flows, with flat and frictional bottom and side walls, as illustrated in Fig. 3.1. The flow configuration is similar to the one studied

in Brodu et al. (2013) with a gap width $W = 68D$. The channel is inclined with an angle θ with respect to the horizontal. $(0x)$ and $(0y)$ are the stream-wise and cross-wise direction of the flow, respectively, and $(0z)$ is the direction perpendicular to the flow base. The stream-wise length of the channel is set to $L = 20D$ and the width W is varied between $20D$ and $140D$. The channel is not bounded in the $(0z)$ direction and we use periodic boundary conditions in the stream-wise direction. The control parameters of the system are the mass hold-up H , the inclination angle θ , and the channel width W .

2.3 Transient

We describe the transient through the mean flow velocity defined as $V = (1/N) \sum_i \sqrt{v_{ix}^2 + v_{iy}^2 + v_{iz}^2}$, where the sum is done over all the particles of the system, N is the total number of the particles, and v_{ix} , v_{iy} and v_{iz} are the instantaneous velocity components of the particle i . As an

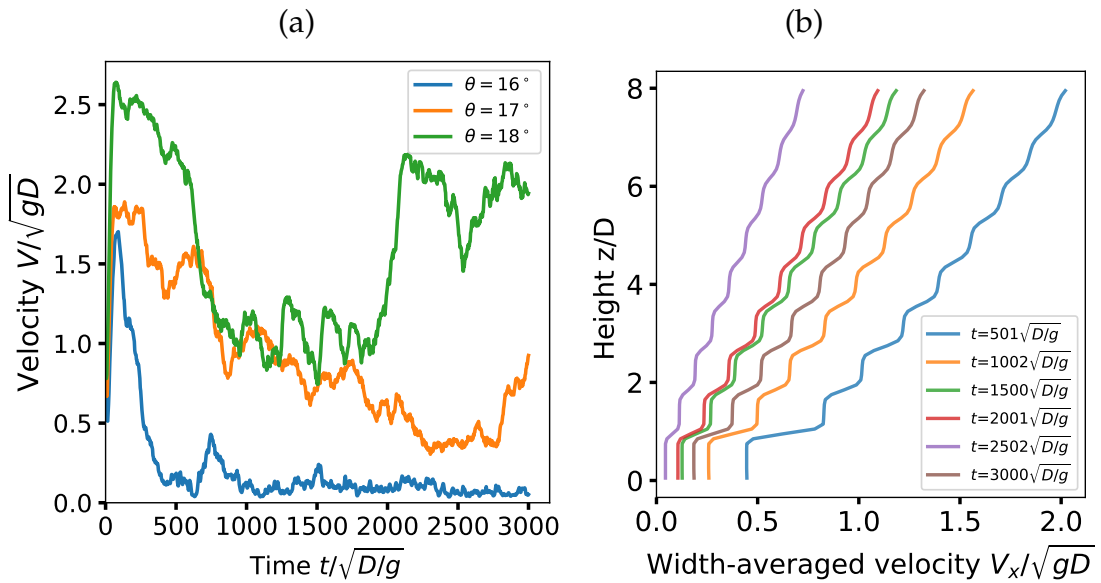


Figure 3.2: (a) Temporal evolution of the mean velocity for shallow angles $\theta = 16^\circ$, 17° and 18° . $H = 5D$ and $W = 40D$. These flows are referred to as intermittent regime. (b) Velocity profiles at different times corresponding to the flow at $\theta = 17^\circ$.

example, we describe the transient regimes according to the angle of inclination for a given mass hold-up $H = 5D$. For small angles, typically below 15° , the flow comes to rest. Between 16° and 18° , after a short transient, the system keeps flowing but with a small mean velocity that fluctuates a lot (see Fig. 3.2). The standard deviation about the mean value is of the order of the latter. We refer to these flows as intermittent regime.

For angles between 20° and 50° , the mean velocity of the flow increases monotonously in course of time towards a limiting value V_L (see Fig. 3.3.a). For a fixed particle hold-up, the steady value increases with increasing angle but the characteristic time to reach the steady state does not vary much with the inclination angle. For practical purpose, it can be interesting to convert the time into a travelling distance defined as the distance travelled by the center of mass of the granular system. We can thus plot the evolution of the mean flow velocity as a function of the travelling distance (see Fig. 3.3). We clearly observe that the travelling distance needed to reach the steady state increases with increasing angle. A quantitative analysis reveals that the characteristic travelling distance L_c , defined as $V(L_c) = 0.9 V_L$, scales as $V_L^{0.85}$ for a given particle hold-up (see Fig. 3.3c). Interestingly, we get the

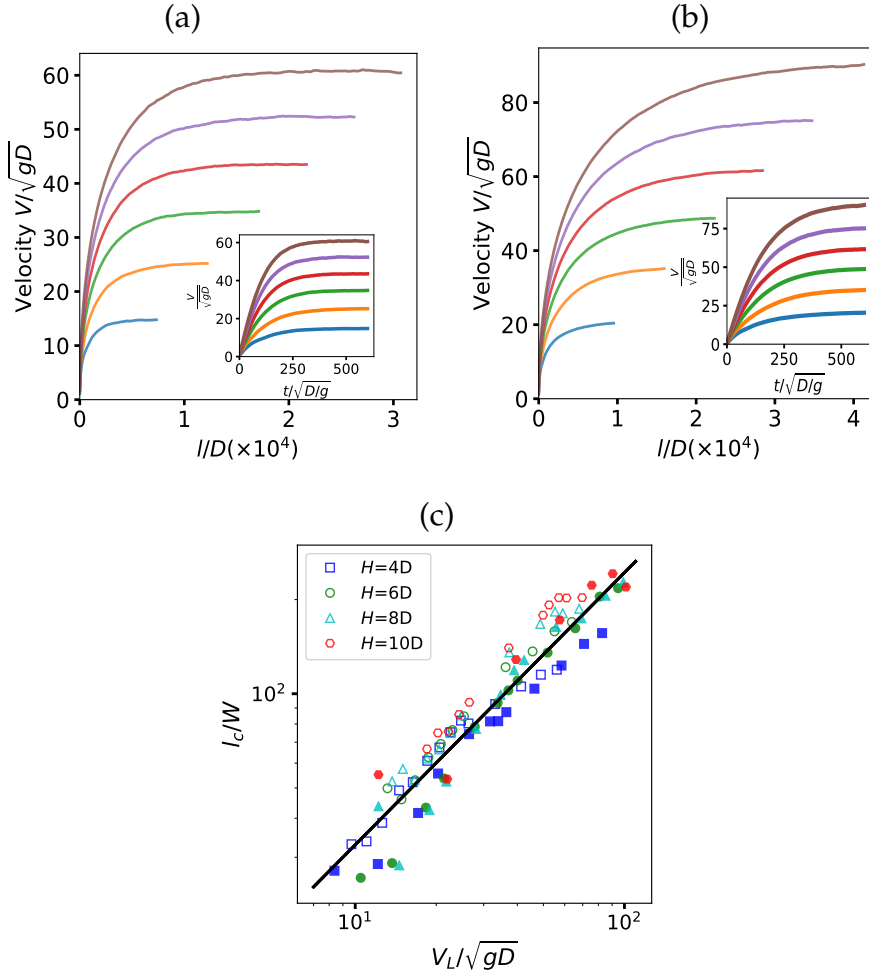


Figure 3.3: Evolution of the mean velocity V as a function as the travelling distance l (defined as the distance travelled by the center of mass of the granular system) for various angles smaller or equal to 50° ($\theta = 20, 25, 30, 35, 40, 45$ and 50°) and $H = 5D$. (a) $W = 40D$ and (b) $W = 68D$. Inset: Corresponding temporal evolution of the mean velocity V . (c) Characteristic length L_c rescaled by W as a function of the steady velocity V_L for various particle hold-up and two gap widths $W = 40D$ (solid symbols) and $W = 68D$ (filled symbols).

same scaling for $W = 68D$ and we can cast the data for both gap widths into a unique scaling law:

$$\frac{L_c}{W} \approx 4.5 \left(\frac{V_L}{\sqrt{gD}} \right)^{0.85}. \quad (3.1)$$

For higher angles (i.e. $\theta \geq 55^\circ$), the transient towards the steady regime is not longer monotone but exhibits an overshoot and then subsequent oscillations around a mean value surprisingly independent of the inclination angle (see Fig. 3.4). This oscillation regime is different from the oscillation regime in Brodu et al. (2015) which is defined through fluctuations of flow structure. The amplitude of the oscillations seems to decay in course of time but it is not possible to tell whether they go to zero or to a finite limit. It would require longer simulations to get a definite answer. Interestingly, the period of oscillation seems to decrease with increasing angle. The peak value corresponding to the overshoot increases with increasing angles but it is reached for roughly the same distance. The transient of these flows thus contrasts markedly with those obtained at smaller angles and are observed both for $W = 40D$ and $W = 68D$. Further analysis reveals that the oscillation of the mean ve-

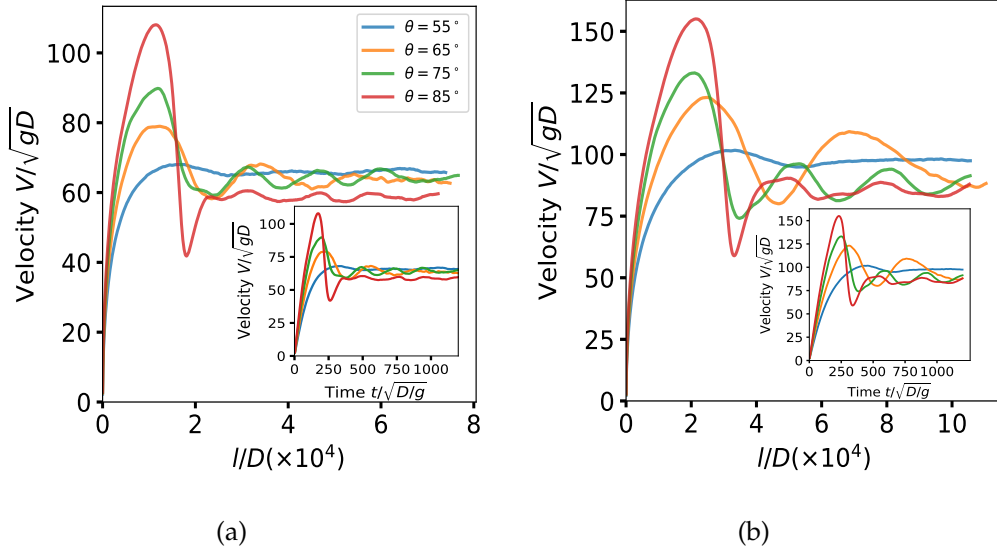


Figure 3.4: Evolution of the mean velocity V as a function of the traveling distance l for very large angles ($\theta = 55, 65, 75$ and 85°) and $H = 5D$. (a) $W = 40D$ and (b) $W = 68D$. Inset: Corresponding temporal evolution of the mean velocity V .

locity has a clear signature in the motion of the center of mass of the granular system. The latter exhibits a vertical oscillation which is out of phase with the former: a maximum of the position of the mass center corresponds to a minimum of the mean velocity. These flows will be referred later to as oscillating flows.

2.4 Phase diagram

In configurations with a gap width $W = 68$, Brodu et al. (2015) identified different steady flow regimes (see Fig. 3.5): i) A unidirectional, dense and layered flow (labelled here after U for unidirectional); ii) A dense and layered flow regime with two longitudinal vortices located at the side walls and close to the free surface (named U S^-); iii) a roll regime R^- which exhibits a pair of counter-rotative longitudinal vortices that spans the entire width of the cell; iv) and v) two types of unusual flows characterized by a dense core floating over a dilute basal layer (referred here after to as "supported regimes");

For $W = 40D$, we observe the same diversity of flow regimes. Interestingly, two additional regimes at high particle hold-up are found: a flow regime with a double dense parts (CR_+^-) and another characterized by the formation of a quasi-static bed below the flowing zone. The latter will be referred to as SSH flow. These new regimes were not observed for $W = 68D$ but probably exist too. Simulations for $W = 68D$ were limited to particle hold-up H smaller or equal to $20D$ and it requires probably higher particle hold-up.

Fig. 3.5 displays the phase diagram for $W = 40D$ in the parameter space (θ, H) . It is very similar to that found for $W = 68D$. For moderate particle hold-up, as we increase the inclination angle, we visit the same successive flow regimes as for $W = 68D$. At moderate angle, we first have dense unidirectional flows (U) with layered structure. Upon increasing inclination angle, a pair of count-rotative longitudinal vortices emerge. In the roll regime, particles at the middle of the cell move downwards whereas particles at the side walls migrate upwards. A further increase of the inclination angle leads to the supported flow regimes characterized by the formation of dense core that float over a dilute basal layer. In the supported regime, the vortices are still present and the convection is even enhanced.

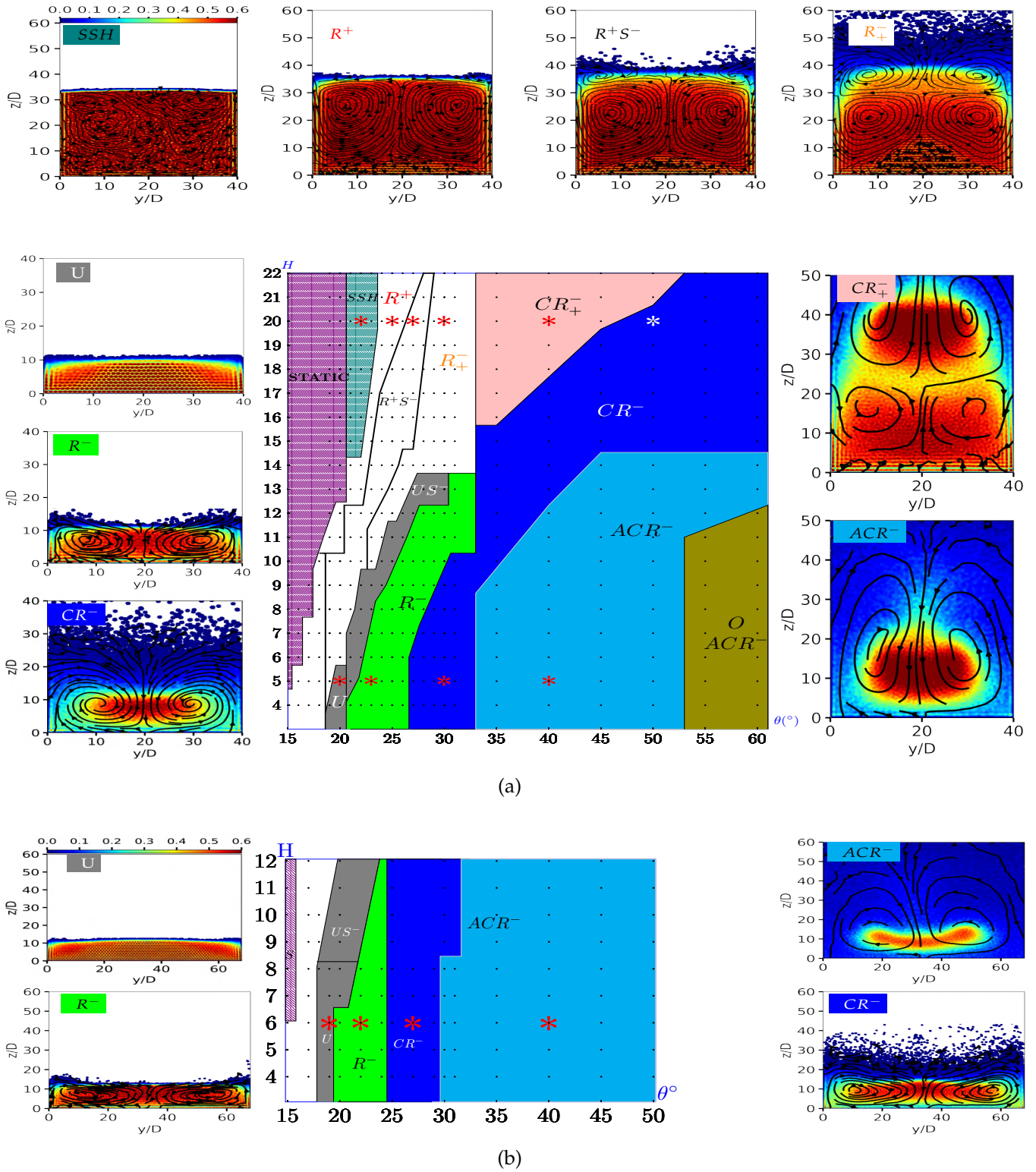


Figure 3.5: Phase diagram in the phase space (H, θ) for $W = 40D$ (a) and $W = 68D$ (b). The regimes are coded by colors. Purple region: states with no flow; White region: intermittent regimes. Gray region: unidirectional SFD flows; Green region: roll regime R^- which exhibits a pair of longitudinal vortices that spans the entire cell width; Blue region: "supported" flows CR^- characterized by a dense core C and a pair of vortices R^- ; Cyan zone: "supported" flows ACR^- with a asymmetric core AC and a pair of vortices R^- ; Pink region: flows with two layers of longitudinal of vortices (a basal pair of vortices R^+ topped by a supported core CR^-); Violet region: oscillating "supported" flows OCR^- . Teal region: SSH flows (flow over a Sided-wall Stabilized Heap); Black dots represent simulations that were achieved (500 for $W = 40D$ and 100 for $W = 68D$). The phase diagram is supplemented with two-dimensional maps representing the particle volume fraction in cross-section of the flow together with the streamlines (left and right panels). These data are averaged over the periodic direction x and over 60 time units.

Differences with the case $W = 68D$ should be however highlighted. First, the transition between the different flow regimes are systematically shifted towards higher angles. Thus, it seems that a decrease of gap width delays the transition. Second, new flow regimes (SSH and CR_{+}^{-}) appear at high particle hold-up and are detailed below.

The SSH regime is obtained at high particle hold-up and moderate angle (i.e., $H > 15D$ and $20^{\circ} < \theta < 24^{\circ}$). It is characterized by a quasi-static bed topped with a flowing layer. This flow regime was already reported and studied numerically (Taberlet et al., 2003; Richard et al., 2008) but with stronger confinement (i.e., smaller gap widths $W = 10$ and $20D$). It is worth noting that longitudinal vortices develop within the flowing layer. These vortices have a reverse direction of rotation in comparison with those developing in the roll and supported flow regime.

The double core (CR_{+}^{-}) regime occurs at high angle and particle hold-up (i.e., $H > 16D$ and $35^{\circ} < \theta < 55^{\circ}$). These flows consist of two superposed dense core separated by a dilute layer. The lower dense core is in contact with the base and a pair of counter-rotating longitudinal vortices develops within it. The direction of rotation is however opposite to that observed in the vortices of the supported flow regime. In the upper dense core, longitudinal vortices are also present and they share the same properties as those of the supported flow regime. In particular, the upper dense core can be termed as supported because it lies on a dilute layer of high energy which keeps it suspended. Second, the direction of rotation is similar to that of the vortices of the supported flow regime.

2.5 Flow features for $W = 40D$

2.5.1 Mean flow velocity

It is interesting to investigate how the mean flow velocity V_L varies with the inclination angle and particle hold-up. We recall that Brodu et al. (2015) reported a simple scaling for the velocity: $V_L \approx H^{\alpha}(A \sin \theta + B)$ with $\alpha \approx 0.25$. The question is to determine whether a similar scaling law holds for smaller gap width W and in particular for $W = 40D$.

For $W = 40D$, we observe clearly two different behaviors of the mean velocity with H for small and large angles, respectively (see Fig. 3.6). At small angles of inclination, we do not observe any dependence of the mean flow velocity with the particle hold-up as soon as H remains moderate (typically $H < 10D$) and the mean flow velocity can be captured with the following simple law:

$$V_L \approx A_L \sqrt{gD} (\sin \theta - \sin \theta_1) \quad \text{for } \theta < \theta_c \quad (3.2)$$

with $A_L = 110 \pm 10$ and $\theta_1 \approx 15.5^{\circ}$. This expression is valid for slope smaller than a critical value θ_c discussed later on. For greater H ($H > 10D$) the mean flow velocity clearly decreases with increasing H and we did find simple laws to describe the observed trends.

At large inclination angles, the trend is reversed: at moderate mass hold-up, the mean flow increases with increasing H while at greater H , the mean velocity stays invariant with changes of H . The change of behaviors between shallow and steep slope at moderate H seems to correspond to the appearance of the supported flow regime. The latter emerges for angles greater than a critical angle $\theta_c \approx 26.5^{\circ}$. The trends of the mean flow velocity for angles greater than θ_c can be approximated by two distinct scaling laws for small and large H :

$$V_L - V_L(\theta_c) \approx B_L \sqrt{gD} \left(\frac{H}{H_c} \right)^{\alpha_L} (\sin \theta - \sin \theta_c) \quad \text{for } \theta > \theta_c \quad (3.3)$$

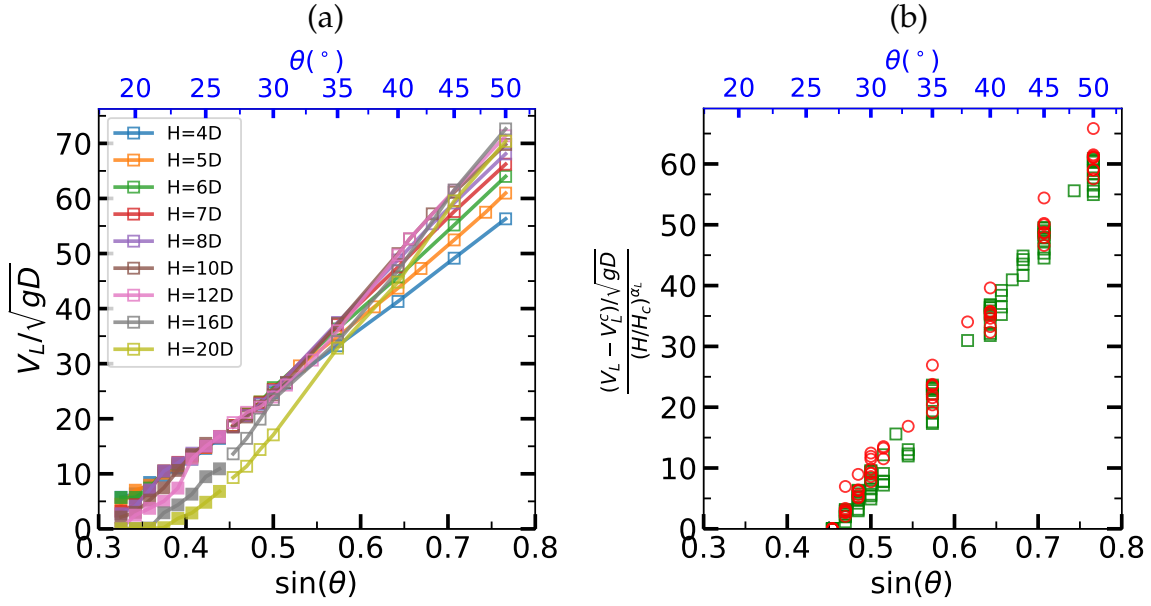


Figure 3.6: (a) Mean flow velocity V_L as a function of the inclination angle θ for various mass holdups H ($W = 40D$). (b) Rescaled flow velocity $(V_L - V_L^c)/(H/H_c)^{\alpha_L}$ as a function of the inclination angle for steep slope (i.e., $\theta > \theta_c \approx 26.5^\circ$). $\alpha_L = 0.3 \pm 0.05$ for $H < H_c$ (green squares) and $\alpha_L = 0$ for $H \geq H_c$ (red circles).

with $B_L = 170 \pm 10$ and $H_c = 14D$. The scaling exponent α_L is found to be equal to $\alpha_L = 0.3 \pm 0.05$ for $H < H_c$ and $\alpha_L \approx 0$ for $H > H_c$. The mean velocity of the supported flows with moderate particle hold-up (i.e., $\theta > \theta_c$ and $H < H_c$) scales as H^{α_L} . The scaling exponent is close to that found for $W = 68D$. Above H_c , the scaling exponent falls to zero. The reason for this change of scaling was not clearly identified.

2.5.2 Packing fraction, velocity and temperature profiles

Fig. 3.7 present the vertical profiles of the packing fraction $\phi(z)$, the longitudinal velocity $V_x(z)$ and the granular temperature $T(z)$ for various SFD regimes.

Fig. 3.7 a, c and d display vertical profiles for increasing inclination angle at a particle hold-up $H = 5$. Upon increasing inclination, we visit successively the unidirectional dense flow regime ($\theta = 20^\circ$), the roll regime ($\theta = 23^\circ$) and the supported regime with a dense supported core ($\theta = 30^\circ$ and 40°). While the unidirectional and roll regime exhibits a Bagnoldian velocity profile, the supported regimes are characterized by a plug flow. In the latter regime, the dense core moves with a quasi-uniform longitudinal velocity above a dilute layer which is strongly sheared. It is also important to note that the slip velocity at the base increases with increasing inclination angle. Temperature profiles indicate that the temperature is always maximum close to the base. For moderate inclination angle (i.e. in the unidirectional dense regime and the roll regime) the temperature decreases monotonically when approaching the free surface. In contrast, at higher inclination angle (i.e., in the supported flow regime), the temperature profile is no longer monotonous: the dense core appears to be colder than the free surface. Increasing the particle hold-up at a fixed inclination angle leads in general to a decrease of the granular temperature.

Fig. 3.7 b, d and e display vertical profiles for much thicker flows with $H = 20$ which includes the new flow regime. At $\theta = 22^\circ$, we get a SSH flow with a static region which spans nearly over the whole flow depth. Only the superficial layers of the system are flowing. At a slightly higher angles (i.e., $\theta = 25^\circ$), we obtain a dense flow which is sheared over the whole

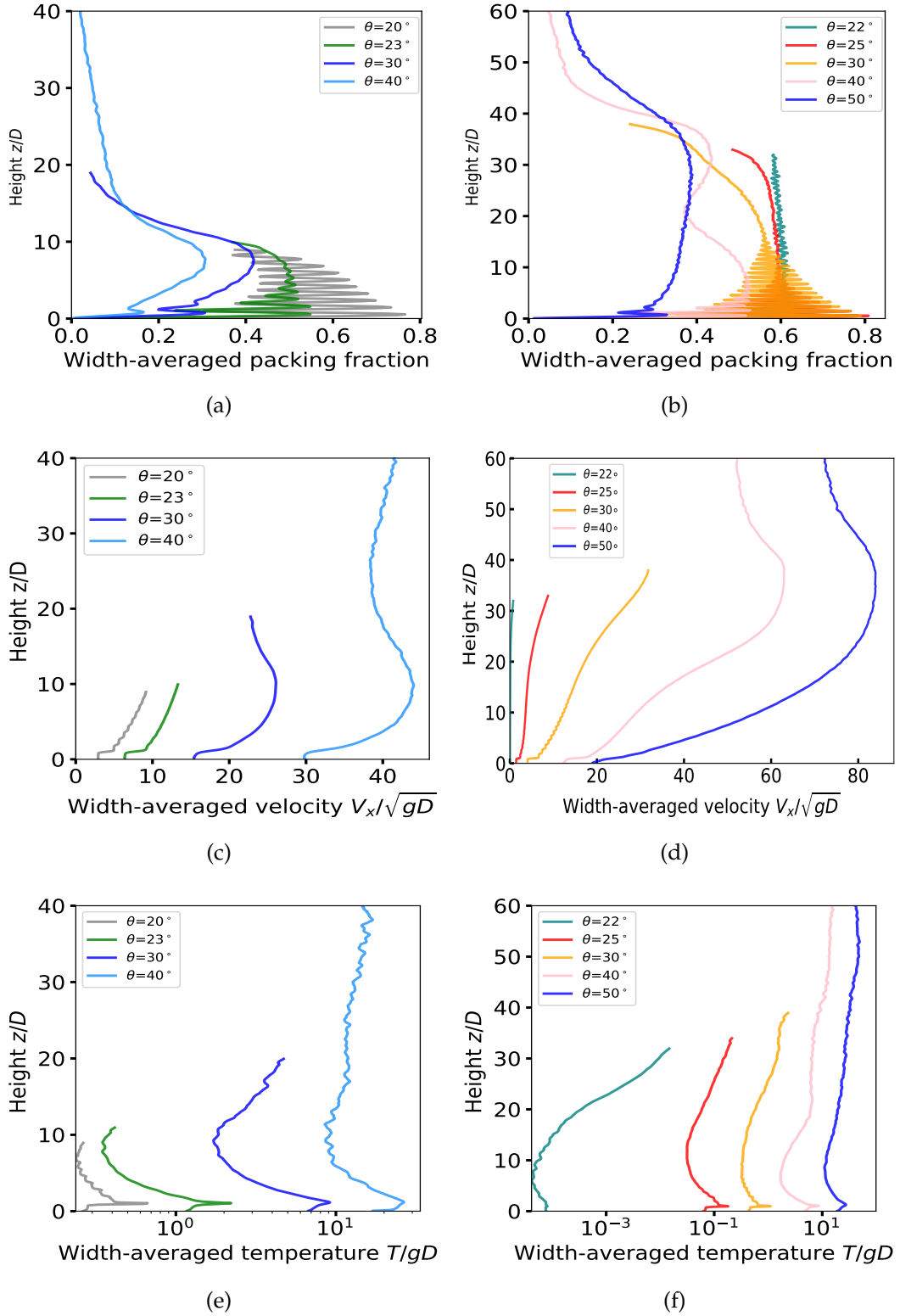


Figure 3.7: Vertical profiles of the packing fraction, the longitudinal flow velocity V_x , and the granular temperature. Quantities were averaged across the cell width (i.e., y direction). (a,c,d) Profiles for $H = 5D$ obtained for various inclinations $\theta = 20^\circ, 23^\circ, 30^\circ$ and 40° : These profiles include an unidirectional dense flow ($\theta = 20^\circ$), a flow with a pair of roll ($\theta = 23^\circ$), a supported flow with a symmetric core ($\theta = 30^\circ$) and an asymmetric core ($\theta = 40^\circ$). (b,d,e) Profiles for $H = 20D$ obtained for various inclinations $\theta = 22^\circ, 25^\circ, 30^\circ, 40^\circ$ and 50° : These profiles represent a SSH flow ($\theta = 22^\circ$), a R^+ flow ($\theta = 25^\circ$), a R^+SR^- flow ($\theta = 30^\circ$), and a flow with a double layer of vortices CR_+^- ($\theta = 40^\circ$) and a supported flow regime with symmetric core ($\theta = 50^\circ$).

depth and exhibits a pair of longitudinal vortices R^+ having a rotation direction opposite to that observed for supported flows. The packing fraction is almost invariant through the depth. Upon a further increase of the inclination angle (i.e., $\theta = 30^\circ$), the flow develops two superposed rows of longitudinal vortices (a R^+ pair of rolls at the base and a R^- pair of rolls at the free surface). The bottom rolls are dense while the upper rolls are slightly more dilute. The flow is the prelude to a new supported regime. Indeed, at a much higher angle (i.e., $\theta = 40^\circ$), the flow splits into two dense cores separated by a dilute region. This is clearly visible on the packing fraction profile. The upper core presents the same features as a supported flow: it is floating over the bottom core and is flowing much faster than the latter. This flow regime still includes superposed vortices: the bottom and upper cores are respectively the location of a R^+ and R^- pair of rolls.

Fig. 3.8 a, c, and d show the cross-wise profiles of the particle velocity, volume fraction and temperature for $H = 5D$ and various inclination angles. Cross-wise profiles of the longitudinal velocity reveal that the sliding velocity at the side-walls is significant and of the same order than the sliding velocity at the bottom. Additionally, we can note that at low angle and moderate inclination (i.e., in the unidirectional dense regime and in the roll regime), the flow is sheared almost uniformly through the whole width. In contrast, at large inclination (i.e., in the supported flow regime) the cross-wise strain rate is much stronger and is essentially localized in the dilute layer close to the vertical walls. Cross-wise profiles of the packing fraction and granular temperature reveal similar features.

2.5.3 Velocity and temperature at the bottom and side walls

Like the mean flow velocity, the velocities at the bottom and side walls exhibit remarkable behaviors when varying the particle hold-up and inclination. For small angles and moderate particle hold-up (i.e., $H < 10D$), both bottom and side walls velocities do not show any dependence with the particle hold-up. They thus behave as V_L and depend only on the inclination angle (see Fig. 3.9). We find that they are similar in magnitude:

$$\frac{V_b}{\sqrt{gD}} \approx \frac{V_w}{\sqrt{gD}} \approx 0.75 \frac{V_L}{\sqrt{gD}} \approx 0.75 A_L (\sin \theta - \sin \theta_1) \quad \text{for } \theta < \theta_c \text{ and } H < 10D \quad (3.4)$$

with $A_L \approx 80$ and $\theta_1 \approx 15.5^\circ$.

	$H < H_c$	$H \geq H_c$
α_L	0.3 ± 0.05	0
α_b	0	-1.5 ± 0.1
α_w	0	0

Table 3.1: Values of the scaling exponents α_L , α_b and α_w for $H < H_c$ and $H \geq H_c$ in the large inclination regime (i.e., for $\theta \geq \theta_c$). $V_L - V_L^c \propto (H/H_c)^{\alpha_L} (\sin \theta - \sin \theta_c)$, $V_b - V_b^c \propto (H/H_c)^{\alpha_b} (\sin \theta - \sin \theta_c)$, and $V_w - V_w^c \propto (H/H_c)^{\alpha_w} (\sin \theta - \sin \theta_c)$

For steeper angles (i.e., $\theta > \theta_c$), the bottom and side walls velocities are still invariant with H as soon as $H < H_c$. This behavior thus differs from V_L which increases with increasing H . They display an affine behavior with $\sin \theta$ as for shallow angle but with a greater slope:

$$V_{b,w}L - V_{b,w}(\theta_c) \approx 100\sqrt{gD} (\sin \theta - \sin \theta_c) \quad \text{for } \theta > \theta_c \text{ and } H < H_c \quad (3.5)$$

For $H > H_c$, the bottom velocity decreases with increasing H while the side wall velocity still remains invariant with H . The decrease of V_b with H can be described by a simple

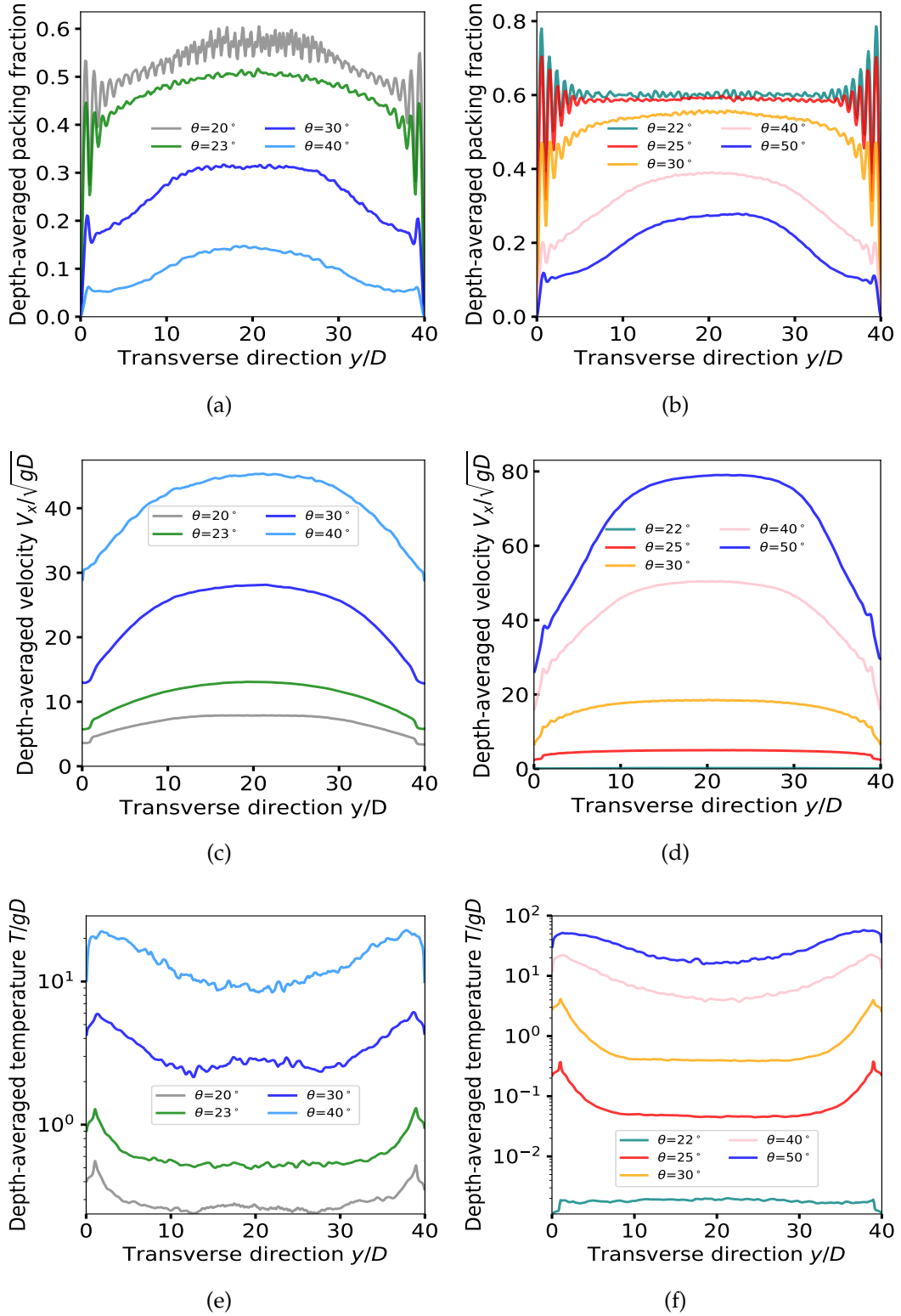


Figure 3.8: Transverse profiles of the packing fraction(a,b), longitudinal velocity(c,d) and temperature (e,f). Quantities were averaged through the depth of the flow from $z = 0$ to $z = h$ (where h corresponds to the height below which 97% of the mass stands). (a,c,e) Profiles for $H = 5D$ obtained for angles $\theta = 20, 23, 30$ and 40° . (b,d,f) Profiles for $H = 20D$ obtained for angles $\theta = 22, 25, 30, 40$, and 50° .

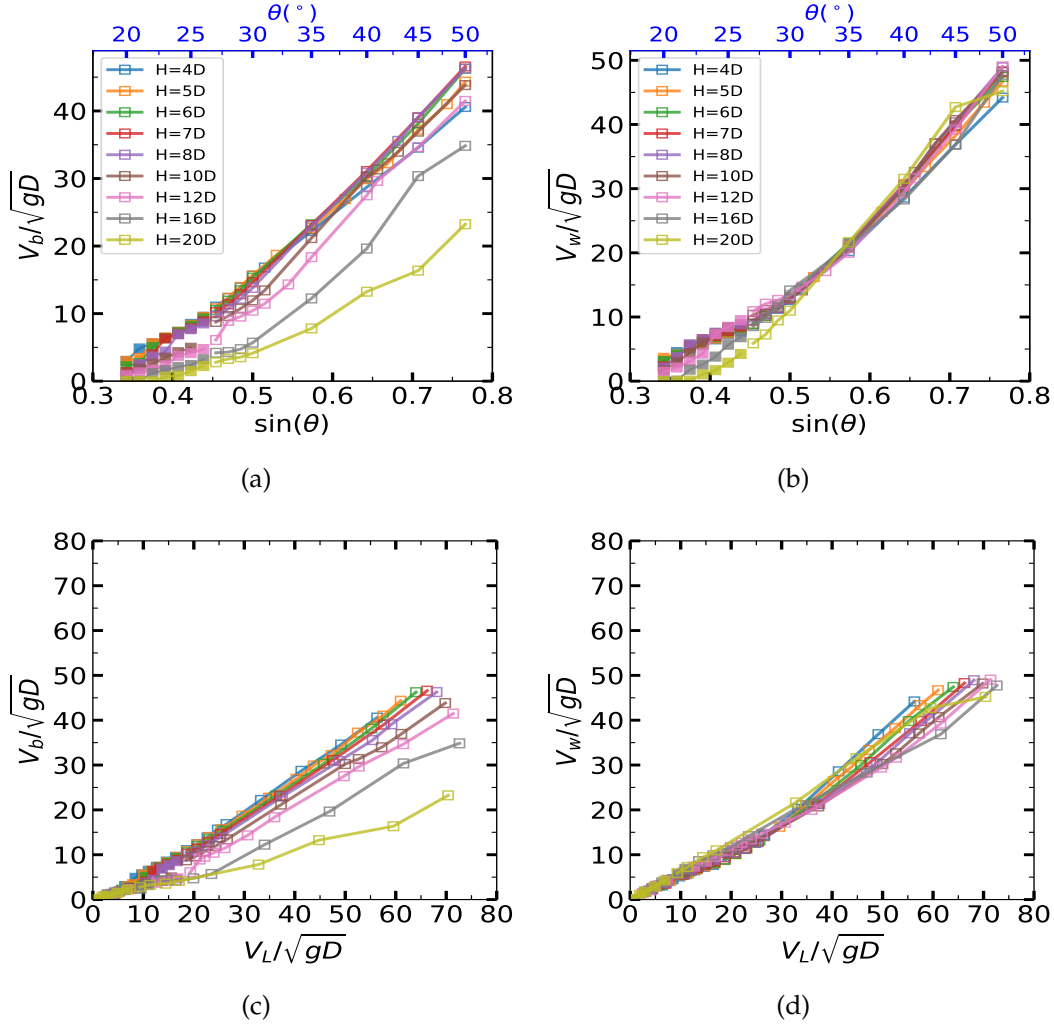


Figure 3.9: V_b (a) and V_w (b) as a function of $\sin \theta$ for various mass holdups H . V_b (c) and V_w (d) as a function of V_L for the same mass holdups H .

scaling law (see Fig. 3.10):

$$V_b - V_b(\theta_c) \approx 100\sqrt{gD} \left(\frac{H}{H_c} \right)^{\alpha_b} (\sin \theta - \sin \theta_c) \quad \text{for } \theta > \theta_c \text{ and } H > H_c \quad (3.6)$$

with $\alpha_b = -1.5 \pm 0.1$.

Let us summarize our findings concerning the bottom and side-wall velocities. We find two distinct regimes for small and large inclinations. The critical angle $\theta_c \approx 26.5^\circ$ delimits these two regimes. The large angle regime coincide with the emergence of the supported flow regime. In the small angle regime, the mean, bottom and side-wall velocities are almost invariant with H as soon as H remains moderate ($H < 10D$). In contrast in the large angle regime, the mean flow velocity increase with increasing hold-up for $H < H_c$ (as a power law with an exponent $\alpha_L = 0.3 \pm 0.05$). while the bottom and side-wall velocities still remains invariant with H . For greater hold-ups (i.e., $H > H_c$), the mean velocity become invariant with increasing H as the side-wall velocity but the bottom velocity exhibits a decrease with H with a power exponent $\alpha_b = -1.5 \pm 0.1$.

At the transition between small and large angle regimes (i.e., for $\theta = \theta_c$), we have introduced critical values V_L^c , V_b^c and V_w^c for the mean, bottom and side-wall velocities, respec-

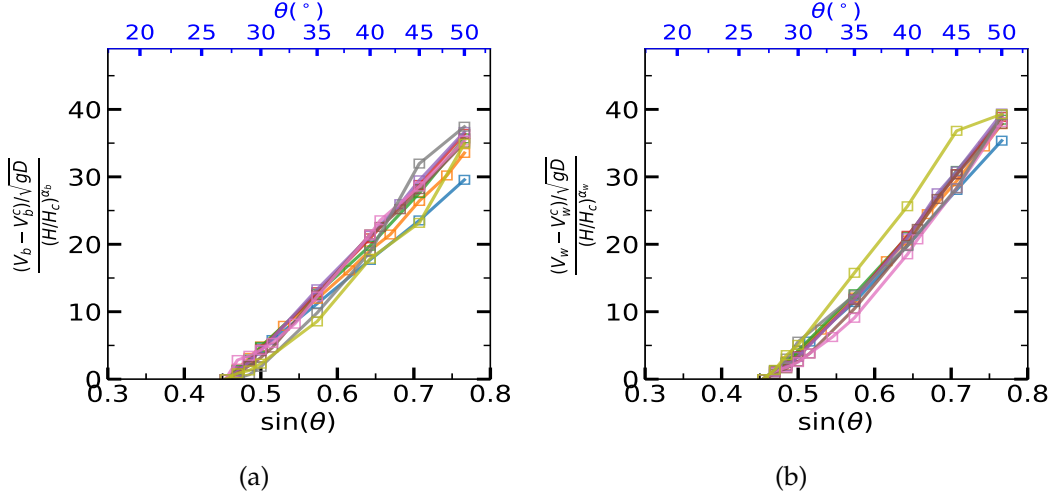


Figure 3.10: Renormalized bottom (a) and side-wall (b) velocities as a function of $\sin \theta$ for steep angles (i.e., $\theta > \theta_c$) and various mass holdups H ranging from $4D$ to $20D$. (a) Rescaled bottom velocity $(V_b - V_b^c)/(H/H_c)^{\alpha_b}$ versus $\sin \theta$; (b) Rescaled side-wall velocity $(V_w - V_w^c)/(H/H_c)^{\alpha_w}$ versus $\sin \theta$. The values of the scaling exponents α_b and α_w are summarized in Table 3.1.

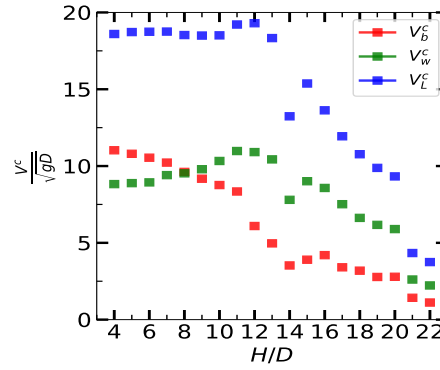


Figure 3.11: Critical velocity V^c for the mean, bottom and side-wall velocities as a function of the mass hold-up H : $V_{L,b,w}^c = V_{L,b,w}(\theta = \theta_c)$ where θ_c is the critical angle that delimits the small and large angle regime. $\theta_c \approx 26.5^\circ$

tively. The latter are almost invariant with H for moderate H (i.e., $H < 10D$) but decreases with increasing H for large H (see Fig. 3.11).

We present in Fig. 3.12.a the variation of the bottom and side-walls temperature as a function of the bottom and side-wall velocities. We observe a nice linear correlation between the square root of the temperature and the velocity at the walls. This correlation also holds at the local scale, i.e., when we compute the temperature and the velocity at the grain scale (see Fig. 3.12.b).

We can note however that the correlation between temperature and wall velocity becomes poorer at large temperature. This would require further studies to understand the dispersion at large temperature.

2.5.4 Characterization of the flow regime transition

We describe the transition between the different flow regimes. Zhu et al. (2020) proposed criteria to identify and characterize the different flow transitions. Some of them are not easy to calculate, which limits the application to experiments. We thus propose some additional

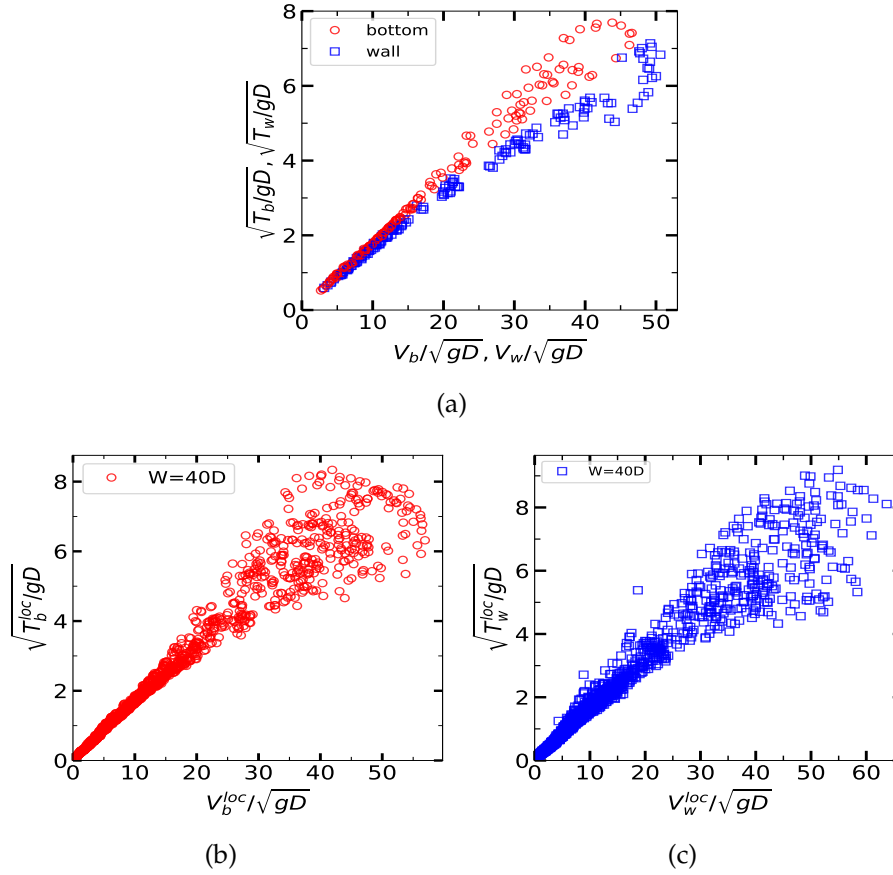


Figure 3.12: (a) Square root of the bottom and side-wall granular temperature ($\sqrt{T_b}$ and $\sqrt{T_w}$) as a function of bottom and side-wall velocity, respectively V_b and V_L , for mass holdups H ranging from $4D$ to $22D$ and inclination angles between $\theta = 19^\circ$ and 50° . (b) and (c) Similar data but computed at the grain scale.

criteria which could be used in experiments. We also provided criteria to identify the new regimes that were not observed for $W = 68D$.

Transition to the supported flow regime: In their article, [Zhu et al. \(2020\)](#) showed that the evolution of the maximum packing fraction ϕ_{max} as a function of the inclination provides a clear indicator of the transition between the roll regime and the supported flows. Here for $W = 40D$, this criterion is also relevant to identify the transition towards supported flows (see Fig. 3.13.a).

The packing fraction is however not easy to get in experiments. We find that another criterion could be used to describe the transition towards the supported flow regime. We noted that in the supported regime there is a significant gaseous atmosphere above the dense core. In this atmosphere, the packing fraction decreases exponentially with the height z as $\phi(z) = \phi(z_{gas}) \exp^{-(z-z_{gas})/L_{gas}}$, where z_{gas} is the height at which starts the atmosphere and L_{gas} is the characteristic layer height of the latter. We present in Fig. 3.13.b the characteristic layer height L_{gas} of the atmosphere. The data indicate that the atmosphere layer height increases significantly with increasing angle for inclination greater than θ_c corresponding to the emergence of supported flows. In contrast, below θ_c , the increase is extremely moderate. The assessment of the height of the upper atmosphere could be thus used successfully to characterize the transition to supported flows.

The depth-averaged longitudinal velocity can be also used to identify the transition to the supported regime. The difference between the maximum of the width-averaged longi-

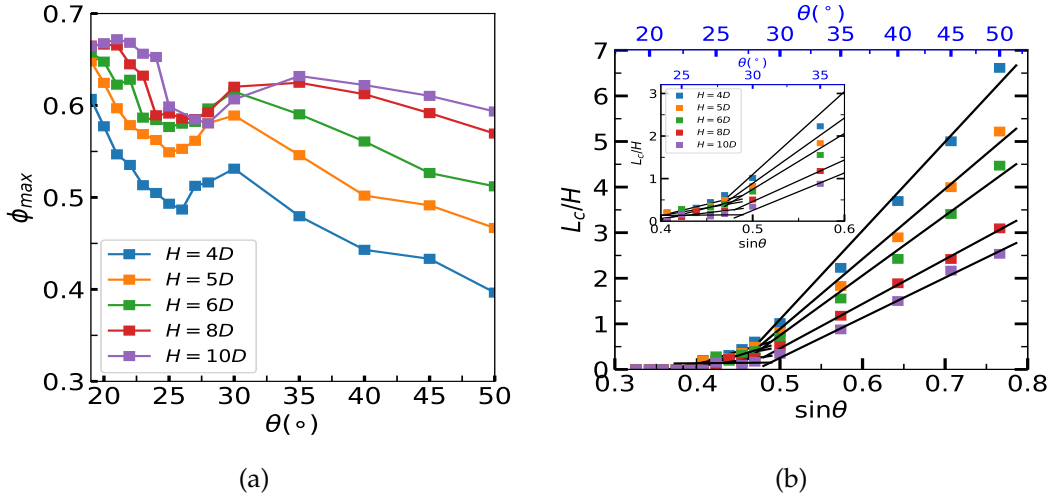


Figure 3.13: (a) Maximum packing fraction ϕ_{max} within the flow as a function of inclination for mass holdup H ranging from $4D$ to $10D$. (b) The characteristic layer height L_{gas} of the upper gaseous of the flow as a function the inclination angle for various particle hold-ups.

tudinal velocity (i.e., $\langle V_x \rangle_z^{max}$) and that at the lateral walls (i.e., V_w) undergoes a drastic change at the transition (see Fig. 3.14). The amplitude of the depth-averaged longitudinal velocity increases with increasing inclination in the small angle regime while in the large angle regime, the latter reaches a plateau or even decreases. The change of behavior of the amplitude of the depth-averaged longitudinal velocity with the slope angle thus provide a useful indicator for the transition to the supported regime.

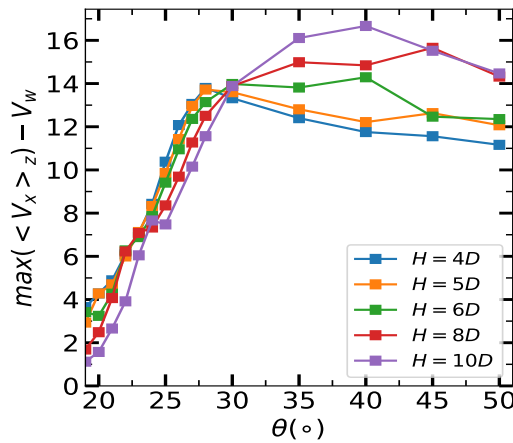


Figure 3.14: Amplitude of the depth-averaged longitudinal velocity as a function the inclination angle for various particle hold-ups.

Roll regime: In our article (Zhu et al., 2020), we showed that the vorticity is the appropriate parameter to delineate the transition from the dense flow regime towards the roll regime. Again this criterion is easily calculated in DEM simulations but hardly accessible to experimental measurements. An alternative way is to take advantage of the vertical profiles of the vertical velocity V_z in the vicinity of the lateral walls. For $H = 5D$ (see Fig. 3.15.a), these profiles indicate clearly the threshold for the appearance of the roll regime. For $\theta = 20^\circ$, the profiles is flat and reduced to zero, indicating that there is no upward nor downward motion at the wall, while for slightly greater angle (i.e. $\theta = 23^\circ$, the profile indicate an upward mo-

tion close to the lateral walls, thus revealing the existence of R^- longitudinal vortices. Upon further increase of the angle, the upward motion at the wall is enhanced. For $H = 20D$, these profiles provide also a clear picture of the presence of the longitudinal vortices (see Fig. 3.15.b). For $\theta = 22^\circ$, no vortices are present while at larger angles (i.e., $\theta = 25$ and 27°), we observe R^+ longitudinal vortices producing a downward motion at the wall. At even large angles (i.e., $\theta = 30^\circ$), the profile of the vertical velocity exhibits two extrema with negative and positive velocity which reveals the presence of two rows of longitudinal vortices with R^+ vortices at the bottom and R^- vortices at the top of the flow: this is the R^+_- flow regime.

As a matter of fact, the vertical profiles of the vertical velocity is useful to reveal the presence of longitudinal vortices. We can use the extrema of the vertical velocity as a good indicator to identify the transition towards the R^- , R^+ and R^+_- regimes. We recall that an

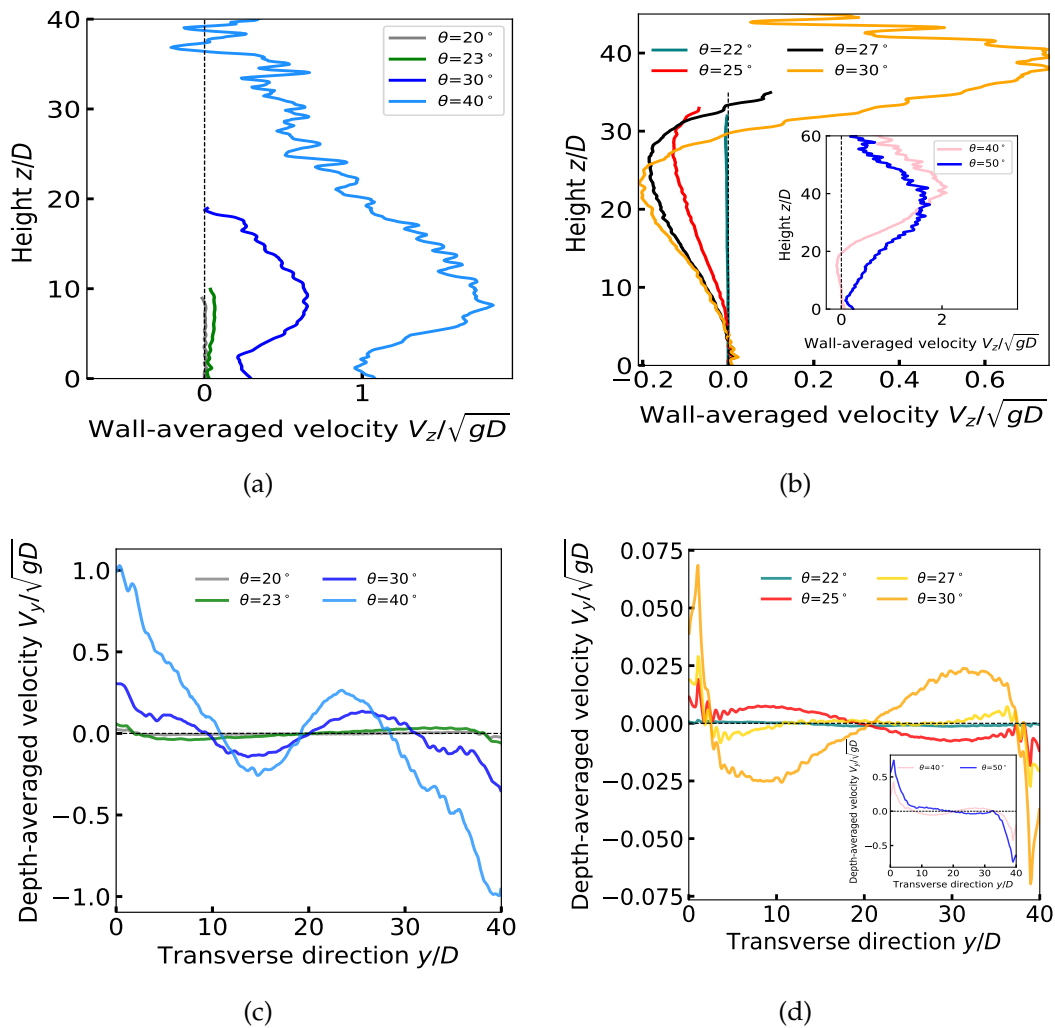


Figure 3.15: Vertical profiles of the vertical velocity V_z computed in the vicinity of the lateral walls (i.e., $0 < y < 5D$ and $35D < y < 40D$) for (a) $H = 5D$ and (b) $H = 20D$, respectively, and various inclinations. Transverse profiles of the depth-averaged transverse velocity V_y for (c) $H = 5D$ and (d) $H = 20D$, respectively, and various inclinations.

extremum with a positive vertical velocity corresponds to a R^- pair of vortices (inducing an upward motion of the particles at the lateral wall) while a negative value stands for a R^+ pair of rolls (inducing a downward motion of the particles at the wall).

We thus have at our disposal two different criteria, one based on the vorticity and used in Zhu et al. (2020) and the other on the extrema of the vertical profiles of the vertical velocity at the walls. Both criteria are compared in Fig. 3.16. The criterion based on the vorticity is the most accurate. It indicates that for small particle hold-ups, vortices appear above a critical angle of about 20° and the critical angle increases slightly with increasing H . At large particle hold-ups (e.g., $H = 20D$) and small inclination angle, the maximum of the vorticity changes sign indicating the presence of R^+ roll. Above a critical angle ($\theta = 27.5^\circ$ for $H = 20D$), the curve splits into two branches revealing the appearance of a second row of vortices with opposite rotation direction. The alternative criterion based on the vertical velocity of the later walls provides similar trends.

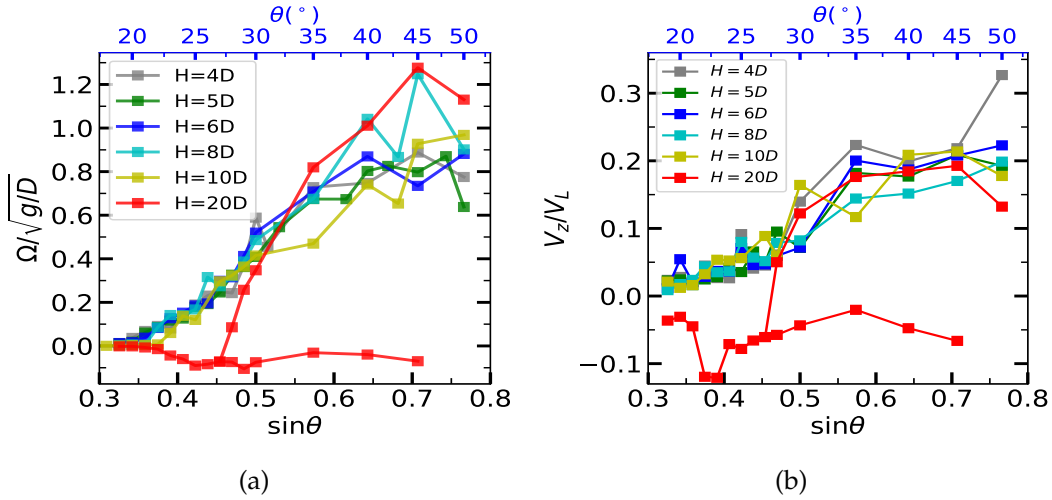


Figure 3.16: Extrema of the vorticity (a) and extrema of the vertical velocity at the wall (b) as a function of the inclination angle for various mass hold-ups.

2.5.5 Effective friction and packing fraction at the boundaries

We now investigate how the effective friction at the boundaries (i.e., bottom and side walls, respectively) varies with the particle hold-up and inclination angle. We recall that the global effective friction μ_b and μ_w , respectively at the base and at the side-walls: $\mu_b = F_T^b / F_N^b$ and $\mu_w = F_T^w / F_N^w$, where F_T is the tangential force exerted by the wall on the flow and F_N is the force normal to the wall.

We also define an effective friction at the local scale, $\mu_b^{loc}(y)$ and $\mu_w^{loc}(z)$. To evaluate these local quantities, we decompose the walls into strips parallel to the flow with a width of a few grain diameters (typically between $2D$ and $10D$ according to the local packing fraction) for which we compute the local tangential and normal forces.

We proceed in the same way to compute local quantities at the walls like the velocity (V_b^{loc} and V_w^{loc}), the pressure (P_b^{loc} and P_w^{loc}), the packing fraction (ϕ_b^{loc} and ϕ_w^{loc}), and the temperature (T_b^{loc} and T_w^{loc}).

In a preceding paper (Zhu et al., 2020), we showed that the global effective friction μ_b and μ_w depend on a unique variable which is a Froude-like number built from the velocity and the pressure at the wall as $Fr_{b,w} = V_{b,w} / \sqrt{P_{b,w} / \rho}$ with $P_b \approx P_w \approx \rho g H \cos \theta$. These laws $\mu_b(Fr_b)$ and $\mu_w(Fr_w)$ were established for confined flows with a gap widths $W = 68D$. We confirm here that for a narrower channel width $W = 40D$ these global laws still hold (see Fig. 3.17.a). We can note that both curves $\mu_b(Fr_b)$ and $\mu_w(Fr_w)$ overlap which is not really

surprising since the bottom and the side-walls have the same mechanical properties. This thus indicates that these laws encode the mechanical interactions between the wall and the particles. We expect that a change of the mechanical properties of the walls or the particles should not alter the general shape of the curve but only in a quantitative way.

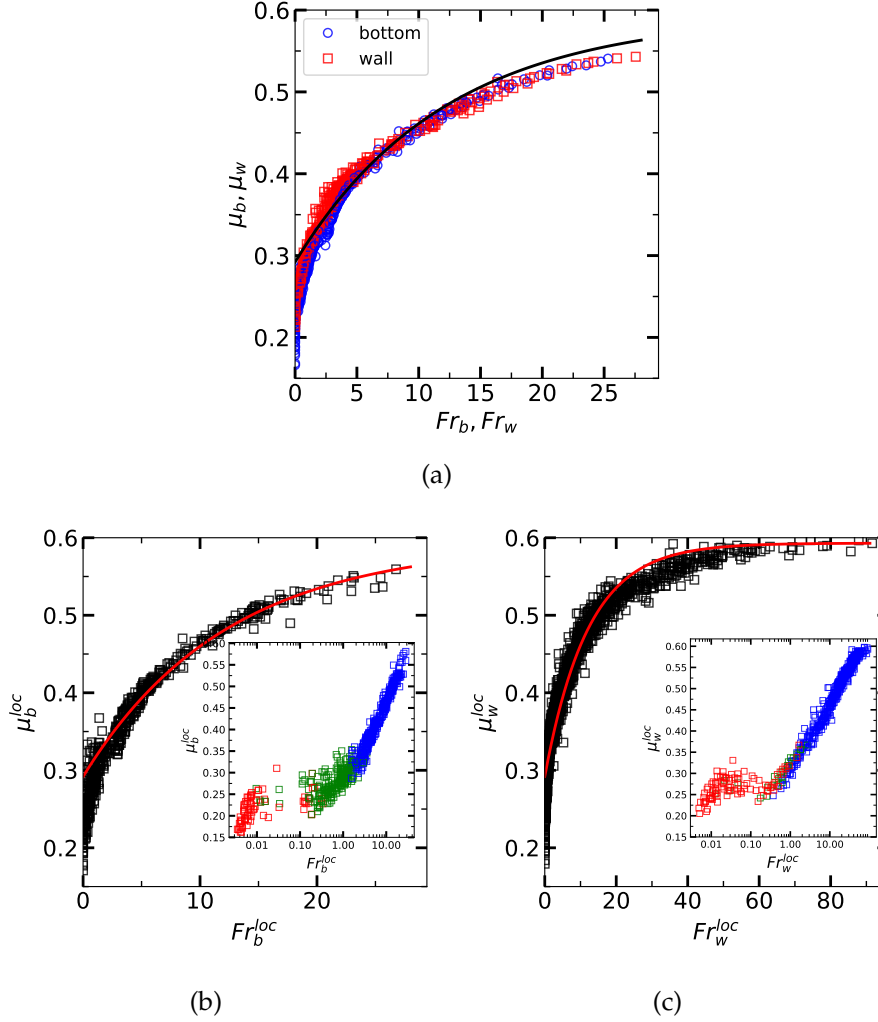


Figure 3.17: (a) Global basal and lateral friction coefficient (μ_b and μ_w) as the function of the global Froude number (Fr_b and Fr_w). $Fr_{b,w} = V_{b,w}/\sqrt{H \cos \theta}$. (b) and (c): Local basal and lateral friction coefficient as the function of the local Froude number. (b) μ_b^{loc} versus $Fr_b^{loc} = V_b^{loc}/\sqrt{P_b^{loc}/\rho}$; (c) μ_w^{loc} versus $Fr_w^{loc} = V_w^{loc}/\sqrt{P_w^{loc}/\rho}$. Insets: Same data in a semi-log plot, red and green symbols correspond to SHH and intermittent regime, respectively. The solid line corresponds to the best fit to the data in (b) using the following exponential form: $\mu_b^{loc} \approx \mu_2 + (\mu_1 - \mu_2)(\exp(-Fr/ Fr_{\mu_0}))$ with $\mu_1 = 0.29$, $\mu_2 = 0.59$, and $Fr_{\mu_0} = 12.2$. This fit is reported in (a) and (c) and captures reasonably well the other data.

In (Zhu et al., 2020), we also showed the above laws established at the system scale holds actually at the local scale. This is also the case here for flows with $W = 40D$ (see Fig. 3.17.b and c). This thus supports the idea that these laws encode particle-wall interactions at the particle scale.

Interestingly, we present in the inset of Fig. 3.17 the effective friction as a function of the logarithm of the Froude number. This representation allows to see what happens at low Froude number (i.e., below 1). These low Froude numbers correspond to the SHH and intermittent regime (red and green symbols in the figure). In the range of Froude number

between 0.01 and 0.1, we observe a plateau corresponding to a friction of 0.25. For very small number Froude number (below 0.01), the effective friction decreases again with decreasing Froude number. This branch correspond to SSH flows and should be taken with caution because the deep part of the flow which is quasi-static may not be in a fully stationary state.

In addition to the effective friction law, we uncover that the packing fraction also obeys a simple law which depends uniquely on the Froude number. The local packing fraction at the bottom and side-wall as a function of the local Froude number is shown in Fig. 3.18.a and b. All the data collapse on a single curve which decreases with increasing Froude number. This decreasing behavior can be reasonably well captured by a law of the following form:

$$\phi_{b,w}^{loc} = \phi_1 + (\phi_2 - \phi_1) \exp\left(-Fr_{b,w}^{loc}/Fr_{\phi_0}\right) \quad (3.7)$$

with $\phi_1 = 0.57$, $\phi_2 = 0.03$ and $Fr_{\phi_0} = 6.8$. The packing fraction at the bottom and the side-walls presents a similar behavior and can be described by the same law with similar fitting parameters.

In (Zhu et al., 2020), we showed the law for the effective friction at the walls are also valid for unsteady flows. It is thus natural to test whether the $\phi^{loc}(Fr^{loc})$ law holds also for unsteady flows. This is indeed the case as illustrated in Fig. 3.18.c. We calculated the local packing fraction at the walls during the transient accelerated regime before reaching the stationary state.

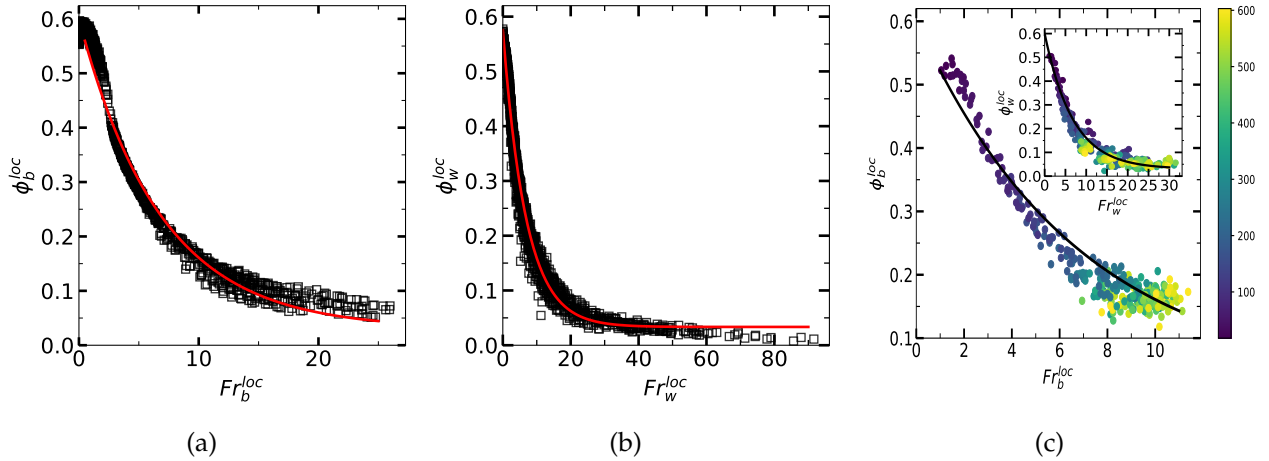


Figure 3.18: (a) The local basal packing fraction on bottom ϕ_b^{loc} as a function of the local basal Froude number $Fr_b^{loc} = V_b^{loc} / \sqrt{P_b^{loc} / \rho}$. (b) The local packing fraction at the side-walls ϕ_w^{loc} as a function of the local side-wall Froude number $Fr_w^{loc} = V_w^{loc} / \sqrt{P_w^{loc} / \rho}$. (c) ϕ_b^{loc} as a function of Fr_b^{loc} for a flow in the transition regime ($\theta = 40^\circ$ and $H = 12D$). Inset: ϕ_w^{loc} as a function of Fr_w^{loc} for the same flow. The solid line is the best fit to the data in (a) using Eq. 3.7. This fit is reported in (b) and (c) and captures well the other data.

Interestingly, the law for the packing fraction holds also at the global scale. If we compute the mean packing fraction at bottom ϕ_b as a function of the global basal Froude number $Fr_b = V_b / \sqrt{H \cos(\theta)}$ (where V_b is the mean velocity at the bottom), we find a nice collapse of the data (see Fig. 3.19). It is also interesting to note that the mean packing fraction of the flow $\bar{\phi}^*$ - defined as $\bar{\phi}^* = \int_0^{h^*} \int_0^W dz dy \phi(y, z)$ where h^* is the height below which one finds 97% of the flowing material - shows also a similar behavior as a function of the global basal Froude number. This relation may be useful for the development of a phenomenological model as discussed later on.

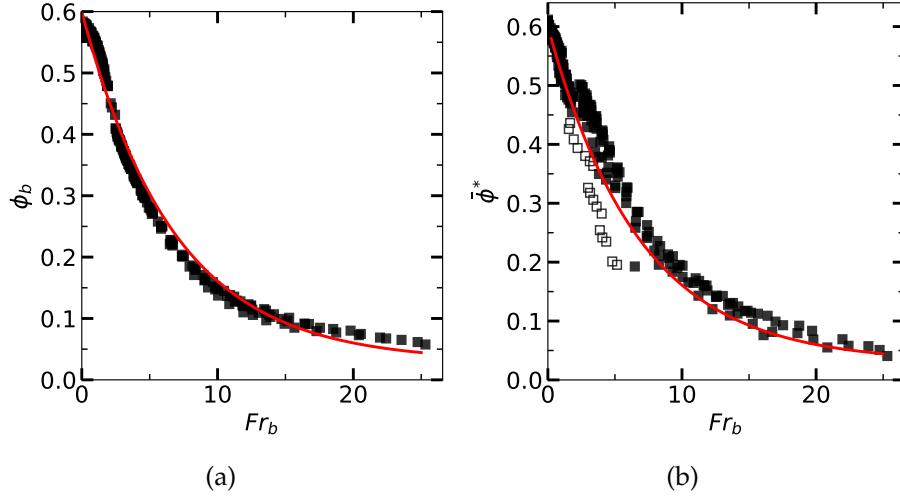


Figure 3.19: (a) Mean packing fraction at the bottom ϕ_b as a function of the global basal Froude number $Fr_b = V_b / \sqrt{H \cos(\theta)}$. (b) Mean mean packing fraction $\bar{\phi}^*$ as a function of the global basal Froude number Fr_b . The flows with two superposed rows of vortices (empty symbols) do not follow the main trends. The solid line represents the best fit obtained for the local law $\phi_b^{loc}(Fr_b^{loc})$ (see Eq. 3.7).

In summary, we showed that the effective friction at the boundaries as well as the packing fraction at the boundaries can be described with simple laws which depend only on the Froude number. These laws, $\mu_{b,w}(Fr_{b,w})$ and $\phi_{b,w}(Fr_{b,w})$, can be seen as the analogue of the laws $\mu(I)$ and $\phi(I)$ introduced in the theological model for dense granular flows. However, they do not have the same status. The laws we established should be taken as boundary conditions for flat boundaries but does not inform about the rheology of the flow.

2.5.6 Effective frictional flow height Z

A force balance applied to our system leads the following relationship:

$$\tan \theta = \mu_b(Fr_b) + \mu_w(Fr_w) \frac{Z}{W} \quad (3.8)$$

where

$$Z = \frac{2}{P_b} \int_0^h dz P(0, z) \quad (3.9)$$

h is defined at the critical altitude below which one finds 100% of the flowing material. To establish this relation, we employ the same assumption as done in [Taberlet et al. \(2003\)](#); [Richard et al. \(2008\)](#). In particular, the pressure $P(y, z)$ within the flow is assumed to be isotropic. The height Z can be seen as an effective frictional height. For dense flows, the frictional height can be identified to the thickness of the flowing layer. For our rapid flows with heterogeneous packing fraction, the relationship between Z and h is not straightforward.

The mass conservation provides us with a simple relationship between h and the mean packing fraction $\bar{\phi}$:

$$h = \frac{H}{\bar{\phi}} \quad (3.10)$$

with

$$\bar{\phi} = \frac{1}{Wh} \int_0^h \int_0^W dy dz \phi(y, z) \quad (3.11)$$

Guided by this relation, we investigate whether the rescaled friction height Z/H obeys also a simple law as a function of the mean packing fraction. When we plot Z/H as a function $\bar{\phi}$ for all SFD flows, we get a nice collapse of the data on a single curve (see Fig. 3.20) which can be approximated by the following functional form:

$$\frac{Z}{H} = \frac{1 + a_\phi(\bar{\phi} - \phi_1)}{\bar{\phi}} \quad (3.12)$$

with $\phi_1 \approx 0.57$ and $a_\phi \approx 1.6$. Note that the determination of the mean packing fraction is very sensitive to the definition of the flow height h . If we use the alternative flow height h^* (defined as the thickness below which 97% of the flowing material stands), the resulting mean packing fraction $\bar{\phi}^*$ is significantly different in particular for very dilute flows. As a consequence, the relationship between Z/H and $\bar{\phi}^*$ differs from that between Z/H and $\bar{\phi}$ (see Fig. 3.20). However the trend remains similar.

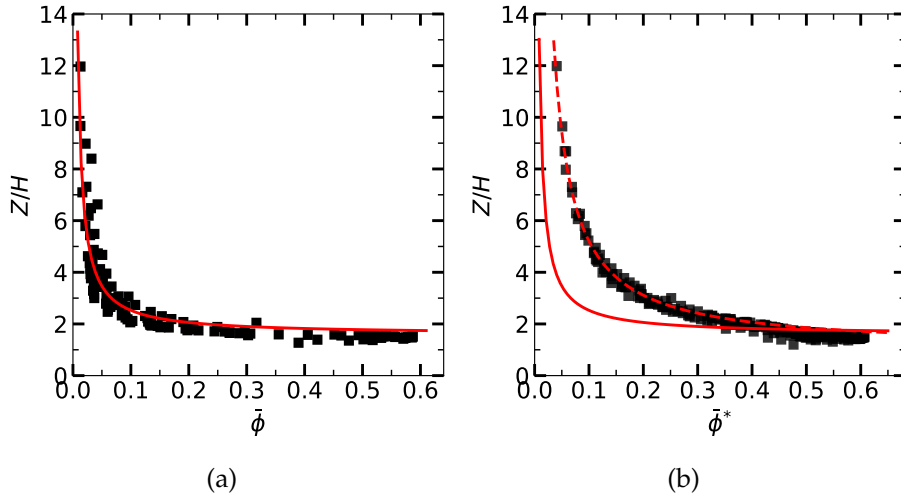


Figure 3.20: (a) Rescaled frictional height Z/H as a function of the mean packing fraction $\bar{\phi}$. (b) Rescaled frictional height Z/H as a function of the mean packing fraction $\bar{\phi}^*$ based on the flow height h^* which is defined as the height where one finds 97% of the flowing material. The solid and dash lines correspond to best fits using Eq. 3.12: $a_\phi \approx 1.6$ and $\phi_1 \approx 0.57$ (solid line), $a_\phi \approx 1.0$ and $\phi_1 \approx 0.57$ (dash line).

2.6 Role of the channel width W

2.6.1 On the critical inclination for the appearance of the supported flows

We investigate first the influence of the gap width W on the appearance of the supported regime. We saw that for $W = 40D$, the supported regime emerges above a critical angle $\theta_c \approx 26.5^\circ$ for $H = 4D$. The latter slightly increases with increasing particle hold-up H .

The numerical simulations show that this critical angle decreases with increasing gap width W (see Fig. 3.21). The data can be captured by the following functional form:

$$\theta_c = \theta_\infty + \frac{W_0}{W - W_c} \quad (3.13)$$

with $\theta_\infty = 22.8^\circ$, $W_0 = 80D$, and $W_c = 18D$. This law predicts that there is a minimum gap width $W_c \approx 18$ below which the supported regime can not occur. This prediction seems

to agree reasonably well with simulations achieved at $W = 20D$ which reveal an absence of supported flows. Interestingly, this law also suggests that supported flows should exist for infinite wide channels. The widest channel width used in the simulations is $W = 140D$ which still reveal the existence of supported flows.

Interestingly, the mean flow velocity V_L^c at the critical inclination as well as the basal and lateral velocities ($V_b(\theta_c)$ and $V_w(\theta_c)$) are independent of the channel width W (see Fig.3.21.b). This suggests that the appearance of the supported regime is governed by the mean flow velocity. Thus as larger channels provide faster flows, the appearance of the supported flow is favoured for wide channels.

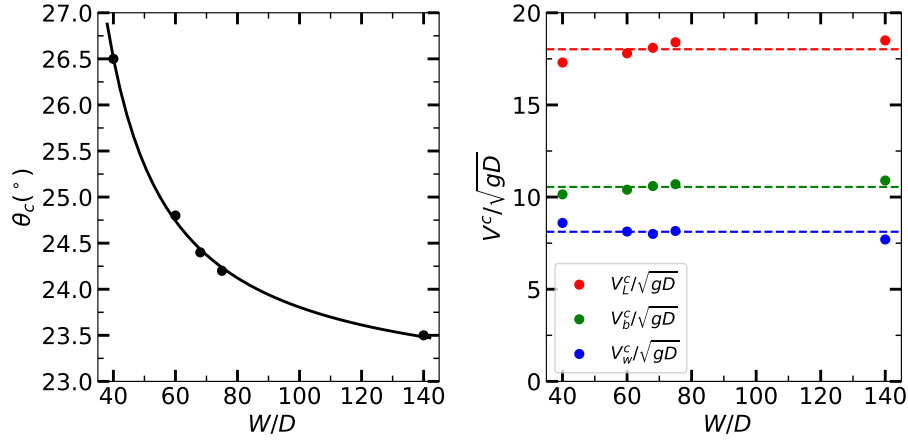


Figure 3.21: (a) Critical inclination θ_c for the appearance of the supported flow regime as a function of W for a fixed hold-up $H = 4D$. The solid line is a least-squares fit with the following functional form: $\theta_c = \theta_\infty + W_0/(W - W_c)$, where $\theta_\infty = 22.8^\circ$, $W_0 = 80D$, and $W_c = 18.3D$. (b) Corresponding mean flow velocity V_L^c as a function of the channel width W .

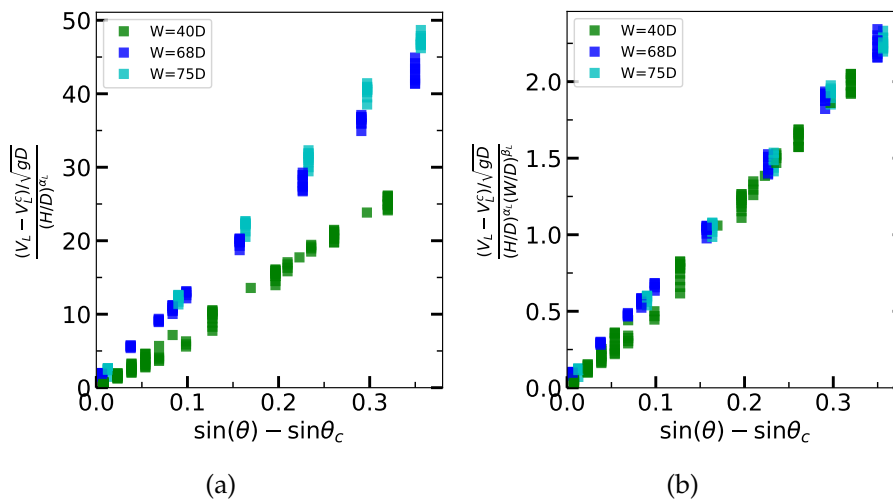


Figure 3.22: (a) Renormalized mean flow velocity $(V_L - V_L^c)/H^{\alpha_L}$ as a function of $\sin \theta - \sin \theta_c$ for supported flows (i.e., $\theta > \theta_c(W)$ and $H \leq H_c(W)$) obtained with channel widths $W = 40D$, $68D$, and $75D$. (b) Renormalized mean flow velocity $(V_L - V_L^c)/H^{\alpha_L} W^{\beta_L}$ as a function of $\sin \theta - \sin \theta_c$. $\alpha_L = 0.3 \pm 0.05$ and $\beta_L = 0.7 \pm 0.05$.

2.6.2 On the velocity scaling

Here, we are interested to determine how the scaling law established for the mean velocity is altered by changing the channel width. We focus here exclusively on the supported flow regime.

The outcomes of the simulations achieved for various channel widths (i.e., $W = 40D$, $68D$ and $75D$) reveal that the mean flow velocity V_L of the supported flows can be well approximated by the following law (see Fig. 3.22):

$$V_L - V_L(\theta_c) \approx 6.6\sqrt{gD} H^{\alpha_L} W^{\beta_L} (\sin\theta - \sin\theta_c) \quad \text{for } \theta > \theta_c(W) \text{ and } H < H_c(W) \quad (3.14)$$

with $\alpha_L = 0.3 \pm 0.05$ and $\beta_L = 0.7 \pm 0.05$. where θ_c is the critical angle for the appearance of the supported flows and H_c is the limit particle hold-up above which the supported regime disappears.

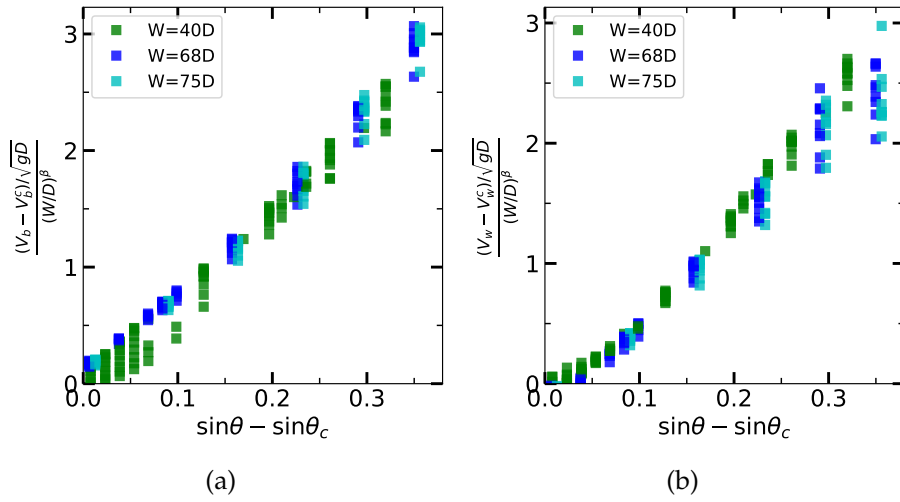


Figure 3.23: Renormalized basal velocity $(V_b - V_b^c)/W^{\beta_b}$ (a) and side-wall velocity $(V_w - V_w^c)/W^{\beta_w}$ (b) as a function of $\sin\theta - \sin\theta_c$, for supported flows (i.e., $\theta > \theta_c(W)$ and $H \leq H_c(W)$) obtained with channel widths $W = 40D$, $68D$, and $75D$. $\beta_b \approx \beta_w = 0.7 \pm 0.05$.

It is also important to note that θ_c depends on W as shown previously and that H_c is also expected to vary with W . For $W = 40D$, H_c is about $14D$. For $W = 68D$, we were not able to determine H_c but we know it is greater than $20D$.

It could be instructive to check whether the basal and lateral wall velocities (V_b and V_w) obeys a similar scaling law with W as for the mean flow velocity. Fig 3.23 shows that the basal and side-wall velocities ($V_b - V_b^c$ and $V_w - V_w^c$) scale reasonably as $W^{0.7}$ as for V_L . We can also note that the linearity with inclination θ still holds when changing W . We also confirm that in the supported flow regime, the basal and side-wall velocities do not show any significant dependence with the particle hold-up H .

2.6.3 On the friction and packing fraction law at the walls

Here we investigate the role of the gap width on the effective friction and packing fraction at the walls. For this, we ran simulation for various gaps widths from $20D$ to $75D$ with in-

clinations ranging from $\theta = 15$ to 50° and particle hold-ups from $4D$ to $22D$.

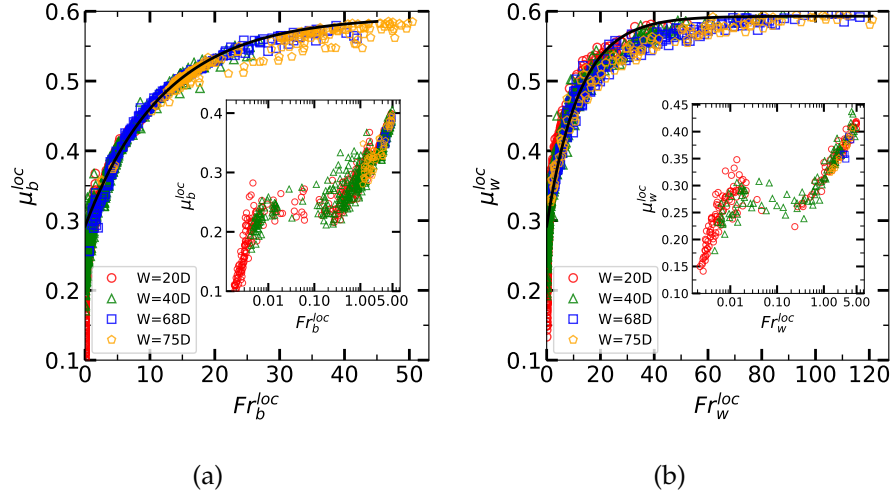


Figure 3.24: Local effective friction as a function of the local Froude number for various gap widths: (a) Bottom friction; (b) Side-wall friction. The solid line in (a) correspond to the best fit to the data using the exponential form: $\mu_b^{loc} = \mu_2 + (\mu_1 - \mu_2) \exp(-Fr/ Fr_{\mu_0})$. $\mu_1 = 0.29$, $\mu_2 = 0.59$, $Fr_{\mu_0} = 12.2$. This fit is reported in (b) and works well.

Fig 3.24 presents the local effective friction law both at the bottom and side-walls as a function of the local Froude number for various channel widths. All the data for different gap widths collapse on a single curve. This means that The local effective friction law do not depend on the gap width. This confirms that the local friction law $\mu_{b,w}^{loc}(Fr_{b,w}^{loc})$ encode the local interactions between the particle and the walls and these interactions are governed by the local Froude number. Importantly, the bottom and side-wall friction laws are similar qualitatively and quantitatively. The inset of Fig. 3.24 makes a focus on very small Froude numbers and indicates there exists a plateau for Froude ranging from 0.01 and 1. For even smaller Froude number, the data should be taken with caution since we are not ensured that the flows with vanishing Froude number are in a fully stationary state.

It is important to mention that the global friction laws $\mu_{b,w}(Fr_{b,w})$ remain as well unchanged by varying the gap width. Concerning the local packing fraction laws at the walls (i.e., $\phi_b^{loc}(Fr_b^{loc})$ and $\phi_w^{loc}(Fr_w^{loc})$), we also obtain an invariance when changing the gap widths as illustrated in Fig. 3.25. This reinforces the relevance of these local laws. In contrast, the corresponding global law for the mean packing fraction of the flow (i.e., $\bar{\phi}^*(Fr_b)$) is less robust to change in W as expected (see Fig. 3.25.d). In particular, the data corresponding to very confined flows (i.e., $W = 20D$) (red squares) deviate from the main trend. We observed as well as a deviation of the law at $W = 40D$ for the thick flows with two rows of vortices (empty green squares).

2.6.4 On the effective frictional flow height Z

We established previously that the rescaled effective frictional flow height Z/H defined by Eq. 3.9 obeys a simple law with the $\bar{\phi}^*$ the mean packing fraction of the flow. The law is found to be remarkably independent of the gap width. This is illustrated in Fig. 3.26. We will see

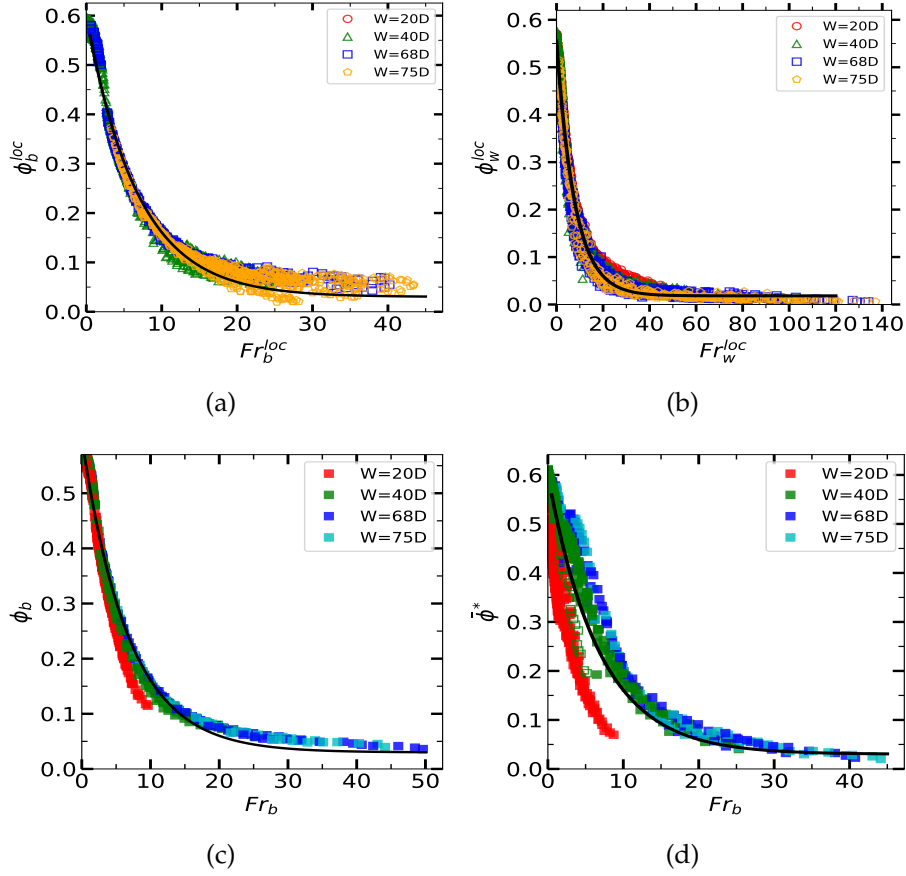


Figure 3.25: Local packing fraction at the base (a) and at the side-walls (b) as a function of the local Froude number for various gap widths. (c) Basal packing fraction ϕ_b as a function of the basal Froude number $Fr_b = V_b / \sqrt{gH \cos \theta}$ for various gap widths; (d) Mean packing fraction $\bar{\phi}^*$ as a function of the basal Froude number Fr_b for various gap widths. The solid line corresponds to the same fit as used in Fig. 3.18.

later on that this law will be useful to propose a phenomenological model that allows to determine the basal and side-walls velocities for a given particle hold-up H , inclination θ and gap width W .

2.7 Kinetic theory for granular gas and $\mu(I)$ rheology

In this section, we investigate which properties of the flow can be described either by the kinetic theory for granular gas or by the $\mu(I)$ rheology.

We recall first the salient features of the kinetic theory for granular gas. For frictionless spheres, Lun et al. (1984) derived constitutive relations. In a simple shearing flow, the granular pressure can be written as

$$P = \rho F_1(\phi) T \quad (3.15)$$

with

$$r = \frac{1 + e}{2} \quad (3.16)$$

$$g_0(\phi) = \frac{2 - \phi}{2(1 - \phi)^3} \quad (3.17)$$

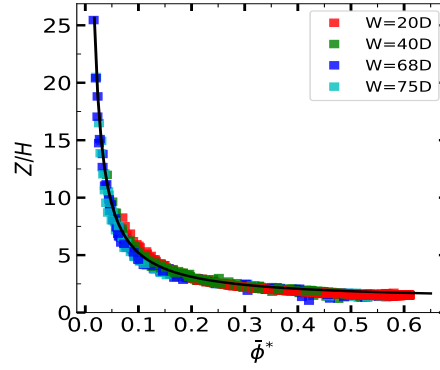


Figure 3.26: Rescaled effective frictional height Z/H as a function of the mean flow packing fraction $\bar{\phi}^*$ for different channel widths $W = 20D$, $W = 40D$, $W = 68D$ and $W = 75D$. The solid line is the best fit obtained for $W = 40D$ (see Eq. 3.12).

where ρ is the particle density and e is the normal restitution coefficient, while the shear stress S in the mean shear direction is expressed as

$$S = \rho D F_2(\phi) \sqrt{T} \dot{\gamma} \quad (3.18)$$

where D is the grain diameter and $\dot{\gamma}$ is the strain rate. F_1 and F_2 are functions of packing fraction and are given by

$$F_1(\phi) = \phi + 4r\phi^2 g_0(\phi) \quad (3.19)$$

$$F_2(\phi) = \frac{5\sqrt{\pi}}{96} \left[\frac{1}{r(2-r)g_0(\phi)} + \frac{83r-1}{5} \frac{r-1}{2-r} \phi + \frac{64}{25} r \left(\frac{3r-2}{2-r} + \frac{12}{\pi} \right) \phi^2 g_0(\phi) \right] \quad (3.20)$$

We first investigate whether the ratio of the pressure to temperature obeys a similar relationship to that given by the kinetic theory (cf. Eq. 3.15). To do this, we compute the local pressure and temperature close to the walls. However, to avoid the singularity introduced by the flat walls, we compute this ratio in the interior of the flow but still close to the wall, i.e., at a distance $d = 1.5D \pm 0.5D$. We recall in the previous section the quantities at the wall were calculated at a distance $d = 0.5D \pm 0.5D$. We will use here a notation with a dagger for the new calculation.

Fig. 3.27.(a,b) shows the evolution of $P_{b^\dagger}^{loc}/T_{b^\dagger}^{loc}$ and $P_{w^\dagger}^{loc}/T_{w^\dagger}^{loc}$ as a function of the local packing fraction at the bottom $\phi_{b^\dagger}^{loc}$ and at side-wall $\phi_{w^\dagger}^{loc}$, respectively. First, we note that there is a nice collapse of the data for various mass hold-up, inclination angle and gap width. This indicates that the ratio P/T depends solely on the packing fraction. The solid line is the prediction of the kinetic theory using Eq. 3.15 where the coefficient of restitution was set to the value used in the simulations (i.e., $e = 0.972$). The latter is in good agreement with the simulations up to a packing fraction of 0.5. Above this value, there is a significant deviation from the main trend. Interestingly, we checked that the ratio between the pressure and the temperature works also at the global scale (see Fig. 3.27.c).

The kinetic theory also tells us that the ratio of the shear to the pressure in the main flow direction obeys a simple relation:

$$\frac{S}{P} = D \frac{F_2(\phi) \dot{\gamma}}{\sqrt{T} F_1(\phi)} \quad (3.21)$$

yielding

$$\frac{S\sqrt{T}}{P\dot{\gamma}} = \frac{F_2(\phi)}{F_1(\phi)} \quad (3.22)$$

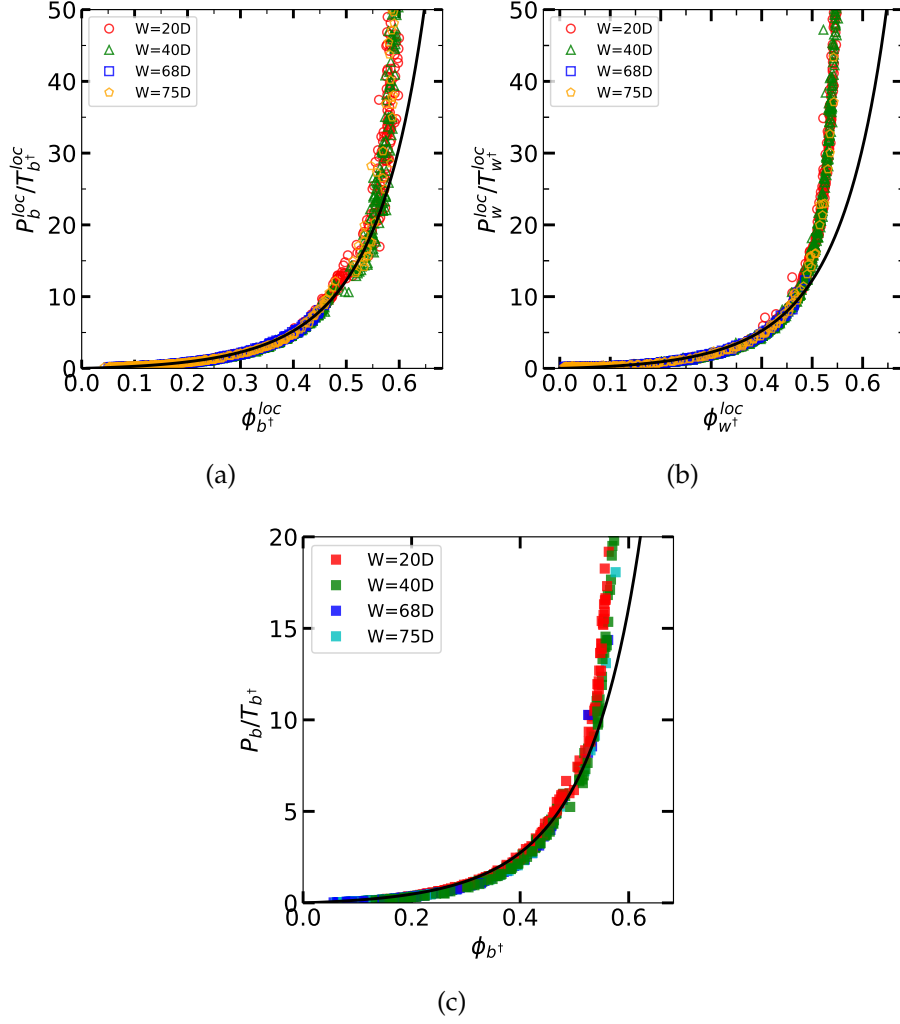


Figure 3.27: (a) $P_{b^+}^{loc}/T_{b^+}^{loc}$ as a function of the local packing fraction at bottom $\phi_{b^+}^{loc}$. (b) $P_{w^+}^{loc}/T_{w^+}^{loc}$ as a function of the local packing fraction at the side-walls $\phi_{w^+}^{loc}$. The solid line is the prediction of the kinetic theory with $e = 0.972$ (see Eq. 3.15). (c) P_{b^+}/T_{b^+} as a function of the mean packing fraction at the bottom ϕ_{b^+} . The solid line is the prediction of the kinetic theory with $e = 0.972$ (see Eq. 3.15).

The above ratio according to the kinetic theory is a function of the packing fraction ϕ through F_1 and F_2 . This could be checked from the data of the simulations. We computed the above ratio close to the bottom wall at a distance $d = 1.5D$ (see Fig. 3.28). The data obtained for various inclinations, particle hold-up and gap width collapse on a unique trend. The prediction of the kinetic theory also agrees remarkably well with the simulation outcomes. These results indicate that the kinetic theory is a good candidate to describe the rheology of our flows. However, it is not capable of predicting properly the slip velocity at the boundaries when they are flat.

Lastly, we made a first attempt to check whether the $\mu(I)$ rheology is relevant to describe the rheology of our flows. To do this, we compute the inertial number in the interior of the flow close to the bottom. Again, the calculation was not made at the wall (i.e., $z = 0.5D$) because the first layer plays a singular role due to the flat boundary. We thus evaluate the inertial number I_b^+ at $z = 1.5D$ and plot the basal friction μ_b as a function of I_b^+ . We obtain a remarkable collapse of the data on a single curve for inertial number smaller than 2.5. Above 2.5, the collapse breaks down and the curve seems to be multi-valued. Similar with Brodu

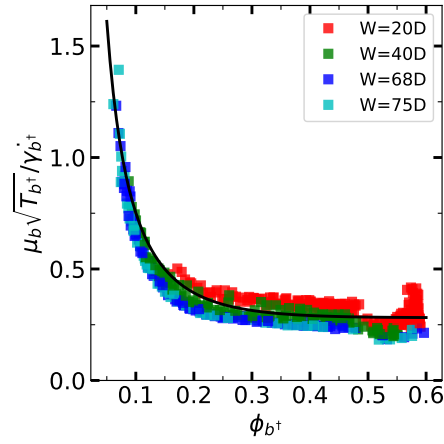


Figure 3.28: $\mu_b \sqrt{T_b} / \dot{\gamma}_{b^+}$ as a function of the mean packing fraction at bottom ϕ_{b^+} . The solid line corresponds to the prediction of the kinetic theory.

et al. (2013), at the transition from the uni-direction to the roll regime the inertial number drops.

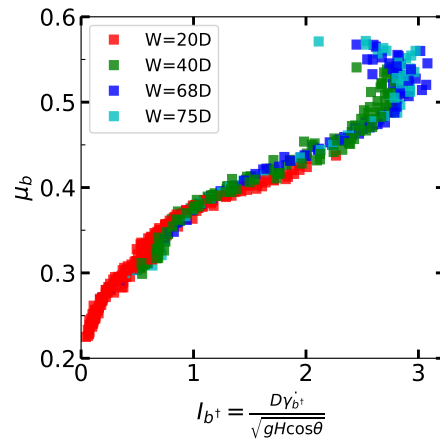


Figure 3.29: μ_b as a function of inertia number at the bottom $I_{b^+} = \frac{D\dot{\gamma}_{b^+}}{\sqrt{gH\cos\theta}}$ for various mass holdup, various inclination and various channel width.

2.8 Phenomenological model for predicting the slip velocities at the boundaries

While the kinetic theory or the $\mu(I)$ rheology may have some potentiality to capture some features of the rheology of our flows, they are not able to predict the slip velocity at flat boundary. From the laws we established, we propose a set of closed equations which provides a theoretical frame to predict the slip velocity of the flow for prescribed mass hold-up, inclination and gap width.

We recall the force balance provide us with the following equation:

$$\tan \theta = \mu_b(Fr_b) + \mu_w(Fr_w) \frac{Z}{W} \quad (3.23)$$

We have seen that the basal and side-wall friction law provide similar trends because they have the same material properties. It is thus legitimate to assume that $\mu_b(Fr_b) \approx \mu_b(Fr_w)$

such that the balance equation reduces to:

$$\tan \theta = \mu_b(Fr_b) \left(1 + \frac{Z}{W} \right) \quad (3.24)$$

We recall that $\mu_b(Fr_b)$ can be approximated by the following exponential function:

$$\mu_b(Fr_b) = \mu_2 + (\mu_1 - \mu_2) \exp(-Fr_b / Fr_{\mu_0}) \quad (3.25)$$

with $\mu_1 \approx 0.29$, $\mu_2 \approx 0.59$ and $Fr_{\mu_0} \approx 12.2$.

We also saw that the rescaled effective frictional height Z obeys a simple law as a function of the mean packing fraction of the flow $\bar{\phi}^*$ which can be expressed as:

$$\frac{Z}{H} = \frac{1 + a_\phi(\bar{\phi}^* - \phi_1)}{\bar{\phi}^*} \quad (3.26)$$

with $a_\phi \approx 1$. Additionally, $\bar{\phi}^*$ was shown to depend only on the basal Froude number and can be described by the following law

$$\bar{\phi}^* = \phi_1 + (\phi_2 - \phi_1) \exp(-Fr_b / Fr_{\phi_0}) \quad (3.27)$$

with $\phi_1 \approx 0.57$, $\phi_2 \approx 0.03$ and $Fr_{\phi_0} \approx 6.8$.

The equation 3.24 completed with Eqs 3.25,3.26 and 3.27 provide a close system of equations to solve for the basal Froude number and the mean flow packing fraction $\bar{\phi}^*$.

2.9 Conclusion

In this article, we studied the influence of the channel width on rapid granular flows. The main effect of the channel width is to change the critical angle or particle hold-up for the appearance of the different flow regimes. As the channel width decreases, the flow regime transition are shifted toward larger angles. This could lead to the disappearance of some flow regimes in the case of very confined flows. As the example, the supported flow regime disappears for gap width smaller than $W = 20D$ while it seems to persist even for very wide channels. In other words, the side-walls are probably not the cause of the "supported" flow regime, but can be the cause of its disappearance.

We also highlighted that flat boundaries induce large slip velocities. We carefully analysed the properties of the flow close to the boundaries. We found the local friction at the boundary can be captured by a simple law which depends only the local Froude number defined as the ratio of the local slip velocity to the square of the local pressure. The local packing fraction at the wall exhibits as well a simple dependence of the local Froude number. These relations provide a relevant framework to predict the slip velocity at the boundary for a given flow configuration.

It would be worth examining in the future several further issues: (i) what is the influence of the wall and particle material properties on the flow regimes and the subsequent friction and packing fraction laws at the walls?; (ii) Can these numerical flow regimes be reproduced in real experiments?; (iii) What is the limit with infinitely large gap width?

3 Perspectives

In this chapter, we studied the effect of channel width on rapid granular flows and showed that many flow features can be drawn independently of the gap width. This is the case for

the friction and packing fraction laws at the walls. Of course, the flow velocity is crucially dependent of the gap width W and we showed that the mean flow velocity as well as the slip velocity at the wall scale as $W^{0.7}$.

In the two next chapter, we will focus on the influence of the mechanical properties of both the particles and the walls on the nature of the flow regime. We will investigate in particular the role of e , μ_{gw} and μ_{gg} .

Chapter 4

The effect of normal restitution coefficient e on confined granular flows

1 Introduction

Few studies have focused on the influence of mechanical parameters on granular flows. As we know, in granular flows, the particles interact via contact forces including collisions and enduring contacts. A collision involving two macroscopic grains is inelastic and thus dissipates energy. The dissipation is commonly characterized by the coefficient of restitution (Ogawa et al., 1980; Lun et al., 1984; Farrell et al., 1986).

This chapter attempts a first global approach of the effect of the normal restitution coefficient between grains: e_n^{gg} on granular flows in inclined channels. In the following, e_n^{gg} will be simply referred to as the restitution coefficient, and denoted by e . This restitution coefficient between particles plays an important role in diluted granular flows McNamara and Young (1994). In contrast, the restitution coefficient between particles has little effect on very dense granular flows Silbert et al. (2001).

In conditions similar to ours, a channel width $W = 20D$ and $e = 0.8$, Zhang et al. (2019) observed a supported flow regime. However, as already mentioned in the preceding chapter, in our simulations with $W = 20D$ and $e = 0.972$, the supported flow regime does not exist. This observation reveals an important influence of the restitution coefficient on the flow regimes, at least for $W = 20D$.

In this chapter, we will rapidly explore the influence of the restitution coefficient e on the flow regimes and on their kinematic properties. We first study the effect of e for a channel width $W = 20D$ and then for $W = 40D$ to see if the effect of e is only important in case of strong confinement, or if it persists as a general effect independent of the channel width.

The outline of the chapter is the following. Section 2 is a short article, published in EPJ Web of Conferences for Powders & Grains 2021, showing the influence of restitution coefficient e when the gap width W is $20D$. It confirms the important role played by e in rapid confined flows. The mean velocity surprisingly increases when decreases e , as a result of the clustering instability. Changes of flow structure and new flow regimes are also mentioned.

In section 3 we study the effect of varying the restitution coefficient on flows in a channel of width $W = 40D$. We are more specifically interested in the effect on the flow regimes, and in the alteration or invariance of the "universal" global laws evidenced in the preceding chapters.

Finally, we conclude in Sect. 4

2 Dissipation in rapid gravitational granular flows (copy of a published article)

Dissipation in rapid gravitational granular flows

Yajuan Zhu^{1,*}, Renaud DELANNAY^{1,**}, and Alexandre VALANCE^{1,***}

¹Univ Rennes, CNRS, Institut de Physique de Rennes, UMR 6251, 35042 Cedex Rennes, France

Abstract. We investigate numerically high speed granular flows down an incline and focus our attention on the influence of the restitution coefficient e of binary collisions on the nature of the flow regimes. We show in particular that e plays a major role in rapid flows. Decreasing e leads in general to denser flows but also quicker flows which was not expected. The increase of the mean flow velocity with decreasing e is explained as the result of the clustering instability which produces a dense and cold core moving very fast as a plug.

1 Introduction

Recently, several works have been devoted to rapid granular flows confined between side walls. Due to side-wall frictional, steady and fully developed flows (SFD flows) have been observed up to large angles of inclination where accelerated ones are usually expected [1–4]. These new SFD regimes present non-trivial features, including secondary flows (rolls) and heterogeneous volume fraction. Among these, the supported flow regime is particularly interesting: It consists of a dense core floating over a dilute flowing layer and may have implications in the context of geophysical flows [2]. In recent numerical works [2, 4], the authors explore extensively and systematically these different flow regimes as a function of the inclination angle θ and of the mass holdup H for a given gap width $W = 68D$ between side walls.

Here we investigate flows with a narrower width $W = 20D$ and a fixed particle hold-up $H = 5D$. We deal with rather small systems and thus have reasonable computing time to obtain SFD flows. This allows to conduct a parametric study to investigate the role of the restitution coefficient e of binary collisions. We report here an unexpected result which could be phrased as follows: the more dissipative the flow are, the faster they run.

2 Simulation setup

The simulation mimics a granular system flowing on a flat base and bounded by two side walls. We used classical discrete element model (DEM). We considered N spheres with a mean diameter D and slight poly-dispersity ($\pm 10\%D$). The motion of each individual particle is computed from forces acting on them, including contact forces with other particles, with basal and side walls and gravity effect. Periodic boundary conditions (PBC) are used in the

x -direction (figure 1). The system length in the stream-wise direction is $L = 20D$ and the width is $W = 20D$. Details of the simulation method are given in [1, 2]. The restitution coefficient e of particle-particle collision is varied between 1 and 0.55 while the one for the particle-wall collision is kept fixed and set to 0.8. Particle-particle and particle-wall friction coefficients are taken from experiments [5] and set to 0.33 and 0.593, respectively.

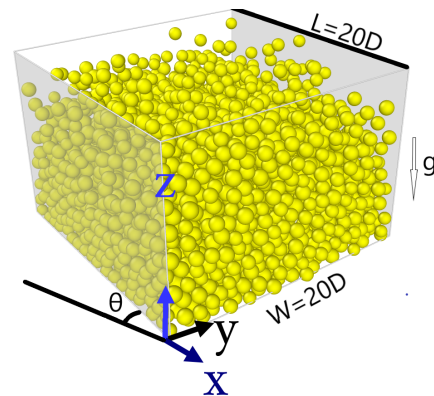


Figure 1: Configuration setup. The granular flow is confined by lateral walls with a width $W = 20D$. Periodic boundary conditions are used in the stream-wise direction with a length L and an angle of inclination θ .

Here we set the particle hold-up H to a fixed value $H = 5D$. The particle hold up represents the depth-integrated particle volume fraction $\phi(z)$: $H = \int_0^\infty \phi(z) dz$ and is directly related to the number of grains N in the system (i.e., $N = 6HLW/\pi D^3$). We have varied the inclination angle between 30° and 50° together with the restitution coefficient e from 1 down to 0.55. An illustration of the different flow regimes obtained when varying these parameters is given in Fig. 2.

*e-mail: yajuan.zhu@univ-rennes1.fr

**e-mail: renaud.delannay@univ-rennes1.fr

***e-mail: alexandre.valance@univ-rennes1.fr

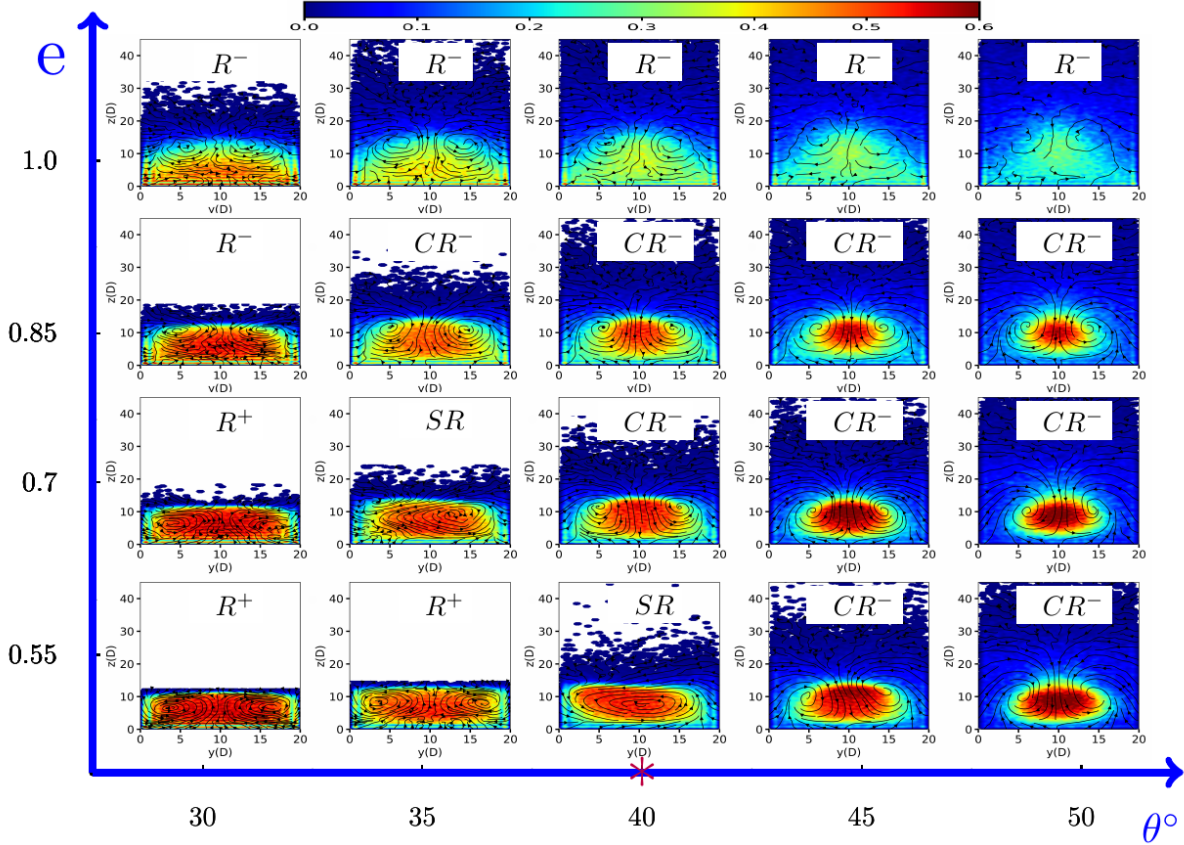


Figure 2: Cross-section of the flow showing the particle volume fraction together with the streamlines for various values of inclination angles and restitution coefficients e . A variety of different flow regimes are observed: (i) Dilute flow regime R^- with a pair of longitudinal rolls R^- leading to a downward motion in the dense part of the flow (i.e., in the center of the cell); (ii) Dense flow regime R^+ with a pair of longitudinal vortices leading to an upward motion in the denser part of the flow; (iii) Supported flow regime CR^- characterized by a dense core C and a pair of longitudinal roll R^- ; (iv) flow regime SR with a single longitudinal vortex.

Preliminary comments can be already made. Increasing the dissipation leads the flow to contract and thus to make it denser. This contraction triggers a transition in the flow regime: the dilute flow regime turns into a supported flow which is characterized by a dense core floating over a dilute and energetic gaseous phase. Additionally, the granular system exhibits secondary flows appearing as a pair of counter-rotative longitudinal vortices. The emergence of longitudinal vortices is a common feature of rapid flows [1, 6, 7]. In the dilute flow regime the pair of vortices (referred as R^-) induces a net downwards motion in the denser part of the flow (i.e., in center of the cell) and an upward motion at the more dilute region of the flow (i.e., at the side-walls). The transition from dilute flow regime to the supported flow regime is accompanied with a reinforcement of the secondary flows. When the restitution coefficient is further decreased, we observe an other transition which modifies the rotation direction of the pair of longitudinal vortices: The downward motion is localized at the side-walls while the upward motion occurs at the center of the cell (R^+ flow regime in Fig. 2). This transition occurs via an intermediate state where one of the two

vortices disappears. The remaining vortex extends over the whole width of the flow leading to a symmetry breaking (SR in Fig. 2).

3 General features of the flow vs inelasticity

We first investigate how the mean flow velocity is altered by the restitution coefficient. Unlike dense flows obtained at shallow angles, our rapid flows show a high sensitivity to the restitution coefficient as illustrated in Fig. 3. Surprisingly, the mean velocity increases with decreasing restitution coefficient. This velocity increase is more and more impressive as the angle of inclination increases. The more the system is dissipative, the faster it goes.

We can anticipate here that this outcome results from the contraction of the flow, which leads to a decrease of the side wall friction. We plot in Fig. 4 the variation of the flowing height h , defined as the height below which one find 97% of the flowing material. The flow height is clearly decreasing with decreasing restitution coefficient. The increase of the mean flow velocity seems to be di-

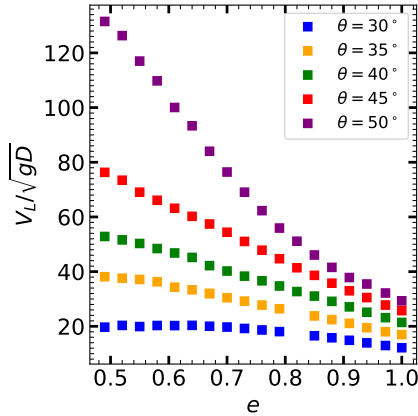


Figure 3: Mean flow velocity as a function of the restitution coefficient for various values of the inclination angle. The hold-up is $H = 5D$.

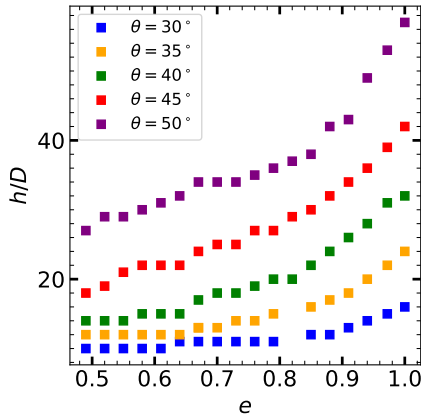


Figure 4: Flow height h as a function of the restitution coefficient for various values of the inclination angle. The hold-up is $H = 5D$.

rectly correlated to the flow contraction. The contraction of the flow can be interpreted as a consequence of the well-known clustering instability in granular gas [8, 9].

4 Concentration, velocity and temperature profiles vs inelasticity

It is instructive now to look more carefully about the flow structure and its change with decreasing restitution coefficient. We first present the vertical and transverse packing fraction profiles for a given angle $\theta = 40^\circ$ and hold-up $H = 5D$ (see Fig. 5). For small inelasticity, the flow at $\theta = 40^\circ$ is rather dilute and the packing fraction decreases monotonically as we move to the free surface. For higher inelasticity the flow undergoes a marked transition where the volume fraction profile is inverted: it first increases and then decreases at larger height. A dense core emerges in the bulk flow with a high packing fraction which increases

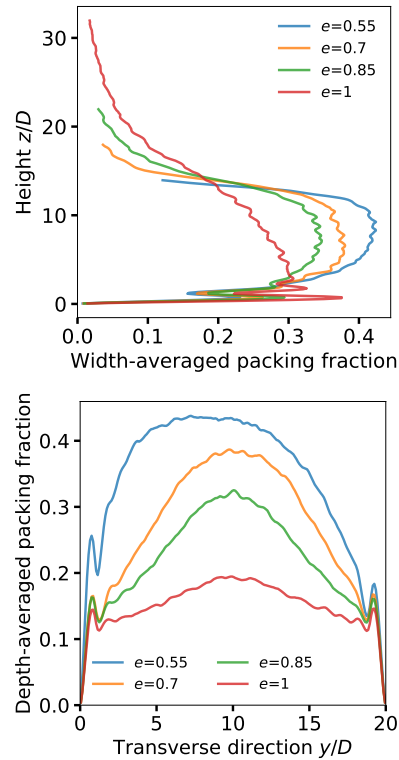


Figure 5: (a) Vertical packing fraction profiles for decreasing restitution coefficient. (b) Corresponding transverse packing fraction profiles. The inclination angle is $\theta = 40^\circ$ and the hold-up is $H = 5D$.

with decreasing restitution coefficient fraction and is surrounded by a dilute atmosphere at the base and at the side-walls. This is the so-called "supported flow" which has been discovered by Brodu et al. in rapid flows [2]. Upon a further decrease of the restitution coefficient, we get another transition characterized by a change of the vortex pattern. The pair of vortices destabilizes and gives rise to a single longitudinal vortex which breaks the symmetry, as can be seen in the transverse packing fraction profile (cf. Fig. 5b).

The influence of the inelasticity is also clearly seen on the vertical velocity profiles (see Fig. 6). For weak inelasticity (i.e., restitution coefficient close to 1), the velocity increases smoothly with increasing height and the slip velocity at the base is moderate. For increasing inelasticity, the slip velocity is increasing drastically. The shape of the velocity profile is also changed with a greater strain rate at the base and almost flat profile within the dense core. This is the classical feature of the supported regime with a dense core flowing as plug and moderately sheared in its interior.

The temperature profiles are also very informative with regards to the role of inelasticity (see Fig. 7). For small inelasticity, the temperature is almost uniform through the depth. This is not the case for larger inelasticity where strong temperature gradients are present. In particular, the base of the flow is very "hot" while the bulk flow is

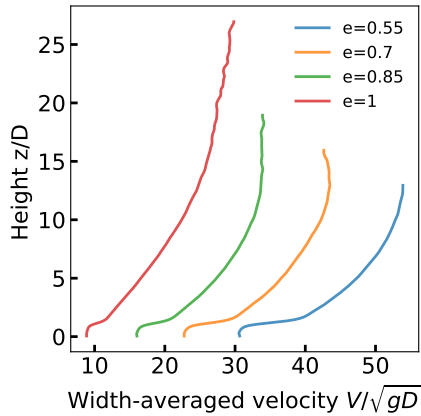


Figure 6: Vertical velocity profiles for decreasing restitution coefficient. The inclination angle is $\theta = 40^\circ$ and the hold-up is $H = 5D$.

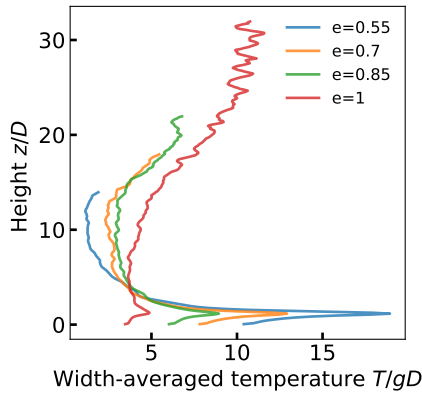


Figure 7: Vertical temperature profiles for decreasing restitution coefficient. The inclination angle is $\theta = 40^\circ$ and the hold-up is $H = 5D$.

very "cold". This contrast of temperature increases with increasing inelasticity. The high temperature at the base is explained by the large slip velocity.

5 Discussion and Conclusion

Our simulation results have shown that the inelasticity plays an important role in the flow structure but also in the mean flow velocity in the context of rapid flows confined between frictional side walls. We found surprisingly that

inelastic flows runs faster than elastic ones. This counter-intuitive feature results in fact from the competition of two antagonist mechanisms. This first one already mentioned earlier in the text is the effect of the flow contraction together with the creation of a dense core for increasing inelasticity. We believe that this is a direct consequence from the cluster instability in granular gas. The flow contraction reduces the area of friction with the side-wall and contribute to an increase of the mean flow velocity. The antagonist mechanism results from the increase of the effective side-wall friction coefficient when the flow velocity increases [4]. We showed indeed in a recent paper that the effective wall friction is an increasing function of the Froude number. Thus for a given inclination angle and particle hold-up, the effective friction increases with increasing velocity. However, the increase of the effective friction coefficient is moderate in comparison with the contraction of the flow such that the latter prevails and is responsible for the mean velocity increase for increasing inelasticity.

The mean flow velocity increases with decreasing e is one of the salient features concerning the role of the inelasticity in the context of rapid granular flows. We also mentioned the change of flow structure with increasing inelasticity, including the transition to the supported flow regime and the appearance of various patterns of longitudinal vortices. Further analysis are required to characterize and understand these flow transitions.

References

- [1] N. Brodu, P. Richard, and R. Delannay, *Physical Review E* **87**(2), 022202 (2013)
- [2] N. Brodu, R. Delannay, A. Valance, and P. Richard, *Journal of Fluid Mechanics* **769**, 218-228 (2015)
- [3] S. Zhang, G. Yang, P. Lin, L. Chen and L. Yang, *Eur. Phys. J. E* **42**, 40 (2019).
- [4] Y. Zhu, R. Delannay, and A. Valance, *Granular Matter* **22**, 82 (2020).
- [5] M.Y. Louge, and S.C. Keast, *Phys. Fluids* **13** (5), 1213 (2001).
- [6] Y. Forterre and O. Pouliquen, *Journal of Fluid Mechanics*, **467**,361–387,(2002)
- [7] T. Börzsönyi, R.E. Ecke and J.N. McElwaine, *Physical review letters*, **103**, 178302, (2009).
- [8] I. Goldhirsch and G. Zanetti, *Phys. Rev. Lett.* **70**, 1619 (1993).
- [9] E. Opsomer, F. Ludewig, and N. Vandewalle, *Eur. Phys. Lett.* **99** (4), 40001 (2012).

3 The effect of normal restitution coefficient e on confined granular flows

3.1 Introduction

As shown in the preceding chapter, flow properties may depend on channel width. For example, in the standard conditions used in chapter 3, there is no supported regime when $W = 20D$, but there are supported regimes for $W \geq 40D$. It is thus important to check that the decreasing of the coefficient of restitution has the same effect of mobilization of the flow, for larger values of W .

Here we study the properties of high-speed granular flows in a smooth channel of width $W = 40D$, when varying the restitution coefficient. For the first time, we observe flows which are still clearly accelerated until the end of the running time $t_{max}/\sqrt{D/g} = 900$. We give the various temporal scenarios and the SFD regimes when they are achieved in a phase diagram in space $(e - \theta)$ for a mass hold-up $H = 5D$. We then focus on the SFD flow regimes. As usually, these flow regimes depend on the mass hold-up. We choose two values of the mass hold-up to exemplify the effect of varying e : $H = 5D$ and $H = 12D$. We study how the mean velocity scaling law is modified by changing the restitution coefficient. Then we investigate the role of e on the global friction at the boundaries and on the mean packing fraction of the flow. At the end, we show the invariance of the rescaled effective frictional height law when e varies.

3.2 Characterization of the flows at $H = 5D$

We use numerical simulations with discrete element model to study the effect of the restitution coefficient e , while fixing the other mechanical parameters to their standard value: $\mu_{gg} = 0.33$, $\mu_{gw} = 0.593$, $e_t^{gg} = 0.25$, $e_n^{gw} = 0.8$, $e_t^{gw} = 0.35$.

3.2.1 Phase diagram in space $e - \theta$

In (Brodu et al., 2015) and the preceding chapters of this thesis, the restitution coefficient was set to $e = 0.972$. All the flows reached a steady state whatever the inclination angle $15^\circ \leq \theta \leq 50^\circ$, the mass hold-ups $4D \leq H \leq 22D$ and the channel width $W = 40D, 68D$, within a running time $t \leq 600\sqrt{D/g}$. To establish the phase diagram $(e - \theta)$ shown in figure 4.2, the channel width and mass hold-up are fixed to $W = 40D$ and $H = 5D$ respectively. The restitution coefficients e varies from 0.49 to 1 over a range of inclinations $20^\circ - 60^\circ$. Our system was run for $t_{max} = 900$ time units (i.e., $\sqrt{D/g}$). For some values of the parameters, the steady flows were not achieved within the usual 600 time units. As a matter of fact, the flows remained accelerated even with a maximum running time equal to 900 time units. We thus report, in our phase diagram, the various scenarios of evolution we observe in our simulations. For each scenario, the temporal evolution of the mean flow velocity is shown in Fig.(4.1(a))

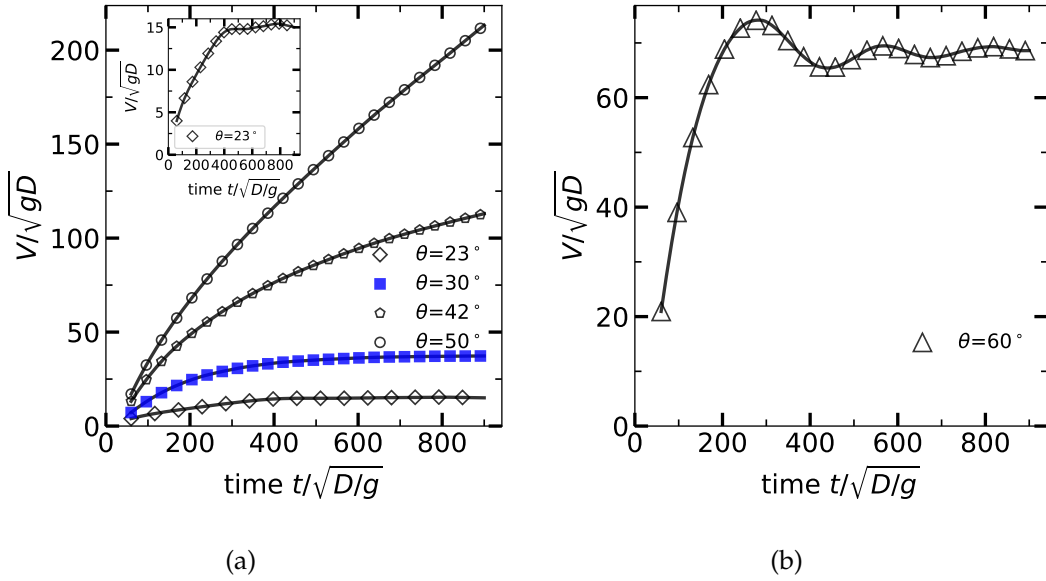


Figure 4.1: The mean velocity V as a function of time t for different values of the inclination angles θ . (a) For $e = 0.64$, the curve $\theta = 23^\circ$ - also shown in insert - presents the intermittent flow regime (\diamond), the curve $\theta = 30^\circ$ presents the scenario (D0) where the flow reaches a SFD flow regime (\square), the curve $\theta = 42^\circ$ presents the scenario (D) where the acceleration monotonically decreases without converging within the maximum running time $t_{max} = 900\sqrt{D/g}$ (\diamond), the curve $\theta = 50^\circ$ presents the scenario (DC) where the acceleration decreases to reach a finite constant value (\circ). (b) For $e = 0.972$, the curve $\theta = 60^\circ$ presents the scenario (O) where the mean velocity oscillates around a fixed value (\triangle).

Scenario D0 (labeled by a square symbol \square): SFD flow regime. The flow reaches a steady state via a monotonic exponential saturation within 1%, in a time less than the maximum running time $t_{max} = 900/\sqrt{D/g}$. The acceleration decreases to zero, reason why we name this scenario D0.

Scenario DC (labeled by a circle symbol \circ): the flow acceleration uniformly decreases down to a non-zero constant before the maximum running time t_{max} . It then keeps its constant and finite value.

Scenario D (labeled by a pentagon symbol \diamond): as for scenario DC, the flows acceleration monotonically decreases with time, but it is still decreasing at the end of the simulation. This scenario is expected to turn into a "D0" or "DC" scenario, after a running time longer than $900/\sqrt{D/g}$.

Scenario O (labeled by a triangle symbol \triangle): the acceleration first decreases and then oscillates around zero. This scenario thus leads to a periodic oscillation of the mean flow velocity around a fixed value. We already met this scenario called oscillating flows in the preceding chapter.

A last scenario (labeled by a lozenge symbols \diamond) leads to an intermittent regime where the mean velocity fluctuates a lot. This concerns flows close to the jamming transition. These flows have been called intermittent flow regime Brodu et al. (2015); Zhu et al. (2020).

In some cases, for the scenario DC, at the end of the simulation, the mean velocity reaches very high values. It then drops rapidly (case labeled by \ominus in figure 4.2). It is difficult to know

if this behavior is physical since, for such high values of the velocity, physical mechanisms which are not encoded in the numerical simulation, as air friction or mechanical rupture of the grains, would intervene. We didn't study this case in details.

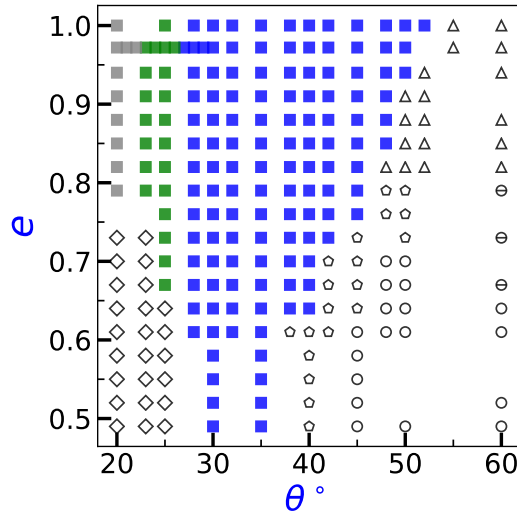


Figure 4.2: Phase diagram in parameter space $e - \theta$ for $H = 5D$ and $W = 40D$, running time $t = 900\sqrt{D/g}$. (\diamond) intermittent regime; (\square) SFD flows with "D0" scenarios (\blacksquare : unidirectional U, \blacksquare : dense rolls R^- , \blacksquare : supported flows CR^-); (\circ) "DC" scenarios (\ominus in case of final drop); (\diamond) "D" scenarios and (\triangle) "O" scenarios.

The phase diagram (figure 4.2) presents interesting features. First we see that the interval of angle within which SFD flows exist reduces when the restitution coefficient e decreases: intermittent flows replace SFD flows at small angles; oscillating flows, and then accelerating flows replace SFD flows at large angles. For small values of e , the SFD domain probably disappears. Small values of e induce a collapse producing nearly jammed flows at small inclination angles. On the contrary, when inclination is larger, in supported regime, the collapse induces a large dense core reaching high velocities and thus accelerating during a very long time.

In the SFD regime, three different flow patterns - already described in previous chapters - exist:

- i) the unidirectional regime (U), with a dense and layered flow;
- ii) the roll regime (R^-) with a pair of longitudinal vortices leading to an downward motion in the denser part of the flow;
- iii) the "supported" regime (CR^-) where the dense core floats on the dilute basal layer.

Besides the reduction of the SFD domain, we don't see much effect on the transition between the different SFD regimes when e varies: the angle θ_c at which the transition to supported regime occurs does not seem to change.

3.2.2 Cross-section of the flows

In the rest of this article, we will focus on the SFD flow regime. To get some insight into what happens to the structure of the SFD flows when the restitution coefficient e decreases, we observe the packing fraction maps. Figure 4.3 presents the cross-section of the flows, showing the particle volume fraction together with the streamlines for various values of inclination angles and restitution coefficients e with $H = 5D$. We notice that the variation of the restitution coefficient has a relatively small effect at $\theta = 25^\circ$ (dense flows R^-) but it

has an obvious influence at larger angles (supported flows CR^-) where large parts of the flow are diluted. We can think that the effect of the restitution coefficient can be related to a variation of the flow concentration: as the restitution coefficient decreases, the flow height decreases, the dense core is larger, and it becomes bigger and bigger. This leads to an increase of the mean packing fraction. Similar results were found in [McNamara and Young \(1994\)](#), where the clusters size and density increase with decreasing restitution coefficient for a 2-D, zero-gravity, system. So the effect of the restitution coefficient on the flow manifests itself in changing the flow concentration. For dense flows, concentration cannot increase much, thus the influence of the restitution coefficient is small. This is in agreement with the results of [Silbert et al. \(2001\)](#): the restitution coefficient has no obvious effect for dense unconfined inclined flows.

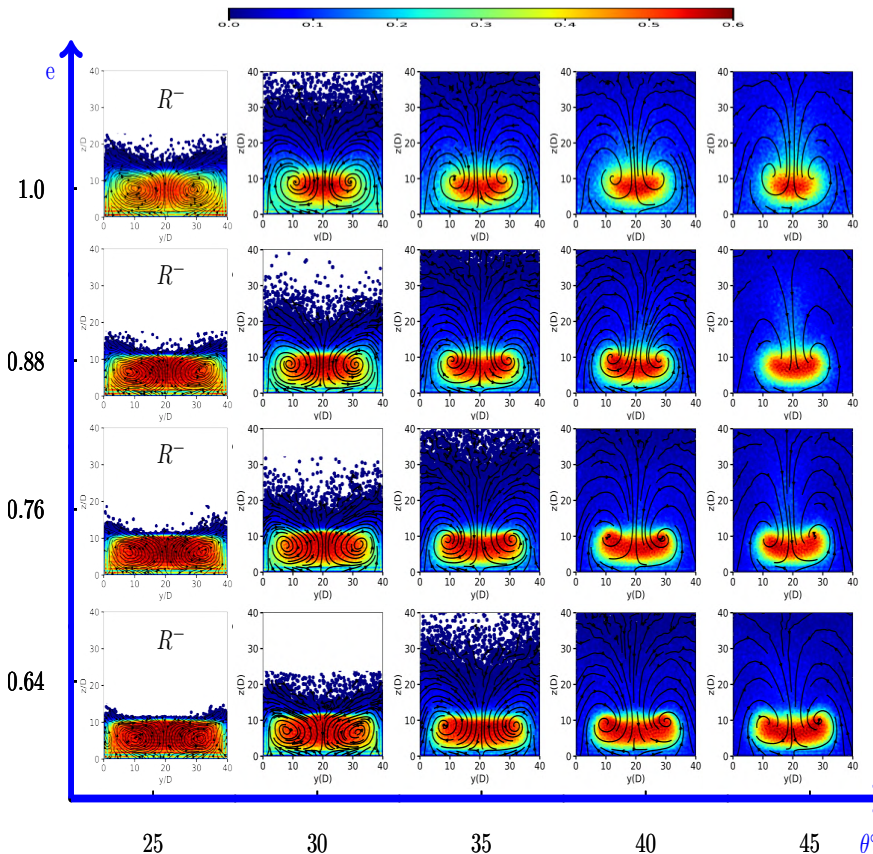


Figure 4.3: Cross-section of the SFD flows showing 2D maps of the packing fraction together with the streamlines for different values of inclination angles and restitution coefficients with $H = 5D$. Two different flow regimes are observed: (i) Dense flow regime R^- with a pair of longitudinal rolls leading to a downward motion in the denser part of the flow (i.e., in the center of the cell); (ii) Supported flow regime CR^- (not labeled on the maps) characterized by a dense core and a pair of longitudinal rolls.

3.2.3 Variation of effective flow height

As shown on figure 4.4(a), the effective height of the flow h^* - defined as the height below which one find 97% of the flowing material - systematically increases with increasing e at a given θ , and with increasing θ at a given e . For the dense flow regime, in agreement with our preceding observations, h^* weakly increases with inclination. But for the supported flow regime, it varies linearly at a high constant rate, independent of the value of e . In this regime, the relationship between the effective flow height and the restitution coefficient can thus be made explicit: $h^* = A \tan \theta - (a_1 + a_2(1 - e^2))$, where the $A = 116 \pm 2$, $a_1 = 45$, $a_2 = 30.8$ (see Fig.4.4(b)). The fit coefficients can depend on H and W .

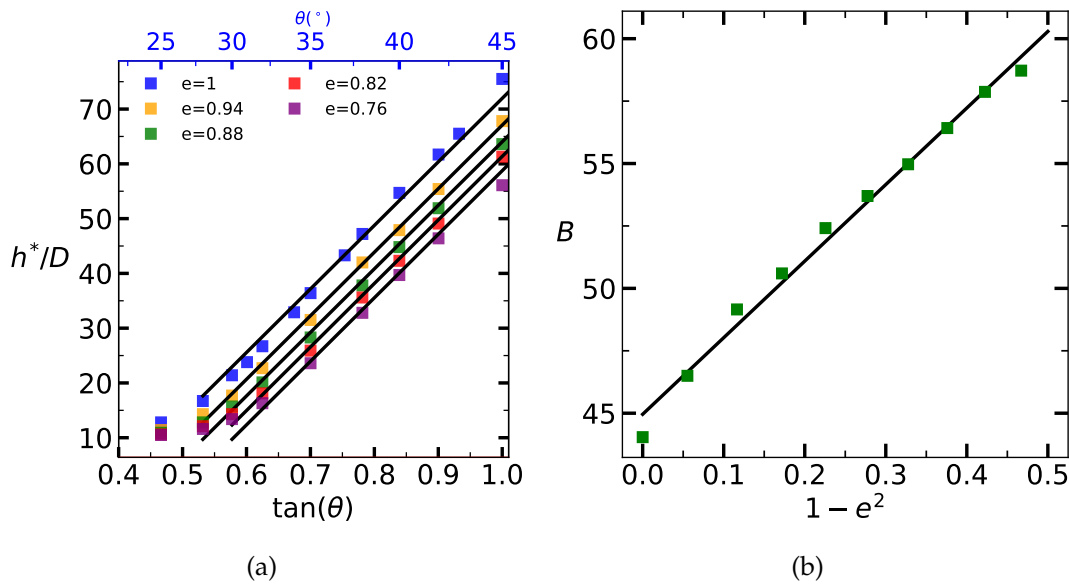


Figure 4.4: (a) Effective height h^* as a function of $\tan \theta$ for various restitution coefficients e , $H = 5D$. The solid line corresponds to: $h^* = A \tan \theta - B$, where $A = 116$ and B is a function of e . (b) Coefficient B as a function of $1 - e^2$, the solid line is $B = a_1 + a_2(1 - e^2)$ with $a_1 = 45$, $a_2 = 30.8$.

3.3 Mean velocity scaling law

3.3.1 Effect of restitution coefficient on mean flow velocity at $H = 5D$

We study here, for $H = 5D$ and $W = 40D$, the effect of the restitution coefficient on the mean velocity of SFD flows. In figure 4.5 we can see how varies the mean steady velocity V_L when we vary the restitution coefficient e between 0.49 and 1, for various inclination angles $\theta \in [25^\circ, 48^\circ]$. The steady velocity V_L clearly increases as the coefficient of restitution e decreases, for all the inclinations. This velocity increase is more and more pronounced as the angle of inclination increases. The same tendency has been seen with channel width $W = 20D$ (figure 3, section 2 of the present chapter).

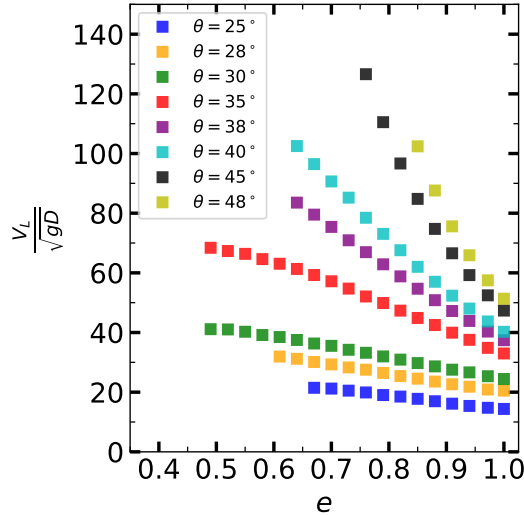


Figure 4.5: The mean stationary velocity V_L as a function of the coefficient of restitution e for $\theta \in \{25^\circ, 28^\circ, 30^\circ, 35^\circ, 38^\circ, 40^\circ, 45^\circ, 48^\circ\}$ and $H = 5D$.

As we can see in figure 4.5, for small inclinations $\theta \leq 35^\circ$, when the coefficient of restitution decreases, the mean velocity first increases linearly and then undergoes inflexion and tends to saturate (see Fig. 4.5). This behavior is similar to the one observed at $W = 20D$ in figure 3, section 2 of the present chapter.

For larger inclinations $\theta > 35^\circ$, when the coefficient of restitution decreases, the mean velocity increases more rapidly without inflexion, and the greater the angle, the faster the speed increases. For these inclinations, the (DO) scenario is rapidly replaced by (D) or (O) scenarios while the velocity increase produced by the contraction of the flow becomes important.

3.3.2 Cross-sections of the flow at $H = 12D$

All the results we have shown up to now are obtained with $H = 5D$. To determine how the velocity scaling law is changed when e varies, we have to characterize flows with different mass hold-up, we performed numerical simulations for flows with $H = nD, n \in \{4, 5, 7, 12, 13, 15\}$. Varying e, H and θ give birth to a huge number of results that are difficult to fully report. We will just see here what is the effect of the variation of the restitution coefficient on flows when $H = 12D$ and then try to use the approach developed in chapter 3 for the velocity scaling law.

The figure 4.6 presents the cross-section maps of the packing fraction together with the streamlines for various values of inclination angles and restitution coefficients e with $H = 12D$. Similarly to the figure 4.3 it shows that the effective flow height h^* decreases with decreasing e , but it also reveals the emergence of new flow regimes. The effect of the decrease of e depends on the angle of inclination.

When $\theta = 30^\circ$ as the flow height decreases, when the diluted part nearly disappears, the rotation direction of the rolls reverses. The regime change from (R^-) to (R^+) . To realize this change, it passes through (at least) another roll regime: R_\pm^\pm , with three pairs of longitudinal rolls with alternate directions of rotation (the upper and the lower are of (R^-) type, the intermediate is of (R^+) type).

When $\theta = 35^\circ$, the flow regime which is initially supported (CR^-) first becomes "one roll" (1R) - a dense regime with a main large roll and some very small rolls - and finally

reaches a dense regime with two pairs of rolls: (R_{\pm}^+), with alternate directions of rotation. The upper pair with an upward motion in the dense middle ((R^+) type), the lower with a downward motion in the middle ((R^-) type).

For $\theta = 40^\circ$, the dense core of the supported regime becomes larger and more symmetric when e decreases. The flow regime then evolve from CR^- to R_{\pm}^+ .

For $\theta = 50^\circ$, the dense core of the supported regime also becomes larger, but the asymmetry of the flow does not disappear. The flow regime evolve from the classical supported regime (CR^-) to a supported regime ($C1R$) which consists in a dense core driven by a large roll and some very small rolls. The $C1R$ regime seems to have a rather complex time evolution with decreases of the main roll which is replaced by a growing secondary roll rotating in the opposite direction. The direction of rotation of the main roll is thus switching over time. We did not study it in details.

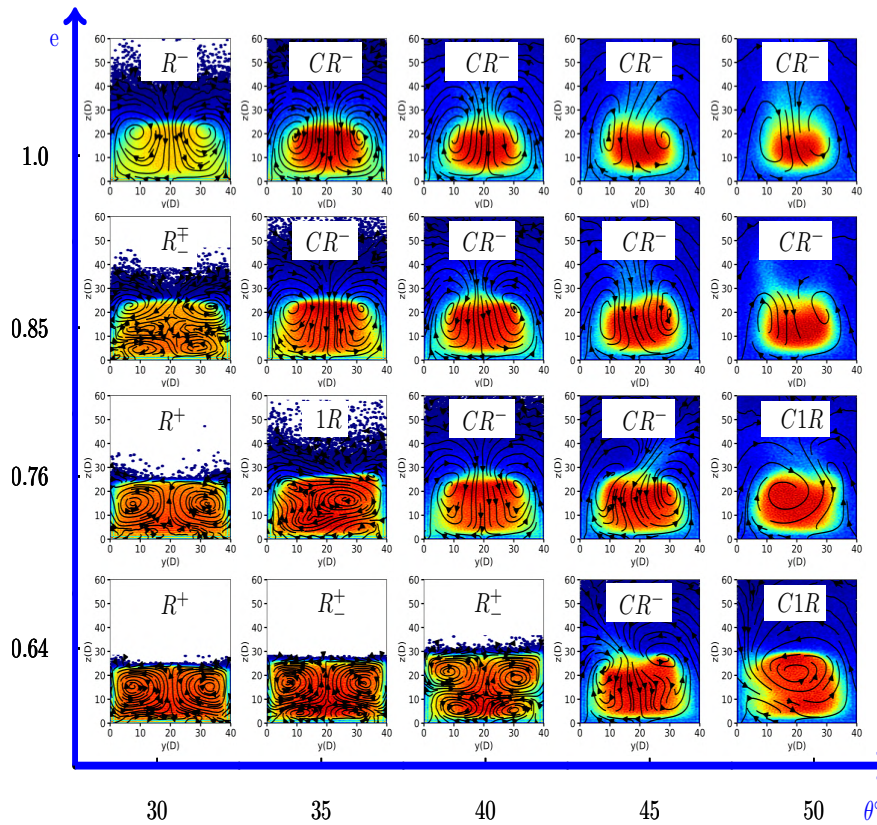


Figure 4.6: Cross-section of the SFD flows showing the particle volume fraction together with the streamlines for various values of inclination angle and restitution coefficient, with $H = 12D$. Various flow regimes are observed: (i) Dilute flow regime R^- ; (ii) Dense flow regime R^+ ; (iii) Three pairs of rolls R_{\pm} ; (iv) Dense flow regime with two pairs of rolls R_{\pm}^+ ; (v) Supported flow regime CR^- characterized by a dense core C and a pair of rolls R^- ; (vi) Dense regime with a main large roll and some very small rolls $1R$; (vii) Dense core with a main large roll and some very small rolls $C1R$.

3.3.3 Mean velocity scaling law

Let us recall that, in chapter 3, we established a mean velocity scaling law for the SFD supported flows appearing for inclinations larger than a critical angle θ_c . The mean velocity for $\theta > \theta_c$ follows a scaling law : $(V_L - V_L^c) = K_L H^{\alpha_L} (\sin \theta - \sin \theta_c)$, with $V_L^c = V_L(\theta_c)$, and a scaling exponent $\alpha_L = 0.3 \pm 0.05$. This was obtained for the standard values of the parameters and thus for $e = 0.972$.

If we want to generalize this approach to other values of e we have first to determine θ_c for these values of e . As we already observed (see Fig. 4.2) for $H = 5D$, the angle θ_c does not change with e . It is thus the same than in chapter 3 : $\theta \approx 26.5^\circ$, for all e . If we assume that there is a scaling of the same form, whatever e , we can then try to adjust the value of the exponent α_L for different values of e . To make this fit we use the mean velocities obtained for $H = nD, n \in \{4, 5, 7, 12, 13, 15\}$ and $\theta > \theta_c$.

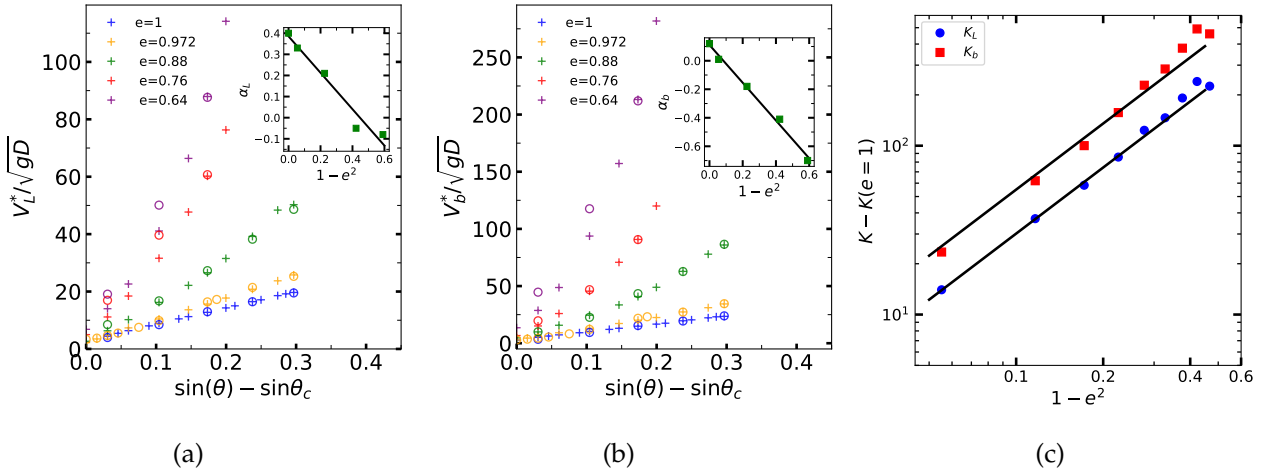


Figure 4.7: (a): renormalized mean velocity V_L^* as a function of $\sin \theta - \sin \theta_c$ for $H = 5D$ (+) and $H = 12D$ (o). The insert shows that α_L is a linear function of $1 - e^2$, the solid line is the affine fit: $\alpha_L = 0.39 - 0.86(1 - e^2)$. (b): renormalized basal velocity V_b^* as a function of $(\sin \theta - \sin \theta_c)$ for $H = 5D$ (+) and $H = 12D$ (o). The insert shows α_b as a function of $1 - e^2$, the solid line is the affine fit: $\alpha_b = 0.11 - 1.33(1 - e^2)$. (c): $K(e) - K(e = 1)$ as a function of $(1 - e^2)$ in log-scale for various inclinations, blue: K_L , red: K_b . The solid line is $K(e) - K(e = 1) = A(1 - e^2)^{1.3}$ where $A_L \approx 600$, $A_b \approx 1100$ and $K_L(e = 1) \approx 65$, $K_b(1) \approx 77$.

Figure 4.7(a) reports the renormalized mean velocity $V_L^* = (V_L - V_L^c) / H^{\alpha_L}$ versus $(\sin \theta - \sin \theta_c)$ for $H = 5D$ and $H = 12D$ and for various restitution coefficients e . The insert of Figure 4.7(a) shows that the exponent α_L seems to be a linear function of $(1 - e^2)$. The exponent α_L increases with e . Figure 4.7(a) confirms the linear behavior of V_L^* as a function of $(\sin \theta - \sin \theta_c)$, but the quality of the linear approximation is lower when e decreases. A linear fit give us $K_L(e)$, figure 4.7(c) shows $K_L(e) - K_L(e = 1)$ as a function of $(1 - e^2)$ in log-scale for various inclinations. The blue solid line shows the least-squares fit with the fitting formula: $K_L(e) - K_L(e = 1) = A_L(1 - e^2)^{k_L}$ with a exponent $k_L = 1.3$, a constant $A_L \approx 600$ and $K_L(e = 1) \approx 65$.

We can also check the basal velocity V_b obeys a similar law, as predicted in chapter 3. The figure 4.7(b) shows the rescaled velocity $V_b^* = (V_b - V_b^c) / H^{\alpha_b}$, with $V_b^c = V_b(\theta_c)$, as a function of $(\sin \theta - \sin \theta_c)$ for $H = 5D$ (+) and $H = 12D$ (o). The insert shows that α_b is a linear function of $(1 - e^2)$ with an affine fit: $\alpha_b = 0.11 - 1.33(1 - e^2)$. We can see that $\alpha_b < \alpha_L$. The slope K_b vary in the same way as K_L : $K_b(e) - K_b(e = 1) = A_b(1 - e^2)^{k_b}$ with the same exponent $k_b = 1.3$, but the constant is different $A_b \approx 1100$ and $K_b(e = 1) \approx 77$ (Fig.

4.7(c)). We see that K_b is larger than K_L whatever e .

We can notice that both exponents α_L and α_b take negative values when e decreases. There is thus an inversion of the behavior of the velocity when H increases: for $e \approx 1$ the velocity increases (weakly) with H , when e is small enough the velocity decreases with H . This behavior is increasingly distant from Bagnold type behavior when e decreases.

3.4 Boundary friction and packing fraction laws

3.4.1 Effective coefficient of friction

If we plot the global effective basal friction coefficient (see Figure 4.8(a)) and side-wall friction coefficient (see Figure 4.8(b)) as functions of the global boundary Froude number for all the SFD flow regimes investigated, with different restitution coefficients e , inclinations θ and mass hold-ups $H = 5D, 12D$, we get a nice collapse of all the data onto a unique curve. The solid line in Figure 4.8 (a,b) presents the usual fit: $\mu(Fr) = \mu_2 + (\mu_1 - \mu_2)(\exp(-Fr/Fr_{\mu_0}))$ with the same values of parameters than in chapter 3: $\mu_1 = 0.292$, $\mu_2 = \mu_{gw} = 0.593$, $Fr_{\mu_0} = 12.2$. We can thus confirm the robustness of the $\mu(Fr)$ boundary friction law.

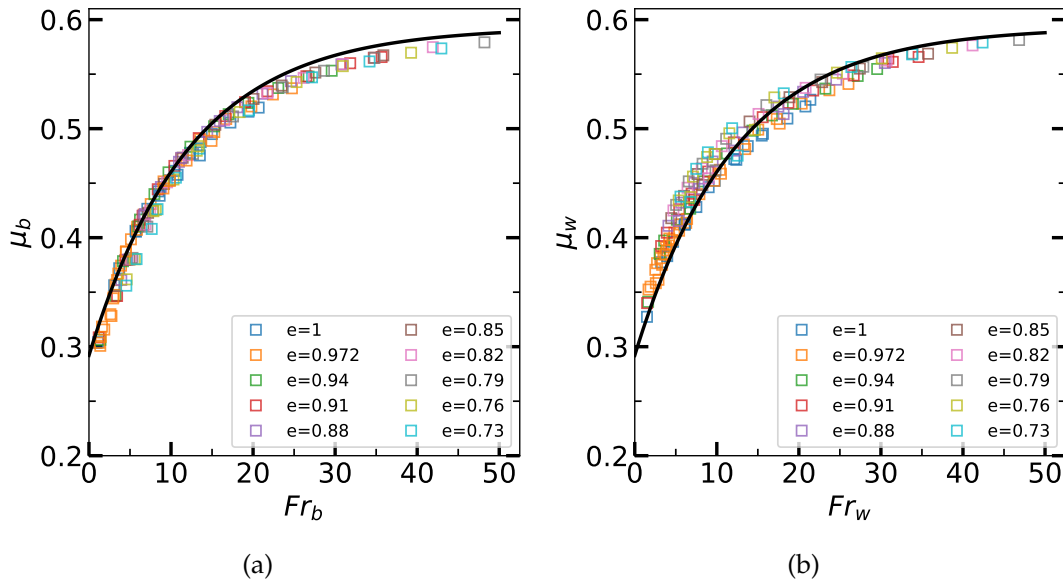


Figure 4.8: Global effective coefficient of friction at the bottom (a) and at the walls (b) as a function of the global boundary Froude number: $Fr_{b,w} = V_{b,w} / \sqrt{gH \cos \theta}$, where $V_{b,w}$ is the sliding velocity at the boundary, for various coefficients of restitution $e = [0.73, \dots, 1]$, mass holdup $H \in \{5D, 12D\}$ and inclination angle in the range 25° to 50° . The solid lines in (a) and (b) present $\mu(Fr) = \mu_2 + (\mu_1 - \mu_2)(\exp(-Fr/Fr_{\mu_0}))$ here $\mu_1 = 0.292$, $\mu_2 = \mu_{gw} = 0.593$, $Fr_{\mu_0} = 12.2$.

3.4.2 Mean packing fraction

In chapter 3 we saw that the mean packing fraction of the flow $\bar{\phi}^*$, calculated over the 97% of the flowing material, also takes a simple functional form which depends on the global basal Froude number Fr_b .

If we compute $\bar{\phi}^*$ as a function of Fr_b using our set of data for $H = 5D$ (see Fig. 4.9(a)). We found that $\bar{\phi}^*$ can always be described as $\bar{\phi}^* = \phi_2 + (\phi_1 - \phi_2)(\exp(-Fr_b/Fr_{\phi_0}))$, where $\phi_1 = 0.65$ whatever e , but ϕ_2 and Fr_{ϕ_0} depend noticeably on e (see Fig. 4.9(b)). We already noticed that the variation of e induces an important variation of the concentration and height

of the flows. It is thus not astonishing to see that the packing fraction law parameters are dependent of e . Both parameters ϕ_2 and Fr_{ϕ_0} increase when e decreases, this corresponds to the contraction of the flow. When e is smaller, the packing fraction limit at large Froude number ϕ_2 is higher and Fr_{ϕ_0} is also larger, the packing fraction decreases more slowly when the Froude number increases. Nevertheless the form taken by the law seems robust, only the values of the parameters change.

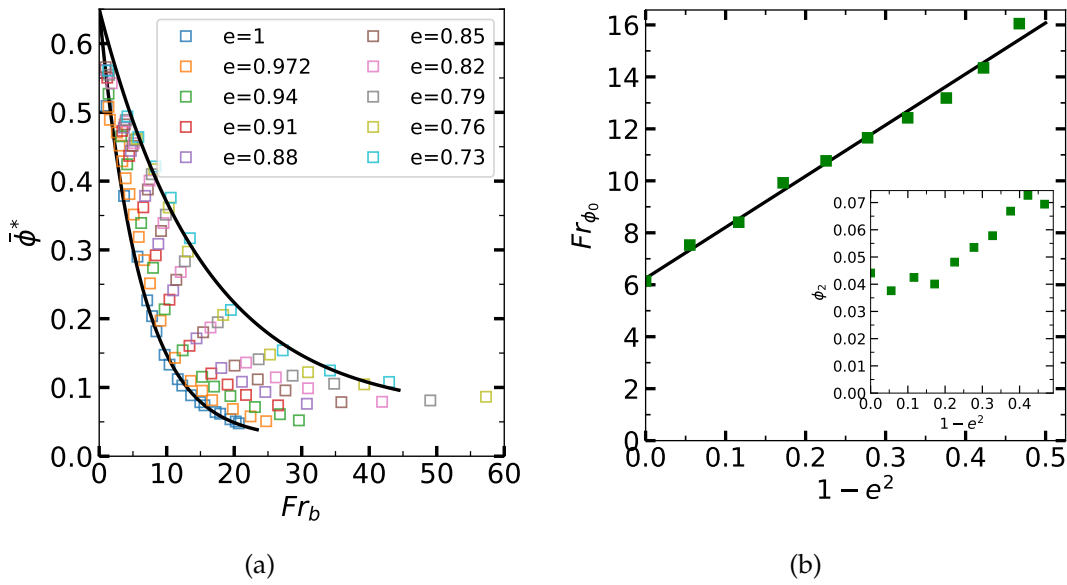
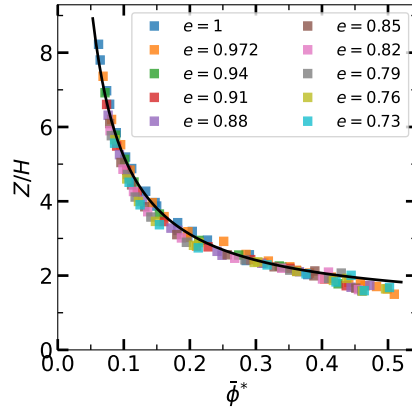


Figure 4.9: (a) $\bar{\phi}^*$ as a function of $Fr_b = V_b / \sqrt{gH \cos \theta}$ for $H = 5D$, various restitution coefficients e , θ in the range 25° to 50° (a) the solid least-squares fit line is $\bar{\phi}^* = \phi_2 + (\phi_1 - \phi_2)(\exp(-Fr_b / Fr_{\phi_0}))$ with $\phi_1 = 0.65$. (b) Presents the variations of Fr_{ϕ_0} with $(1 - e^2)$, with a continuous fit line: $Fr_{\phi_0} = 6.26 + 19.3(1 - e^2)$, ϕ_2 is shown in insert.

3.5 Effective frictional flow height Z

As showed in chapter 3, the rescaled effective frictional flow height Z/H obeys a simple law with the mean packing fraction $\bar{\phi}^*$. This law is independent of θ , of W , and of H . In this paragraph, we will see this relationship also does not depend on the mechanical parameters e . The figure 4.10 shows Z/H as a function of $\bar{\phi}^*$ for various restitution coefficients e . It demonstrates that the law of effective frictional flow height is invariant when we change the restitution coefficient e .



(a)

Figure 4.10: The rescaled effective frictional flow height Z/H as a function of mean packing fraction $\bar{\phi}^*$ for various inclinations in the range 25° to 50° and mass hold-ups $H \in \{5D, 12D\}$. Z is calculated by $\tan(\theta) = \mu_b + \mu_w \frac{Z}{W}$. The fit curves is: $Z/H = (1 + (\bar{\phi}^* - 0.57))/\bar{\phi}^*$.

4 Conclusion and perspectives

In this chapter, we focused on the role of the dissipation on confined granular flows. We highlighted that the mean velocity increases with decreasing e , a result that is somewhat counter-intuitive but that can be explained by the contraction of the flow induced by clustering. When e was small enough we observed the emergence of new scenarios of evolution of the system (D and DC). We also uncovered new SFD flow regimes, like the "single roll" $1R$, the "two pairs rolls" R_-^+ , a "three pairs rolls" R_-^\pm and a regime with a dense core and a single roll $C1R$. We gave the mean and sliding velocities scaling laws for various e and we extended the boundary friction law $\mu(Fr)$, thus showing its robustness. We tested the mean packing fraction law $\bar{\phi}^*(Fr)$ for various e , this relation is invariant in its form, but the values of the parameters change with e . We checked and confirmed the universality of the rescaled effective frictional flow height law Z/H vs $\bar{\phi}^*$.

Altogether we have seen that the restitution coefficient has a noticeable and very interesting effect on confined flows in smooth channels. It is now very tempting to look at the effect of other mechanical parameters: the friction coefficients μ_{gw} and μ_{gg} .

Chapter 5

The effect of mechanical parameters e , μ_{gw} , μ_{gg} on granular flows

1 Introduction

This chapter deals with the effect of mechanical parameters e , μ_{gw} and μ_{gg} on confined granular flows.

We saw in the previous chapter that the restitution coefficient for particle-particle collision plays an important role in the flow structure. For rapid and heterogeneous flows, a change of the restitution coefficient may radically modify the structure of the flow. We showed also that the mean flow velocity surprisingly increases with decreasing restitution coefficient.

In this chapter, we supplement the research on the effect of restitution coefficient e between particles and investigate in addition the role of the friction coefficient μ_{gw} between wall and particle and of the friction coefficient μ_{gg} between particles. We consider flows confined between two lateral walls with a gap width $W = 40D$.

We first analyse how the mechanical parameters affect the different flow regimes and modify the mean flow velocity. We then investigate how the friction and packing fraction laws at the walls (i.e., $\mu_{b,w}(Fr_b)$ and $\phi_{b,w}(Fr_w)$) are affected by a change of the mechanical parameters.

2 Phase diagram in the parameter space $e - \theta$, $\mu_{gw} - \theta$, $\mu_{gg} - \theta$

In chapter 2 and 3, the values of e , μ_{gw} and μ_{gg} were kept constant and set to: $e = 0.972$, $\mu_{gw} = 0.593$ and $\mu_{gg} = 0.33$. These values were referred to as standard values. Here, we present the different flow regimes we obtained when we vary one mechanical parameter while the two other are kept constant and set to the standard values.

2.1 Parameter space $e - \theta$

We already have seen in chapter 4 the phase diagram in the parameter space $(e - \theta)$ for $H = 5D$, $W = 40D$ and all the mechanical parameters except e set to the standard values. We recall it in Fig 5.1.

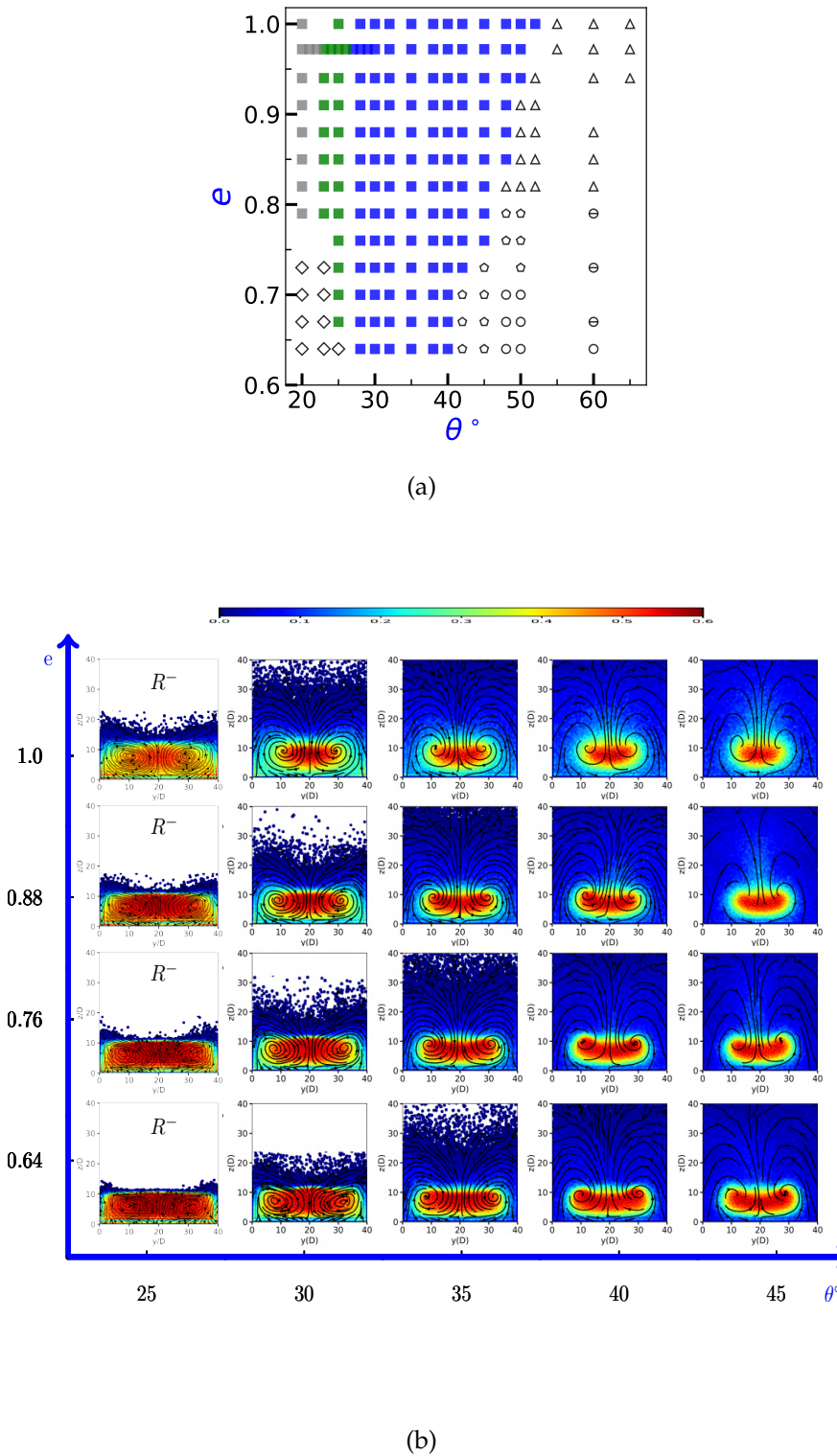


Figure 5.1: (a) Phase diagram in the parameter space ($e - \theta$) for $H = 5D$ and $W = 40D$. Mechanical parameters: $\mu_{gw} = 0.593$ and $\mu_{gg} = 0.33$. (\square) SFD flows with "D0" scenarios (gray: U , green: R^- , blue: CR^- ; (\diamond) "DC" scenarios; (\circ) "D" scenarios and (\triangle) "O" scenarios. (b) Cross-section of the SFD flows showing the 2D map of the packing fraction together with the streamlines. Only the regimes different from the supported regime are labeled. We recall that the R^- regime corresponds to a flow with a pair of two longitudinal vertices with a downward motion in the denser part of the flow.

To prevent the reader from having to go back to the previous chapter we recall the different temporal scenarios observed in our simulations:

- the D0 scenario (\square) leads to a stationary flow after a monotonic exponential saturation within a finite time smaller than the maximum running time $t_{max} = 900/\sqrt{D/g}$.
- the DC scenario (\circ) leads to a flow with a constant and finite acceleration after a finite transient where the flow acceleration uniformly decreases down to a constant value before the maximum running time t_{max} .
- the D scenario (\diamond) is characterized by a finite acceleration which is still decreasing at the end of the simulation.
- the O scenario (\triangle) leads to an oscillating state characterized by a periodic oscillation of the mean flow velocity.
- a last scenario (\diamond) leads flows close to the jamming transition to an intermittent regime where the mean velocity fluctuates a lot.

As already mentioned, when the dissipation increases, the region with steady states (\square) shrinks. We observe in particular that the transition from supported flows (blue square) to oscillating flows (empty triangle) occurs at smaller angle when e decreases. This is a quite surprising effect but it is related to the fact that the main effect of increasing dissipation is to make the core of the supported flows denser and to make it go faster as discussed in details in chapter 4.

2.2 Parameter space $\mu_{gw} - \theta$

We present in Fig 5.2 the phase diagram in the parameter space ($\mu_{gw} - \theta$) for $H = 5D$ and $W = 40D$. The mechanical parameters except μ_{gw} are set to the standard values. We vary the particle-wall friction μ_{gw} from 0.2 to 1.5. We note that there is a drastic reduction of the region with SFD flows when μ_{gw} gets smaller than 0.5. In particular for $\mu_{gw} = 0.4$, SFD flows are obtained only for angles smaller than 25° . This means that the wall friction plays a major role in the existence of steady flows at large inclination angles.

It is important to realize here that the particle-particle dissipation and the wall-particle friction have opposite effects. While increasing particle-particle dissipation leads to faster and faster flows, increasing wall friction reduces the flow velocity and allows SFD flows at larger and larger angle.

2.3 Parameter space $\mu_{gg} - \theta$

In Fig 5.3, we present the phase diagram in the parameter space ($\mu_{gg} - \theta$) for $H = 5D$ and $W = 40D$. μ_{gg} varies from 0.1 to 1 while the other mechanical parameters are set to the standard values. The particle-particle friction μ_{gg} does not have a major effect on the domain of existence of stationary flows. However, a new flow regime is observed when μ_{gg} is set to 0.1. This regime shares many features with the supported flow regime. It has a dense core surrounded by a dilute atmosphere but the latter is not longer suspended but lies directly on the basal wall. We name it WCR^- flow.

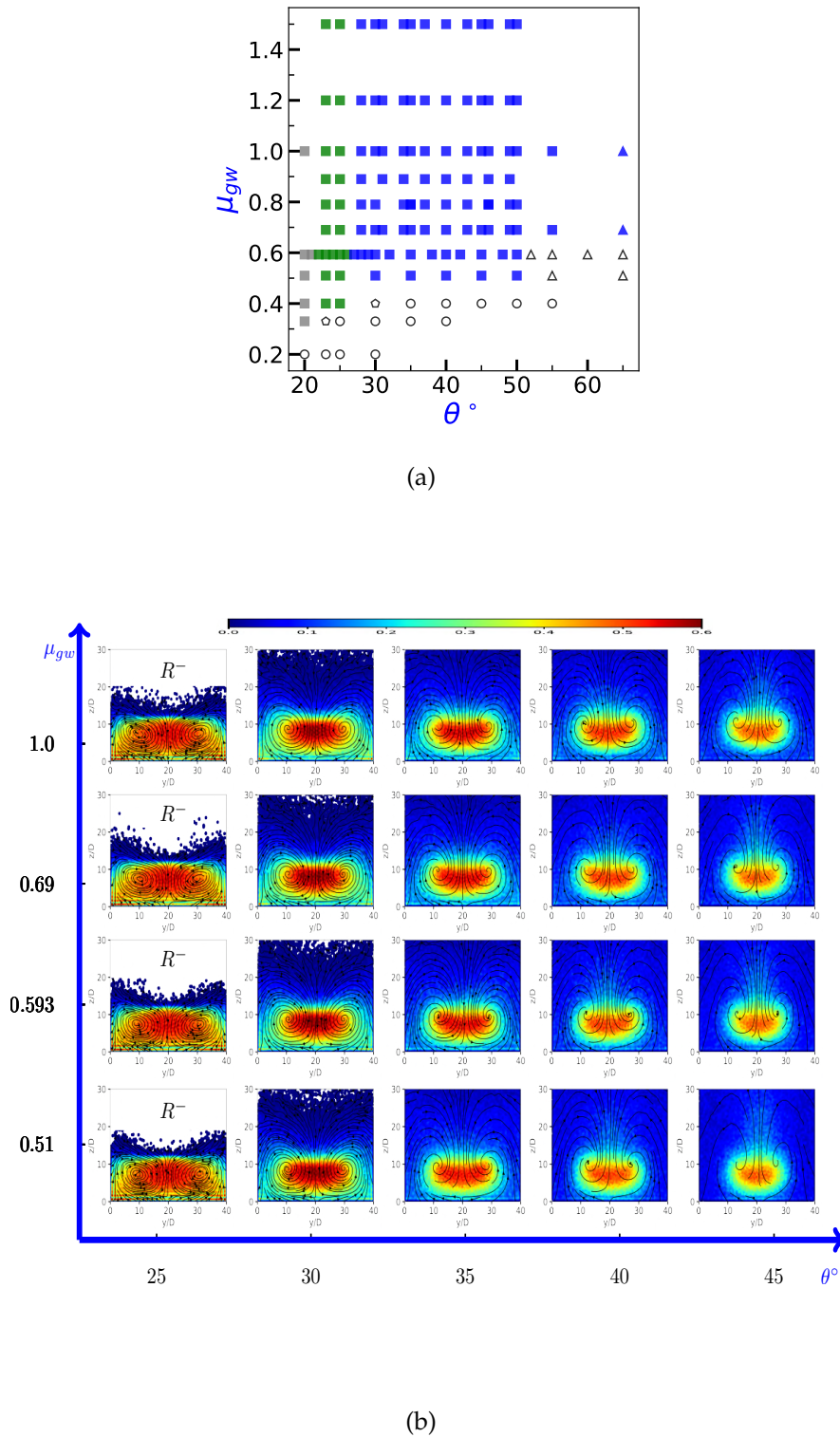
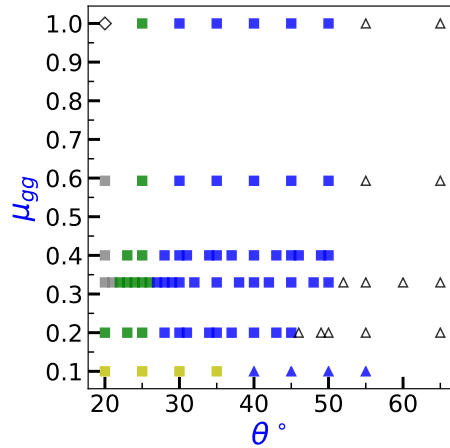
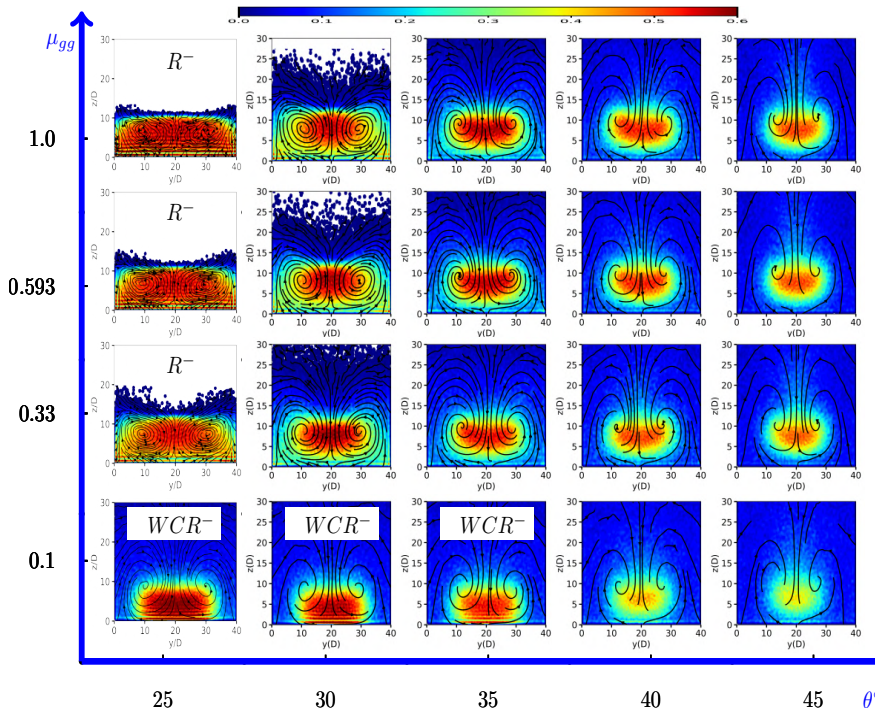


Figure 5.2: (a) Phase diagram in the parameter space ($\mu_{gw} - \theta$) for $H = 5D$ and $W = 40D$. Mechanical parameters: $e = 0.972$ and $\mu_{gg} = 0.33$. (\square) SFD flows with "D0" scenarios (gray: U , green: R^- , blue: CR^- ; (\circ) "DC" scenarios; (\circ) "D" scenarios and (\triangle) "O" scenarios. (b) Cross-section of the SFD flows showing the 2D map of the packing fraction together with the streamlines. Only the regimes different from the supported regime are labeled.



(a)



(b)

Figure 5.3: (a) Phase diagram in the parameter space ($\mu_{gg} - \theta$) for $H = 5D$ and $W = 40D$. Mechanical parameters: $e = 0.972$ and $\mu_{gw} = 0.593$. (\square) SFD flows with "D0" scenarios (gray: U , green: R^- , blue: CR^- , yellow : WCR^-); (\triangle) "O" scenarios. (b) Cross-section of the SFD flows showing the 2D map of the packing fraction together with the streamlines. Only the regimes different from the supported regime are labeled. A new regime (WCR^-) is observed: it has similar features as a supported flow but the dense core is not longer suspended but lies on the bottom.

3 Kinematic and structural properties of the flow

3.1 Mean flow velocity vs mechanical parameters

We analyse here the effect of the mechanical parameters e , μ_{gw} and μ_{gg} on the mean flow velocity. As previously, only one parameter is varied while the two other are kept fixed and are set up to the standard values. We focus here on steady flows and their mean stationary velocity V_L .

In Fig. 5.4, we can see the evolution of the mean flow velocity when we vary independently e , μ_{gw} and μ_{gg} . e and μ_{gw} have significant effect on the mean flow velocity. Decreasing e and μ_{gw} always lead to faster and faster flows. However, the mechanism leading to this velocity increase is different. As discussed in the previous chapter, the particle-particle collision dissipation favours the contraction of the flow resulting in a diminution of the contribution of the side-wall friction in the force balance which accelerates the flow. Concerning the effect of the wall-friction, it is a direct reduction of the microscopic wall friction which leads to faster flows.

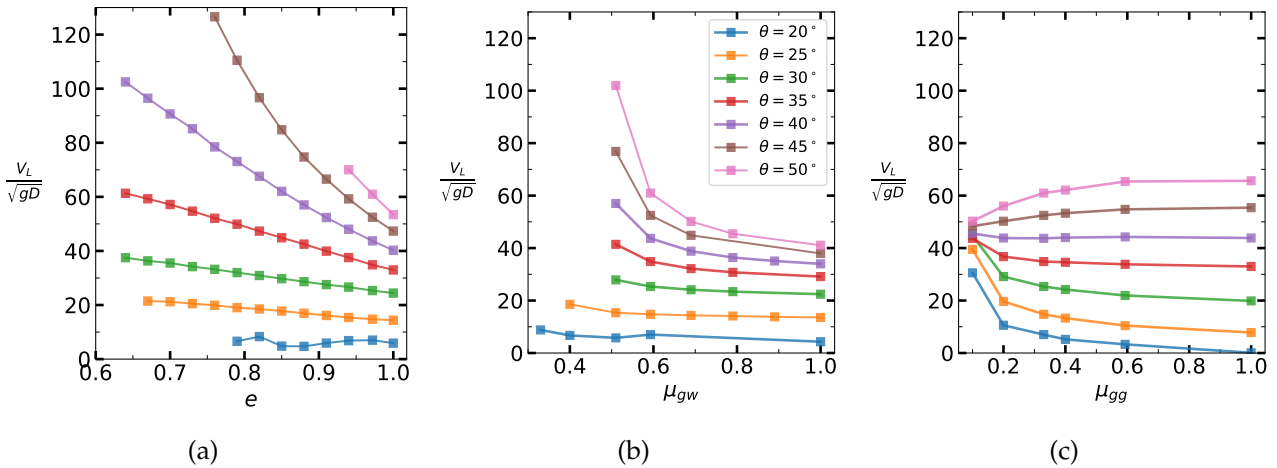


Figure 5.4: (a) Mean flow velocity V_L as a function of e for different inclinations; (b) V_L as a function of μ_{gw} for different inclinations; (c) V_L as a function of μ_{gg} for different inclinations. Only one mechanical parameters is varied while the other are set to the standard values ($e = 0.972$, $\mu_{gg} = 0.33$, and $\mu_{gw} = 0.593$). $H = 5D$ and $W = 40D$.

The effect of μ_{gg} on the mean flow velocity seems to be more subtle. We identify two different evolution according to the inclination. Below 40° , the velocity decreases with increasing friction. However, above 40° , we observe a reverse trend: the velocity surprisingly increases with increasing friction. The mechanism here is possibly the same as that observed for e . The internal particle friction participates to the internal dissipation and can act in the way as e . The mechanism is probably more efficient at large inclination angles where we observe supported flows but the reason for a transition between the two contrasting behaviours is not completely understood.

In Fig. 5.5, we present the same data in Fig 5.4 but plotted as a function of the inclination. In almost all the cases (except for $\mu_{gg} = 0.1$), for prescribed mechanical parameters, the flow velocity always increases with increasing inclination. When e or μ_{gw} is decreased, the mean flow velocity systematically increases. This is not the case when μ_{gg} is varied as previously mentioned. There is a focus point where all the curves cross at angle $\theta = 40^\circ$. This focus point delineates two contrasting behaviours: below it, velocity decreases with increasing

friction while above it, the reverse trend is seen. We will see later on how the focus point varies when e and μ_{gw} are different from the standard values.

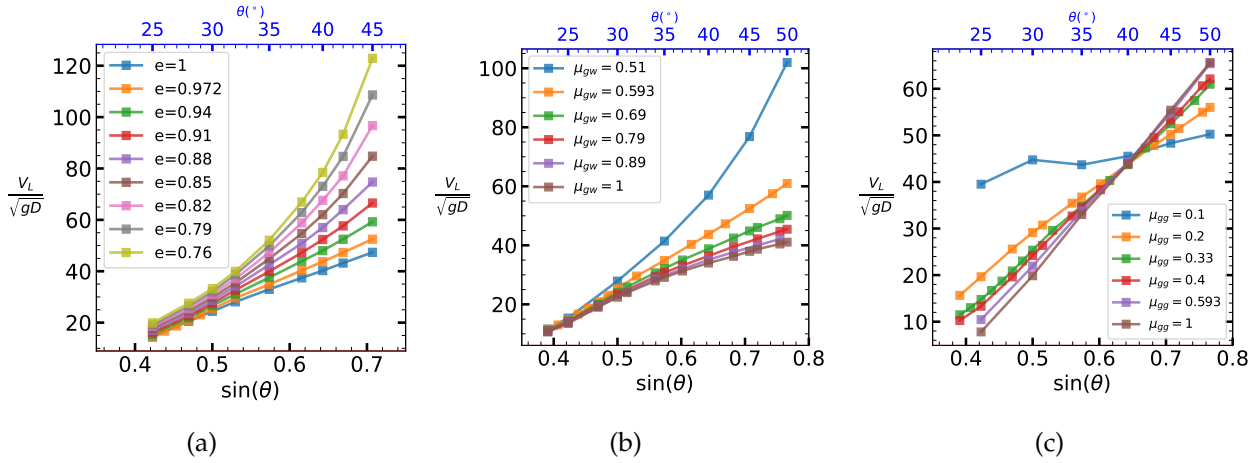


Figure 5.5: Mean flow velocity V_L as a function of $\sin \theta$ for various values of e (a), of μ_{gw} (b) and μ_{gg} (c). $H = 5D$ and $W = 40D$.

3.2 Packing fraction, velocity and temperature profiles vs e

In this section, we will scrutinize the effect of e on the packing fraction, velocity and temperature profiles.

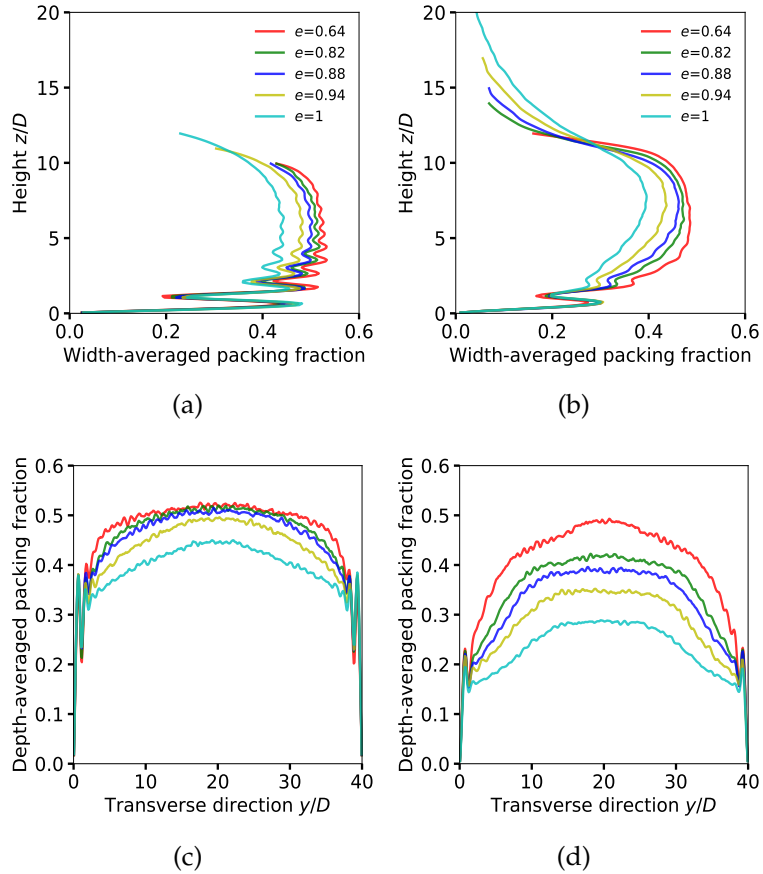


Figure 5.6: Vertical (a and b) and transverse (c and d) profiles for the packing fraction for various e . (a) and (c) $\theta = 25^\circ$ and $H = 5D$ (roll regime); (b) and (d) $\theta = 30^\circ$ and $H = 5D$ (supported regime). Mechanical parameters $\mu_{gg} = 0.33$, and $\mu_{gw} = 0.593$.

The friction coefficients μ_{gw} and μ_{gg} are kept constant and set to the standard values ($\mu_{gg} = 0.33$, $\mu_{gw} = 0.593$).

Volume fraction profiles

Figure 5.6 shows the vertical and transverse profiles of the packing fraction for various e and two inclination angles: $\theta = 25$ and 30° . At $\theta = 25^\circ$, we have a roll flow (R^-) and at $\theta = 30^\circ$ a supported flow (CR^-). When the restitution coefficient decreases, the flow contracts and densifies. Unlike the volume fraction that remains constant at the boundaries, the volume fraction far from the border increases with decreasing e .

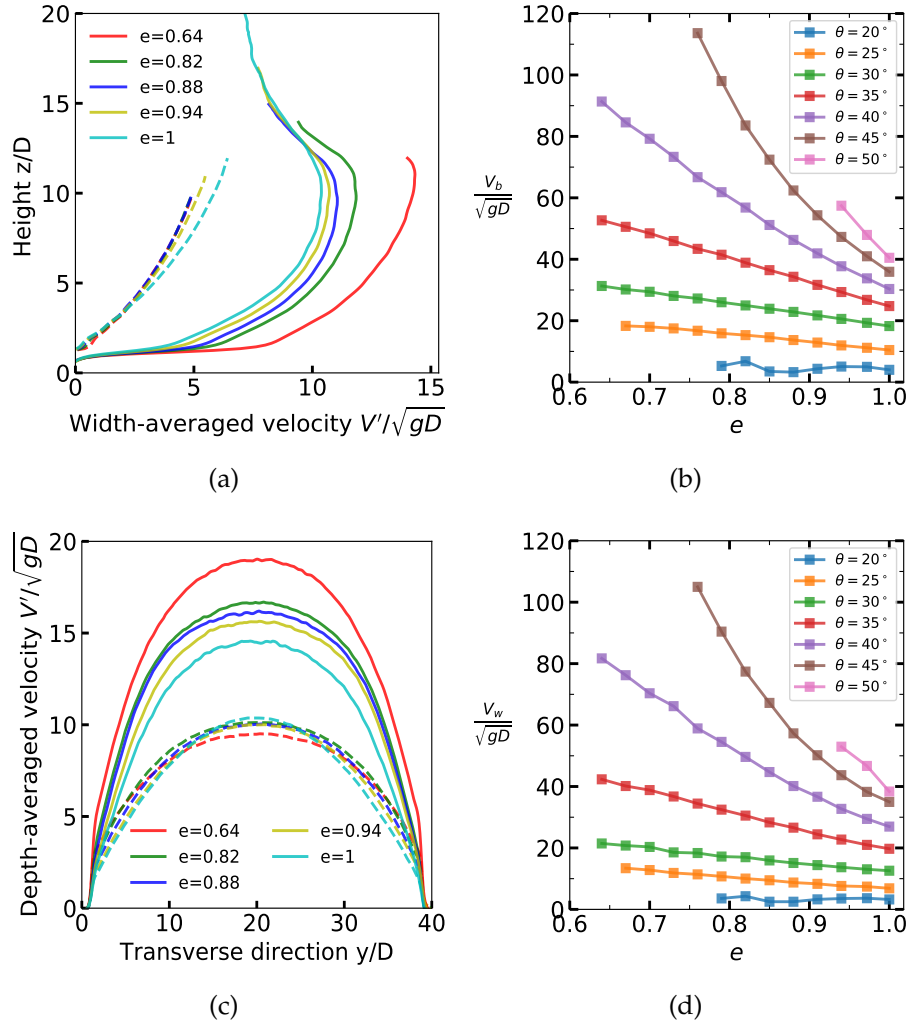


Figure 5.7: (a) Vertical and (c) transverse profiles of the stream-wise flow velocity $V' = V - V_{b,w}$ for various e and two angles $\theta = 25^\circ$ (dashed lines) and $\theta = 30^\circ$ (solid lines). (b) and (d) corresponding slip velocity V_b and V_w . $H = 5D$ and $W = 40D$. Mechanical parameters $\mu_{gg} = 0.33$, and $\mu_{gw} = 0.593$.

Velocity profiles

Figure 5.7 shows the vertical and transverse profiles of the stream-wise velocity $V' = V - V_{b,w}$ for the same flows as those displayed in the previous figure. We recall that the basal and lateral velocity (V_b and V_w) are calculated at a distance $d = 0.5D \pm 0.5$ from the walls. We can see that the velocity increase with decreasing e is essentially due to an augmentation of the slip velocity at the wall. The form of the vertical and transverse profiles is almost unchanged once the slip velocity is withdrawn. We can see a slight evolution but which remains small in comparison with the change of the sliding velocity.

Granular temperature profiles

Figure 5.8 displays the vertical and transverse profiles of the granular temperature corresponding to the flows shown in Figs 5.6 and 5.7. These profiles reveal that the granular temperature within the bulk flow decreases with increasing dissipation. The decrease is more pronounced in the supported regime (at $\theta = 30^\circ$) than in the roll regime (at $\theta = 25^\circ$). At the walls, the trend is reversed. The temperature increases with increasing dissipation.

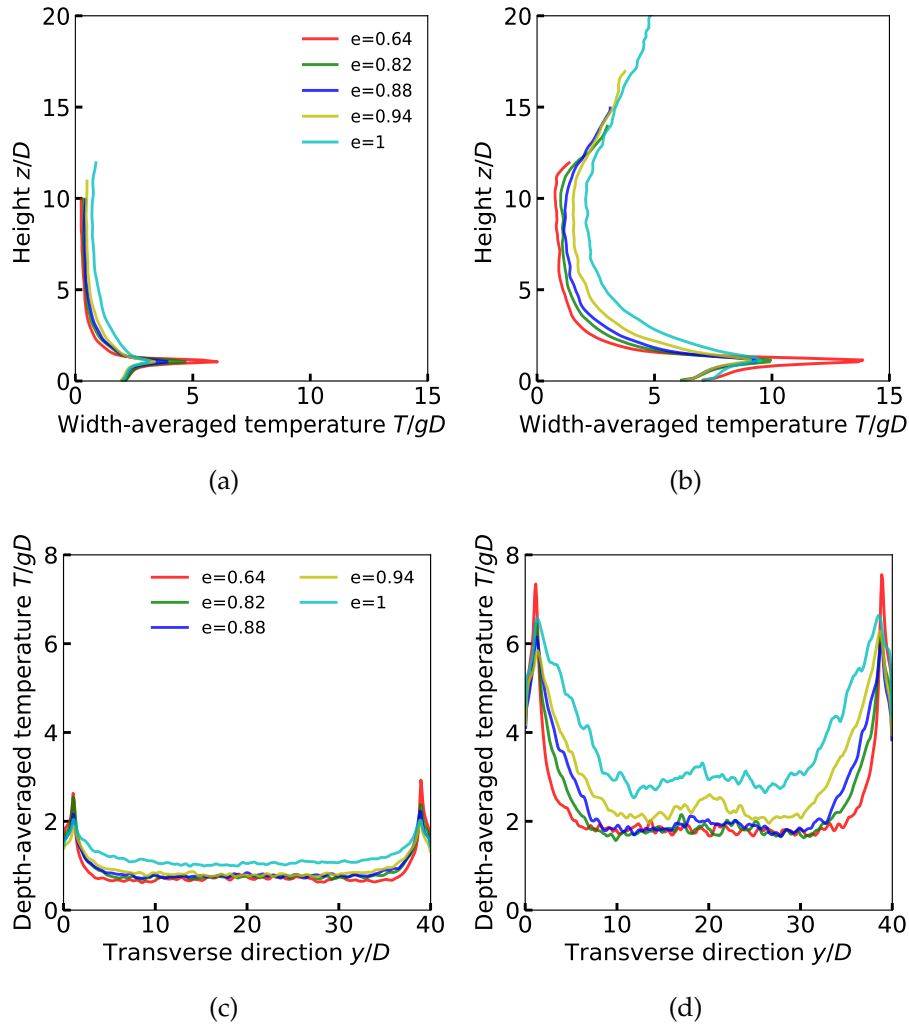


Figure 5.8: Vertical (a and b) and transverse (c and d) profiles of the granular temperature for various e . (a) and (c) $\theta = 25^\circ$ and $H = 5D$ (roll regime); (b) and (d) $\theta = 30^\circ$ and $H = 5D$ (supported regime). Mechanical parameters $\mu_{gg} = 0.33$, and $\mu_{gw} = 0.593$.

3.3 Packing fraction, velocity and temperature profiles vs μ_{gw}

We now look at the influence of the wall friction on the flow structure.

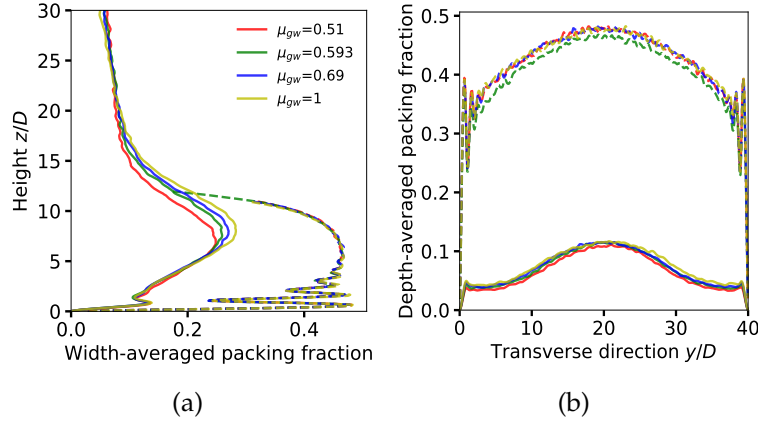


Figure 5.9: Vertical (a) and transverse (b) profiles of the packing fraction for various μ_{gw} at two different inclinations: $\theta = 25^\circ$ and $H = 5D$ (dashed lines, R^- flow), and $\theta = 45^\circ$ and $H = 5D$ (solid lines, CR^-). $W = 40D$. Mechanical parameters: $\mu_{gg} = 0.33$ and $e = 0.972$.

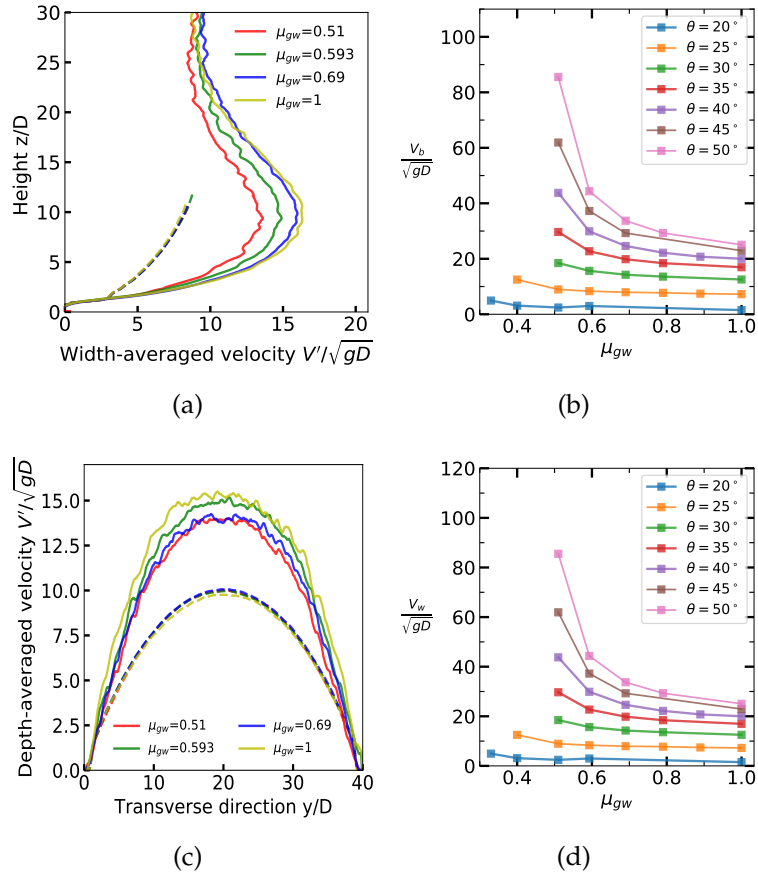


Figure 5.10: (a) Vertical and (c) transverse profiles of the stream-wise flow velocity $V' = V - V_{b,w}$ for various μ_{gw} and two angles $\theta = 25^\circ$ (dashed lines) and $\theta = 45^\circ$ (solid lines). (b) and (d) corresponding slip velocity V_b and V_w . $H = 5D$ and $W = 40D$. Mechanical parameters: $\mu_{gg} = 0.33$ and $e = 0.972$.

Volume fraction profiles

Figure 5.9 presents the vertical and transverse profiles of the packing fraction for various μ_{gw} and two inclination angles ($\theta = 25$ and 45°). At $\theta = 25^\circ$, we have a roll flow (R^-) and at

$\theta = 45^\circ$) a supported flow (CR^-). The packing fraction is weakly dependent of μ_{gw} both at $\theta = 25^\circ$ (dashed lines) and at $\theta = 45^\circ$ (solid lines).

Velocity profiles

Figure 5.10 presents the vertical and transverse profiles of the stream-wise velocity $V' = V - V_{b,w}$ for the same flows as those displayed in the previous figure. When we subtract the sliding velocity to the profiles, they are almost invariant with μ_{gw} . The major effect of the wall friction is to alter the sliding velocity which increases with decreasing μ_{gw} .

Granular temperature profiles

Figure 5.11 displays the vertical and transverse profiles of the granular temperature corresponding to the flows shown in Figs 5.9 and 5.10. The granular temperature generally decreases with increasing wall friction. This decrease is clearly visible at $\theta = 45^\circ$. It exists also at $\theta = 25^\circ$ but it is not visible on the graph because the temperature scale is not appropriate. We can note also that the decrease is more pronounced at the walls.

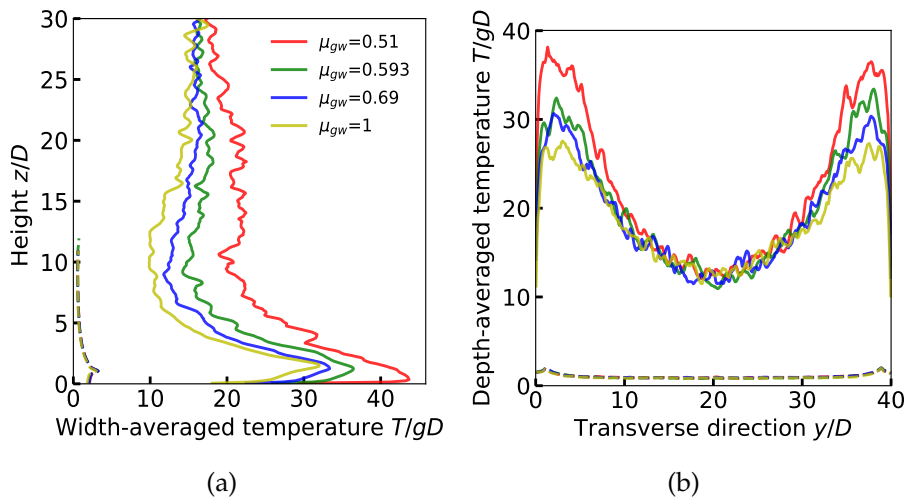


Figure 5.11: Vertical (a) and transverse (b) profiles of the granular temperature for various μ_{gw} and two inclination angles: $\theta = 25^\circ$ and $H = 5D$ (dashed lines, roll regime), and $\theta = 45^\circ$ and $H = 5D$ (solid lines, supported regime). $W = 40D$. Mechanical parameters: $\mu_{gg} = 0.33$ and $e = 0.972$.

3.4 Packing fraction, velocity and temperature profiles vs μ_{gg}

We finally discuss on the influence of the particle friction on the flow structure.

Volume fraction profiles

Figure 5.12 presents the vertical and transverse profiles of the packing fraction for various μ_{gg} and two inclination angles ($\theta = 25$ and 45°).

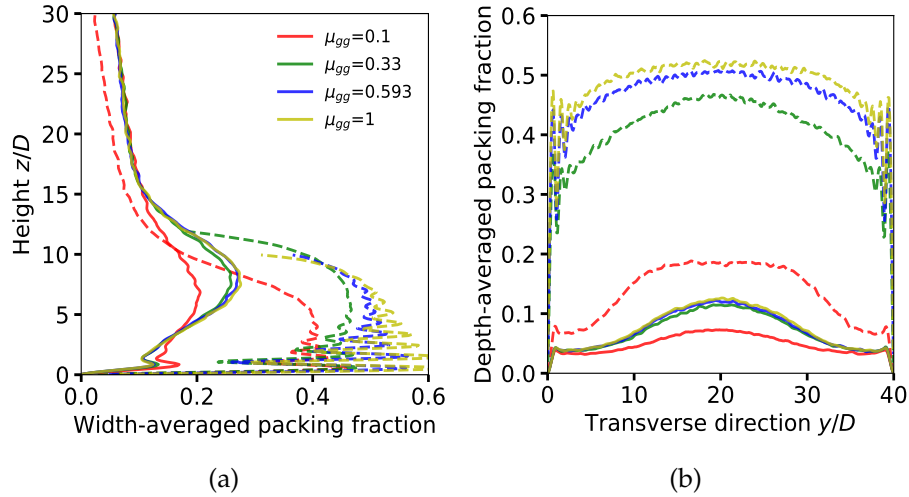


Figure 5.12: Vertical (a) and transverse (b) profiles of the packing fraction for various μ_{gg} at two different inclinations: $\theta = 25^\circ$ and $H = 5D$ (dashed lines), and $\theta = 45^\circ$ and $H = 5D$ (solid lines, CR^-). $W = 40D$. Mechanical parameters: $\mu_{gw} = 0.593$ and $e = 0.972$.

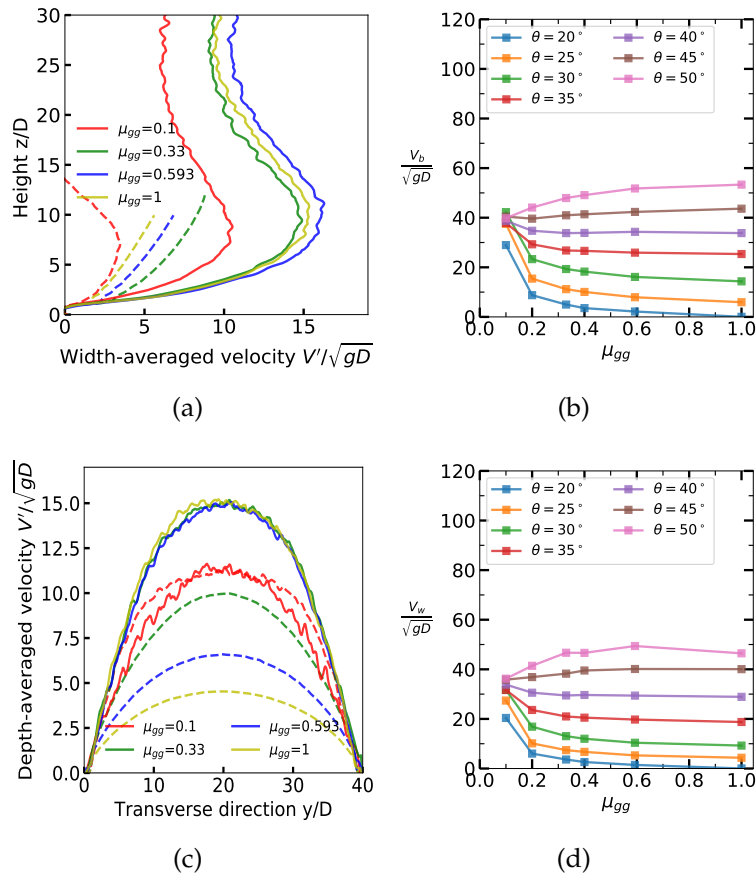


Figure 5.13: (a) Vertical and (c) transverse profiles of the stream-wise flow velocity $V' = V - V_{b,w}$ for various μ_{gg} and two angles $\theta = 25^\circ$ (dashed lines) and $\theta = 45^\circ$ (solid lines). (b) and (d) corresponding slip velocity V_b and V_w . $H = 5D$ and $W = 40D$. Mechanical parameters: $\mu_{gw} = 0.593$ and $e = 0.972$.

At $\theta = 45^\circ$, we have supported flows, while at $\theta = 25^\circ$ we have roll flows except at very low friction where we enter a WCR^- flow, a supported-like flow with a dense core lying on the bottom like a non-wetting drop.

At $\theta = 25^\circ$, the packing fraction increases with increasing μ_{gg} . The situation is different at higher angles where supported flows exist. The packing fraction profiles are almost unchanged when the friction is decreased. However, for a very small friction (i.e., $\mu_{gg} = 0.1$) we observe a significant change which however does not alter the nature of the flow regime. The low friction case seems to be singular and will be discussed in more details later on.

Velocity profiles

Figure 5.13 displays the vertical and transverse profiles of the stream-wise velocity $V' = V - V_{b,w}$ for the same flows as those displayed in the previous figure. When we subtract the sliding velocity to the profiles, the latter remains almost unchanged as long as the particle friction is not too weak. For $\mu_{gg} = 0.1$, we observe a significant change of the profiles both at $\theta = 25^\circ$ and 45° . As previously mentioned, the evolution of the sliding velocity with μ_{gg} is not monotonic. The sliding velocity decreases with increasing friction for inclinations smaller than 40° but a reversed trend is observed at high angle. At the moment, we do not have a clear explanation for this cross-over.

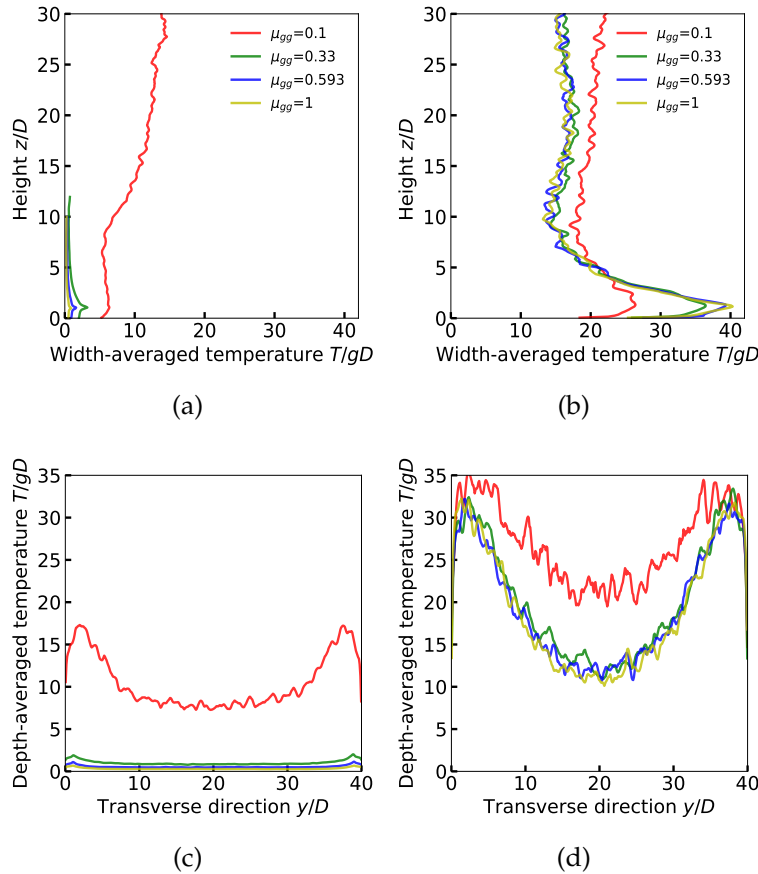


Figure 5.14: Vertical (a and b) and transverse (c and d) profiles of the granular temperature for various e . (a) and (c): $\theta = 25^\circ$ and $H = 5D$; (b) and (d): $\theta = 45^\circ$ and $H = 5D$ (supported regime). $W = 40D$. Mechanical parameters $e = 0.972$, and $\mu_{gw} = 0.593$.

Granular temperature profiles

Figure 5.14 presents the vertical and transverse profiles of the granular temperature corresponding to the flows shown in Figs 5.12 and 5.13. The granular temperature is expected

to increase with decreasing particle friction. At $\theta = 25^\circ$, the temperature increases with decreasing μ_{gg} . This increase is moderate as long as the particle friction is greater or equal to 0.33. In contrast, as the particle friction is decreased to 0.1, we see a significant increase of the granular temperature. At $\theta = 45^\circ$, there is almost no variation as long as the particle friction is greater or equal to 0.33. When $\mu_{gg} = 0.1$, the temperature increase is localized in the upper zone, where the packing fraction decreases with z . Surprisingly, the temperature clearly decreases in the lower dense part, where the packing fraction is uniform and at its maximum.

Low particle friction case $\mu_{gg} = 0.1$

In the previous discussion, we observed that the low friction case ($\mu_{gg} = 0.1$) leads drastic changes in the flow structure and the emergence of a new regime WCR^- with a dense core wetting the bottom wall. Here we will study how the flow structure changes for increasing angle when the particle friction is set to 0.1.

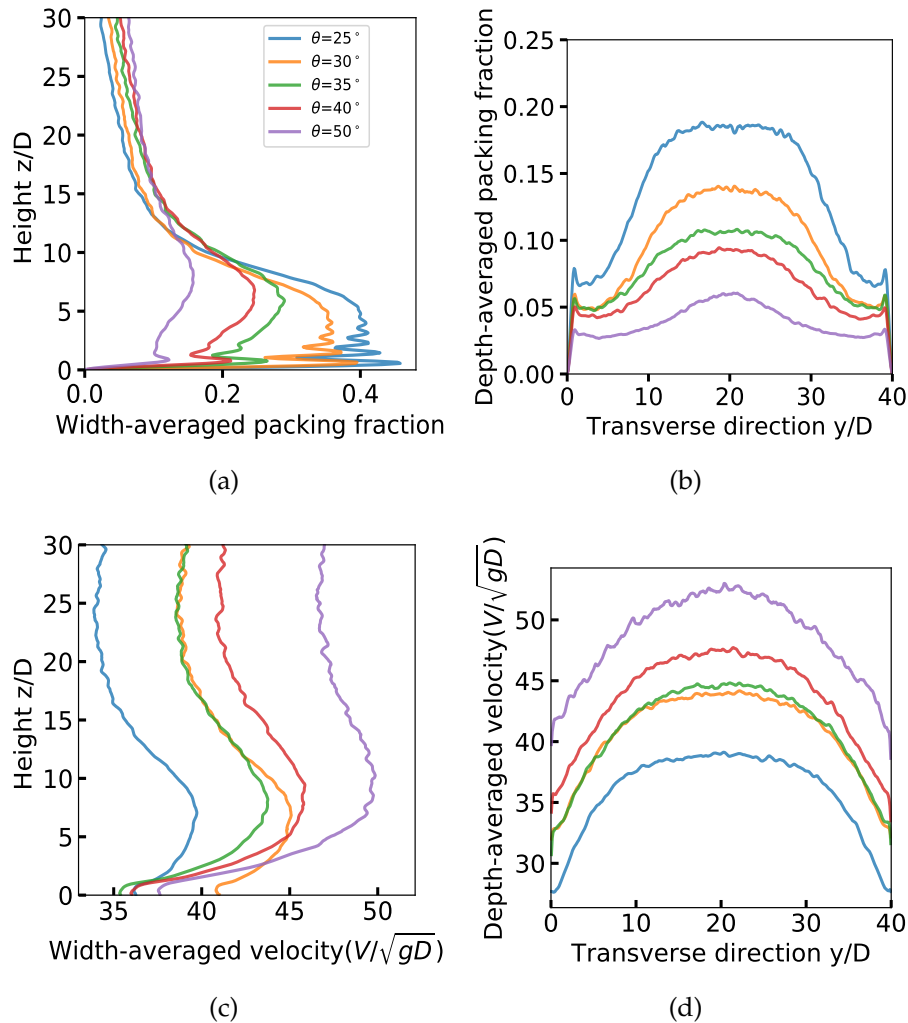


Figure 5.15: Vertical (a and c) and transverse (b and d) profiles of the packing fraction and stream-wise velocity for increasing inclination angles. $H = 5D$ and $W = 40D$. Mechanical parameters: $\mu_{gg} = 0.1$, $e = 0.972$, and $\mu_{gw} = 0.593$.

Figure 5.15 presents vertical and transverse profiles of the packing fraction and stream-

wise velocity for increasing inclination angles with $\mu_{gg} = 0.1$. Generally, the velocity always increases monotonically with increasing angle. Here, this is not the case. First, the velocity increases from 25° to 30° , decreases from 30° to 35° and then monotonically increases for angles greater than 40° . The velocity decrease from 30° to 35° coincides with the detachment of the dense core from the bottom wall. At the moment, we do not have identified the mechanisms which could explain these observations.

3.5 Cross-influence of the mechanical parameters

Here, we study the cross-influence of the mechanical parameters. e is set to the standard value and we vary both the particle and wall friction coefficient as illustrated in Fig. 5.16. We saw that when we vary the particle friction μ_{gg} , we have a change of behaviour above a critical angle where the velocity increases with increasing particle friction. This cross-over regime was found at $\theta = 40^\circ$ when e and μ_{gw} are set to the standard values. It is clearly identified as the locus where the iso-particle friction curves $V_L(\theta)$ cross as shown in Fig. 5.16.a. Fig. 5.16.b indicates that the cross-over regime is shifted to higher angles as μ_{gw} increases. Again, we do not have explanation for this but this illustrate that the cross-variation of the mechanical parameters have non-trivial effects on the nature and velocity of the flow regime.

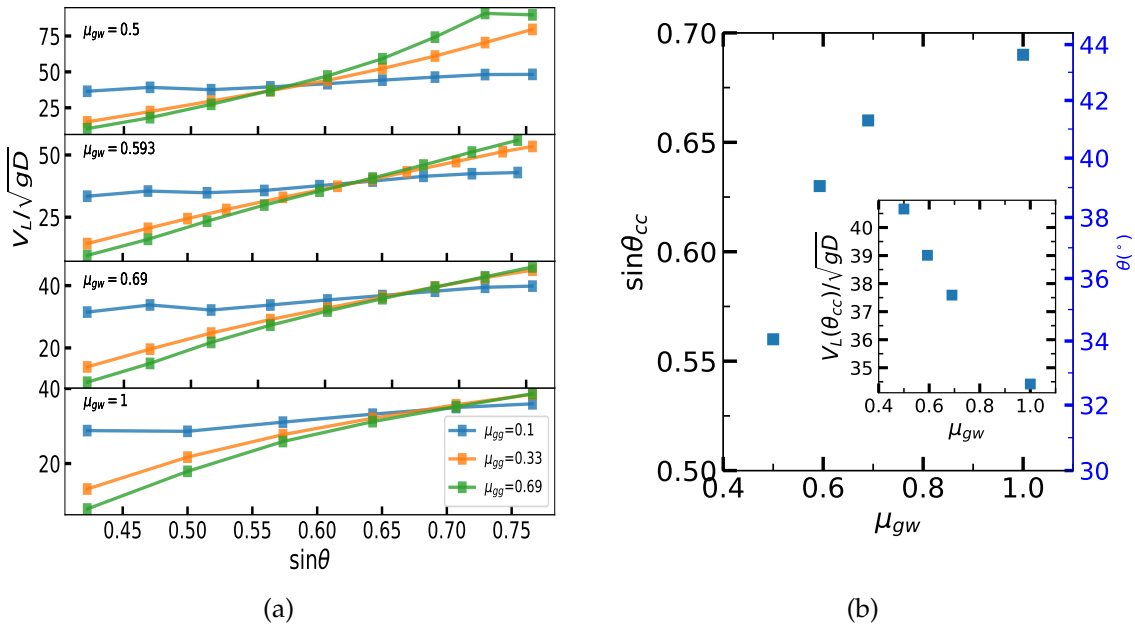


Figure 5.16: (a) V_L as a function of inclination angles for cross-variations of the particle and wall friction coefficient. $e = 0.972$, $H = 5D$ and $W = 40D$. (b) Critical inclination angle of the cross-over regime as a function of μ_{gw} . Inset: corresponding flow velocity at the cross-over regime.

4 Friction and packing fraction laws

Here we want to know whether the friction and packing fraction laws, $\mu_{b,w}(Fr_{b,w})$ and $\phi_{b,w}(Fr_{b,w})$, still holds when we vary the mechanical parameters and if so, how their shape are modified.

4.1 Local effective friction law

Figure 5.17 presents the local basal and lateral friction as a function of the local Froude number for varying restitution coefficient e . As already mentioned in the preceding chapter, for each value of e , the data still collapse on a master curve which do not differ much from that obtained with the standard value of the restitution coefficient (solid line). It thus indicates that particle-particle coefficient restitution has no effect on the effective wall friction and confirms that the effective friction law encodes the local interaction between the wall and the particle. We expect a different story with μ_{gw} .

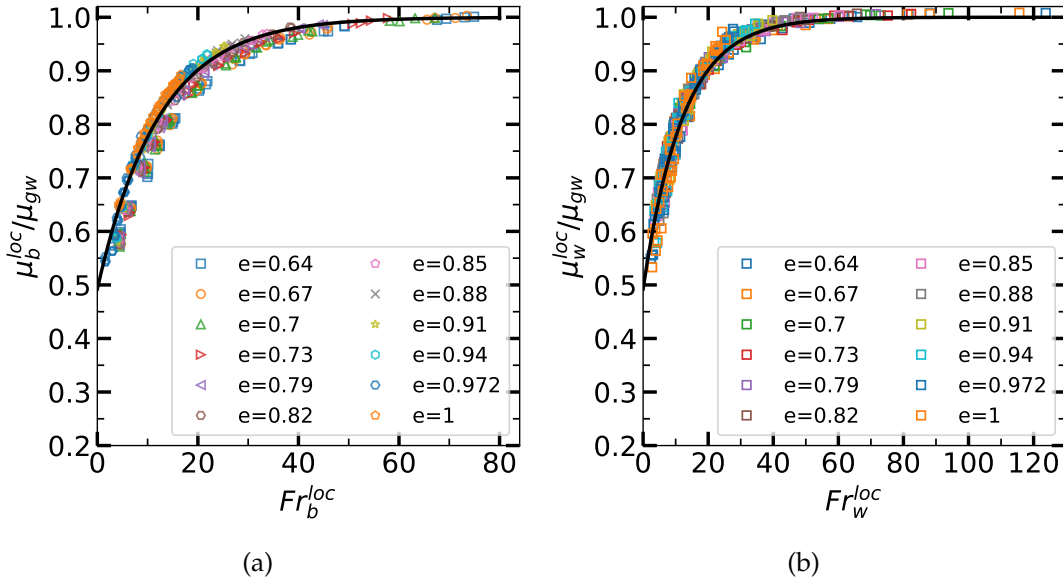


Figure 5.17: Local effective basal (a) and lateral (b) friction as a function of the local Froude number for various coefficient of restitution ranging from 0.64 to 1: (a) μ_b^{loc}/μ_{gw} vs Fr_b^{loc} and (b) μ_w^{loc}/μ_{gw} vs Fr_w^{loc} . Mechanical parameters: $\mu_{gw} = 0.593$ and $\mu_{gg} = 0.33$. The solid line corresponds to the fit obtained for the standard values of the mechanical parameters using the following form: $\mu_{b,w}^{loc} = \mu_2 + (\mu_1 - \mu_2) \exp(-Fr_{b,w}^{loc}/Fr_{\mu_0})$ with $\mu_1 = 0.29$, $\mu_2 = 0.59$ and $Fr_{\mu_0} = 12.2$

We recall that the local wall friction law is well captured by the following exponential law:

$$\mu_{b,w}^{loc} = \mu_1^{loc} + (\mu_2^{loc} - \mu_1^{loc}) \exp(-Fr/ Fr_{\mu_0}^{loc}) \quad (5.1)$$

where μ_1^{loc} , μ_2^{loc} and Fr_{μ_0} are fitting parameters. μ_1^{loc} is the minimum friction while μ_2^{loc} is the asymptotic value of the friction obtained at large Froude number. The previous results indicate that the fitting parameters of the law are independent of the particle-particle coefficient restitution e . We find: $\mu_1^{loc} = 0.29$, $\mu_2^{loc} = \mu_{gw}$ and $Fr_{\mu_0} = 12.2$.

Figure 5.18 displays the local basal and lateral friction as a function of the local Froude number for increasing particle-wall friction coefficient μ_{gw} . For a given μ_{gg} , the data still collapse on a master curve which differ from that obtained with the standard value of the particle-wall friction. The asymptotic value μ_2^{loc} is changed as expected and is roughly equal to the microscopic value of the particle-wall friction μ_{gw} . The minimal friction value μ_1^{loc} is however invariant when changing μ_{gw} : $\mu_1^{loc} \approx 0.29$. The characteristic Froude number Fr_{μ_0} is found to increase with increasing μ_{gw} from 10 to 30.

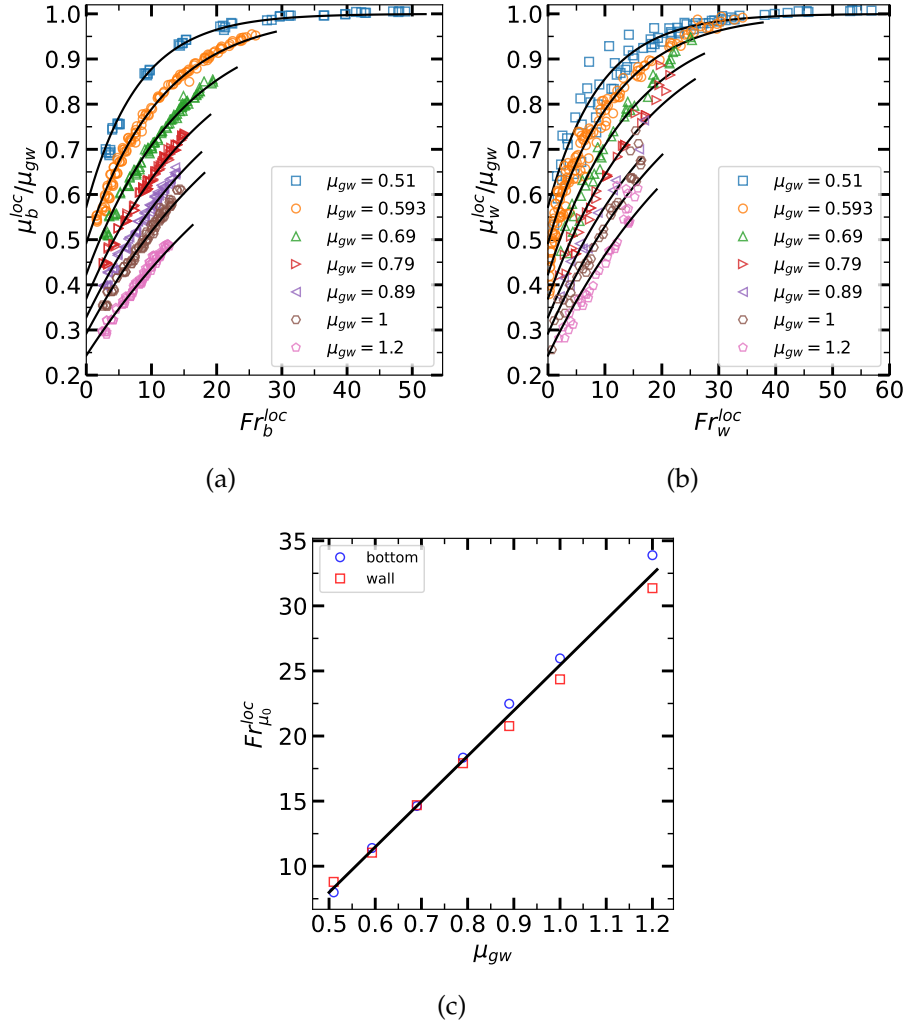


Figure 5.18: Local effective basal (a) and lateral (b) friction as a function of the local Froude number for various wall-particle friction coefficient ranging from 0.51 to 1.2: (a) μ_b^{loc}/μ_{gw} vs Fr_b^{loc} and (b) μ_w^{loc}/μ_{gw} vs Fr_w^{loc} . The solid lines corresponds to the best fit using Eq. 5.1. The best fits gives: $\mu_1^{loc} = 0.292$, $\mu_2^{loc} = \mu_{gw}$ and $Fr_{\mu_0}^{loc} \approx 35(\mu_{gw} - 0.3)$. (c) Variation of $Fr_{\mu_0}^{loc}$ with μ_{gw} . Other Mechanical parameters: $\mu_{gg} = 0.33$ and $e = 0.972$.

Finally, changing the particle-particle friction leads to modification of the local wall friction law (see Fig. 5.19). The change of the law is seen only through the minimum friction coefficient μ_1^{loc} which increases from 0.25 to 0.35 when μ_{gg} is varied from 0.2 to 1. For very weak value of the particle-wall friction ($\mu_{gg} = 0.1$), the collapse on a master curve remains uncertain.

4.2 Global effective friction law

We also checked that the global effective friction law holds as well when the mechanical parameters are changed. We recall that for the global law, the effective friction and the Froude number are calculated at the scale of the entire wall. We find the same evolution of the global friction law with the mechanical parameters as for the local one. The data can be reasonably well described with a similar exponential law:

$$\mu_{b,w} = \mu_1 + (\mu_2 - \mu_1) \exp(-Fr/Fr_{\mu_0}) \quad (5.2)$$

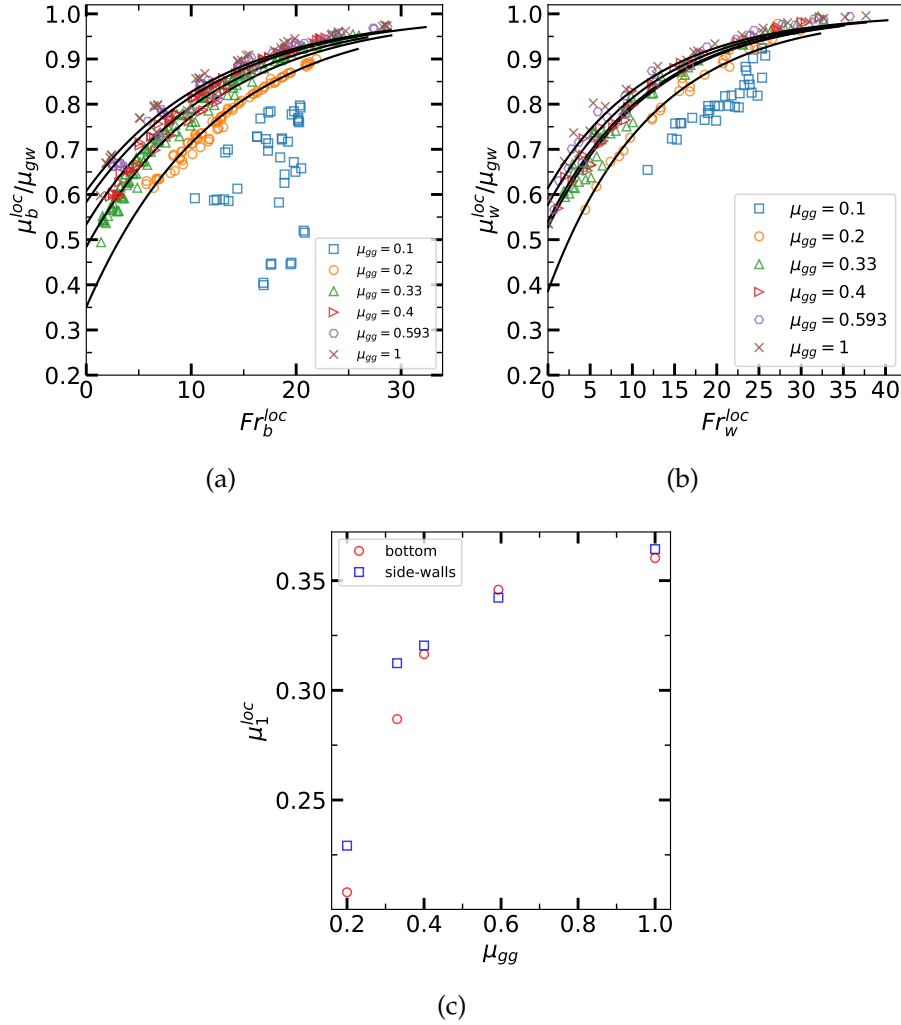


Figure 5.19: Local effective basal (a) and lateral (b) friction as a function of the local Froude number for different particle-particle friction coefficient ranging from 0.1 to 1: (a) μ_b^{loc}/μ_{gw} vs Fr_b^{loc} and (b) μ_w^{loc}/μ_{gw} vs Fr_w^{loc} . The solid lines corresponds to the best fit using Eq. 5.1. The best fits give: μ_1^{loc} ranging from 0.2 to 0.35, $\mu_2^{loc} = \mu_{gw} = 0.593$ and $Fr_{\mu_0}^{loc} = 12.2$. (c) Variation of $Fr_{\mu_0}^{loc}$ with μ_{gg} . Other mechanical parameters: $\mu_{gw} = 0.593$ and $e = 0.972$.

where μ_1 and Fr_{μ_0} are fitting parameters depending on the mechanical parameters. μ_2 represents the asymptotic value of the friction and is bounded by the microscopic value of the particle-wall friction such $\mu_2 = \mu_{gw}$.

Fig. 5.20 displays the evolution of the global effective bottom friction μ_b as a function of the local Froude number Fr_b when e , μ_{gw} and μ_{gg} are varied successively. The variation of the fitting parameters μ_1 and Fr_{μ_0} with the mechanical parameters are illustrated in Fig. 5.21.

As a summary, e does not alter the friction law, while μ_{gw} essentially acts on the asymptotic value μ_2 but also on the characteristic Froude number Fr_{μ_0} . Concerning the influence of μ_{gg} , it modifies the minimum value μ_1 of the friction.

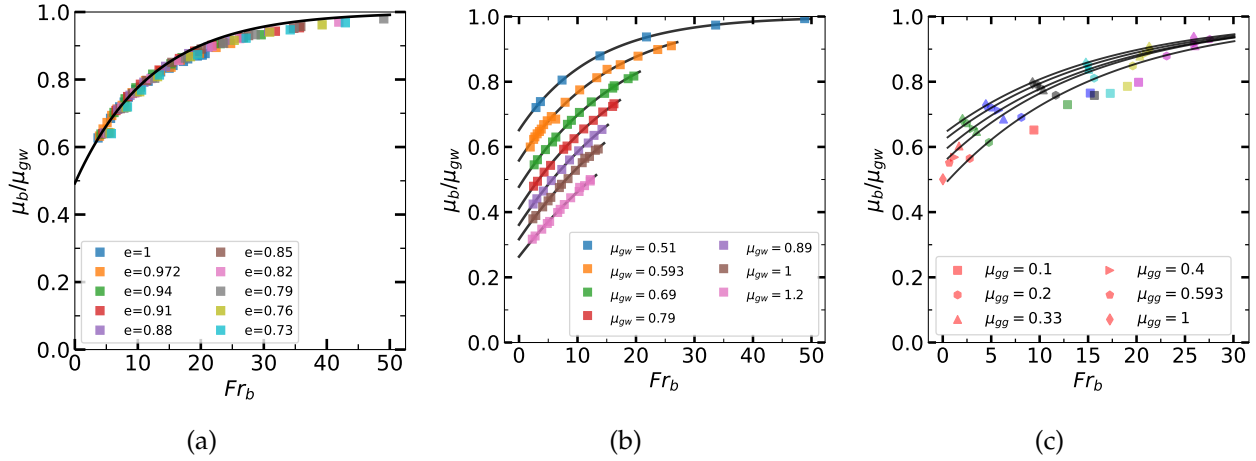


Figure 5.20: Global effective bottom friction law as a function of the global Froude number $Fr_b = V_b / \sqrt{gH \cos \theta}$ for varying mechanical parameters: (a) Varying e ; (b) Varying μ_{gw} and (c) varying μ_{gg} . The solid lines are fits of the form: $\mu_b = \mu_2 + (\mu_1 - \mu_2) \exp(-Fr_b / Fr_{\mu_0})$ with $\mu_2 = \mu_{gw}$. (a) $\mu_1 = 0.292$ and $Fr_{\mu_0} = 12.2$, (b) $\mu_1 \approx 0.3$ and Fr_{μ_0} increases from 10 to 50 with increasing μ_{gw} ; (c) μ_1 increases from 0.3 to 0.4 with increasing μ_{gg} (see details in Fig. 5.21).

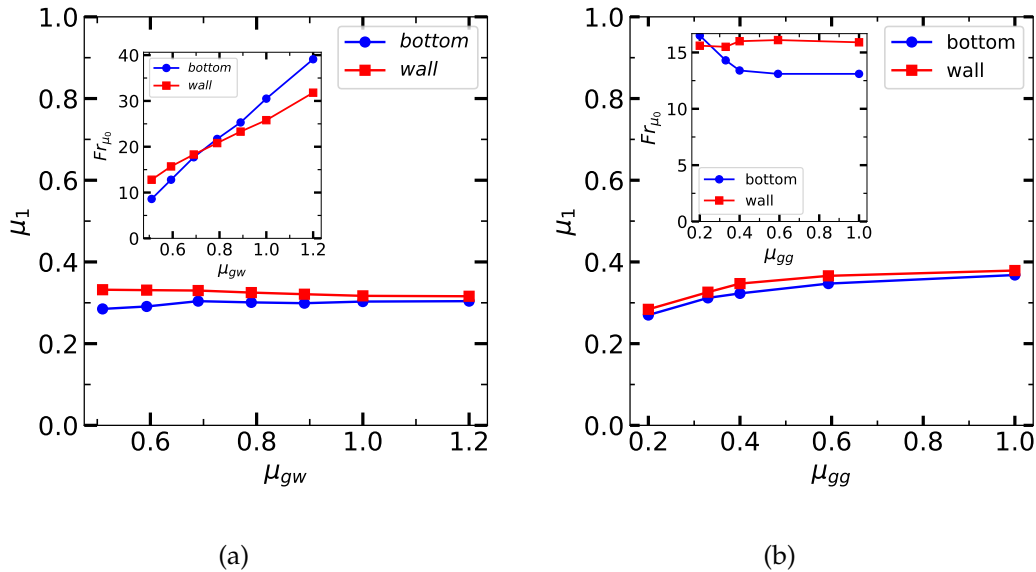


Figure 5.21: Fitting parameters μ_1 and Fr_{μ_0} as a function of μ_{gw} (a) and μ_{gg} (b). Mechanical parameters: (a) $e = 0.972$ and $\mu_{gg} = 0.33$; (b) $e = 0.972$ and $\mu_{gw} = 0.593$.

4.3 Packing fraction law

In chapter 3, we provided a local packing fraction law, $\phi_{b,w}^{loc}(Fr_{b,w}^{loc})$, which was robust and invariant with the channel width. Here we want to know how this law is affected when the mechanical parameters e , μ_{gw} and μ_{gg} are varied.

Figure 5.22 presents the local bottom packing fraction as a function of the local Froude number. The local side-wall friction (not shown here) exhibits the same behaviour. As for the effective wall friction, the packing fraction at the wall can be approximated by the following

exponential law:

$$\phi_{b,w}^{loc} = \phi_1^{loc} + (\phi_2^{loc} - \phi_1^{loc}) \exp\left(-Fr/Fr_{\phi_0}^{loc}\right) \quad (5.3)$$

where ϕ_1^{loc} , ϕ_2^{loc} and $Fr_{\phi_0}^{loc}$ are fitting parameters that depends a priori on the mechanical parameters e , μ_{gw} and μ_{gg} .

The data reveal that e and μ_{gw} have a significant effect on the packing fraction law while the influence of μ_{gg} is rather weak. At a given Froude number, decreasing e (i.e., increasing the dissipation) leads to larger packing fraction at the wall. In contrast, increasing the wall-particle friction μ_{gw} results in smaller packing fraction. These contrasting behaviours may be one of the possible causes explaining why the mean flow velocity increases with increasing particle-particle dissipation but decreases with increasing wall-particle friction.

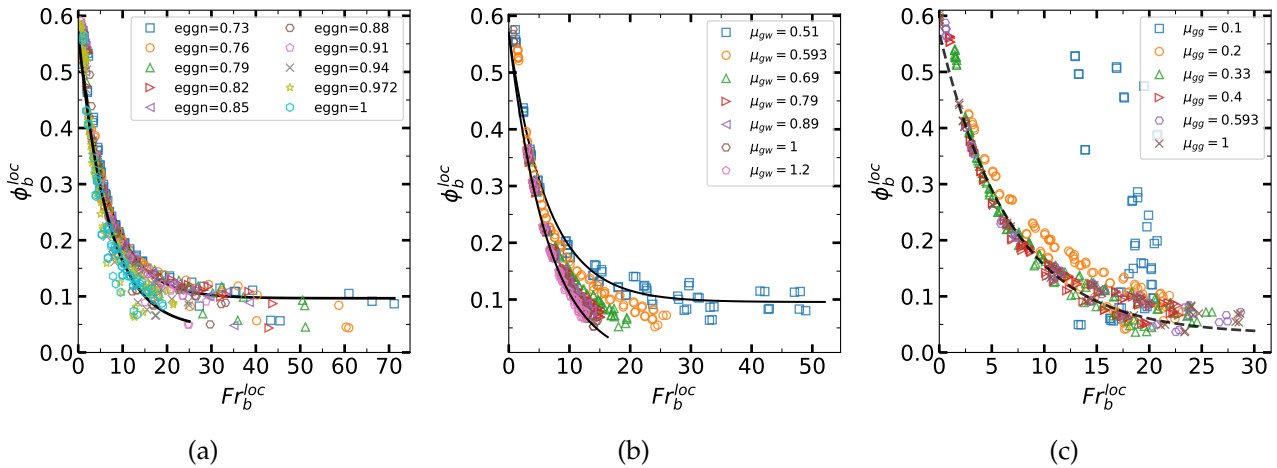


Figure 5.22: Local packing fraction at the wall ϕ_b^{loc} as a function of the local Froude number $Fr_b^{loc} = V_b^{loc} / \sqrt{P_b^{loc} / \rho}$ for various e (a), μ_{gw} (b) and μ_{gg} (c). The solid lines are the best fits using Eq. 5.3. Only the data corresponding to the two limit values of the range of variation of the mechanical parameters are adjusted. Fitting parameters: ϕ_1^{loc} and $Fr_{\phi_0}^{loc}$ are almost invariant with e , μ_{gw} and μ_{gg} ($\phi_1^{loc} \approx 0.57$ and $Fr_{\phi_0}^{loc} \approx 6.8$); ϕ_2^{loc} depends both on e and μ_{gw} but not on μ_{gg} (see Fig. 5.23).

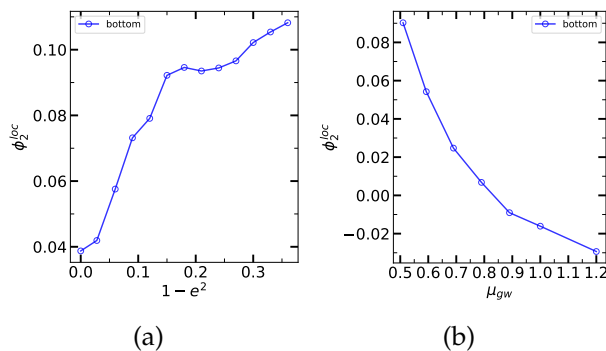


Figure 5.23: Variation of the fitting parameter ϕ_2^{loc} with $(1 - e^2)$ (a) and μ_{gw} (b).

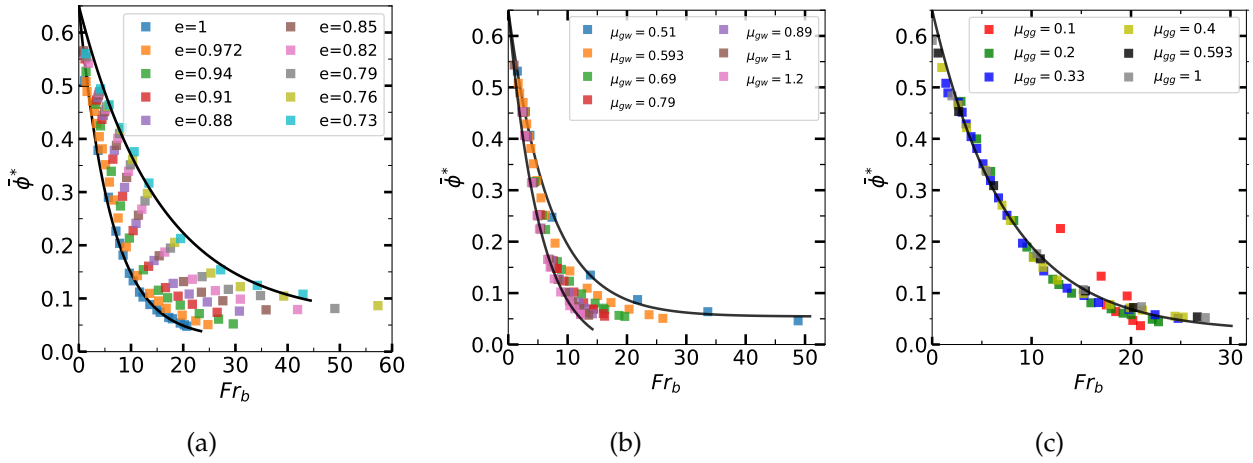


Figure 5.24: Mean packing fraction $\bar{\phi}^*$ as a function of the global Froude number $Fr_b = V_b / \sqrt{gH \cos \theta}$ for various e (a), μ_{gw} (b) and μ_{gg} (c). The solid lines are the best fits using Eq. 5.3. Only the data corresponding to the two limit values of the range of variation of the mechanical parameters are adjusted. Fitting parameters: ϕ_1 is invariant with e , μ_{gw} and μ_{gg} ($\phi_1 \approx 0.65$). In contrast, ϕ_2 and Fr_{ϕ_0} depends on e and μ_{gw} but not on μ_{gg} . For (c): $\phi_2 \approx 0.025$ and $Fr_{\phi_0} \approx 7.5$.

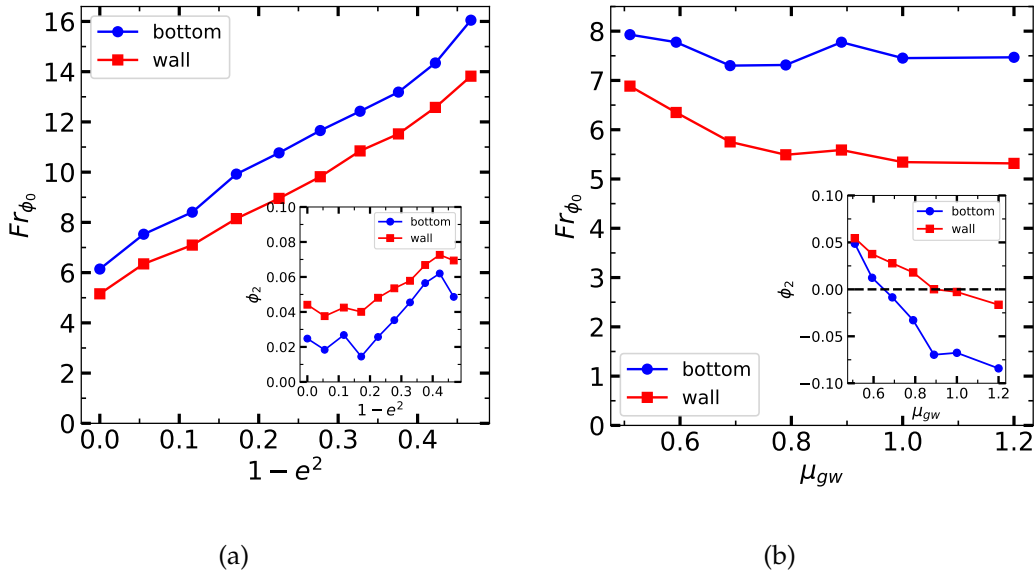


Figure 5.25: Variation of the fitting parameters ϕ_2 and Fr_{ϕ_0} with $1 - e^2$ (a) and μ_{gw} (b).

We observe the same trends for the global law, $\bar{\phi}^*$ versus the global basal Froude Fr_b , as illustrated in Fig. 5.24.

4.4 Effective frictional flow height Z

In chapter 3, we determined a law for the effective frictional height Z as a function the mean flow packing fraction $\bar{\phi}^*$. We saw that this law robust to change of gap widths.

We show here that the law for the effective frictional flow height is also robust when we vary the mechanical parameters e , μ_{gw} and μ_{gg} . The robustness of the law is illustrated in Fig. 5.26.

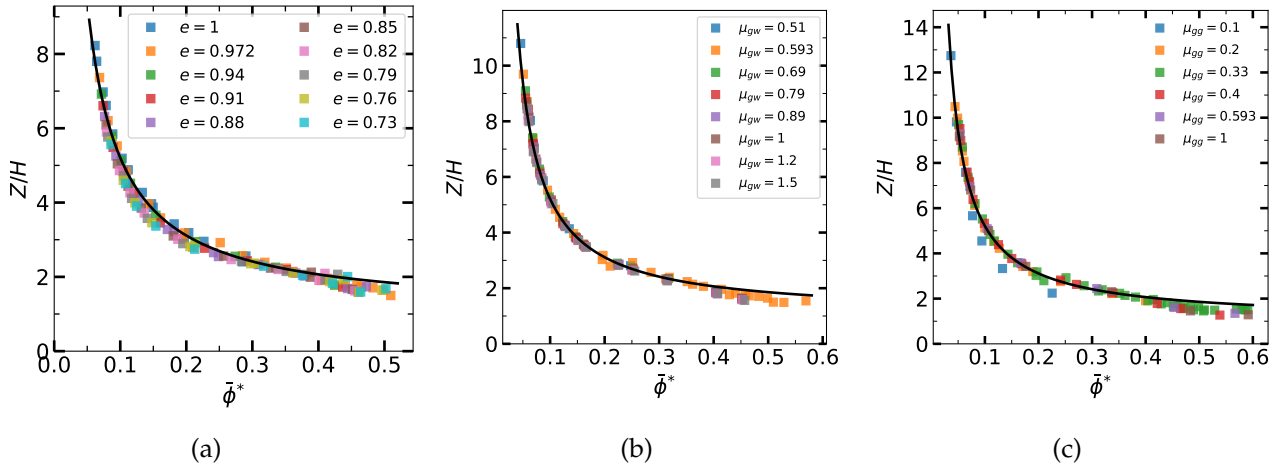


Figure 5.26: Rescaled effective frictional height Z/H as a function of the mean flow packing fraction $\bar{\phi}^*$ for various e (a), μ_{gw} (b) and μ_{gg} (c). Solid curve: $Z/H = (1 + (\bar{\phi}^* - 0.57)) / \bar{\phi}^*$.

5 Conclusion

In this chapter, we completed the study of the role of the mechanical parameters. We studied in details the effect of e , μ_{gw} and μ_{gg} on the structural properties of the flow, the mean flow velocity and also on the friction and packing fraction laws.

We found contrasting effects. e and μ_{gw} have a monotonic influence on the mean flow velocity. Increasing e or μ_{gw} leads to a diminution of the flow velocity. This is not the case for μ_{gg} . We indeed a cross-over regime characterized by a critical angle. Below it, the mean flow velocity decreases with increasing particle friction, while above it, the reverse trend is observed.

We also highlighted that the flow features at the wall can be described by simple laws, in particular the wall friction and packing fraction. We showed that these laws are robust when changing the mechanical parameters. Only their form is sensitive to changes of e , μ_{gw} and μ_{gg} .

Finally, we confirm that the effective frictional flow height Z when rescaled by H obeys a universal law as a function of the mean flow packing fraction. This law is independent on the gap width and on the microscopic mechanical parameters. It strongly suggests that this law should result from a conservation equation we have not yet identified.

Lastly, the set of the three laws, $\mu_{b,w}(Fr_{b,w})$, $\bar{\phi}^*(Fr_b)$ and Z/H versus $\bar{\phi}^*$, combined with the force balance equation (i.e., $\tan \theta = \mu_b(Fr_b) + \mu_w(Fr_w) \frac{Z}{W}$) should help us in understanding how the mean flow velocity varies with the mechanical parameters of the granular system. This is a future line of investigation.

Note also that we restrained our analysis to flows with a given mass hold-up ($H = 5D$), so we were not able to determine how the scaling law of the mean flow velocity with H is affected by changes of the mechanical parameters. This will be a future study.

Chapter 6

Conclusion and perspectives

1 Conclusion

In this thesis, we investigated rapid granular flows confined between two flat lateral walls by exploring extensively and systematically the parameter space $H - \theta$ for various channel widths $W = 20, 40, 60, 68, 75$, and $140D$, and the parameter spaces $e - \theta$, $\mu_{gw} - \theta$, and $\mu_{gg} - \theta$ for two different channel widths ($W = 20D$ and $W = 40D$). A reach variety of flow regimes were uncovered, including flows with pairs of longitudinal vortices (i.e., R^+ , R^- , R_+^-), supported flows (CR^- , CR_+^- and ACR^-) and oscillating supported flows (OCR^-).

Among these flow regimes, "supported" flows are ubiquitous. Under prescribed mechanical parameters, there is a minimum channel width below which supported flows non longer exist. In contrast, we did not find an upper limit in gap width above which the supported flows would disappear. In other words, side-walls confinement is probably not the cause of the existence of "supported" flow regime, but it is clearly the cause of its disappearance. For the standard values of the mechanical parameters ($e = 0.972$, $\mu_{gg} = 0.33$ and $\mu_{gw} = 0.593$), the minimum gap width is found to be about $20D$. This critical value can be however lowered if, for example, the dissipation in the particle collision is increased.

We uncovered that supported flows obey a simple scaling law with the particle hold-up H and the gap width W : $V_L - V_L^c \propto W^{0.7} H^{0.3}$, where V_L^c is the critical velocity of the appearance of the supported flows. For a given gap width, the supported flows emerges above a critical angle θ_c that decreases with increasing gap width. For $W = 40D$, $\theta_c \approx 26.5^\circ$ while for $W = 140D$, $\theta_c \approx 23.5^\circ$.

Importantly, for these rapid flows, the mean velocity is essentially controlled by the sliding velocity so that both velocities are strongly correlated. It thus appears that understanding how the sliding velocity evolves with H , θ and W is a crucial issue. We consequently studied in details the evolution of the flow features at the bottom and lateral walls.

We evidenced that the local effective wall friction $\mu_{b,w}^{loc}$ and the local packing fraction at the walls $\phi_{b,w}^{loc}$ can be both described by a unique curve (for a fixed set of mechanical parameters) that depends solely of the Froude number defined as $V_{b,w} / \sqrt{P_{b,w} / g}$ as:

$$\mu^{loc} = \mu_2^{loc} + (\mu_1^{loc} - \mu_2^{loc}) \exp\left(-\frac{Fr^{loc}}{Fr_{\mu_0}}\right) \quad (6.1)$$

$$\phi^{loc} = \phi_2^{loc} + (\phi_1^{loc} - \phi_2^{loc}) \exp\left(-\frac{Fr^{loc}}{Fr_{\phi_0}}\right) \quad (6.2)$$

where μ_1^{loc} , μ_2^{loc} , $Fr_{\mu_0}^{loc}$, ϕ_1^{loc} , ϕ_2^{loc} , and $Fr_{\phi_0}^{loc}$ are fitting parameters. These laws have been

established for steady flows but we showed that they hold as well for unsteady flows.

Importantly, we found that these laws are robust to changes of the particle and wall mechanical properties. Only, the fitting parameters of these laws are affected by such changes. We studied extensively how the exact form of these laws are modified when we vary successively e , μ_{gw} and μ_{gg} . We showed that e has a very weak effect on the friction law whereas changes of μ_{gg} and μ_{gw} have a quantitative effect on the fitting parameters of the friction law. These changes were not fully understood and demand to be further analyzed by cross-variations of the mechanical parameters.

We also investigated how the mean flow evolves when we vary the mechanical parameters. We found complex evolutions. While increasing the particle-wall friction coefficient μ_{gw} leads to an expected decrease of the mean velocity, increasing the particle-particle restitution coefficient e results in a surprising augmentation of the mean flow velocity, explained by the contraction of the flow and the subsequent reduction of the contribution of the wall friction. The effect of the coefficient of friction between grains is even more subtle: we found that there is a critical inclination below which the mean flow velocity decreases with increasing μ_{gg} and above which the trend is reserved. This critical inclination depends essentially on μ_{gw} . These variations of the mean velocity are essentially caused by changes of the sliding velocity and may be useful to guide practical researches for determining the optimum condition to minimize the energy dissipation during the transportation of granular materials.

We strongly believe that the local friction and packing fraction law may be used successfully as a reliable boundary condition for flows running on smooth walls. In addition, we uncovered that the rescaled frictional flow height Z/H obeys a universal law as a function of the mean packing fraction $\bar{\phi}^*$:

$$\frac{Z}{H} = \frac{1 + (\bar{\phi}^* - 0.57)}{\bar{\phi}^*} \quad (6.3)$$

This law is independent of the inclination angle, gap width and of the mechanical parameters.

Finally, we suggest that a phenomenological model can be built using the force balance equation,

$$\tan \theta = \mu(Fr) \left(1 + \frac{Z}{W}\right) \quad (6.4)$$

supplemented with the global version of the effective wall friction and packing friction law, $\mu(Fr)$ and $\bar{\phi}^*(Fr)$, and Eq. 6.3 for the frictional flow height Z . This model provides a set of closed equations to solve the Froude number, the mean packing fraction and the sliding velocity for prescribed inclination θ , particle hold-up H and gap width W .

2 Perspectives

We identified at least two important avenues for future researches: (i) To confirm the numerical findings in real experiments and ii) to extend these numerical outcomes to unsteady flows.

Both issues are actually strongly linked. Those rapid flows are difficult to be achieved in real experiments as steady and fully developed flows because it requires chute flows with long running distances. Therefore, experimental rapid flows are often observed in non-mature states. Thus, if we have a clear understanding of unsteady or non-uniform flows, it could greatly help the analysis and interpretation of rapid experimental flows.

We started to address these issues and present here some preliminary results. We confirmed that the friction and packing friction laws still hold for unsteady flows that are in the route towards the stationary state. During this transient where the flow has a finite but declining acceleration in course of time, the flow visits successive states that resemble steady states but are obtained at smaller inclination angles. In other words, at each time of its evolution, we can find a correspondence between the actual flow features and a steady state obtained at a smaller inclination. This finding is very important since it allows to get some information about steady state flows from unsteady or non-uniform flows.

We used this conclusion in our experimental research which is not reported in the manuscript because of lack of time but will be published in the near future. We were able to confirm several numerical findings and to give credits to the relevance of the wall and packing fraction laws. We also identified most of the flow regimes seen in the simulations: R^- , R^+ , CR^-

Other avenues of research would be interesting as well. We disregard small inclinations and large mass hold-up regime which would merit attention too. We also concentrate our efforts on what happens close to the boundary. The next step would be to investigate the rheology of these rapid flows and to determine whether the kinetic theory or the $\mu(I)$ rheology are relevant to describe some of internal features of the flow. Experimental researches on rapid flows are jeopardized by the lack of information about the internal flow structure and stresses. Effort should be made in the development of new experimental techniques to probe the interior of the flow because the classical imaging techniques are limited to the characterization of what happens at the wall and the free surface.

Bibliography

- C. Ancey. Dry granular flows down an inclined channel: Experimental investigations on the frictional-collisional regime. *Phys. Rev. E*, 65:011304, Dec 2001. doi: 10.1103/PhysRevE.65.011304. URL <https://link.aps.org/doi/10.1103/PhysRevE.65.011304>.
- C. Ancey, P. Coussot, and P. Evesque. A theoretical framework for granular suspensions in a steady simple shear flow. *Journal of Rheology*, 43(6):1673–1699, 1999. doi: 10.1122/1.551067. URL <https://doi.org/10.1122/1.551067>.
- R. Artoni, A. C. Santomaso, M. Go', and P. Canu. Scaling laws for the slip velocity in dense granular flows. *Phys. Rev. Lett.*, 108:238002, Jun 2012. doi: 10.1103/PhysRevLett.108.238002. URL <https://link.aps.org/doi/10.1103/PhysRevLett.108.238002>.
- D. A. Augenstein and R. Hogg. An experimental study of the flow of dry powders over inclined surfaces. *Powder Technology*, 19(2):205 – 215, 1978. ISSN 0032-5910. URL <http://www.sciencedirect.com/science/article/pii/0032591078800291>.
- R. A. Bagnold. Experiments on a gravity-free dispersion of large solid spheres in a newtonian fluid under shear. *Proceedings of the Royal Society of London. Series A. Mathematical and Physical Sciences*, 225(1160):49–63, 1954. doi: 10.1098/rspa.1954.0186. URL <https://royalsocietypublishing.org/doi/abs/10.1098/rspa.1954.0186>.
- O. Baran, D. Ertas, T. C. Halsey, G. S. Grest, and J. B. Lechman. Velocity correlations in dense gravity-driven granular chute flow. *Physical Review E*, 74(5), Nov 2006. ISSN 1550-2376. doi: 10.1103/physreve.74.051302. URL <http://dx.doi.org/10.1103/PhysRevE.74.051302>.
- T. Barker, D. Schaeffer, P. Bohorquez, and J. Gray. Well-posed and ill-posed behaviour of the $\mu(i)$ -rheology for granular flow. *Journal of Fluid Mechanics*, 779:794 – 818, 2015.
- W. Bi, R. Delannay, P. Richard, N. Taberlet, and A. Valance. Two- and three-dimensional confined granular chute flows: experimental and numerical results. *Journal of Physics: Condensed Matter*, 17(24):2457–2480, June 2005. doi: 10.1088/0953-8984/17/24/006. URL <https://hal.archives-ouvertes.fr/hal-01127765>.
- T. Börzsönyi, R. Ecke, and J. McElwaine. Patterns in flowing sand: Understanding the physics of granular flow. *Phys. Rev. Lett.*, 103:178302, Oct 2009. doi: 10.1103/PhysRevLett.103.178302. URL <https://link.aps.org/doi/10.1103/PhysRevLett.103.178302>.
- N. Brodu, P. Richard, and R. Delannay. Shallow granular flows down flat frictional channels: Steady flows and longitudinal vortices. *Phys. Rev. E*, 87:022202, Feb 2013. doi: 10.1103/PhysRevE.87.022202. URL <https://link.aps.org/doi/10.1103/PhysRevE.87.022202>.

- N. Brodu, R. Delannay, A. Valance, and P. Richard. New patterns in high-speed granular flows. *Journal of Fluid Mechanics*, pages 1–11, Apr. 2015. doi: 10.1017/jfm.2015.109. URL <https://hal.archives-ouvertes.fr/hal-01122926>.
- E. S. Calder, R. Lockett, R. S. J. Sparks, and B. Voight. Mechanisms of lava dome instability and generation of rockfalls and pyroclastic flows at Soufrière Hills Volcano, Montserrat. In *The Eruption of Soufrière Hills Volcano, Montserrat from 1995 to 1999*. Geological Society of London, 01 2002. ISBN 9781862390980. doi: 10.1144/GSL.MEM.2002.021.01.08. URL <https://doi.org/10.1144/GSL.MEM.2002.021.01.08>.
- F. da Cruz, S. Emam, M. Prochnow, J. Roux, and F. Chevoir. Rheophysics of dense granular materials: Discrete simulation of plane shear flows. *Phys. Rev. E*, 72:021309, Aug 2005. doi: 10.1103/PhysRevE.72.021309. URL <https://link.aps.org/doi/10.1103/PhysRevE.72.021309>.
- R. Delannay, M. Louge, P. Richard, N. Taberlet, and A. Valance. Towards a theoretical picture of dense granular flows down inclines. *Nature Materials*, Feb. 2007. doi: 10.1038/nmat1813. URL <https://doi.org/10.1038/nmat1813>.
- R. Delannay, A. Valance, A. Mangeney, O. Roche, and P. Richard. Granular and particle-laden flows: from laboratory experiments to field observations. *Journal of Physics D: Applied Physics*, 50(5):053001, jan 2017. doi: 10.1088/1361-6463/50/5/053001. URL <https://doi.org/10.1088%2F1361-6463%2F50%2F5%2F053001>.
- T. Drake. Structural features in granular flows. *Journal of Geophysical Research: Solid Earth*, 95(B6):8681–8696, 1990. doi: 10.1029/JB095iB06p08681. URL <https://agupubs.onlinelibrary.wiley.com/doi/abs/10.1029/JB095iB06p08681>.
- T. Drake. Granular flow: physical experiments and their implications for microstructural theories. *Journal of Fluid Mechanics*, 225:121–152, 1991. doi: 10.1017/S0022112091001994.
- J. Duran. Sables, poudres et grains. introduction à la physique des milieux granulaires. 01 1997.
- P. Eshuis, D. van der Meer, M. Alam, H. J. van Gerner, K. van der Weele, and D. Lohse. Onset of convection in strongly shaken granular matter. *Phys. Rev. Lett.*, 104:038001, Jan 2010. doi: 10.1103/PhysRevLett.104.038001. URL <https://link.aps.org/doi/10.1103/PhysRevLett.104.038001>.
- M. Farrell, C. K. K. Lun, and S. B. Savage. A simple kinetic theory for granular flow of binary mixtures of smooth, inelastic, spherical particles. *Acta Mechanica*, 63, 1986. doi: 10.1007/BF01182539. URL <https://doi.org/10.1007/BF01182539>.
- T. Faug, P. Childs, E. Wyburn, and I. Einav. Standing jumps in shallow granular flows down smooth inclines. *Physics of Fluids*, 27(7):073304, 2015. doi: 10.1063/1.4927447. URL <https://doi.org/10.1063/1.4927447>.
- Y. Forterre and O. Pouliquen. Longitudinal vortices in granular flows. *Phys. Rev. Lett.*, 86:5886–5889, Jun 2001. doi: 10.1103/PhysRevLett.86.5886. URL <https://link.aps.org/doi/10.1103/PhysRevLett.86.5886>.

- Y. Forterre and O. Pouliquen. Stability analysis of rapid granular chute flows: formation of longitudinal vortices. *Journal of Fluid Mechanics*, 467, 2002. doi: 10.1017/S0022112002001581.
- Y. Forterre and O. Pouliquen. Flows of dense granular media. *Annual Review of Fluid Mechanics*, 40(1):1–24, 2008. doi: 10.1146/annurev.fluid.40.111406.102142. URL <https://doi.org/10.1146/annurev.fluid.40.111406.102142>.
- C. Goujon, N. Thomas, and B. Dalloz-Dubrujeaud. Monodisperse dry granular flows on inclined planes: Role of roughness. *The European Physical Journal E*, 11, 2003. ISSN 1292-895X. doi: 10.1140/epje/i2003-10012-0. URL <https://doi.org/10.1140/epje/i2003-10012-0>.
- J. Heyman, P. Boltenhagen, R. Delannay, and A. Valance. Experimental investigation of high speed granular flows down inclines. *EPJ Web Conf.*, 140:03057, 2017. doi: 10.1051/epjconf/201714003057. URL <https://doi.org/10.1051/epjconf/201714003057>.
- A. Holyoake and J. McElwaine. High-speed granular chute flows. *Journal of Fluid Mechanics*, 710, 2012. doi: 10.1017/jfm.2012.331.
- P. JOP, Y. FORTERRE, and O. POULIQUEN. Crucial role of sidewalls in granular surface flows: consequences for the rheology. *Journal of Fluid Mechanics*, 541(-1):167, Oct 2005. ISSN 1469-7645. doi: 10.1017/s0022112005005987. URL <http://dx.doi.org/10.1017/S0022112005005987>.
- T. S. Komatsu, S. Inagaki, N. Nakagawa, and S. Nasuno. Creep motion in a granular pile exhibiting steady surface flow. *Phys. Rev. Lett.*, 86:1757–1760, Feb 2001. doi: 10.1103/PhysRevLett.86.1757. URL <https://link.aps.org/doi/10.1103/PhysRevLett.86.1757>.
- V. Kumaran and S. Bharathraj. The effect of base roughness on the development of a dense granular flow down an inclined plane. *Physics of Fluids*, 25(7):070604, 2013. doi: 10.1063/1.4812806. URL <https://doi.org/10.1063/1.4812806>.
- M. Louge and S. Keast. On dense granular flows down flat frictional inclines. *Physics of Fluids*, 13(5):1213–1233, 2001. doi: 10.1063/1.1358870. URL <https://doi.org/10.1063/1.1358870>.
- C. K. K. Lun, S. B. Savage, D. J. Jeffrey, and N. Chepuriniy. Kinetic theories for granular flow: inelastic particles in couette flow and slightly inelastic particles in a general flowfield. *Journal of Fluid Mechanics*, 140:223–256, 1984. doi: 10.1017/S0022112084000586.
- GDR MiDi. On dense granular flows. *The European Physical Journal E*, 14(4):341–365, Aug 2004. ISSN 1292-895X. doi: 10.1140/epje/i2003-10153-0. URL <https://doi.org/10.1140/epje/i2003-10153-0>.
- S. McNamara and W. R. Young. Inelastic collapse in two dimensions. *Phys. Rev. E*, 50:R28–R31, Jul 1994. doi: 10.1103/PhysRevE.50.R28. URL <https://link.aps.org/doi/10.1103/PhysRevE.50.R28>.
- S. Ogawa, A. Umemura, and N. Oshima. On the equations of fully fluidized granular materials. *Applied Mathematics and Physics (ZAMP)*, 31, 1980. doi: 10.1007/BF01590859. URL <https://doi.org/10.1007/BF01590859>.

- O. Pouliquen. Scaling laws in granular flows down rough inclined planes. *Physics of Fluids*, 11(3):542–548, 1999. doi: 10.1063/1.869928. URL <https://doi.org/10.1063/1.869928>.
- V. J. L. Ralaiarisoa, A. Valance, N. Brodu, and R. Delannay. High speed confined granular flows down inclined: numerical simulations. *EPJ Web Conf.*, 140:03081, 2017. doi: 10.1051/epjconf/201714003081. URL <https://doi.org/10.1051/epjconf/201714003081>.
- M. Ramaioli. Granular flow simulations and experiments for the food industry. page 104, 2008. doi: 10.5075/epfl-thesis-3997. URL <http://infoscience.epfl.ch/record/114765>.
- P. Richard, A. Valance, J. F. Métayer, P. Sanchez, J. Crassous, M. Y. Louge, and R. Delannay. Rheology of confined granular flows: scale invariance, glass transition, and friction weakening. *Physical Review Letters*, 101(24):248002, Dec. 2008. doi: 10.1103/PhysRevLett.101.248002. URL <https://hal.archives-ouvertes.fr/hal-00673366>.
- S. B. Savage and K. Hutter. The motion of a finite mass of granular material down a rough incline. *Journal of Fluid Mechanics*, 199:177–215, 1989. doi: 10.1017/S0022112089000340.
- L. Silbert, G. Grest, S. Plimpton, and D. Levine. Boundary effects and self-organization in dense granular flows. *Physics of Fluids*, 14(8):2637–2646, 2002. doi: 10.1063/1.1487379. URL <https://doi.org/10.1063/1.1487379>.
- L. E. Silbert, D. Ertas, G. S. Grest, T. C. Halsey, D. Levine, and S. J. Plimpton. Granular flow down an inclined plane: Bagnold scaling and rheology. *Phys. Rev. E*, 64:051302, Oct 2001. doi: 10.1103/PhysRevE.64.051302. URL <https://link.aps.org/doi/10.1103/PhysRevE.64.051302>.
- I. Smith and G. T. *Correlating laboratory and pilot scale reflux classification of fine coal*. PhD thesis, 2015.
- N. Taberlet, P. Richard, A. Valance, W. Losert, J. M. Pasini, J. T. Jenkins, and R. Delannay. Superstable granular heap in a thin channel. *Phys. Rev. Lett.*, 91:264301, Dec 2003. doi: 10.1103/PhysRevLett.91.264301. URL <https://link.aps.org/doi/10.1103/PhysRevLett.91.264301>.
- J. Torres-Serra, E. Romero, A. Rodriguez-Ferran, J. Caba, X. Arderiu, J. Padullés, and J. González. Flowability of granular materials with industrial applications - an experimental approach. volume 140, page 03068, 06 2017. doi: 10.1051/epjconf/201714003068.
- A. Treiman and M. Louge. Martian slope streaks and gullies: Origins as dry granular flows. 2004.
- T. Weinhart, A. R. Thornton, S. Luding, and O. Bokhove. Closure relations for shallow granular flows from particle simulations. *Granular Matter*, 14, July 2012. doi: 10.1007/s10035-012-0355-y. URL <https://doi.org/10.1007/s10035-012-0355-y>.
- S. Zhang, G. Yang, P. Lin, L. Chen, and L. Yang. Inclined granular flow in a narrow chute. *Eur. Phys. J. E*, 541(-1):40, April 2019. ISSN 1469-7645. doi: 10.1140/epje/i2019-11796-8. URL <http://dx.doi.org/10.1017/S0022112005005987>.

- Y. Zhu, D. R., and A. Valance. High-speed confined granular flows down smooth inclines: scaling and wall friction laws. *Granular Matter*, 22:40, 09 2020. ISSN 1434-7636. doi: 10.1007/s10035-020-01053-7. URL <https://doi.org/10.1007/s10035-020-01053-7>.